THE UNIVERSITY OF QUEENSLAND

AUSTRALIA

Quantum optomechanics in the unresolved sideband regime

James Bennett

B.Sc. (Hons)

A thesis submitted for the degree of Doctor of Philosophy at The University of Queensland in 2017

School of Mathematics and Physics,

ARC Centre of Excellence for Engineered Quantum Systems (EQuS)

Abstract

A cavity optomechanical system is formed when the resonance frequency of an optical cavity is dependent upon the position of a mechanical oscillator. This is achieved in a plethora of physical systems, spanning the range from cold atom clouds trapped in miniaturised optical cavities through to the kilogram-scale test masses of the four kilometre long advanced Laser Interferometer Gravitational-wave Observatory. The dynamical coupling between light and vibration thus engendered modifies both the optical and mechanical behaviours, and is responsible for a number of intriguing phenomena. Indeed, with optomechanical tools it becomes possible to observe the fact that macroscopic mechanical oscillators are governed by the laws of quantum mechanics, rather than familiar classical equations of motion. The preparation of mechanical oscillators in truly quantum states, such as squeezed states and two-mode entangled states, has already been experimentally demonstrated. It is predicted that further advances along these lines will permit sensitive tests of fundamental physics, in addition to delivering significant improvements to sensor and information processing technologies.

The majority of optomechanical protocols developed to date operate in the so-called *resolved sideband limit*, where the cavity bandwidth is small compared to the mechanical resonance frequency. This ensures that the optical cavity may be employed as a frequency-selective element for performing coherent control, but it also limits the quantity of circulating optical power and prevents one from reaching the standard quantum limit for position and force detection.

In this thesis we report research that has expanded the optomechanical toolbox in the *un*resolved sideband regime, where the linewidth of the cavity is larger than the mechanical resonance frequency. This is a natural operating regime for large-mass and/or low-frequency mechanical oscillators; micro-cavity devices with small mode volumes and large optomechanical coupling rates; high-bandwidth, high-quantum-efficiency position and force detection; optical pulse manipulation; and hybrid devices couple to low-frequency quantum ancillae, such as the motional degrees of freedom of cold atoms.

We begin this thesis by providing introductory material which covers advances in optomechanics and related fields; useful theoretical tools and their physical meanings; and some insights into technical details. These materials are included in the hope that they might be useful to other researchers in the field.

Our first contribution to optomechanics in the unresolved sideband regime is a theoretical study of a remotely-coupled hybrid atom–optomechanical system. This uses a cloud of cold atoms as a 'quantum handle' with which to control the state of a mechanical oscillator. The two systems are coupled *via* light, which significantly relaxes experimental requirements on integration of vacuum and cryogenic apparatus. We derive the conditions under which laser cooling of the atomic ensemble permits one to sympathetically cool the mechanical oscillator to its ground state and show that they are experimentally feasible. In addition, we combine this with feedback cooling of the mechanical device and show that there is a significant improvement in cooling capacity in the majority of parameter regimes.

We then detail a novel pulsed optomechanical interface that permits one to perform optical–

mechanical state swaps in the unresolved sideband limit. This can rapidly transfer quantum information between the light and mechanics for storage or for the preparation of nonclassical states. Our protocol involves a single deep-sub-mechanical-period optical pulse which interacts with a mechanical oscillator three times over half a mechanical period. This procedure can be used to perform near-ground state cooling, prepare squeezed mechanical states, and engineer nonclassical vibrational states which exhibit Wigner negativity. These are important building block for probing quantum decoherence and macroscopicity.

The final theoretical proposal contained in this thesis involves a squeezing-driven thermodynamic machine that operates in a regime where the common rotating wave approximation (RWA) does not provide an accurate description of the resonator's dynamics. We show that this device can act as a heat engine, a refrigerator, or a heat pump, depending upon the parameters chosen. Remarkably, this rich behaviour vanishes in the RWA limit, leaving only the heat pump phase. This points to the emergence of rich thermodynamical behaviours beyond the RWA regime. Furthermore, we provide an outline of how a sequence of pulsed optomechanical interactions may be used to squeeze an arbitrary initial mechanical state over a timescale much shorter than the mechanical period.

Finally, we present a summary of experimental work aimed at fabricating low-frequency (f), high-quality-factor (Q) mechanical oscillators from epitaxial silicon carbide films. Optical characterisation of our doubly-clamped beam resonators reveals $Q \times f$ products of $\sim 10^{12}$ Hz, making them state-of-the-art for room temperature string resonators at the time of publication. This indicates that they are well-isolated from their thermal environment, although not yet in the quantum coherent oscillation regime at room temperature. The insights gained during the fabrication and testing of these devices will inform the design of next-generation, high-Q SiC mechanical oscillators for optomechanical and electromechanical applications.

Declaration by author

This thesis is composed of my original work, and contains no material previously published or written by another person except where due reference has been made in the text. I have clearly stated the contribution by others to jointly-authored works that I have included in my thesis.

I have clearly stated the contribution of others to my thesis as a whole, including statistical assistance, survey design, data analysis, significant technical procedures, professional editorial advice, and any other original research work used or reported in my thesis. The content of my thesis is the result of work I have carried out since the commencement of my research higher degree candidature and does not include a substantial part of work that has been submitted to qualify for the award of any other degree or diploma in any university or other tertiary institution. I have clearly stated which parts of my thesis, if any, have been submitted to qualify for another award.

I acknowledge that an electronic copy of my thesis must be lodged with the University Library and, subject to the policy and procedures of The University of Queensland, the thesis be made available for research and study in accordance with the Copyright Act 1968 unless a period of embargo has been approved by the Dean of the Graduate School.

I acknowledge that copyright of all material contained in my thesis resides with the copyright holder(s) of that material. Where appropriate I have obtained copyright permission from the copyright holder to reproduce material in this thesis.

Publications during candidature

Peer-reviewed research papers

1. [1] **J. S. Bennett**, L. S. Madsen, M. Baker, H. Rubinsztein-Dunlop, and W. P. Bowen, Coherent control and feedback cooling in a remotely coupled hybrid atom–optomechanical system, *New Journal of Physics* 16, 083036, 2014

2. [2] **J. S. Bennett**, K. Khosla, L. S. Madsen, M. R. Vanner, H. Rubinsztein-Dunlop, and W. P. Bowen, A quantum optomechanical interface beyond the resolved sideband limit, *New Journal of Physics* 18, 053030, 2016

3. [3] A. R. Kermany, **J. S. Bennett**, V. M. Valenzuela, W. P. Bowen, and F. Iacopi, Potential of epitaxial silicon carbide microbeam resonators for chemical sensing (review article), *Physica Status Solidi A* DOI 10.1002/pssa.201600437, 2016

4. [4] A. R. Kermany, **J. S. Bennett**, G. A. Brawley, W. P. Bowen, and F. Iacopi, Factors affecting the $f \times Q$ product of 3C-SiC microstrings: What is the upper limit for sensitivity?, *Journal of Applied Physics* 119, 055304, 2016

Other published work

- **J. S. Bennett**, W. P. Bowen, Quantum measurement: Coping with pressure (News and Views), *Nature Physics* 1745-2481, 2016

Preprints

- **J. S. Bennett**, L. S. Madsen, H. Rubinsztein-Dunlop, and W. P. Bowen, Quantum thermodynamics beyond the rotating wave approximation, *arXiv* quant-ph 1705.09174v1, 2017

Conference abstracts

- **J. S. Bennett** *et al.*, Combining Feedback Cooling and Optomechanics with Cold Atoms, EQuS Annual Workshop, Mudjimba (QLD, Australia), 3rd December 2013—poster accompanied by abstract and three-minute spoken summary

- **J. S. Bennett** *et al.*, Combining Feedback Cooling and Optomechanics with Cold Atoms, EQuS Optomechanics Incubator, Brisbane (QLD, Australia), 6th December 2013—poster accompanied by abstract

- **J. S. Bennett** *et al.*, Feedback Cooling in Hybrid Atom–Optomechanical Systems, American Institute of Physics March Meeting, BAPS.2014.MAR.P1.339, Denver (Colorado, USA), 5th March 2014—poster accompanied by abstract

- **J. S. Bennett** *et al*., Combining Hybrid Atom–Optomechanics and Feedback Cooling, Gordon Research Conference (and the associated Gordon Research Seminar), Ventura Beach (California, USA), 8th & 11th March 2014—poster accompanied by abstract

- **J. S. Bennett** *et al*., Feedback cooling in hybrid atom–optomechanical systems, EQuS Optomechanics Incubator and Annual Workshop, Sydney (NSW, Australia), December 2014—poster accompanied by abstract

- **J. S. Bennett** *et al*., Pulsed optomechanics allows optomechanical state transfer in the Doppler regime, Teach at the Beach (student conference hosted by the Optical Society of America student chapter at UQ), Stradbroke Island (QLD, Australia), October 2014—oral presentation accompanied by abstract

- **J. S. Bennett** *et al*., Comparing Feedback Damping and Sympathetic Cooling in a Remotely-Coupled Hybrid Atom–Optomechanical System, Australian Institute of Physics Congress, Canberra (ACT, Australia), December 2014—oral presentation accompanied by abstract

- **J. S. Bennett** *et al*., A Pulsed Quantum Optomechanical Light–Matter Interface, WOMBAT (Workshop on OptoMechanics and Brillouin scattering: fundamentals, Applications and Technologies), Sydney (NSW, Australia), 22nd July 2015—oral presentation accompanied by abstract

- **J. S. Bennett** *et al*., A quantum optomechanical interface beyond the resolved sideband regime, EQuS Optomechanics Incubator, Brisbane (QLD, Australia), December 2015—poster accompanied by abstract

- **J. S. Bennett** *et al*., A quantum optomechanical interface beyond the resolved sideband regime, EQuS Optomechanics Incubator, Benowa (QLD, Australia), December 2015—poster accompanied by abstract and three-minute spoken summary

- **J. S. Bennett** *et al*., A Pulsed Quantum Optomechanical Light–Matter Interface, C3QS (Coherent Control of Complex Quantum Systems), Onna (Okinawa, Japan), April 2016—poster accompanied by abstract and three-minute spoken summary

- **J. S. Bennett** *et al*., Freezing the Decoherence of a Mechanical Oscillator with Unitary Interactions, APPC-AIP (Asia Pacific Physics Conference and 22nd Australian Institute of Physics Congress), Brisbane (QLD, Australia), December 2016—oral presentation accompanied by abstract. Winner of The Optical Society Best Student Paper Prize 2016.

Publications included in this thesis

1. **J. S. Bennett**, L. S. Madsen, M. Baker, H. Rubinsztein-Dunlop, and W. P. Bowen, Coherent control and feedback cooling in a remotely coupled hybrid atom–optomechanical system, *New Journal of Physics* 16, 083036, 2014
Incorporated as Chapter 4 with minor modifications.

Contributor	Statement of contribution	%
J. S. Bennett	writing of text	70
	proof-reading	60
	theoretical derivations	70
	numerical calculations	100
	preparation of figures	90
L. S. Madsen	writing of text	10
	proof-reading	10
	supervision, guidance	25
	theoretical derivations	10
	preparation of figures	3
M. Baker	writing of text	5
	proof-reading	5
	supervision, guidance	10
	theoretical derivations	10
H. Rubinsztein-Dunlop	writing of text	5
	proof-reading	10
	supervision, guidance	25
	preparation of figures	3
	initial concept	50
W. P. Bowen	writing of text	10
	proof-reading	15
	supervision, guidance	40
	theoretical derivations	10
	preparation of figures	4
	initial concept	50

- **Conception and design**.
  J.S.B. examined several different potential geometries for the proposed system before choosing the one featured in this paper. This was critically important, as it is impossible to reach the quantum ground state (a key research goal) in some geometries.
- **Analysis and interpretation**.
  J.S.B. performed the majority of analytical and numerical calculations included in this work.
- **Drafting and production of significant parts of scholarly work**.
  J.S.B. wrote the majority of the paper and prepared the figures with assistance as indicated above.

2. **J. S. Bennett**, K. Khosla, L. S. Madsen, M. R. Vanner, H. Rubinsztein-Dunlop, and W. P. Bowen, A quantum optomechanical interface beyond the resolved sideband limit, *New Journal of Physics* 18, 053030, 2016

Incorporated as Chapter 5 with minor modifications.

Contributor	Statement of contribution	%
J. S. Bennett	writing of text	70
	proof-reading	60
	theoretical derivations	70
	numerical calculations	90
	preparation of figures	90
K. Khosla	writing of text	2
	proof-reading	5
	theoretical derivations	15
	numerical calculations	10
L. S. Madsen	writing of text	10
	proof-reading	5
	supervision, guidance	25
M. R. Vanner	writing of text	3
	proof-reading	0
	supervision, guidance	10
	theoretical derivations	5
H. Rubinsztein-Dunlop	writing of text	5
	proof-reading	10
	supervision, guidance	25
	preparation of figures	3
W. P. Bowen	writing of text	10
	proof-reading	15
	supervision, guidance	40
	preparation of figures	4
	initial concept	100

- **Conception and design**.
  A fundamental question arising from our previous publication (how can one swap the states of two systems *via* an interaction with an ancilla when it is not possible to perform full swaps with the ancilla?) was answered by J.S.B. and W.P.B. This lead W.P.B. to propose the scheme presented in this paper.
- **Analysis and interpretation**.
  J.S.B. performed the majority of analytical and numerical calculations included in this work.
- **Drafting and production of significant parts of scholarly work**.
  J.S.B. wrote the majority of the paper and prepared the figures with assistance as indicated above.

3. A. R. Kermany, **J. S. Bennett**, G. A. Brawley, W. P. Bowen, and F. Iacopi, Factors affecting the $f \times Q$ product of 3C-SiC microstrings: What is the upper limit for sensitivity?, *Journal of Applied Physics* 119, 055304, 2016

4. A. R. Kermany, **J. S. Bennett**, V. M. Valenzuela, W. P. Bowen, and F. Iacopi, Potential of epitaxial silicon carbide microbeam resonators for chemical sensing (review article), *Physica Status Solidi A* DOI 10.1002/pssa.201600437, 2016

These two articles have been incorporated into Chapter 7. The break-downs given below apply to the published papers, *not* the thesis chapter. Chapter 7 was prepared by J.S.B. by compiling relevant data and figures from the published papers, trimming irrelevant material, re-writing approximately 70% of the text, and adding new (*i.e.* previously unpublished) explanations, data, and figures. For example, § 7.6 and § 7.8 are composed of entirely new material, as are Fig. 7.6, Fig. 7.7, Fig. 7.8, Fig. 7.9, Fig. 7.10, and Fig. 7.13.

Contributor	Contribution to 3.	%	Contribution to 4.	%
A. R. Kermany	writing of published text	70	writing of published text	70
	proof-reading	60	proof-reading	70
	preparation of figures	80	preparation of figures	20
	device fabrication	100	review of literature	60
	theoretical derivations	80		
	numerical calculations	100		
J. S. Bennett	writing of published text*	5	writing of published text*	5
	proof-reading	10	proof-reading	10
	preparation of figures	10	preparation of figures	65
	experimental measurements	95	review of literature	10
			theoretical calculations	70
G. A. Brawley	writing of published text	5		
	experimental measurements	5		
	supervision, guidance	10		
	theoretical derivations	10		
	preparation of figures	4		
V. M. Valenzuela			writing of published text	5
			preparation of figures	5
			review of literature	10
			theoretical calculations	30
W. P. Bowen	writing of published text	10	writing of published text	10
	proof-reading	10	proof-reading	10
	preparation of figures	3	preparation of figures	5
	supervision, guidance	40	supervision, guidance	30
	initial concept	30	review of literature	5
F. Iacopi	writing of published text	10	writing of published text	10
	proof-reading	10	proof-reading	10
	preparation of figures	3	preparation of figures	5
	supervision, guidance	40	supervision, guidance	70
	theoretical derivations	10	review of literature	15
	initial concept	70		

- **Conception and design**.

  J.S.B. and G.A.B. designed, constructed, and assembled the experimental apparatus and method needed for paper 3.

  J.S.B. and W.P.B. conceived the additions to paper 4 (originally conceived by A.R.K. and F.I.)—specifically, the sections concerning mass sensing; the literature review of achievable mass sensitivity; and the calculations of theoretical limits of SiC devices.
- **Analysis and interpretation**.

  J.S.B. collected the experimental data and analysed them to extract resonator parameters for paper 3.

  J.S.B. and V.M.V. completed the literature review of mechanical parameters which was begun by A.R.K., and performed calculations of the theoretical performance of the devices. This was a significant portion of the work, requiring approximately three weeks to complete.
- **Drafting and production of significant parts of scholarly work**.

  A.R.K. wrote the majority of papers 3 and 4, with additions by J.S.B. and W.P.B.

  J.S.B. proof-read and edited both papers; supplied significant figures—including a graphical summary of performance achieved by resonators in the literature—and the appropriate captions and discussion.

  As noted above, J.S.B. consolidated and re-wrote the majority of both papers for inclusion in this thesis; also added new, unpublished material that expands on the experiments and other SiC resonators not featured in the original papers.

Contributions by others to the thesis

Ann Bui (Chapter 1 & 8), Kiran Khosla (Chapter 3), and Nicholas Wyatt (Chapter 7) assisted with proof-reading.

Lars S. Madsen, Warwick P. Bowen, and Halina Rubinsztein-Dunlop provided critical feedback, editing, and supervision throughout my candidature.

Several micrographs were provided by Christopher Baker, Warwick P. Bowen, Eric Romero-Sánchez, and Atieh R. Kermany, as acknowledged in the text.

Fig. 2.1 reproduced from [5], ©APS; reused with permission (License 4134590858663).

Fig. 2.3 reproduced from [6], ©APS; reused with permission (License 4136230123632).

All other contributions are as acknowledged in 'Publications included in this thesis.'

Statement of parts of the thesis submitted to qualify for the award of another degree

None.

Acknowledgments

This document is the culmination of many hours of work, very few of which were spent in a vacuum.

Thank you to my office mates over the past years: Tihan Bekker, Stefan Förstner, Glen Harris, Terry McRae, Andreas Næsby, Ulysse Najar, Jonathan Swaim, Nicholas Wyatt, Changqiu 'Sarah' Yu, and Xiuwen Zhou. In addition to tolerating my love of music and swords, you have provided many excellent teaching and learning opportunities, and debates—both in physics and outside!

I have worked alongside many excellent scientists at The University of Queensland; Ardalan Armin, Christopher Baker, Sahar Basiri-Esfahani, Thomas Bell, Robin Cole, Ulrich Hoff, Atieh Kermany, Zulfiqar Khan, Isaac Lenten, Nicolas Mauranyapin, David McAuslan, Nicholas McKay-Parry, Tyler Neely, Martin Ringbauer, Eric Romero-Sánchez, Eoin Sheridan, Alex Szorkovszky, Michael Taylor, Victor Valenzuela, and Yimin Yu. George Brawley, Glen Harris, Kiran Khosla, and Yauhen 'Eugene' Sachkou provided particularly important technical discussions.

I also wish to acknowledge extremely useful discussions with Ronnie Kosloff, Klemens Hammerer, Philipp Treutlein, and Andreas Jöckel from external institutions.

My co-authors have my gratitude for their roles: Mark Baker, George Brawley, Francesca Iacopi, Atieh Kermany, Kiran Khosla, Victor Valenzuela, and Michael Vanner.

The experimental portion of my work would not have been possible without the Australian National Fabrication Facility and Griffith University. The UQ Physics Workshop staff—Neil 'Griff' Griffiths, Dave Perkins, and Alan Reid—have been invaluable for their technical skills and, at times, their fashion advice.

The efforts of Ruth Forrest, Kaerin Gardner, Murray Kane, Tara Massingham, Danette Peachey, Tara Roberson, Jenny Robinson, and Lisa Walker made administration far less of a burden that it would have been. Sam Zammit was very helpful setting up and maintaining my work computer.

I acknowledge support by the Australian Federal Government *via* an Australian Government Research Training Program Scholarship. My supervisors have also graciously supported my work, sent me to many conferences, and provided all of the laboratory equipment necessary: even when I accidentally burnt out that €5000 amplifier...

On that note, my supervisors have been excellent to me: patient when patience was required, demanding when needed, but always encouraging. I have been given many opportunities by your work and your wisdom. Thank you Warwick, Halina, and Lars.

Josh, thanks for the consistent lunch dates at Physiol, even if your ruthenium complexes meant you were always late.

Thank you Ann, who "Lovingly smiled at [my] humour, and encouraged [my] passion towards writing, swords, and Christianity."

Finally, my parents and family are owed a great debt of gratitude for supporting me through all of this. They might not know much physics, but they do know how to deal with a tired and grumpy son/brother/Nuncle who gets far better treatment than he deserves. Thank you Mum, Dad, Moo, Bec, and Ryler.

Keywords

Quantum optomechanics, pulsed optomechanics, atom–optomechanics, quantum thermodynamics, quantum interfaces

Australian and New Zealand Standard Research Classifications (ANZSRC)

ANZSRC code: 020604, Quantum optics, 70%
ANZSRC code: 020699, Quantum physics not elsewhere classified, 20%
ANZSRC code: 020603, Quantum information, computation and communication, 10%

Fields of Research (FoR) Classification

FoR code: 0206, Quantum physics, 80%
FoR code: 0299, Other physical sciences, 20%

Contents

List of figures

List of tables

List of abbreviations and symbols

Symbol	Description
AC	Alternating Current
AFM	Atomic Force Microscopy/Microscope
AM	Amplitude Modulation
ANFF	Australian National Fabrication Facilities
AOM	Acousto–Optic Modulator
APS	American Physical Society
BEC	Bose–Einstein Condensate/Condensation
BMME	Born–Markov Master Equation
CVD	Chemical Vapour Deposition
DC	Direct Current
d-c	Doubly–Clamped
DNA	DeoxyriboNucleic Acid
EOM	Electro-Optic Modulator
FEM	Finite-Element Method
FWHM	Full Width at Half-Maximum
LC	Inductor (L)–Capacitor (C)
LIGO	Laser Interferometer
	Gravitational-wave Observatory
LO	Local Oscillator
LPF	Low-Pass Filter(ing)
MEMS	Micro-Electro Mechanical Systems
NEMS	Nano-Electro Mechanical Systems
ODE	Ordinary Differential Equation
OMIA	Opto-Mechanically-Induced Absorption
OMIT	Opto-Mechanically-Induced Transparency
PM	Phase Modulation
PSD	Power Spectral Density
PZT	Pb (lead) Zirconate Titanate
QED	Quantum Electro-Dynamics

Symbol	Description
QMFSS	Quantum-Mechanics-Free Sub-System
QND	Quantum Non-Demolition (interaction or measurement)
RF	Radio Frequency
RWA	Rotating/Resonant Wave Approximation
s-c	Singly-Clamped
SEM	Scanning Electron Microscope/Microscopy
SMF	Single Mode Fibre
TED	Thermo-Elastic Dissipation
TiS	Titanium-Sapphire (laser)
3C-SiC	3-Cubic Silicon Carbide

Symbol	Description
$\mathbb{1}$	Identity matrix
$\hat{\rho}$	Density operator
$\hat{x}$	Position operator
X	Dimensionless position operator, amplitude quadrature
$\hat{p}$	Momentum operator
P	Dimensionless momentum operator, phase quadrature
m	Mass, modulation depth
M	Effective mass
ω_{M}	Mechanical resonance frequency (angular)
f_n	Resonance frequency (not angular) of n^{th} mode
Ω	Oscillation frequency, modulation frequency
a ($a^\dagger$) or b ($b^\dagger$)	Annihilation (creation) operators
a_{in} (a_{out})	Input (output) annihilation flux operator
α, β	Coherent amplitude, mean field (expectation value)
$\hat{D}(\beta)$	Displacement operator, amplitude β
$S(\xi_{\mathrm{s}})$	Squeezing operator
r_{s}	Squeezing parameter magnitude
θ_{s}	Squeezing parameter half-angle, angle of squeezed quadrature
Γ	Mechanical loss rate, FWHM
Q	Q ('quality') factor
κ_{int}	Optical linewidth (intrinsic)

Symbol	Description
κ	Optical linewidth (coupling contribution)
g	Optomechanical coupling coefficient
g_0	Single-photon optomechanical coupling rate
$\bar{n}$	Thermal occupancy, effective occupancy
T	Temperature
C	Cooperativity
Δ	Detuning of optical drive from cavity
N	Mean photon number
$\mathscr{F}$	Fidelity, finesse
A	Drift matrix
$S_{ff}[\omega]$	Power spectrum
$\check{\delta}_\tau$	Representation of Dirac δ
	broadened by finite measurement time
$\boldsymbol{X}$	'Vector' containing X and P
$\boldsymbol{q}$	'Vector' containing arbitrary system operators
V	Covariance matrix
V_{SS}	Steady-state covariance matrix
V_{FF}	Covariance of thermal force
δX, δP, *etc.*	Fluctuation operators
$W(\boldsymbol{r})$	Wigner function
$P_{\mathrm{GS}}(\alpha)$	Glauber-Sudarshan P-function
$Q_{\mathrm{H}}(\alpha)$	Husimi Q-function
$\tilde{f}(\omega)$	Fourier transform of function $f(t)$
χ	Mechanical susceptibility, characteristic function,
	QND interaction strength
$\mathscr{V}$	Mode volume
μ	Rescaled pulse interaction strength,
	degree of squeezing
η_{M}	Mechanical 'efficiency'
ε	Inverse Q factor, coupling to cold bath
M_{hom}	Homogeneous part of evolution (matrix)
σ	Frequency shift due to damping,
	residual mean stress
$\Delta\sigma$	Gradient stress
R	Surface area to volume ratio
L–w–t	Length, width, thickness

Chapter 1

Introduction

1.1 Quantum optomechanics

Optomechanics is fundamentally concerned with the transfer of momentum between light and mechanical degrees of freedom. Though the first experimental confirmation that light does carry momentum was performed as far back as 1901 [7, 8], the modern field of optomechanics did not arise until *circa* 1960. At that time a key goal was the detection of gravitational waves using resonant bars [9] or large interferometers with mechanically-compliant mirrors. Quantum mechanics entered the picture when it was shown that vacuum fluctuations of the optical field set a limit to how sensitively the necessary position measurements can be made [10–13], and that the mechanical vibrations themselves could be on the quantum scale [9, 14].

Nowadays, quantum optomechanics is most readily understood in the context of an optical cavity with a mechanically compliant mirror. Motions of the mirror change the resonance frequency of the cavity, which in turn modulates the force applied to the mirror *via* radiation pressure. This archetypical system is depicted in Fig. 1.1.

Optomechanical systems have now undeniably entered the quantum regime. In 2011, two landmark studies [15, 16] successfully applied the technique of optomechanical sideband cooling (introduced in § 2.2.3) to prepare mechanical oscillators in their quantum ground states[1]. Later studies have demonstrated progress even further into the quantum world, such as observing the zero-point motion of a mechanical oscillator [18], generating ponderomotive squeezing [19–21], measuring mechanical squeezing below the ground state variance [22], and directly detecting the radiation pressure noise that arises from quantisation of the electromagnetic field [23–25], to name only a few.

It is likely that quantum optomechanics will play an important role in investigating the quantum-to-classical transition [26], and also diversify into practical applications that leverage quantum techniques to achieve performance beyond that available classically, *e.g.* quantum-enhanced magnetometry [27], mass sensing [28], accelerometry [29], and the landmark detection of gravitational waves [30].

[1] O'Connell *et al.* were the first to cool a solid-state mechanical oscillator to its motional ground state [17], but this was achieved without using optomechanical methods. Ground state cooling will be discussed further in § 2.2.3

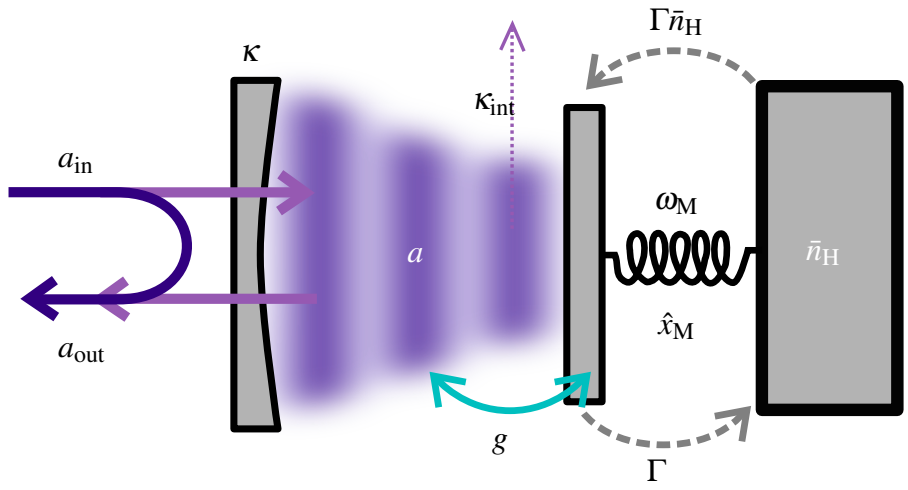

Figure 1.1: Archetypical optomechanical system formed by an optical cavity with one compliant mirror. The cavity is pumped by the field a_{in} to maintain a large mean photon occupancy in the mode a. Radiation pressure couples the mirror to the optical field at a rate g. Phonons can leak from the oscillator at a rate Γ, and thermal phonons enter at $\Gamma\bar{n}_{\mathrm{H}}$, where $\bar{n}_{\mathrm{H}}$ is the bath occupancy. Optical excitations can leave *via* the input–output coupler at rate κ, or be damped by absorption or scattering into other modes at rate κ_{int}. Further discussion of these parameters can be found in Chapter 2.

To date, the majority of *quantum* optomechanics has resided in the so-called resolved sideband limit. This is the regime in which the optical cavity's linewidth is smaller than the mechanical resonance frequency ($\kappa \ll \omega_{\mathrm{M}}$). The cavity therefore acts like a frequency-selective filter which can be used to control photon-phonon scattering processes (*cf.* § 2.2). A well-developed toolbox of 'canonical' optomechanical manipulation techniques exists in this limit.

There are many compelling reasons to consider the converse situation, where the linewidth is much larger than the mechanical frequency ($\kappa \gg \omega_{\mathrm{M}}$). This is variously known as the unresolved sideband limit, the high-bandwidth limit, or the 'bad-cavity' limit. For instance, one may be interested in using low-frequency oscillators (*e.g.* [31]) so that they can be coupled to other systems with low-frequency resonances (as in a hybrid atom–optomechanical system, Chapter 4), to ensure that the mirror has a large mass for studies of gravitation [30] or collapse mechanisms [26], or because one can obtain higher mechanical Q factors at low frequencies if the resonator is material-damping limited (due to the Akhiezer effect [32, 33]). Alternatively, one may wish to obtain a large optomechanical coupling rate—a large force per photon, characterised by the rate g_0—by employing an optical cavity with a small mode volume [34, 35]. This typically increases the optical linewidth. Finally, the regime of large linewidth lends itself to large circulating cavity power and efficient position detection, making it an appropriate limit for measurements of position at the standard quantum limit (SQL) [36].

The toolbox for quantum control of oscillators in the unresolved sideband regime is notably more sparse than its resolved counterpart. However, this situation is beginning to change. The work presented in this thesis represents further progress towards quantum optomechanics in the unresolved sideband limit.

It is worth noting that many systems display physics that are entirely analogous to that of the archetypical cavity system shown in Fig. 1.1. Key examples include electromechanical devices,

where the mechanical degree of freedom modulates the capacitance [37] or inductance [38] of an LC (inductor–capacitor) circuit; dielectrics (including superfluids) suspended or trapped inside rigid cavities, which alter their effective path length [39–43]; polarised spin ensembles [44–46] interacting with an optical cavity; and atomic clouds in rigid cavities, where the self-organised atom clouds act as a mirror [47–49]. Thus, much of the theory content of this thesis can equally well be translated for use in these alternative physical settings.

1.2 Outline of thesis

This thesis is designed such that it can be read as a stand-alone introduction to quantum optomechanics in addition to detailing the key goals and outcomes of our work in the field. As such, the remainder of Chapter 1 will be spent introducing the basic language and notation of quantum optics, which forms the basis of our work.

Part I of the thesis will cover important theoretical and experimental tools, progress in the field of optomechanics, and recent advances in optomechanics beyond the resolved sideband regime. Chapter 2 will introduce the unitary and dissipative dynamics of optomechanical devices and show how they may be utilised in the resolved sideband limit. It will then go on to introduce schemes for optomechanical systems that operate outside of the resolved sideband limit. Chapter 3 will provide further clarification of some technical points, and will introduce important theoretical and experimental tools which are to be used in later portions of this thesis.

Part II will detail our novel theoretical proposals. Chapter 4 details our proposal for a cavity-enhanced hybrid atom–optomechanical system. In Chapter 5 we discuss a quantum light–matter interface based on pulsed optomechanics. Finally, in Chapter 6 we will consider a thermodynamic engine which demonstrates that the rotating wave approximation—which is commonly used in optomechanics—can lead to incorrect predictions in quantum thermodynamics.

Part III covers our experimental characterisation of silicon carbide (SiC) micromechanical resonators that are suitable for optomechanics in the unresolved sideband regime. This is detailed in Chapter 7.

Chapter 8 summarises the key research outcomes presented in this thesis, and details some directions which further research could take.

Finally, the Appendices will include summaries of important mathematical relations and derivations that would otherwise interrupt the main text. The reader will be pointed towards the Appendices where appropriate.

1.3 Primer on quantum optics

Quantum optomechanics is couched in the language of quantum optics. In this section we will briefly introduce some of the basic theory needed to continue.

In many ways quantum optics is the physics of the simple harmonic oscillator. Harmonic oscillators are ubiquitous physical systems, encompassing fundamental particles, trapped ions and neutral atoms, optically– and magnetically–tweezed particles, low-amplitude elastic modes and pendula, electromagnetic field modes, LC circuits, and many other situations.

A harmonic oscillator of mass M and resonance (angular) frequency Ω is classically described by the Hamiltonian function

$$\mathscr{H}(x,p) = \frac{1}{2}\left(\frac{p^2}{M} + M\Omega^2 x^2\right),$$

in which x is the position and p is the conjugate momentum.

The quantum mechanical description of a harmonic oscillator is very similar, except that x and p become non-commuting Hermitian operators ($\hat{x}$ and $\hat{p}$) that obey the canonical commutation relation

$$[\hat{x},\hat{p}] = \hat{x}\hat{p} - \hat{p}\hat{x} = \mathrm{i}\hbar\mathbb{1}.$$

$\mathbb{1}$ is the identity operator, and $\hbar \approx 1.0546 \times 10^{-34}$ Js is the reduced Planck constant.

Although $\hat{x}$ and $\hat{p}$ correspond to observables, in many situations it is extremely useful to consider the non-Hermitian operator

$$a = \sqrt{\frac{M\Omega}{2\hbar}}\left(\hat{x} + \mathrm{i}\frac{\hat{p}}{M\Omega}\right).$$

By construction, we have $\left[a, a^\dagger\right] = \mathbb{1}$, where the 'dagger' (†) represents the Hermitian conjugate [2]. We can then write the Hamiltonian operator as

$$\hat{H} = \hbar\Omega\left(a^\dagger a + \frac{1}{2}\mathbb{1}\right). \tag{1.1}$$

1.3.1 Fock states

The Hamiltonian commutes with the Hermitian operator $a^\dagger a$. This means that they share a complete set of simultaneous eigenstates [50]. Let us then consider the action of a upon an eigenstate of $\hat{n}$, which we represent as $|n\rangle$ satisfying the eigenvalue equation $\hat{n}|n\rangle = n|n\rangle$. We find that

$$\begin{aligned}
\hat{n}(a|n\rangle) &= (\hat{n}a)|n\rangle \\
&= (\hat{n}a + a\hat{n} - a\hat{n})|n\rangle \\
&= (a\hat{n} - [a,\hat{n}])|n\rangle \\
&= (na - a)|n\rangle \\
&= (n-1)(a|n\rangle).
\end{aligned}$$

An analogous calculation yields

$$\hat{n}\left(a^\dagger|n\rangle\right) = (n+1)\left(a^\dagger|n\rangle\right).$$

[2] We will not place a 'hat' on operators unless there is potential for confusion between them and their eigenvalues (*e.g.* for the number operator). Eigenvalues and/or expectation values of annihilation operators will be written in Greek letters throughout this thesis.

From these relations we can see that a converts an eigenstate of the Hamiltonian into another eigenstate with $\hbar\Omega$ less energy, whereas $a^\dagger$ raises the energy by $\hbar\Omega$. For this reason $a^\dagger$ and a are known as the creation and annihilation operators, or simply the raising and lowering operators.

In the absence of external forces the annihilation operator has extremely simple time-dependence (in the Heisenberg picture), *viz.*

$$a(t) = a(0)\,\mathrm{e}^{-\mathrm{i}\Omega t}. \tag{1.2}$$

A full calculation of the Hamiltonian's spectrum shows that the energy eigenvalues are in fact quantised in units of $\hbar\Omega$, so that $n \in \mathbb{W}$ corresponds to the number of excitations in a given eigenstate. $\hat{n}$ is therefore known as the number operator. Each excitation can be thought of as a bosonic (quasi)particle; the quanta of an electromagnetic field are known as photons, whilst the quanta of a vibrational mode are called phonons.

The number eigenstates are known as Fock states, and they obey

$$\begin{aligned}
\hat{H}\,|n\rangle &= \hbar\Omega\left(n+\frac{1}{2}\right)|n\rangle \;\forall\, n \in \{0,1,2,\ldots\} && \text{(1.3a)}\\
a\,|n\rangle &= \sqrt{n}\;|n-1\rangle && \text{(1.3b)}\\
a^\dagger\,|n\rangle &= \sqrt{n+1}\;|n+1\rangle && \text{(1.3c)}\\
\langle n|m\rangle &= \delta_{n,m} && \text{(1.3d)}\\
\sum_{n=0}^{\infty}|n\rangle\langle n| &= \mathbb{1} && \text{(1.3e)}\\
\langle n|\,\hat{x}\,|n\rangle &= 0 && \text{(1.3f)}\\
\langle n|\,\hat{p}\,|n\rangle &= 0, && \text{(1.3g)}
\end{aligned}$$

in which $\delta_{n,m}$ is the Kronecker delta.

The eigenket with the lowest energy is called the vacuum or ground state, $|0\rangle$. Unlike the other Fock states, the vacuum maps onto itself when acted upon by the annihilation operator; it satisfies $a\,|0\rangle = 0\,|0\rangle$. All of the Fock states may be generated by repeatedly applying the creation operator to $|0\rangle$, *viz.*

$$|n\rangle = \frac{\left(a^\dagger\right)^n}{\sqrt{n!}}\,|0\rangle\,.$$

Unlike the classical case, where the minimum energy configuration has zero energy, the quantum ground state has a finite energy of $\hbar\Omega/2$ *i.e.* 'half a quantum' worth of energy. This zero-point energy can be thought of as a manifestation of the non-commutativity of $\hat{x}$ and $\hat{p}$, and it gives rise to the so-called vacuum noise that enforces the Heisenberg uncertainty relation (*cf.* § 1.3.4, Eqn (1.8)).

1.3.2 Coherent states

The ground state is also the simplest example of another important class of states of the harmonic oscillator: the coherent states. Physically, the coherent states have two key properties;

- the mean values of $\hat{x}$ and $\hat{p}$ in a coherent state map out a classical trajectory, and

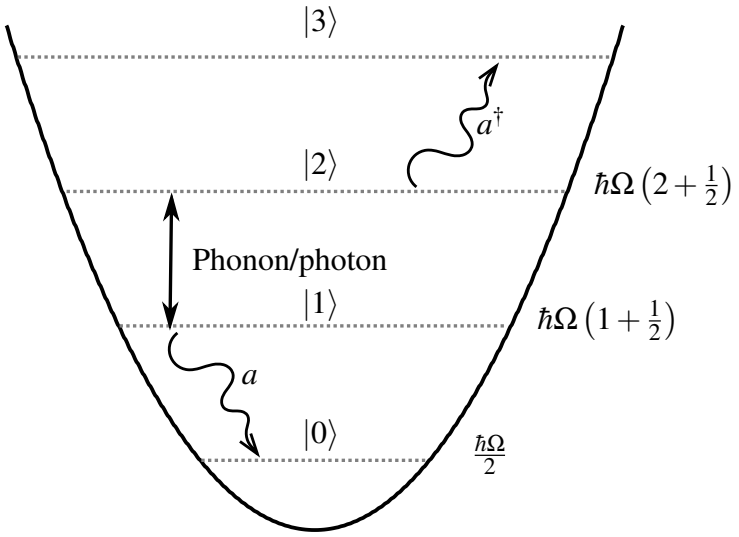

Figure 1.2: Energy levels of a simple harmonic oscillator. Each excitation corresponds to the creation of a bosonic (quasi)particle with energy $\hbar\Omega$. The excitations of an optical field are called photons; those of an acoustic field or vibration are phonons. The annihilation operator moves one 'rung' down the 'ladder' of energy levels by destroying an excitation, whilst $a^\dagger$ creates an excitation.

- the noise statistics are identical to those of the vacuum state.

Clearly the only Fock state that satisfies these is $|0\rangle$. It was shown by Glauber [51] that we must instead look to the eigenstates of the annihilation operator; that is, a coherent state $|\alpha\rangle$ satisfies

$$a|\alpha\rangle = \alpha|\alpha\rangle .$$

The annihilation operator is not Hermitian, and therefore α may be a complex number.

We saw already that Fock states can be generated from the vacuum by applying the operator $\left(a^\dagger\right)^n (n!)^{-1/2}$ to them. Similarly, coherent states may be built from the vacuum by applying

$$\hat{D}(\alpha) = \exp\left\{\alpha a^\dagger - \alpha^* a\right\}.$$

$\hat{D}$ is unitary, obeys $\hat{D}^\dagger(\alpha) = \hat{D}(-\alpha)$, and is called the displacement operator because it shifts the expectation value of a according to

$$\hat{D}(\alpha)^\dagger a \hat{D}(\alpha) = a + \alpha.$$

As we shall see in § 3.1.2, this has the effect of displacing the oscillator's Wigner function in phase space.

It will occasionally be useful to connect the coherent states to the Fock states through the relation

$$|\alpha\rangle = \mathrm{e}^{-\frac{1}{2}|\alpha|^2} \sum_{\mathrm{n}=0}^{\infty} \frac{\alpha^n}{\sqrt{n!}} |n\rangle .$$

However, it is often the case that we can perform calculations without leaving the coherent state representation. This is especially useful when considering quantum analogues of classical phase space

distributions (§ 3.2). In this setting it is useful to know that the coherent states are non-orthogonal and overcomplete, meaning that

$$\begin{aligned}\langle\beta|\alpha\rangle &= \exp\left\{-\frac{1}{2}|\alpha|^2-\frac{1}{2}|\beta|^2+\beta^*\alpha\right\}\\ \mathbb{1} &= \frac{1}{\pi}\int \mathrm{d}^2\alpha\ |\alpha\rangle\langle\alpha|\,.\end{aligned}$$

A summary of these properties and further technical details can be found in App. A.1.

1.3.3 Correspondence between the harmonic oscillator and optical fields

Having introduced the harmonic oscillator in the context of the mechanical oscillator, we are now ready to examine the correspondence between an optical field mode and a harmonic oscillator. We will provide a heavily abbreviated outline of the derivation; for a thorough treatment see [52].

In free space the Hamiltonian of the classical electromagnetic field is

$$\mathscr{H} = \frac{\varepsilon_0}{2}\int \mathrm{d}^3\boldsymbol{r}\ \left(\boldsymbol{E}\cdot\boldsymbol{E}+c_0^2\boldsymbol{B}\cdot\boldsymbol{B}\right),$$

in which the electric field is $\boldsymbol{E}(\boldsymbol{r},t)$, the magnetic field is $\boldsymbol{B}(\boldsymbol{r},t)$, ε_0 is the permittivity of free space, and c_0 is the speed of light. The dynamics induced by this Hamiltonian are conveniently summarised by the equation of motion for the vector potential $\boldsymbol{A}(\boldsymbol{r},t)$, which—in the Coulomb gauge—satisfies

$$\nabla^2\boldsymbol{A} = \frac{1}{c_0^2}\frac{\partial^2\boldsymbol{A}}{\partial t^2} \tag{1.4a}$$

$$\nabla\cdot\boldsymbol{A} = 0\ (\text{Coulomb gauge}), \tag{1.4b}$$

and encodes the physical fields according to

$$\boldsymbol{B} = \nabla\times\boldsymbol{A} \tag{1.5a}$$

$$\boldsymbol{E} = -\frac{\partial\boldsymbol{A}}{\partial t}. \tag{1.5b}$$

∇ is the usual vector differential operator.

Eqn (1.4a) can be solved by separation of variables. For a monochromatic field

$$\boldsymbol{A}(\boldsymbol{r},t) = \alpha(t)\,\boldsymbol{u}(\boldsymbol{r})+\alpha^*(t)\,\boldsymbol{u}^*(\boldsymbol{r})$$

in which we have introduced the complex amplitude $\alpha(t)$ and the complex mode shape $\boldsymbol{u}(\boldsymbol{r})$. We then find that $\boldsymbol{u}(\boldsymbol{r})$ satisfies the Helmholtz equation, whilst $\alpha(t)=\alpha(0)\,\mathrm{e}^{-\mathrm{i}\Omega t}$. This is precisely the behaviour we saw for the annihilation operator in Eqn (1.2).

To complete the analogy we rescale α by a factor of $\mathrm{i}\sqrt{\frac{\hbar}{2\Omega\varepsilon_0}}$, employ Eqn (1.5) to rewrite the Hamiltonian in terms of the new complex amplitude, and then integrate over the spatial degrees of freedom $\boldsymbol{r}$ to obtain the Hamiltonian

$$\mathscr{H} = \hbar\Omega\frac{\alpha^*\alpha+\alpha\alpha^*}{2}.$$

Thus, when this is quantised by identifying α with the annihilation operator we obtain the usual quantum harmonic oscillator Hamiltonian, Eqn (1.1).

In the case that the mode function is real the quantised fields are then [52]

$$\hat{\boldsymbol{E}}(\boldsymbol{r},t) = -\sqrt{\frac{\hbar\Omega}{2\varepsilon_0}}\left[a^\dagger(t)+a(t)\right]\boldsymbol{u}(\boldsymbol{r}) \tag{1.6a}$$

$$\hat{\boldsymbol{B}}(\boldsymbol{r},t) = -\sqrt{\frac{\hbar}{2\Omega\varepsilon_0}}\left[\mathrm{i}\left(a^\dagger(t)-a(t)\right)\right]\nabla\times\boldsymbol{u}(\boldsymbol{r}). \tag{1.6b}$$

1.3.4 Quadrature operators and squeezing

By inspecting Eqn (1.6) we can see that the electric and magnetic fields are essentially determined by the operators $a^\dagger(t)+a(t)$ and $\mathrm{i}\left(a^\dagger(t)-a(t)\right)$. In the quantum optics community these are collectively known as the quadrature operators. We will use the symbols X and P to denote them, *viz.*

$$X = a^\dagger + a \tag{1.7a}$$

$$P = \mathrm{i}\left(a^\dagger - a\right). \tag{1.7b}$$

This choice of notation is no coincidence; for a mechanical harmonic oscillator X and P are precisely the operators obtained by rescaling $\hat{x}$ and $\hat{p}$ such that their ground state variances become unity. Given that $[X,P]=2\mathrm{i}$ this rescaling procedure is sometimes referred to as 'setting $\hbar=2$'.

In the context of optics X is known as the amplitude quadrature, whilst P is the phase quadrature. To understand these names we will introduce the 'ball-and-stick' graphical representation of a coherent state. This is a simple precursor to the more general Wigner function which will be discussed in § 3.1.2. The 'stick' is given by the expectation value of a, and the 'ball' represents the quantum noise around the expectation value, as shown in Fig. 1.3. Thus, if we consider a coherent state $|\alpha\rangle$ where α is large and real then noise on X alters the length of the stick, whilst noise on P alters its phase angle.

The Heisenberg uncertainty relation becomes

$$\left\langle \delta X^2\right\rangle \left\langle \delta P^2\right\rangle \geq 1, \tag{1.8}$$

in which $\delta X = X - \langle X\rangle$ is a fluctuation operator (deviation from the mean value). Thus, any coherent state saturates Eqn (1.8).

There is no physical reason why one quadrature cannot have a variance less than that of the ground state; the variance of the orthogonal (that is, canonically conjugate) quadrature simply needs to be increased such that Eqn (1.8) is satisfied. States with these features are called squeezed states. Physically, they are produced by nonlinear processes such as the Kerr nonlinearity. Mathematically, they are generated through the action of the squeezing operator

$$S(\xi_\mathrm{s}) = \exp\left\{\frac{1}{2}\left(\xi_\mathrm{s}^* a^2 - \xi_\mathrm{s}\, a^{\dagger\,2}\right)\right\},$$

which modifies the annihilation operator according to

$$S^\dagger a S = a\cosh r_\mathrm{s} - a^\dagger \mathrm{e}^{\mathrm{i}2\theta_\mathrm{s}}\sinh r_\mathrm{s},$$

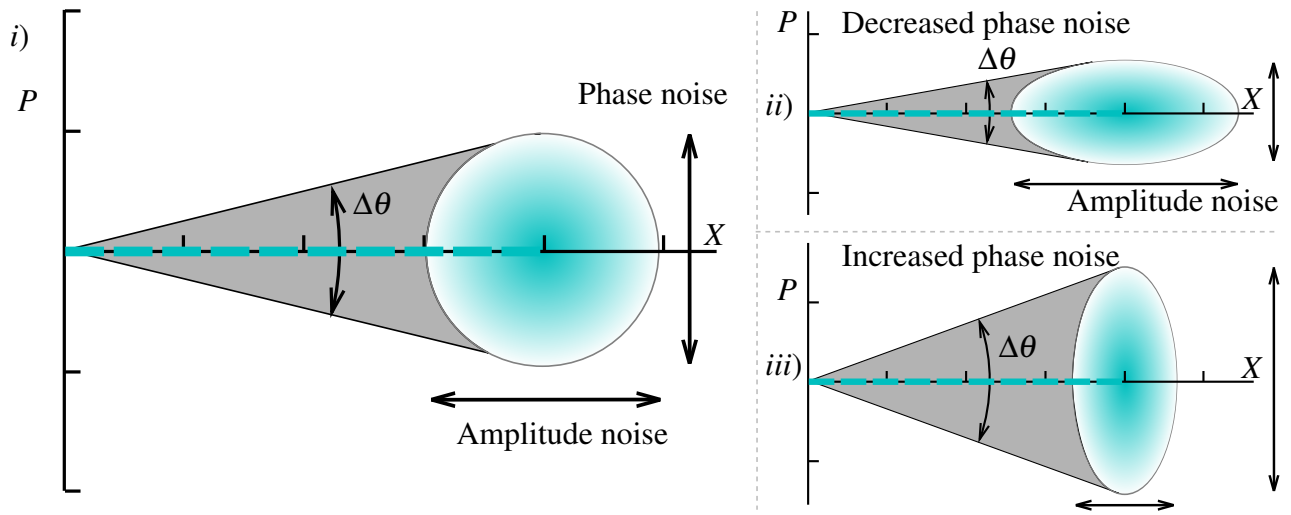

Figure 1.3: 'Ball-and-stick' representation of quantum states. The 'stick' (dashed) is the phasor representing the mean amplitude *i.e.* $\langle\alpha\rangle$. The 'ball' shows the quantum noise variance.
i) A coherent state $|\alpha = 2\rangle$. Note that $\langle X\rangle = 4$. The ball represents the vacuum noise, which is equal on all quadratures.
ii) A phase-squeezed state. The fluctuations of P have been reduced at the expense of increasing fluctuations in X.
iii) An amplitude-squeezed state. The reduction of the amplitude noise increases the uncertainty of the phase ($\Delta\theta$).

with $\xi_s = r_s e^{i2\theta_s}$.

When applied to the ground state, the squeezing angle θ_s determines which quadrature operator is reduced to below the ground state variance; if $\theta_s = 0$ it is X, if $\theta_s = \pi/2$ it is P, and for an arbitrary θ_s it is the 'rotated' quadrature operator

$$X(\theta_s) = e^{i\theta_s} a^\dagger + e^{-i\theta_s} a.$$

This 'squeezed' quadrature has a variance of e^{-2r_s}. The orthogonal quadrature

$$P(\theta_s) = X(\theta_s + \pi/2) = i\left[e^{i\theta_s} a^\dagger - e^{-i\theta_s} a\right]$$

becomes amplified or 'antisqueezed' to a variance of e^{+2r_s}.

It is also possible to apply the squeezing operator to other states, such as the Fock states. The effect is to create or destroy correlated pairs of photons.

Examples of bright amplitude- and phase-squeezed states are shown in the ball-and-stick representation in Fig. 1.3. Mathematically, these are given by displacing a squeezed vacuum, *viz.* $|\psi\rangle = \hat{D}(\alpha) S(\xi_s) |0\rangle$.

Part I

The state of the art

Chapter 2

Cavity optomechanics

In this chapter we will introduce the physics of cavity quantum optomechanics and provide a brief overview of the relevant literature. Important concepts will be introduced along the way, but the majority of the mathematical 'heavy lifting' and other technicalities will be relegated to Chapter 3.

2.1 Open-system dynamics in optomechanics

A cavity optomechanical device is fundamentally an open quantum system; its behaviour can be understood in terms of unitary dynamics induced by an interaction Hamiltonian, plus non-unitary dynamics that describe the photonic and phononic channels that link the system with its environment. These will be introduced in turn in § 2.1.1 and § 2.1.3, and then we will discuss the different operating regimes which can be accessed (§ 2.1.4).

A selection of optomechanical devices that have been used experimentally is shown in Fig. 2.1. Remarkably, these are all described very well by the few key concepts that we introduce in the following sections.

2.1.1 Unitary dynamics

In quantum mechanics the dynamics of a closed system—one that has no interactions with the outside world—are described by unitary transformations generated by a Hermitian Hamiltonian operator $\hat{H} = \hat{H}^\dagger$. As we show in this section, the optomechanical interaction permits such a description. This is promising because unitary dynamics are coherent, and thus can be used to generate nonclassical effects such as two-body entanglement.

To explain the optomechanical coupling we first recall that the resonance frequencies of a Fabry-Pérot [53] cavity are determined by the condition that an integer number of half-wavelengths must fit between the mirrors; thus the cavity's spectrum is dynamically modulated as the length of the cavity fluctuates because of the compliant end mirror. In return, the oscillator is subject to an optical force that depends on the number of photons in the cavity. Each subsystem back-acts on the other.

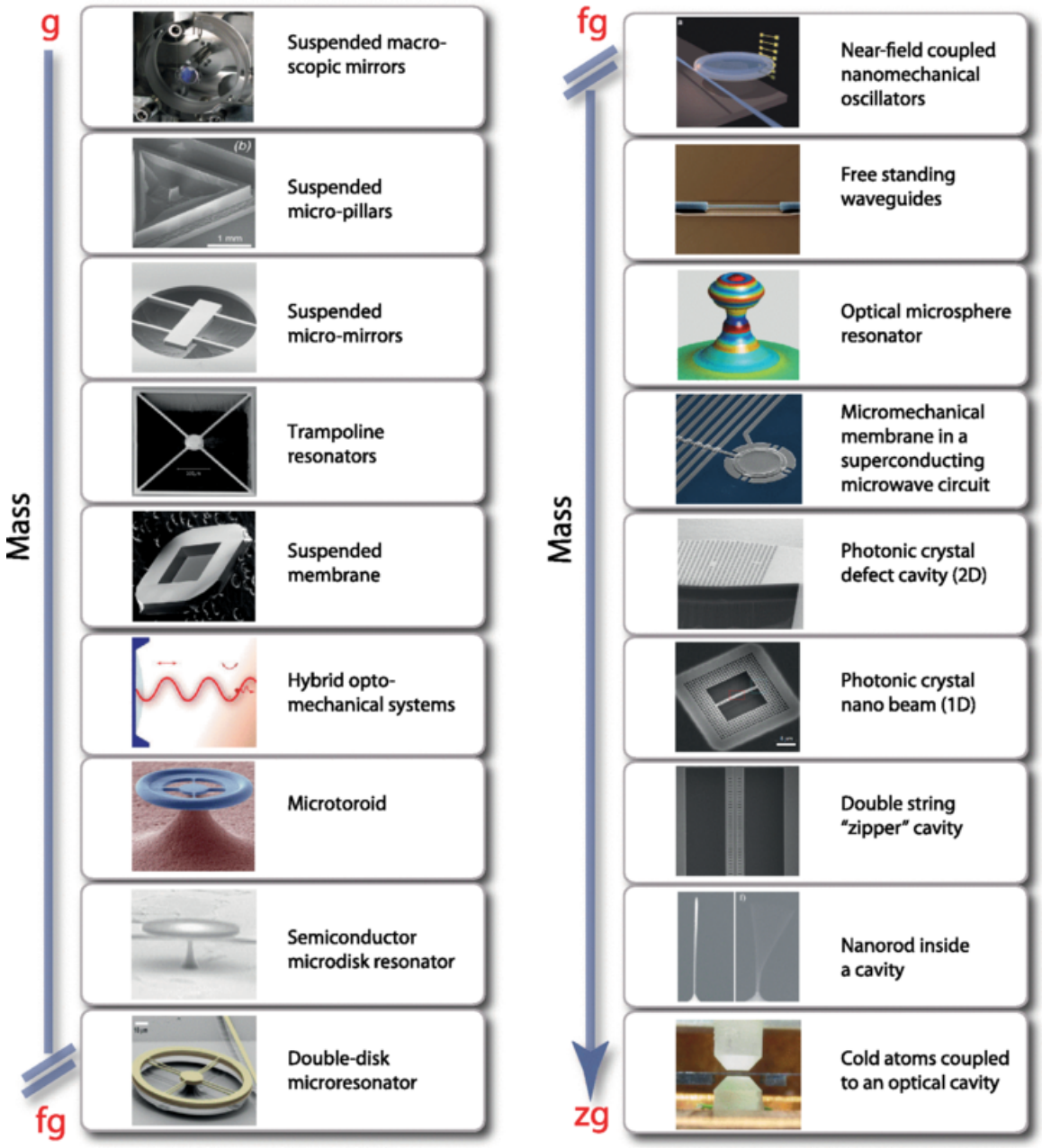

Figure 2.1: A selection of (opto)mechanical systems spanning eighteen orders of magnitude in mass and over seven orders of magnitude in resonance frequency. The optical forces acting in each can be loosely classed into radiation pressure (suspended mirrors, pillars, whispering gallery resonators), the optical gradient force (evanescently-coupled resonators, hybrid optomechanics, double-disk resonators, cold atoms), and electrostrictive forces (photonic–phononic crystals, zipper cavity, free-standing waveguides). Figure reproduced from [5], © APS; reused with permission.

This suggests that the optomechanical coupling can be modelled by the Hamiltonian

$$\hat{H} = \hbar\omega_{\mathrm{L}}\left(\hat{x}_{\mathrm{M}}\right) a^{\dagger}a + \hbar\omega_{\mathrm{M}} b^{\dagger}b, \tag{2.1}$$

where the optical and mechanical annihilation operators are a and b respectively. The mechanical resonance frequency is fixed at ω_{M}, but the optical resonance frequency is a function of the mechanical position operator $\hat{x}_{\mathrm{M}}$. We have neglected the zero-point energy $\hbar\omega/2$ of each oscillator without loss of generality[1].

For the majority of experiments performed to date the $\hat{x}_{\mathrm{M}}$ dependence of ω_{L} is well-approximated by the first order Taylor expansion $\omega_{\mathrm{L}} = \omega_{\mathrm{L},0} + g\hat{x}_{\mathrm{M}}$, where

$$g = \left.\frac{\partial\omega_{\mathrm{L}}}{\partial x_{\mathrm{M}}}\right|_{x_{\mathrm{M}}=0}$$

is the optomechanical coupling coefficient (with dimensions of frequency per length). With this substitution Eqn (2.1) becomes

$$\hat{H}_{\mathrm{OM}} = \hbar g\hat{x}_{\mathrm{M}} a^{\dagger}a. \tag{2.2}$$

We have omitted the terms $\hbar\omega_{\mathrm{L},0}a^{\dagger}a$ and $\hbar\omega_{\mathrm{M}}b^{\dagger}b$, which correspond to the free evolution of the cavity and mechanics, leaving only the interaction term.

Using the dimensionless position operator X_{M} we may rewrite Eqn (2.2) as

$$\hat{H}_{\mathrm{OM}} = \hbar g_0 X_{\mathrm{M}} a^{\dagger}a. \tag{2.3}$$

The single-photon optomechanical coupling rate

$$g_0 = g x_{\mathrm{ZP}} = g\sqrt{\frac{\hbar}{2M\omega_{\mathrm{M}}}}$$

describes the frequency shift of the cavity per zero-point displacement of the oscillator; it also controls the force exerted per intracavity photon.

From here one arrives at the 'canonical' optomechanical Hamiltonian by noting that g_0 is usually extremely small, in a sense we shall make more precise below. Physically, this means that the coherent optomechanical coupling is totally overwhelmed by incoherent loss processes whenever the photon number $a^{\dagger}a$ is low; in order to do anything interesting we had better put lots of photons into the cavity. Pumping the cavity with a bright field suffices for this task. Mathematically, the pump displaces the annihilation operator so that $\langle a\rangle = \alpha$ with $|\alpha| \gg 1$. The amplitude α can be complex in general, but in many cases we can choose to use the cavity field as a phase reference and set $\alpha \in \mathbb{R}$. We therefore make the replacement $a \to \alpha + \delta a$, where $\delta a = a - \alpha$ is a fluctuation operator that describes excursions away from the mean field. The key approximation that can then be made is dropping products of fluctuation operators, *viz.*

$$\begin{aligned} a^{\dagger}a &= \alpha^2 + \alpha\left(\delta a^{\dagger} + \delta a\right) + \delta a^{\dagger}\delta a \\ &\approx \alpha^2 + \alpha\left(\delta a^{\dagger} + \delta a\right). \end{aligned}$$

[1] If we include the zero-point energy we find that there is a dynamical Casimir force exerted upon the oscillator, but this term is entirely negligible in almost all relevant circumstances (for cases where it is not, see [54, 55]). Similarly, this Hamiltonian neglects any Doppler shifts induced by the mirror's motion, which are typically small. See [56] and [57] for discussion of these points.

This procedure is known as linearisation, and is justifiable when $\langle \delta a^\dagger \delta a \rangle \ll \left\{ \alpha^2, \alpha^2 \left\langle \left(\delta a^\dagger + \delta a \right)^2 \right\rangle \right\}$. With this approximation Eqn (2.3) becomes

$$\hat{H}_{\mathrm{OM}} = \hbar g_0 \alpha^2 X_{\mathrm{M}} + \hbar g_0 \alpha X_{\mathrm{M}} \left(\delta a^\dagger + \delta a \right).$$

Finally, it is usual to shift the origin of the position coordinate such that the mean optical force does not appear in the Hamiltonian. We will detail this procedure in Chapter 4. However, in the majority of the optomechanics literature there is no notational distinction made between shifted and un-shifted coordinates. Following this convention, we arrive at

$$\hat{H}_{\mathrm{OM}} = \hbar g_0 |\alpha| X_{\mathrm{M}} \delta X_{\mathrm{L}}. \tag{2.4}$$

In this form we can explicitly see that the radiation pressure force is proportional to the amplitude quadrature $\delta X_{\mathrm{L}} = \delta a^\dagger + \delta a$, and that the interaction rate has been boosted from g_0 to $g_0 |\alpha|$. It is even possible, as we shall see below, to reach the strong coupling regime, where this boosted coupling exceeds all of the rates associated with loss processes.

For further discussion of the optomechanical Hamiltonian, see [31].

2.1.2 Physical basis of optical force

In all of the optomechanical devices depicted in Fig. 2.1 the mechanical degree of freedom is subject to an optical force

$$\hat{F}_{\mathrm{opt}} = \frac{1}{\mathrm{i}\hbar} \left[\hat{p}_{\mathrm{M}}, \hat{H}_{\mathrm{OM}} \right] = -\hbar g \alpha \delta X_{\mathrm{L}},$$

yet there are many mechanisms underlying the generation of this force.

In the canonical cavity system the force is simply radiation pressure exerted by the photons reflecting from the mirror. This holds for macro- and microscopic mirrors, membranes, *etc.* It also gives rise to the forces experienced by mechanical modes in whispering gallery mode resonators, where light is confined to the periphery of the resonator by 'continuous total internal refection' at the air–material interface [58].

The gradient force is a second variety of optical force. When a dielectric material is polarised in an inhomogeneous field it develops a dipole moment that interacts with the field to produce a net force. This is the phenomenon which enables evanescently-coupled near-field optomechanics [59] and optically-trapped mechanical resonators [60]. Cold atoms also experience a gradient force due to the dynamical Stark shift [61].

When the field is tightly confined inside a microstructure electrostriction can play a significant role [35,62]. This force arises because of a coupling between the strain in the material and its refractive index; modulating the strain thereby modulates the optical path length and *vice versa*. This is a key effect in photonic–phononic crystal resonators and free-standing waveguide resonators, where it is responsible for Brillouin scattering [35, 62–64].

2.1.3 Dissipative dynamics

Unitary dynamics do not suffice to describe the behaviour of a real optomechanical device. The optical cavity will be coupled to an input field mode, and will have internal scattering and absorption that remove photons from the system. Furthermore, the mechanical mode is unavoidably coupled to a hot thermal bath composed of other elastic and acoustic modes. All of these processes introduce noise and can degrade the 'quantumness' of the optomechanical device.

Throughout this thesis we will use the input–output formalism (*e.g.* [50, 65]) to describe the dissipative behaviour of the optical field. This is based around two key equations;

$$\frac{\mathrm{d}a}{\mathrm{d}t} = \frac{1}{\mathrm{i}\hbar}\left[a,\hat{H}\right] - \frac{\kappa+\kappa_{\mathrm{int}}}{2}a + \sqrt{\kappa}\,a_{\mathrm{in}} + \sqrt{\kappa_{\mathrm{int}}}\,a_{\mathrm{vac}} \tag{2.5a}$$

$$a_{\mathrm{out}} = \sqrt{\kappa}\,a - a_{\mathrm{in}}. \tag{2.5b}$$

Eqn (2.5a) describes the dynamics of the cavity field; the first term corresponds to the Hamiltonian evolution, the second to the net loss, the third to the bright drive field, and the last to vacuum noise introduced by unwanted scattering or absorption inside the cavity. An associated quantity is the so-called escape efficiency

$$\eta_{\mathrm{esc}} = \frac{\kappa}{\kappa+\kappa_{\mathrm{int}}}, \tag{2.6}$$

which is equal to the probability that a cavity photon successfully couples into the desired output mode. A cavity with $0 < \eta_{\mathrm{esc}} < 1/2$ is said to be undercoupled because a cavity photon is more likely to be lost than coupled into the target mode. Conversely, the $1/2 < \eta_{\mathrm{esc}} \leq 1$ situation is known as overcoupling. At critical coupling, $\eta_{\mathrm{esc}} = 1/2$, the promptly-reflected field and that leaking from the cavity mode destructively interfere on resonance, giving $\langle a_{\mathrm{out}}\rangle_{\Delta=0} = 0$. As we will see in § 2.2.5, in this thesis it is generally justifiable for us to operate in the $\eta_{\mathrm{esc}} \to 1$ limit and neglect κ_{int}.

Eqn (2.5b) provides the boundary condition linking a with the input and output fields, a_{in} and a_{out}. The input and output field operators have units of $\mathrm{Hz}^{-1/2}$, so that $a_{\mathrm{in}}^{\dagger}a_{\mathrm{in}}$ can be interpreted as the incoming photon flux operator [31]. For a coherent drive $a_{\mathrm{in}} = \alpha_{\mathrm{in}} + \delta a_{\mathrm{in}}$, where the fluctuation operator has the properties

$$\langle \delta a_{\mathrm{in}}\rangle = 0, \tag{2.7a}$$

$$\left\langle \delta a_{\mathrm{in}}^{\dagger}(t)\,\delta a_{\mathrm{in}}\left(t'\right)\right\rangle = 0, \tag{2.7b}$$

$$\left\langle \delta a_{\mathrm{in}}(t)\,\delta a_{\mathrm{in}}^{\dagger}\left(t'\right)\right\rangle = \delta\left(t-t'\right), \tag{2.7c}$$

which are the statistics of a continuum of modes in the vacuum state. Thermal fluctuations of the cavity drive are negligible in optomechanics because the photon energy is much larger than the typical thermal energy $k_{\mathrm{B}}T$, where T is the temperature. Even at relatively long telecommunications wavelengths (1550 nm) the occupancy at $T = 300$ K is only

$$\bar{n} = \left(\mathrm{e}^{\hbar\omega/k_{\mathrm{B}}T} - 1\right)^{-1} \sim 10^{-14}.$$

This is not generally true in the very closely related fields of electromechanics and cold atom optomechanics, that operate at much lower frequencies where thermal occupation can be significant; there

have even proposals for extracting work from the cosmic microwave background using cold atom optomechanics [66, 67].

Of course, in a typical optomechanical system the solid-state mechanical resonator is of vastly lower frequency again, so that even under cryogenic conditions $\bar{n}$ is usually much larger than one[2]. This means that optomechanical devices can be strongly perturbed by thermal excitations which couple into the mechanical resonance at a rate of approximately $\Gamma\bar{n}$, where Γ is the mechanical decay rate.

In the optomechanics literature it is extremely common to use Eqn (2.5a) to model the mechanical oscillator; one simply substitutes $\kappa \to \Gamma$, $\kappa_{\text{int}} = 0$, and $a_{\text{in}} \to b_{\text{TH}}$, where b_{TH} is a thermal noise drive with

$$\langle b_{\text{TH}} \rangle = 0, \tag{2.8a}$$

$$\left\langle b_{\text{TH}}^{\dagger}(t)\, b_{\text{TH}}\left(t'\right) \right\rangle = \bar{n}\delta\left(t-t'\right), \tag{2.8b}$$

$$\left\langle b_{\text{TH}}(t)\, b_{\text{TH}}^{\dagger}\left(t'\right) \right\rangle = (\bar{n}+1)\,\delta\left(t-t'\right). \tag{2.8c}$$

However, this model is not always sufficient; in particular, it is not valid if the damping rate Γ is comparable to or larger than ω_{M}, or if one cares about dynamics that occur on timescales shorter than the resonant period [68]. We will present an alternative—arguably more realistic—model in § 3.4 (and App. A.3), and discuss some of the technicalities surrounding Markovian Langevin equations (and their related master equations, *etc.*) in App. A.10.

2.1.4 Operating regimes

From the above sections we can see that there are a number of parameters which describe the processes which occur in optomechanical systems. The full set for most situations is the single-photon optomechanical coupling rate, the boosted optomechanical coupling rate, the mechanical resonance frequency, the optical detuning, the optical and mechanical linewidths, and the mechanical bath occupancy, *viz.*

$$\{g_0, g_0|\alpha|, \omega_{\text{M}}, \Delta, \kappa, \Gamma, \bar{n}\}.$$

Reviews of typical parameters are available in the literature (*e.g.* [5, 69]).

A number of different operating regimes can be identified by the relationships between these parameters. The terminology for each regime is very closely related to similar situations encountered in ion trapping, atom trapping, and cavity quantum electrodynamics (QED).

- **Underdamped regime** $\Gamma < 2\omega_{\text{M}}$. An excitation of the mechanical mode will 'ring' for many mechanical periods. We will restrict our attention to the high-Q limit, where $Q = \omega_{\text{M}}/\Gamma \gg 1$. The Q factor, or 'quality', determines how rapidly energy leaks from the oscillator. Loosely, it can be thought of as the number of oscillations that a coherent excitation will persist for [70]. The opposite regime—overdamping—is not of interest in this thesis.

[2]There are notable exceptions to this rule of thumb, such as the demonstration of ground state cooling of a 6 GHz oscillator in a dilution refrigerator by O'Connell *et al.* [17]. They used piezoelectric resonator with an extremely high frequency.

- **Quantum coherent oscillation regime** $Q > \bar{n}$. Less than one phonon enters the oscillator (on average) per mechanical cycle. The majority of optomechanical protocols require that this be satisfied, although it has been suggested that pulsed schemes can circumvent this restriction [71]. Employing the high-temperature approximation $\bar{n} \approx k_{\mathrm{B}}T/\hbar\omega_{\mathrm{M}}$ yields

$$Q \times f > \frac{2\pi k_{\mathrm{B}}T}{\hbar},$$

  where $f = \omega_{\mathrm{M}}/2\pi$ is the mechanical resonance frequency (not angular frequency). This motivates the use of the $Q \times f$ product as a metric for how well isolated the oscillator is from its thermal environment (*e.g.* [72, 73], § 7.4). It thus plays a crucial role in the vast majority of quantum optomechanics, in addition to more 'applied' settings such as mass or chemo-sensing (see Chapter 7).

- **Weak-coupling regime** $g_0|\alpha| \ll \{\Gamma, \kappa\}$. In this case the unitary dynamics are slower than the loss processes. This is a typical operating regime. Some quantum behaviours can still be accessed in this limit.

- **Strong-coupling regime** $g_0|\alpha| \gg \{\Gamma, \kappa\}$. A key feature of the strong-coupling regime is hybridisation of the mechanical mode and the optical fluctuations [74] that manifests as a frequency gap (splitting) between the normal modes. The magnitude of the splitting is $2g_0|\alpha|$. This has been achieved experimentally *e.g.* [75–78].

- **Quantum coherent coupling regime** $g_0 > \{\kappa, \Gamma\bar{n}\}$. An optomechanical device in the quantum coherent coupling regime can exchange excitations between the mechanical and optical degrees of freedom faster than a noise photon or phonon enters [70]. This occurs in a phase-coherent manner. This regime—intermediate between the strong- and ultrastrong-coupling cases—was first experimentally realised in spoked microtoroid resonators [78].

- **Ultrastrong-coupling regime** $g_0|\alpha| > \omega_{\mathrm{M}}$. No experiment in optomechanics has yet reached this regime, though related cavity QED experiments have [79]. An experimental signature of ultrastrong-coupling is a photon blockade effect, where photons exiting the cavity are nonclassically anti-bunched [80].

- **Single-photon strong-coupling regime** $g_0 > \{\Gamma, \kappa\}$. The optomechanical coupling rate is sufficient to detune the cavity by more than one linewidth when one photon is added. It is characterised by strong photon blockade effects, hybridisation of the optical and mechanical fields, and non-classical interferences between quanta [70]. In this limit one cannot linearise the optomechanical Hamiltonian. No solid-state optomechanical device has been created that operates in the single-photon strong-coupling regime; however, it has been observed in cold atom optomechanics [81]. This could provide a route to nonclassical state formation using single photons [82].

- **High-cooperativity regime** $C > \bar{n}$. The radiation pressure shot noise—the noise arising from quantisation of the cavity mode—dominates over the stochastic thermal noise [23]. The cooperativity C is a dimensionless parameter that is analogous to the Purcell factor of cavity QED [83]. It compares the coherent coupling rate to the incoherent loss rates, *viz.*

$$C = \frac{4g_0^2 |\alpha|^2}{\Gamma\kappa}. \tag{2.9}$$

  As we will see in § 4.2.6, the cooperativity is equal to the effective number of noise phonons introduced by radiation pressure shot noise. It also plays an important role in sideband cooling, linear position measurement, and feedback cooling [83], as shown in § 2.3.1. Note that $C > \bar{n}$ does not necessarily imply that the system is strongly-coupled.

Of course, there are also the resolved and unresolved sideband regimes. These are so integral to this thesis that we will introduce them in their own sections: § 2.2 will detail the resolved sideband regime and the unresolved sideband regime will be examined in § 2.3.

2.2 Resolved sideband limit

In the resolved sideband limit it is possible to use the cavity as a filter to suppress or enhance particular scattering processes. We will introduce the mathematical tools that let us take advantage of this, and then employ them in two special cases to see the main processes underlying optomechanical protocols that operate in the resolved sideband regime ($\kappa < \omega_{\mathrm{M}}$).

2.2.1 Rotating frame transformation

The transformation to a 'rotating frame'[3] is an extremely useful procedure. It amounts to introducing envelope operators that are stationary under free dynamics, and vary slowly when interactions are present. We have actually already sneaked this transformation into the preceding discussion: specifically, when linearising the optomechanical Hamiltonian (§ 2.1.1). Note that this procedure can be applied outside of the resolved sideband regime, but we are introducing it here because the rotating frame transformation motivates the approximations that we will use later in this section.

The simplest possible example of a rotating frame transformation is for a lone classical oscillator with complex amplitude α and frequency Ω. We know that the solution to the equation of motion is $\alpha(t) = \alpha_0 \mathrm{e}^{-\mathrm{i}\Omega t}$; thus we can introduce an envelope $\bar{\alpha}(t) = \alpha(t)\,\mathrm{e}^{+\mathrm{i}\Omega t} = \alpha_0$, which has no dynamics. To see why this process is described as 'moving to a rotating frame,' note that the original phasor α—that rotates at Ω—has been converted into a stationary phasor $\bar{\alpha}$; it is as if our new real and imaginary axes are co-rotating with the original phasor.

[3] The procedure is closely related to moving to the interaction (Dirac) picture [50], and should not be confused with the use of rotating spatial coordinates ('references frames') in classical mechanics.

We will continue to use the overbar notation through this section, for pedagogical reasons, but note that beyond that we will not make a notational distinction between the lab and rotating frames. This is in line with the literature.

For the optomechanical Hamiltonian we perform the rotating frame transformation by introducing an operator $\bar{a} = a(t)\,\mathrm{e}^{+\mathrm{i}\omega_\mathrm{D} t}$ which rotates at the drive frequency, and $\bar{b} = b(t)\,\mathrm{e}^{+\mathrm{i}\omega_\mathrm{M} t}$. Then the equations of motion in the 'lab' (original) frame

$$\begin{aligned}\frac{\mathrm{d}a}{\mathrm{d}t} &= -\mathrm{i}\omega_\mathrm{L} a + \frac{1}{\mathrm{i}\hbar}\left[a, \hat{H}_\mathrm{OM}\right] + \sqrt{\kappa}\, a_\mathrm{in} - \frac{\kappa}{2}a \\ \frac{\mathrm{d}b}{\mathrm{d}t} &= -\mathrm{i}\omega_\mathrm{M} b + \frac{1}{\mathrm{i}\hbar}\left[b, \hat{H}_\mathrm{OM}\right] + \sqrt{\Gamma}\, b_\mathrm{TH} - \frac{\Gamma}{2}b\end{aligned}$$

can be converted to the rotating frame by using the product rule, *viz.*

$$\frac{\mathrm{d}a}{\mathrm{d}t} = \frac{\mathrm{d}}{\mathrm{d}t}\left(\bar{a}(t)\,\mathrm{e}^{-\mathrm{i}\omega_\mathrm{D} t}\right) = \frac{\mathrm{d}\bar{a}}{\mathrm{d}t}\mathrm{e}^{-\mathrm{i}\omega_\mathrm{D} t} - \mathrm{i}\omega_\mathrm{D}\bar{a}(t)\,\mathrm{e}^{-\mathrm{i}\omega_\mathrm{D} t}.$$

The result is

$$\begin{aligned}\frac{\mathrm{d}\bar{a}}{\mathrm{d}t} &= \mathrm{i}\Delta\bar{a} + \frac{1}{\mathrm{i}\hbar}\left[\bar{a}, \hat{H}_\mathrm{OM}\right] + \sqrt{\kappa}\,\bar{a}_\mathrm{in} - \frac{\kappa}{2}\bar{a} \\ \frac{\mathrm{d}\bar{b}}{\mathrm{d}t} &= \frac{1}{\mathrm{i}\hbar}\left[\bar{b}, \hat{H}_\mathrm{OM}\right] + \sqrt{\Gamma}\,\bar{b}_\mathrm{TH} - \frac{\Gamma}{2}\bar{b}.\end{aligned}$$

Note that the noise operators have the same statistics as before because they are all Markovian. The quantity $\Delta = \omega_\mathrm{D} - \omega_\mathrm{L}$ is the detuning; when the cavity is driven below resonance $\Delta < 0$.

Expressing the interaction part of the Hamiltonian in terms of the rotating operators gives

$$\bar{H}_\mathrm{OM} = \hbar\alpha g_0\left(\bar{a}^\dagger\bar{b}\mathrm{e}^{-\mathrm{i}(\omega_\mathrm{M}+\Delta)t} + \bar{b}^\dagger\bar{a}\mathrm{e}^{+\mathrm{i}(\omega_\mathrm{M}+\Delta)t} + \bar{a}\bar{b}\mathrm{e}^{-\mathrm{i}(\omega_\mathrm{M}-\Delta)t} + \bar{a}^\dagger\bar{b}^\dagger\mathrm{e}^{+\mathrm{i}(\omega_\mathrm{M}-\Delta)t}\right). \tag{2.10}$$

On the face of it, we have only made things more difficult by moving into a rotating frame; the Hamiltonian now has explicit time dependence! Fortunately, from this point it is simple to apply a common approximation which will dramatically simplify the Hamiltonian.

2.2.2 Resonant drive

To introduce some of the terminology which will be used in the following sections, let us briefly consider the $\Delta = 0$ (resonant) case. The optical mode thus evolves according to

$$\delta\dot{\bar{a}} = -\mathrm{i}g_0|\alpha|\left(\bar{b}\mathrm{e}^{-\mathrm{i}\omega_\mathrm{M} t} + \bar{b}^\dagger\mathrm{e}^{+\mathrm{i}\omega_\mathrm{M} t}\right) + \sqrt{\kappa}\,\delta\bar{a}_\mathrm{in} - \frac{\kappa}{2}\delta\bar{a}.$$

It is evident from the first terms that the mechanical mode is scattering photons by $\pm\omega_\mathrm{M}$; the $\bar{b}$ term annihilates a phonon to create a photon of higher energy, whilst the $\bar{b}^\dagger$ term absorbs energy from a photon to create a phonon. The scattered photons effectively form two new fields that are known as sidebands because they sit symmetrically around the pump frequency. It is common practice to refer to the higher-frequency sideband as the 'blue' sideband, and the lower-frequency as the 'red'. In § 3.5.3 we will see how sidebands can be used to describe a modulation of the drive field; it turns out that in the resonant case the optical field acquires a phase modulation that depends on X_M. This allows measurement-based feedback cooling (§ 2.3.1).

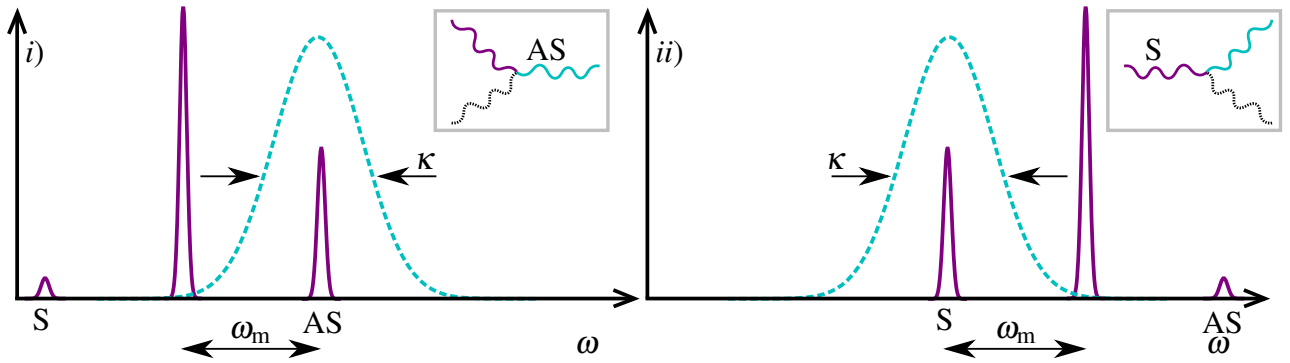

Figure 2.2: Depiction of sideband cooling and parametric heating.
i) Optomechanical sideband cooling. The pump (tall purple peak) is detuned by one resonance frequency to the red of the cavity resonance (dashed cyan line). The anti-Stokes (AS) scattering process is resonantly enhanced, leading to annihilation of phonons from the mechanical mode. This is approximately a beamsplitter interaction.
ii) Optomechanical parametric heating. Detuning the pump to the blue of the cavity resonance suppresses the anti-Stokes peak and enhances Stokes (S) scattering, leading to the creation of correlated pair of excitations in the optical and mechanical modes. In the quantum limit this performs a two-mode squeezing operation which can generate bipartite entanglement.
Insets show the anti-Stokes and Stokes scattering terms. Photons at the pump frequency are shown as purple lines; photons inside the cavity are cyan. Phonons are shown as dotted black lines.

2.2.3 Sideband cooling

Consider driving the cavity at $\Delta = -\omega_{\mathrm{M}}$. In the literature this is referred to as driving 'on the red sideband'. Eqn (2.10) becomes

$$\bar{H}_{\mathrm{OM,red}} = \hbar\alpha g_0 \left(\bar{a}^\dagger \bar{b} + \bar{b}^\dagger \bar{a} + \bar{a}\bar{b}\mathrm{e}^{-2\mathrm{i}\omega_{\mathrm{M}}t} + \bar{a}^\dagger \bar{b}^\dagger \mathrm{e}^{+2\mathrm{i}\omega_{\mathrm{M}}t}\right).$$

We will now introduce the rotating wave approximation (RWA), which is used extensively throughout quantum optics, quantum electrodynamics, nuclear magnetic resonance, and other fields of physics. Physically, the RWA amounts to neglecting interactions that are far off-resonant, because they 'average' to zero over the timescales on which resonant processes evolve [70]. Mathematically, the essential idea is to drop terms that oscillate quickly compared to the evolution of the envelope operators. Thus, if ω_{M} is sufficiently large compared to g_0, κ, and Γ, we may assume that $2\omega_{\mathrm{M}}$ is 'fast' and drop the last two terms of $\bar{H}_{\mathrm{OM,red}}$. This leaves

$$\bar{H}_{\mathrm{OM,red}} = \hbar\alpha g_0 \left(\bar{a}^\dagger \bar{b} + \bar{b}^\dagger \bar{a}\right). \tag{2.11}$$

In fact, this is the Hamiltonian that generates a beamsplitter transformation [5, 50]. The first term annihilates a phonon and creates a photon, whilst the second term represents the complementary process of annihilating a photon to produce a phonon.

In the presence of the strong, detuned pump we see anti-Stokes scattering; a phonon provides the energy needed to allow a drive photon into the cavity mode. A graphical depiction is given in Fig. 2.2, panel *i*). This effect underlies sideband cooling, an active cooling technique that can be thought of as a continuous beamsplitter interaction that swaps vacuum noise onto the mechanical state. Sideband

cooling to the quantum ground state was a key experimental goal in the community, until it was achieved in both optomechanical [15] and electromechanical [16] devices in 2011. In optomechanics, an oscillator is said to be 'ground state cooled' or 'near ground state cooled' if $\langle \hat{n}_{\mathrm{M}} \rangle < 1$.

Unlike the classical case, where the oscillator may be made arbitrarily cold, the quantum treatment of sideband cooling reveals that there is a fundamental minimum achievable temperature [84]. Its origin is radiation pressure noise caused by the photon statistics of the drive field. For a coherent drive [85] the minimum occupancy when driven on the red sideband is

$$\langle \hat{n} \rangle_{\mathrm{min}} = \frac{\Gamma \bar{n}_{\mathrm{H}} + \Gamma_{\mathrm{opt}} \bar{n}_{\mathrm{opt}}}{\Gamma + \Gamma_{\mathrm{opt}}}, \tag{2.12}$$

with

$$\Gamma_{\mathrm{opt}}\big|_{\Delta=-\omega_{\mathrm{M}}} = \Gamma \frac{C_{\mathrm{M}}}{1 + (\kappa/4\omega_{\mathrm{M}})^2}$$

and

$$\bar{n}_{\mathrm{opt}}\big|_{\Delta=-\omega_{\mathrm{M}}} = \left(\frac{\kappa}{4\omega_{\mathrm{M}}} \right)^2.$$

Thus in the large-cooperativity ($C_{\mathrm{M}} > \bar{n}_{\mathrm{H}} \gg 1$) limit

$$\langle \hat{n} \rangle_{\mathrm{min}} \approx \left(\frac{\kappa}{4\omega_{\mathrm{M}}} \right)^2,$$

which may be made arbitrarily small as the sideband resolution parameter $\omega_{\mathrm{M}}/\kappa$ is increased. Importantly, this implies that outside of the resolved sideband regime it is not possible to reach the ground state [85]. Physically, this is because the neglected $\bar{a}\bar{b} + \bar{a}^\dagger \bar{b}^\dagger$ terms contribute to the overall interaction and act to heat the oscillator.

This physics is startlingly similar to Raman cooling of trapped ions in the Lamb-Dicke or 'tight-binding' regime [74], and, as we shall see in § 2.3, many of the schemes proposed for replacing sideband cooling in the unresolved sideband regime are inspired by the ion trapping community.

The beamsplitter interaction also makes it possible to swap non-trivial quantum states from an optical field onto the mechanical oscillator, and *vice versa*. This has been experimentally achieved at the classical level in an optomechanical crystal [86], and at the quantum level in an electromechanical device [87], where microwave fields travelling in a transmission line were successfully stored in the vibrational mode of a compliant capacitor and read-out again.

A variety of other schemes exploiting the beamsplitter interaction have also been proposed, *e.g.* [88–90].

2.2.4 Parametric heating and entanglement

The opposite case is, of course, driving on the blue sideband of the cavity. In this case $\Delta = +\omega_{\mathrm{M}}$, and dropping the fast terms from Eqn (2.10) leaves

$$\bar{H}_{\mathrm{OM,blue}} = \hbar \alpha g_0 \left(\bar{b}\bar{a} + \bar{a}^\dagger \bar{b}^\dagger \right). \tag{2.13}$$

This Hamiltonian is recognisable as a two-mode squeezing operation, which generates entanglement between the mechanical and cavity modes [5, 50]. The first term can be interpreted as annihilating a photon-phonon pair, whereas the second term creates a pair. In optomechanics the strong optical drive biases the interaction towards creating a cavity photon and allowing the excess energy to become a phonon.

If one does not have access to the optical mode then the extra phonons added to the oscillator appear to simply be thermal noise, hence the term 'parametric heating' [70]. This is identical to two-mode squeezing achieved in light, where each mode alone has thermal statistics, but when they are allowed to interfere on a beamsplitter the output modes exhibit quantum squeezing.

In general, driving on the blue sideband leads to instability, because the light amplifies the mechanical vibration. This places a limit on how much entanglement can be generated in any experiment before nonlinearities become significant and saturate the process [91, 92]. Nevertheless, two-mode entanglement has been generated and verified experimentally [93] in an electromechanical system.

It has also been proposed that coupling two macroscopic oscillators to a single optical cavity that is driven on the blue sideband can generate entanglement between the mechanical degrees of freedom [94].

2.2.5 Limitations of the resolved sideband regime

Though there are powerful tools available to us in the resolved sideband regime, there are also potential drawbacks. Firstly, it may not be possible or practical to achieve the necessary linewidths, as might be the case for extremely low-frequency oscillators, or minuscule optical cavities (which tend to have larger g_0 and κ). If the requirement $\kappa \ll \omega_{\mathrm{M}}$ is met, the red and blue sidebands are so far-detuned from the cavity resonance frequency that relatively large optical powers are required to populate the cavity and boost the optomechanical coupling rate. This may be an issue in cases where the total incident power is limited, such as when optical nonlinearities are significant in the input–output mode. Conversely, when driven on-resonance the optomechanical interaction is effectively suppressed by the fact that the Stokes and anti-Stokes sidebands lay far beyond the cavity resonance [70]. Finally, a sideband-resolved optical cavity will severely distort sub-mechanical-period pulses because they contain significant power outside of the cavity's bandwidth.

2.3 Unresolved sideband limit

In the unresolved sideband regime κ is much greater than ω_{M}, so the mechanical sidebands are also cavity-enhanced. In essence, the cavity acts as an optical amplifier. This is a desirable property in a number of situations, most notably in quantum-limited position and force sensing [95], where the

standard quantum limit[4] can be approached in the 'bad-cavity' regime [36,70]. A strongly-overcoupled cavity also assists in permitting broadband sensor operation with high quantum efficiency (high escape efficiency η_{esc}, Eqn (2.6)), both of which are crucial for many applications. For example, the advanced LIGO detectors include a signal recycling mirror to increases their arms' linewidths for precisely these reasons [95].

As covered in § 2.2.5, the unresolved sideband limit is also the natural operating regime for low-frequency and/or high-mass mechanical resonators, especially those coupled to miniaturised optical cavities with small mode volumes, or ancillae with low resonance frequencies.

Many researchers have been pushing into the unresolved sideband limit and bringing it fully into the fold of quantum mechanics. We will examine some of the techniques for quantum control that have been developed in this regime.

Ground state cooling of macroscopic oscillators in the unresolved sideband regime was an unrealised goal of the community until recently. The first experimental demonstration was performed only this year [96] by Clark *et al.*, who used an electromechanical device (further discussion below). Nevertheless, there are dozens of unrealised and interesting proposals for other methods of cooling and manipulating mechanical oscillators in the unresolved sideband regime. We will examine some of these now.

Yong-Chun *et al.* [97] categorise cooling proposals into three categories.

- **Parameter modulations**. This class of proposal relies on controlling one or more of the system parameters, typically the optomechanical coupling rate or the mechanical frequency. One key example is the work of Machnes *et al.* [98,99], which predicts rapid cooling in both the resolved and unresolved sideband regimes. They show that interference between multiple sub-period pulses can cancel off the 'heating terms' ($\bar{a}\bar{b} + \bar{a}^\dagger\bar{b}^\dagger$) in the optomechanical interaction, leaving only the cooling terms ($\bar{a}^\dagger\bar{b} + \bar{b}^\dagger\bar{a}$). The concept of suppressing undesirable interactions by coherent cancellation is borrowed from related schemes in ion trapping [98]. Other parameter modulation schemes involve varying the detuning [88], the optomechanical coupling rate [89], the mechanical frequency [100–102], and the input optical power [101]. Measurement-based feedback (§ 2.3.1) may be considered to be a special case of a parameter modulation.
- **Hybrid systems**. Another route to achieving quantum control beyond the resolved sideband limit is to interface the optomechanical device with an auxiliary quantum system. Superconducting circuits [103], cold atoms (to be discussed in § 2.3.3), ions, nitrogen–vacancy centres in diamonds [104], and various other ancillae have been proposed in the literature [105,106]. In this thesis we will concentrate on cold atoms. Note that hybrid systems are predicted to allow much more than simply cooling.
- **Novel coupling mechanisms**. Finally, we may turn to more general optomechanical couplings than those discussed thus far. Some examples are provided in § 2.4.

[4]The standard quantum limit to continuous position measurement arises because the phase and amplitude noise of light are noncommuting variables. Pumping more strongly decreases the phase noise of the measurement, but increases the back-action due to radiation pressure shot-noise. The SQL is the point at which these are balanced [70].

We argue that there are two further categories that are not covered by the above.

- **Multimode optomechanics**. One can easily imagine generalising the treatments thus far to including multiple optical and/or mechanical modes. This can allow exploitation of mechanical scattering between different optical modes, or *vice versa*, leading to effects such as optomechanically-induced transparency (OMIT) [107–110] and optomechanically-induced absorption (OMIA) [111]. For example, Ojanen and Børkje [112] have proposed that interference between different scattering paths can suppress optical heating and allow ground state cooling in the unresolved sideband limit. In one of their schemes an auxiliary cavity must be sideband-resolved, but a second scheme removes this limitation by introducing a fourth mode [5]. Related work by Liu *et al.* also predicts ground state cooling using OMIT [113].
- **Nonclassical optical resources**. A beautiful theoretical study and experimental demonstration by Clark *et al.* [96], published quite recently, shows the power of using nonclassical states of light in the unresolved sideband regime. Injecting nonclassical squeezed light into the cavity permitted them to reduce the radiation pressure back-action below that generated by a typical coherent state drive. Remarkably, they found that above a finite critical squeezing parameter it is possible to arrange for the effective optical bath temperature to be precisely zero, unlike the resolved sideband case where this is only achieved asymptotically [96]. Using this method they cooled an electromechanical oscillator to $\langle \hat{n}_{\mathrm{min}} \rangle = 0.19 \pm 0.01$ with a sideband resolution factor of only $\omega_{\mathrm{M}}/\kappa = 0.3$.

2.3.1 Measurement and feedback

In a classical setting it is quite natural to consider measuring the state of the system and then performing some form of feedback to alter its dynamics. In the language of control theory, one obtains an error signal from the 'plant' (system), and the 'controller' processes this signal in order to actuate the plant. It is not immediately clear that such a scheme will work in the quantum regime because the uncertainty principle enforces a measurement–disturbance relation, but calculations and experimental demonstrations have demonstrated its utility.

In the context of optomechanics, ground state cooling *via* feedback was proposed by Mancini *et al.* in 1998. They considered measuring the phase fluctuations exiting an optomechanical cavity using homodyne (§ 3.5) detection. The resulting signal is ideally composed of two components: one corresponding to the mechanical position, and the other to the vacuum phase noise. By differentiating this one obtains a signal proportional to momentum, which can be used to exert a force on the oscillator such that $\hat{F}_{\mathrm{FB}} \propto -\hat{p}_{\mathrm{M}}$. This damps the resonator without introducing extra thermal noise.

Classically, such a set-up can make the oscillator arbitrarily cold, because the measurement noise can be zero. In the quantum case one finds that a minimum temperature emerges because of the

[5] In this second proposed scheme, Ojanen and Børkje also allow one oscillator to modulate the rate of photon exchange between two optical cavities, rather than the cavity resonance frequency directly [112].

vacuum phase noise. In the unresolved sideband regime with high cooperativity $C \gg \bar{n}$ this is given by

$$\langle \hat{n} \rangle_{\min} \approx \frac{\bar{n}}{2C}.$$

Genes *et al.* [114] have proven that feedback cooling is best implemented in the unresolved sideband regime.

Optomechanical feedback cooling has been demonstrated in a number of experiments [115, 116], and the existence of an optimum feedback gain—a feature that arises from the optical phase noise—confirmed [117]. Actuation has been performed electrostatically [117–120], and by amplitude modulating a bright auxiliary optical field [116, 121, 122].

A modified form of 'stochastic feedback' is predicted to even allow quantum squeezing of the mechanical motion [123].

2.3.2 Coherent control

Given the successes of feedback control we are compelled to ask if we might do better by eliminating the measurement step *i.e.* allowing the controller and actuator to also be quantum systems that process and feedback quantum information, not a classical measurement record [124]. This avoids introducing projection noise associated with continuous measurement. Schemes based on this idea are examples of coherent control, proposed by Lloyd in 2000 [124].

The hybrid and pulsed optomechanical systems that we will discuss below (§ 2.3.4 and § 2.3.3) may be considered to be forms of coherent control.

2.3.3 Hybrid atom–optomechanics

A hybrid atom–optomechanical device couples atomic degrees of freedom to the motion of a mechanical oscillator. The atoms can be considered to be a quantum 'handle' with which to manipulate the mechanical oscillator; they thus constitute the controller portion of a coherent control system.

Atom–optomechanical devices can be broadly categorised into four varieties; internal or external, and integrated or remotely-coupled. External systems couple to the motional degrees of freedom of the atoms, instead of internal degrees of freedom such as electronic energy levels (or coherences between them). Integrated systems require the atoms and the mechanical oscillator to be close together in space, whilst remotely-coupled systems relax this requirement.

- **Internal & integrated**. These are by far the most theoretically-researched hybrid atom–optomechanical systems to date, being essentially cavity QED systems. A plethora of proposals exist for two-level atoms [125–128], three-level atoms [129–132], and even four-level atoms [133] inside optomechanical cavities.
  Several studies predict mechanical cooling *via* the atom (*e.g.* [125, 132–134]) by either allowing the atom to accept excitations from the mechanical oscillator and then spontaneously decay into radiative modes, or by using coherences between the atomic energy levels to suppress the heating terms in the optomechanical Hamiltonian [132–134].

Additional effects such as mechanical bistability (also encountered in bare optomechanics [135]), perfect photon absorption [136], photon blockade and anti-bunching [126], bi- and tri-partite entanglement [129, 134, 137], and steady-state mechanical squeezing [127] have also been predicted, usually in the atomic strong-coupling regime (where the atom–cavity coupling rate is larger than the spontaneous decay rate). This is one hurdle to their realisation in experiments.

A second notable hurdle is integrating ultra-high vacuum apparatus—required for atomic systems—with the cryogenic systems required for the mechanical oscillator to be pre-cooled sufficiently to reach the quantum regime. This is a significant challenge, but one that has been overcome by some groups (*e.g.* [138]). Alternative proposals call for atoms, or atom-like emitters, to be embedded into the mechanical device itself (*e.g.* [139]).

- **Internal & remotely-coupled**. There are comparatively few proposals or experiments in this case, where an oscillator is coupled to the internal degrees of freedom of a distant atom (or ensemble thereof). Notable examples have come from the Treutlein, Hammerer, Zoller, and Polzik groups [140–142]. All rely on the fact that a well-polarised spin ensemble can be described in terms of its mean values and fluctuation operators which are analogous to the position and momentum of a harmonic oscillator. In this setting the 'spin' ensemble is the electronic energy levels of the atoms, and the coupling to light is provided by the Faraday interaction [143].

  The first proposal employs two sequential interactions to generate atom–mechanical entanglement. A travelling wave optical mode is allowed to transmit through an optomechanical cavity, and the resulting phase fluctuations are converted into Faraday-active polarisation rotations by a filter. These are then allowed to interact with a cold atomic cloud. Measuring the output field with homodyne (§ 3.5.1) detection projects the atoms and oscillator into an Einstein–Podolsky–Rosen (EPR) [144] entangled state, which can be used as a resource to *e.g.* teleport a state from the atomic ensemble to the mechanical resonator [140]. This is in principle essentially independent of the mechanical thermal environment.

  A second proposal uses the same effect, but allows the interaction to occur continuously in time and does away with the measurement step [141]. This has the potential to ground-state cool oscillators in the mega- to -gigahertz frequency range, and could permit the precise level of control available for atomic internal states to be brought to bear on mechanical devices.

  Recent work by the Polzik group (still in pre-print at the time of writing [142]) has used a remotely-coupled hybrid system to experimentally realise the 'quantum-mechanics-free subsystem' (QMFSS) concept introduced by Tsang and Caves in 2012 [145]. The essential observation is that the relative position of two oscillators can be made to commute with itself at all times if one oscillator has a 'negative mass', *i.e.* the Hamiltonian is of the form

$$\hat{H} = \frac{\hat{p}_1^2}{2M_1} + \frac{M_1\Omega^2\hat{x}_1^2}{2} - \frac{\hat{p}_2^2}{2|M_2|} - \frac{|M_2|\,\Omega^2\hat{x}_2^2}{2}.$$

  Note that the second oscillator is not simply experiencing an inverted potential: it is stably trapped, but adding an excitation to the negative-mass oscillator reduces its energy [145]. Such

a 'negative mass' oscillator can be realised by preparing a spin ensemble in a highly-polarised spin inversion state [142]. They used this to demonstrate a back-action evading measurement of the relative position operator $\hat{x}_1 - \hat{x}_2$. Such systems can evade the SQL to force and position detection, making them attractive for sensor applications.

A final proposal [146] by Sanz-Mora *et al.* only deals with coupling *via* classical electromagnetic fields.

- **External & integrated**. In this category the mirror is coupled to the motion of an atomic cloud trapped in the intracavity field. One proposal by Singh *et al.* calls for a Bose-Einstein condensate formed within the optical cavity [147], whilst Hammerer *et al.* [148] have predicted that a single atom in a membrane-in-the-middle cavity can reach the strong coupling limit and permit quantum state transfer.

  Although multi-atom systems are rather complicated, Mesier *et al.* [149] showed that in many situations the optical scattering from the atoms forms them into an effective Bragg 'mirror'. This permits one to understand the system dynamics in terms of a reduced description involving only a single atomic position coordinate. This is widely-employed in the field of cold atom optomechanics in rigid cavities (*e.g.* review in [72]).

  Experimentally, the chief difficulty in realising these systems is integrating cryogenics into the set-up to pre-cool the mechanical oscillator without compromising optical access for pumping, or raising the pressure inside the chamber [138].

- **External & remotely-coupled**. This category is the most relevant to this thesis (see Chapter 4). The atomic motion is coupled to a remote mechanical oscillator. This has the dramatic advantage of allowing the two subsystems to be prepared separately *i.e.* there is no need to integrate cryogenic apparatus with ultra-high vacuum systems. It is also eminently suitable for applications involving low-frequency mechanical oscillators, as trapped atoms typically have mechanical frequencies of only $\omega_{\mathrm{at}} \sim 10^3$–$10^6$ Hz.

  Remotely-couple hybrid atom–optomechanical devices of this variety were first proposed by Hammerer *et al.* [150], and experimentally realised by Camerer *et al.* [6]. They observed incoherent coupling and sympathetic cooling in a system with no optical cavity, as seen in Fig. 2.3. This was followed by a proposal to enhance the coupling using optical cavities [151], which was then experimentally achieved in 2015 by Jöckel *et al.* [152]. The system has been used to cool a membrane to 650 mK from room temperature, and has recently been shown to allow mechanical amplification *via* collectively-enhanced atomic motion [153].

  Our contributions to this field will be examined in Chapter 4.

2.3.4 Pulsed optomechanics

In nearly all of the preceding discussion the cavity has been driven by a monochromatic or weakly-modulated field. It is natural to ask what happens in the limit of a broadband drive field *i.e.* a pulsed

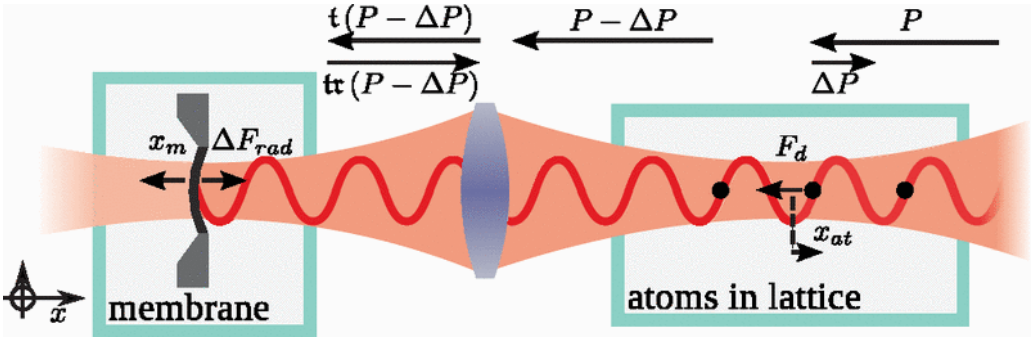

Figure 2.3: Remotely-coupled hybrid atom–optomechanical device (realised by Camerer *et al.* [6]). Light is incident from the right and reflects from the micromechanical membrane, forming a standing wave into which atoms are loaded. The atoms scatter light out of the incident field as a function of their position (x_{at}), modulating the forward-scattered power $P-\Delta P$. This alters the radiation pressure force ΔF_{rad} exerted on the mirror (transmissivity t, reflectivity r, position x_{m}). An effective X–X coupling emerges when the optical field is adiabatically eliminated. Laser cooling of the atomic centre-of-mass motion sympathetically cools the oscillator. Figure reproduced from [6], © APS; reused with permission.

optical input. This situation was first explored by Vanner *et al.* in 2011 [154], and has since enjoyed a wealth of theoretical progress.

Deep sub-mechanical-period pulsed optomechanics generates a quantum non-demolition (QND) interaction between the mechanical oscillator and pulse. QND interactions are accessible in the resolved-sideband limit, but these interactions probe the envelope of the X_{M} operator (the X_{M} quadrature), rather than the position itself [90, 155]. Both are forms of back-action evading measurements, in that the measurement process does not disturb the measured operator [14].

The original proposal [154] was phrased in terms of measurement operators, which we will not make use of in this thesis. Instead, we will provide the theory in a language that is relevant to our discussion of pulsed optomechanical interfaces in Chapter 5.

Suppose that we have access to a broadband cavity with a small optomechanical coupling, such that $\kappa \gg \omega_{\mathrm{M}} \gg g_0$. If a bright, pulsed pump beam is applied to the cavity the replacement $a \to \alpha(t) + \delta a(t)$ may be made, where the displaced annihilation operator $\delta a(t)$ is zero mean and $\alpha(t)$ is the mean intracavity amplitude induced by the pump. Then

$$\hat{H} = \hbar g_0 X_{\mathrm{M}} \left(|\alpha(t)|^2 + \alpha^* \delta a(t) + \alpha(t)\, \delta a^\dagger(t) + \delta a^\dagger(t)\, \delta a(t) \right).$$

These quantities are written with explicit time dependence to show that they depend on the pulse used to illuminate the cavity.

As is common, we neglect the 'small' term $\delta a^\dagger(t)\, \delta a(t)$ (*cf.* § 2.1.1). Thus we arrive at the effective linearised Hamiltonian [154]

$$\hat{H} = \hbar |\alpha(t)|\, g_0 X_{\mathrm{M}} \check{X}_{\mathrm{L}}(t) + \hbar g_0 X_{\mathrm{M}} |\alpha(t)|^2 \tag{2.14}$$

Throughout this section, and Chapter 5 we will write the time-dependent fluctuation operators with a 'check' accent ($\check{\cdot}$) to distinguish them from the collective pulse quadratures that we introduce below.

The drive field is described by a mean amplitude $\alpha_{\rm in}(t)$, normalised such that the average number of photons in the input pulse envelope is

$$N = \int_{-\infty}^{\infty} \mathrm{d}t \;\; |\alpha_{\rm in}(t)|^2 \gg 1,$$

and the instantaneous amplitude and phase noise operators, $\check{X}_{\rm L,in}(t)$ and $\check{P}_{\rm L,in}(t)$. The latter are defined by analogy with the intracavity field. The optical field exiting the cavity is connected to the intracavity mode and input field through the input–output relation, Eqn (2.5b). This takes the form

$$\check{X}_{\rm L,out}(t) = \sqrt{\kappa}\,\check{X}_{\rm L}(t) - \check{X}_{\rm L,in}(t), \tag{2.15}$$

with a similar expression holding for the phase fluctuations [50].

If the bandwidth of the pulse is large compared to both the mechanical frequency and the thermal heating rate $\Gamma \times (\bar{n}_{\rm H} + 1/2)$ we may neglect the damped dynamics of the oscillator over the duration of the interaction; furthermore, the large cavity linewidth (compared to the pulse bandwidth) allows the optical fields to be adiabatically eliminated (as will be described in § 3.3.1). Together, these approximations yield effective Langevin equations of the form

$$\begin{aligned}
\dot{X}_{\rm M} &= 0 && \text{(2.16a)}\\
\dot{P}_{\rm M} &= -\frac{8g_0|\alpha_{\rm in}(t)|}{\kappa}\left(\check{X}_{\rm L,in}(t) + |\alpha_{\rm in}(t)|\right) && \text{(2.16b)}\\
\check{X}_{\rm L,out}(t) &= \check{X}_{\rm L,in}(t), && \text{(2.16c)}\\
\check{P}_{\rm L,out}(t) &= \check{P}_{\rm L,in}(t) - \frac{8g_0|\alpha_{\rm in}(t)|}{\kappa} X_{\rm M}, && \text{(2.16d)}
\end{aligned}$$

in which we have used (2.5b) to obtain (2.16c) & (2.16d).

Integrating (2.16a) and (2.16b) over the duration of the pulse and employing the fact that the pulse envelope changes rapidly compared to $\omega_{\rm M}^{-1}$ allows us to obtain the following transformation between the initial and final mechanical operators (final operators are primed).

$$\begin{aligned}
X'_{\rm M} &= X_{\rm M},\\
P'_{\rm M} &= P_{\rm M} + \chi\sqrt{N} + \chi\int_{-\infty}^{\infty} \mathrm{d}t \;\; \frac{|\alpha_{\rm in}(t)|}{\sqrt{N}}\check{X}_{\rm L,in}(t), && \text{(2.17)}
\end{aligned}$$

where the interaction strength is $\chi = -8g_0\sqrt{N}/\kappa$. We see that the weighted optical amplitude fluctuations have been transferred onto the mechanical momentum $P'_{\rm M}$, along with a classical momentum kick $\chi\sqrt{N}$. It is possible to subtract off the classical kick by performing a displacement on the mechanical oscillator immediately after the interaction; this can be done using open-loop control with very little added noise (*e.g.* [156]).

Motivated by the form of (2.17), we factorise the pulse envelope into the form $\alpha_{\rm in}(t) = \sqrt{N}\,f(t)$; thus the integral of $|f(t)|^2$ over the whole pulse is unity. Multiplying (2.16c) & (2.16d) by $|f(t)|$ and integrating, we find

$$X'_{\rm L} = X_{\rm L},\; P'_{\rm L} = P_{\rm L} + \chi X_{\rm M}, \tag{2.18}$$

in which the collective pulse quadratures X_{L} and P_{L} ($[X_{\mathrm{L}}, P_{\mathrm{L}}] = [X_{\mathrm{M}}, P_{\mathrm{M}}] = 2\mathrm{i}$) have been defined by

$$\begin{aligned} X_{\mathrm{L}} &= \int_{-\infty}^{\infty} \mathrm{d}t \;\; |f(t)|\, \check{X}_{\mathrm{L,in}}(t)\,, \\ P_{\mathrm{L}} &= \int_{-\infty}^{\infty} \mathrm{d}t \;\; |f(t)|\, \check{P}_{\mathrm{L,in}}(t)\,. \end{aligned}$$

Note that these quadratures are zero-mean by construction. Similar relations hold for X'_{L} and P'_{L}, with the input fields replaced by $\check{X}_{\mathrm{L,out}}(t)$ and $\check{P}_{\mathrm{L,out}}(t)$ respectively.

The evolution described by (2.17) (including a mechanical displacement) and (2.18) is thus a standard QND interaction between the mechanical oscillator and the collective quadratures of the optical pulse;

$$X'_{\mathrm{M}} = X_{\mathrm{M}}, \qquad P'_{\mathrm{M}} = P_{\mathrm{M}} + \chi X_{\mathrm{L}}, \tag{2.19a}$$

$$X'_{\mathrm{L}} = X_{\mathrm{L}}, \qquad P'_{\mathrm{L}} = P_{\mathrm{L}} + \chi X_{\mathrm{M}}. \tag{2.19b}$$

Each oscillator acquires information about one quadrature of the other during this interaction. This is a back-action evading in the sense that the light records the position of the mechanical oscillator without affecting X_{M}; all of the back-action goes onto the momentum operator [6].

Applications of pulsed optomechanics

The original proposal for pulsed optomechanics put forward that it may be used to create and verify quantum states *via* measurement. In principle, the QND interaction allows one to project the position into a sub-vacuum-variance state at the beginning of the preparation scheme, and a subsequent pulse one quarter of a mechanical cycle later projects the orthogonal quadrature. One thus conditionally achieves a very low entropy state. The Wigner function can then be reconstructed by performing further QND measurements on identically-prepared states at different delay times *à la* quantum state tomography [157]. These predictions were experimentally tested by Vanner *et al.* [158] in a 2013 study that successfully cooled a mode of a cantilever 'lollipop' resonator from 1100 K[7] to 16 K. To our knowledge, this is the only pulsed optomechanics experiment realised to date.

A 2012 study by Pikovski *et al.* [159] suggested that pulsed optomechanics may be used to probe putative Planck scale physics, on the grounds that the canonical commutation relation $[\hat{x}_{\mathrm{M}}, \hat{p}M] = \mathrm{i}\hbar\mathbb{1}$ must require modification if there is a minimum possible length scale. Their scheme requires four pulsed QND interactions that map the commutator onto the optical field for sensitive read-out.

Khosla *et al.* [160] showed that pulsed optomechanics can be used to generate an optomechanical geometric phase—an additional phase that depends upon, in this case, the area enclosed by a loop traversed through phase space. This can permit the generation of states with Wigner negativity [160]. Recently, the same authors have proposed a means of performing quantum state preparation and tomography outside of the quantum coherent oscillation ($Q > \bar{n}$) regime by employing recycled pulses

[6] Of course, the free evolution of the oscillator will rotate the back-action on P_{M} into X_{M} at later times.

[7] The bulk material was at room temperature, but an incoherent drive was applied prior to the first pulse to raise the mode temperature to 1100 K.

with short delays between them [71]. In § 6.8 we will see one scenario where this could potentially be applied.

As a final example, Vostrosablin *et al.* have shown that two oscillators that interact in serial with a common optical mode *via* QND interactions can become entangled [161]. This scheme requires classical measurement and feedforward to complete the entangling process between the distant mechanical oscillators. A related procedure proposed by the same authors could allow entanglement to be generated between multiple optical modes using a pulsed optomechanical transducer [162].

2.4 Other optomechanical couplings and techniques

The literature review provided above has not come close to doing full justice to the breadth of optomechanics and related topics. In the interests of completeness, in this section we will list some exciting sub-fields which we are not going to touch upon in the remainder of this thesis.

- Optomechanics with nonlinear mechanical devices can be used to investigate the quantum-to-classical transition and a means of creating nonclassical states [163].
- Alternatively, nonlinear optomechanical measurement and control can be used to create nonclassical states of linear oscillators [164, 165].
- There are systems in which the optomechanical coupling is quadratic in X_{M} [47, 166, 167], which can enable phonon number measurements.
- If the oscillator modulates the cavity linewidth instead of its frequency the system is said to be dissipatively coupled [168–173], as opposed to the dispersive (frequency-shifting) coupling which we consider in this thesis. This has been realised experimentally [174].
- Photothermal or bolometric forces—forces induced by optical absorption within the material of the resonator—can be used for quantum optomechanics. Ironically, it is possible to cool a mechanical mode by heating the bulk material [175]. This may be encouraged by choosing the material carefully [176]. One intriguing application is to the photothermal control of third-sound (thin film) waves in He-3 superfluids coated on whispering gallery-mode resonators [177, 178].
- Hybrid optoelectromechanical systems can be used to interface optical and microwave phonons at the single-quantum level. It is hoped that this will provide a means of connecting fibre networks to processing nodes in a ‘quantum internet’ [103, 179–183].

Comprehensive reviews can be found in the literature (*e.g.* [5, 31, 37, 105]), and in the textbooks that are beginning to emerge in the field [70, 72].

Chapter 3

Tools of the trade

In this chapter we will introduce and describe several theoretical and experimental tools which will be used throughout what follows. The intent is to provide useful background for those reading this thesis, and to assist those who might benefit from applying these tools in their own research setting. We have assumed familiarity with elementary quantum mechanics throughout. A 'primer' on quantum optics notation and terminology has been provided in § 1.3.

3.1 Describing quantum states

In classical physics we are usually able to specify the behaviour of a system with a finite number of quantities: position, momentum, orientation, and so forth. Quantum mechanics generally requires a more complicated method of specifying the state of a system. In this thesis we will make heavy use of the covariance matrix formalism and the Wigner function, which we introduce in this section.

3.1.1 Covariance matrices

Recall that any pure state $|\psi\rangle$ has an associated density operator $\hat{\rho}_\psi = |\psi\rangle\langle\psi|$ such that the expectation value of an arbitrary operator $\hat{O}$ is given by $\langle\hat{O}\rangle = \mathrm{Tr}\{\hat{\rho}\hat{O}\}$. This property holds for incoherent mixtures of states, where the density operator becomes

$$\hat{\rho} = \sum_j \mathscr{P}_j \left|\psi_j\right\rangle\!\left\langle\psi_j\right|$$

for any partitioning of $\hat{\rho}$ into pure states $\left|\psi_j\right\rangle$ (that are not necessarily orthogonal). The positive, real weighting factors are interpreted as classical probabilities, and so $\mathscr{P}_j$ must sum to unity.

If we know the density operator $\hat{\rho}$ then it is in principle straightforward to apply the Born rule to calculate the full statistics of any observable $\hat{O} = \hat{O}^\dagger$, where the dagger indicates the Hermitian conjugate. Conversely, if the full statistics of *all* observable operators (including their higher moments) are known then we can reconstruct $\hat{\rho}$. This is in general an extremely difficult problem to tackle for arbitrary continuous variable states [157], potentially requiring an infinite set of moments. However, it

often happens that the statistics of all operators are Gaussian *i.e.* all higher-order moments of their probability distributions are determined solely by the first and second moments. When this is the case a quite compact description can be employed: the covariance matrix.

The simplest case of interest is a single mode harmonic oscillator with dimensionless position and momentum X and P satisfying $[X,P] = 2\mathrm{i}$. All observable operators for this system can be built entirely from X and P (*e.g.* the Hamiltonian is $\propto X^2 + P^2$), so if we know their statistics we can calculate everything else. Let us arrange the operators into a vector-like object $\boldsymbol{X} = (X\ P)^{\mathrm{T}}$. The covariance matrix V is then given by

$$V = \frac{1}{2}\left[\left\langle \delta\boldsymbol{X}\ \delta\boldsymbol{X}^{\mathrm{T}}\right\rangle + \left\langle \delta\boldsymbol{X}\ \delta\boldsymbol{X}^{\mathrm{T}}\right\rangle^{\mathrm{T}}\right], \tag{3.1}$$

where $\delta\boldsymbol{X} = \boldsymbol{X} - \langle\boldsymbol{X}\rangle$ describes the fluctuations away from the mean value $\langle\boldsymbol{X}\rangle$. To understand the meaning of each element of V we will expand the definition in terms of the individual fluctuation operators δX and δP to obtain

$$V = \begin{pmatrix} \langle\delta X^2\rangle & \frac{1}{2}\langle\delta X\delta P + \delta P\delta X\rangle \\ \frac{1}{2}\langle\delta X\delta P + \delta P\delta X\rangle & \langle\delta P^2\rangle \end{pmatrix}.$$

In this form it is clear that the diagonal elements are the variances of X and P respectively, whilst the off-diagonal element (there being only one unique element because $V = V^{\mathrm{T}}$) measures the strength of correlations between X and P. With this definition the covariance matrix of any coherent state is equal to the identity matrix.

It is worth noting that the elements of V are always real, and that the Heisenberg uncertainty principle requires $\det\{V\} \geq 1$. This is because the eigenvalues of V can be identified as the variances of the squeezed and antisqueezed quadratures.

Multimode covariance matrices

It is possible to extend the definition of the covariance to include n modes; one simply uses Eqn (3.1) with $\delta\boldsymbol{X} = (\delta X_1\ \delta P_1\ \delta X_2\ \delta P_2\ \cdots\ \delta X_n\ \delta P_n)^{\mathrm{T}}$. The n^{th} 2×2 diagonal block can be interpreted as the covariance matrix for the n^{th} mode once all other modes have been traced out. Off-diagonal blocks encode the correlations between the modes.

Note that in the multimode case the eigenvalues of V do not correspond to the squeezed and antisqueezed quadrature variances; instead, the *symplectic* eigenvalues correspond to the maximum and minimum variances in a common mode basis. We will not make use of this feature in this thesis.

Common covariance matrices

Some common covariance matrices are given in Tab. 3.1. It is worth noting that any Gaussian state can be generated by applying squeezers, rotations, and displacement operators to a thermal state, so that an arbitrary (single-mode) Gaussian state is characterised entirely by the finite set of numbers

State	Covariance matrix
$\|0\rangle$	$\mathbb{1}$
Thermal	$(2\bar{n}+1)\mathbb{1}$
Squeezed	$\begin{pmatrix} \cosh(2r_{\rm s}) - \sinh(2r_{\rm s})\cos(2\theta_{\rm s}) & -\sinh(2r_{\rm s})\sin(2\theta_{\rm s}) \\ -\sinh(2r_{\rm s})\sin(2\theta_{\rm s}) & \cosh(2r_{\rm s}) + \sinh(2r_{\rm s})\cos(2\theta_{\rm s}) \end{pmatrix}$
Generic	$\mathrm{S}(r_{\rm s},\theta_{\rm s})\mathrm{V}_{\rm thermal}S^{\rm T}(r_{\rm s},\theta_{\rm s}) = (2\bar{n}{+}1)\ \mathrm{S}(r_{\rm s},\theta_{\rm s})S^{\rm T}(r_{\rm s},\theta_{\rm s})$

Table 3.1: Some common single-mode covariance matrices which will be encountered in this thesis. The thermal state is characterised by a single parameter, $\bar{n}$, which is the thermal occupancy of the mode. The squeezed (vacuum) state requires two parameters: the squeezing magnitude $r_{\rm s}$ and the squeezing angle $\theta_{\rm s}$. A generic covariance matrix may be obtained by squeezing a thermal state; the squeezing operation is represented by the matrix $S(r_{\rm s},\theta_{\rm s})$. Note that displacement operations alter the mean values $\langle \boldsymbol{X}\rangle$; they do not alter the covariance matrix.

$\{\bar{n}, r_{\rm s}, \theta_{\rm s}, \langle \boldsymbol{X}\rangle\}$. For this reason, squeezers, displacements, and rotations are known as Gaussian operations[1].

3.1.2 Wigner functions

A well-known method of specifying the state of a classical particle is to give its location in phase space: that is, its position and momentum at a given time t. If this and the Hamiltonian are known then it is possible to determine the trajectory that the particle will follow in the future. In the quantum setting this is not possible because the uncertainty principle forbids us from specifying a single point in phase space; there are no simultaneous eigenstates of position and momentum. we must instead settle for some sort of distribution. Although many different proscriptions for associating a density operator $\hat{\rho}$ with a phase space distribution exist—including the Glauber–Sudarshan P-function [51, 185], and the Husimi Q-function [186]—in this thesis we will only make use of the Wigner function, W [187], and the characteristic function, χ.

We have selected the Wigner function because it does not suffer from any singularities—unlike the P-function—and it furnishes us with a relatively simple metric for nonclassicality—unlike the Q-function. $W(\boldsymbol{r})$ is therefore well-suited to use in numerical calculations. We discuss these features further in § 3.2.

Formally, the Wigner function W is a real-valued function of the phase space point $\boldsymbol{r} = (x\ p)^{\rm T}$, where the position coordinate x and its conjugate momentum p can be interpreted as eigenvalues of the dimensionless position and momentum operators[2]. It behaves very similarly to a classical joint

[1] Any Hamiltonian that can be expressed as a quadratic form generates a Gaussian operation [184].

[2] This sets our normalisation convention for the Wigner function.

probability distribution, in that

$$\int_{-\infty}^{\infty} \mathrm{d}^2\boldsymbol{r}\, W(\boldsymbol{r}) = 1 \tag{3.2a}$$

$$\int_{-\infty}^{\infty} \mathrm{d}x\, W(\boldsymbol{r}) = \langle P|\,\hat{\rho}\,|P\rangle \tag{3.2b}$$

$$\int_{-\infty}^{\infty} \mathrm{d}p\, W(\boldsymbol{r}) = \langle X|\,\hat{\rho}\,|X\rangle\,; \tag{3.2c}$$

i.e. it is normalised and it reproduces the correct marginal distributions when the orthogonal axis is integrated out. Note that the right-hand sides of Eqn (3.2b) and Eqn (3.2c) are precisely the probability densities obtained from the Born rule. We have used the convention $X\,|X\rangle = x\,|X\rangle$ with $\langle X|X'\rangle = \delta(x-x')$. The second property holds for any orthogonal pair of quadratures, not just X and P. However, as we shall see, W does have peculiarities that are not permitted in proper probability distributions, such as taking on negative values. For this reason the Wigner function is usually referred to as a *quasiprobability* distribution.

Formal definition: single mode

We will first introduce the characteristic function, defined by

$$\chi(\beta) = \mathrm{Tr}\left\{\hat{\rho}\hat{D}(\beta)\right\}, \tag{3.3}$$

where β is a complex number and $\hat{D}(\beta)$ is the displacement operator defined in the usual way, *i.e.*

$$\hat{D}(\beta) = \exp\left\{\beta a^\dagger - \beta^* a\right\}, \tag{3.4}$$

with $a = (X + \mathrm{i}P)/2$.

As the name implies, χ is the quantum analogue of the characteristic function encountered in classical probability theory. For our purposes, it is sufficient to note that χ is one-to-one with the density matrix $\hat{\rho}$, such that one may be uniquely recovered from the other; χ therefore suffices to totally characterise the state [50].

Unfortunately, χ is also rather difficult to visualise, as it is generally complex-valued. However, we can recover the real-valued Wigner function from it *via* the transformation

$$W(\boldsymbol{r}) = \frac{1}{(2\pi)^2}\int \mathrm{d}^2\beta\; \chi(\beta)\exp\{-\mathrm{i}\boldsymbol{r}\cdot\boldsymbol{\varpi}\boldsymbol{\beta}\}, \tag{3.5}$$

in which

$$\boldsymbol{\varpi} = \begin{pmatrix} 0 & 1 \\ -1 & 0 \end{pmatrix}$$

and $\boldsymbol{\beta} = (\Re\{\beta\}\ \Im\{\beta\})^{\mathrm{T}}$. Note the useful properties $\boldsymbol{\varpi}^{\mathrm{T}} = -\boldsymbol{\varpi}$ and $\boldsymbol{\varpi}\,\boldsymbol{\varpi}^{\mathrm{T}} = \boldsymbol{\varpi}^{\mathrm{T}}\boldsymbol{\varpi} = -\mathbb{1}$). The inverse transformation is

$$\chi(\beta) = \int \mathrm{d}^2\boldsymbol{r}\, W(\boldsymbol{r})\exp\{+\mathrm{i}\boldsymbol{r}\cdot\boldsymbol{\varpi}\boldsymbol{\beta}\}. \tag{3.6}$$

These transformations are sometimes called symplectic Fourier transforms, and are closely related to the Fourier transform that we will introduce in § 3.3.1. This allows us to see that $\boldsymbol{\beta}$ can be interpreted

as a vector in the space that is reciprocal to phase space, much as time and frequency are reciprocal variables.

From Eqn (3.5) we can see several useful properties of the Wigner function.

- $W(\boldsymbol{r}) < 0$ is possible for some finite subset of the phase space (it cannot be everywhere negative because of the normalisation property Eqn 3.2a). The meaning of Wigner negativity is discussed in § 3.2. It can be proven that all non-Gaussian Wigner functions that correspond to pure states *must* violate non-negativity [188].
- $W(\boldsymbol{r})$ is bounded above and below: $|W| \leq 1/2\pi$.
- $W(\boldsymbol{r})$ for a mixed state is the normalised sum of $W(\boldsymbol{r})$ for each component pure state (for any partitioning of the mixed state into pure states). That is, for any set of Wigner functions W_j corresponding to pure states $\left|\psi_j\right\rangle$ (that are not necessarily orthogonal) we may write
$$\hat{\rho} = \sum_j \mathscr{P}_j \left|\psi_j\right\rangle\!\left\langle\psi_j\right| \Leftrightarrow W(\boldsymbol{r}) = \sum_j \mathscr{P}_j W_j(\boldsymbol{r})$$
where the weights $\mathscr{P}_j$ sum to one. Note that this property does *not* hold for pure state superpositions.
- For any operator f one may calculate the corresponding function on phase space $\breve{f}$ using the Weyl transform.
$$\breve{f}(\boldsymbol{r}) = \frac{1}{\pi}\int \mathrm{d}^2\boldsymbol{\beta}\, \mathrm{Tr}\left\{f\hat{D}(\boldsymbol{\beta})\right\} \exp\left\{-\mathrm{i}\boldsymbol{r}\cdot\boldsymbol{\varpi}\boldsymbol{\beta}\right\}.$$
Note the close relationship between this and the definition of the characteristic function. It is also important to note that in general the Weyl transform of a product of operators is not equal to the product of their Weyl transforms. Functions of only one quadrature (*e.g.* $f(X)$ or $f(P)$) are useful exceptions.
- The expectation value of an operator f is determined using
$$\langle f\rangle = \int \mathrm{d}^2\boldsymbol{r}\, W(\boldsymbol{r})\,\breve{f}(\boldsymbol{r}).$$
- As a corollary of the above, the purity of the state is given by
$$\mathrm{Tr}\left\{\hat{\rho}^2\right\} = 4\pi\int_{-\infty}^{\infty} \mathrm{d}^2\boldsymbol{r}\, W^2(\boldsymbol{r})$$
- Similarly, the Schumacher fidelity [189] $\mathscr{F} = \langle\psi|\hat{\rho}|\psi\rangle$ between W and a target pure state with Wigner function $W_{|\psi\rangle}$ is
$$\mathscr{F} = 4\pi\int \mathrm{d}^2\boldsymbol{r}\, W(\boldsymbol{r}) W_{|\psi\rangle}(\boldsymbol{r}). \tag{3.7}$$

Formal definition: multimode

It is possible to extend the definition of the Wigner function to include multiple modes in a higher-dimensional phase space. Details are given in App. A.4. We will make some use of this in Chapter 5.

Gallery of Wigner functions

Some examples of important Wigner functions are given in Tab. 3.2. Related plots are shown in Fig. 3.1.

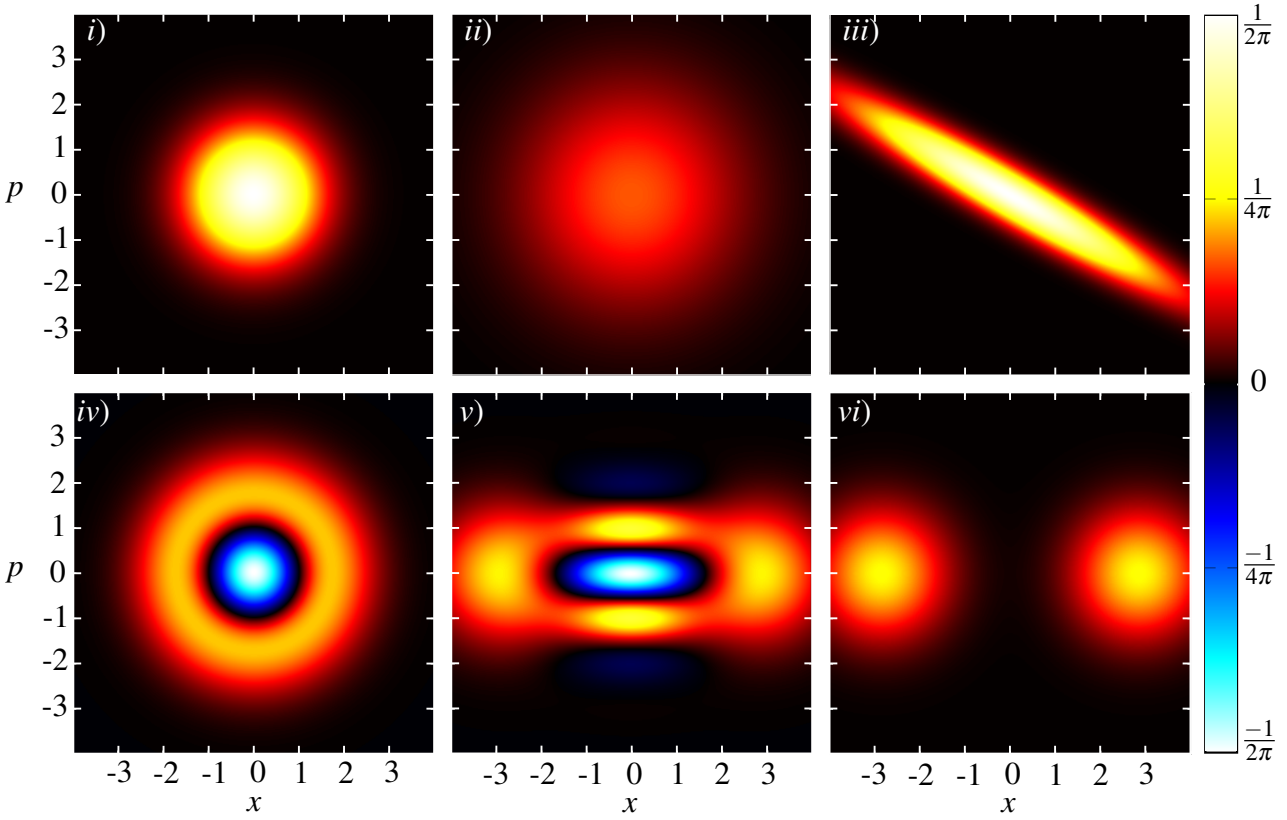

Figure 3.1: Examples of Wigner functions. Panels *i*)–*iii*) show Gaussian states; panels *iv*)–*vi*) show non-Gaussian states. Wigner negativity appears as blue–white areas.
i) Ground state ($|0\rangle$). Its rotational symmetry demonstrates that the variance is equal in all directions through phase space. All coherent states have the same Wigner function up to translations in phase space.
ii) Thermal state with $\bar{n} = 1$. The Wigner function is still everywhere positive and rotationally symmetric.
iii) Squeezed state with $r_s = 1$ and $\theta_s = \pi/3$. The rotational symmetry is broken; the quadrature at $\pi/3$ is reduced to a variance below the ground state variance, whilst the variance in the orthogonal direction is amplified.
iv) Wigner function of the Fock state $|1\rangle$. Unlike the Gaussian states, this Wigner function exhibits extremely strong negativity near the origin.
v) A low-amplitude odd $(-)$ cat state with $\alpha = \sqrt{2}$. The 'interference' pattern along the p axis and the presence of strong negativity indicate coherence between the two 'lobes' at $x = \pm 2\sqrt{2}$.
vi) An incoherent mixture of the coherent states $|\alpha\rangle$ with $\alpha = \sqrt{2}$. This is considered a 'classical' state because the Wigner function is everywhere positive, unlike the cat state in panel *v*). Note the absence of the 'interference' fringes and their accompanying negativity.

State	$\chi(\beta)$	$W(x,p)$
$\|0\rangle$	$\exp\left\{-\frac{1}{2}\|\beta\|^2\right\}$	$(2\pi)^{-1}\exp\left\{-\frac{1}{2}\boldsymbol{r}\cdot\boldsymbol{r}\right\}$
Thermal	$\exp\left\{-\frac{1}{2}(2\bar{n}+1)\|\beta\|^2\right\}$	$(2\pi(2\bar{n}+1))^{-1}\exp\left\{-\frac{1}{2(2\bar{n}+1)}\boldsymbol{r}\cdot\boldsymbol{r}\right\}$
Gaussian	$\exp\left\{-\frac{1}{2}\boldsymbol{\beta}^{\mathrm{T}}\boldsymbol{\varpi}^{\mathrm{T}}V\boldsymbol{\varpi}\boldsymbol{\beta}\right\}\times$ $\exp\left\{\mathrm{i}\langle\boldsymbol{X}\rangle\cdot\boldsymbol{\varpi}\boldsymbol{\beta}\right\}$	$\left(2\pi\|V\|^{1/2}\right)^{-1}\exp\left\{-\frac{1}{2}\,\delta\boldsymbol{r}^{\mathrm{T}}V^{-1}\delta\boldsymbol{r}\right\}$
$\|1\rangle$	$\exp\left\{-\frac{1}{2}\|\beta\|^2\right\}\left(1-\|\beta\|^2\right)$	$(2\pi)^{-1}\exp\left\{-\frac{1}{2}\boldsymbol{r}\cdot\boldsymbol{r}\right\}(\boldsymbol{r}\cdot\boldsymbol{r}-1)$
$\|2\rangle$	$\frac{1}{2}\exp\left\{-\frac{1}{2}\|\beta\|^2\right\}\left(2-4\|\beta\|^2+\|\beta\|^4\right)$	$(4\pi)^{-1}\exp\left\{-\frac{1}{2}\boldsymbol{r}\cdot\boldsymbol{r}\right\}\times$ $\left(2+p^4+x^4-4x^2-4p^2+2p^2x^2\right)$
$\|n\rangle$	$\mathrm{e}^{-\frac{1}{2}\|\beta\|^2}\mathscr{L}_n\left(\|\beta\|^2\right)$	$(2\pi)^{-1}(-1)^n\exp\left\{-\frac{1}{2}\boldsymbol{r}\cdot\boldsymbol{r}\right\}\mathscr{L}_n(\boldsymbol{r}\cdot\boldsymbol{r})$
Cat (α)	$\left(1\pm\mathrm{e}^{-2\|\alpha\|^2}\right)^{-1}\mathrm{e}^{-\frac{1}{2}\|\beta\|^2}\times$ $\left[\begin{array}{c}\cosh[\alpha^*\beta-\beta^*\alpha]\pm\\ \mathrm{e}^{-2\|\alpha\|^2}\cosh[\alpha^*\beta+\beta^*\alpha]\end{array}\right]$	$\mathrm{e}^{-\frac{1}{2}\boldsymbol{r}\cdot\boldsymbol{r}}\left(2\pi\left(1\pm\mathrm{e}^{-2\|\alpha\|^2}\right)\right)^{-1}\times$ $\left[\begin{array}{c}\mathrm{e}^{-2\|\alpha\|^2}\cosh(2\boldsymbol{r}\cdot\boldsymbol{\alpha})\pm\\ \cos(2\boldsymbol{r}\cdot\boldsymbol{\varpi}\boldsymbol{\alpha})\end{array}\right]$

Table 3.2: A selection of Wigner functions and their characteristic functions. In the Gaussian expression $\delta\boldsymbol{r}=\boldsymbol{r}-\langle\boldsymbol{X}\rangle$. The n^{th} Fock state is $|n\rangle$, and $\mathscr{L}_n$ is the n^{th} Laguerre polynomial defined by $\mathscr{L}_n(x)=\mathrm{e}^x(n!)\frac{\mathrm{d}^n}{\mathrm{d}x^n}[x^n\mathrm{e}^{-x}]$. The odd and even ($\pm$ respectively) 'cat' states are pure superpositions of coherent states, parametrised by the coherent amplitude α such that $|\psi^{\pm}\rangle\propto|\alpha\rangle\pm|-\alpha\rangle$.

3.2 Classifications of nonclassicality

Deciding what is and is not 'truly quantum mechanical' has been a vexing problem since the earliest days of quantum theory. There have been numerous attempts to categorise quantum states according to how nonclassical they are—in the sense that classical mechanics or classical statistical mechanics fail to account for their experimental properties—but there is still no single widely-accepted metric for nonclassicality [190]. In this section we will provide a brief discussion of Wigner negativity, one of the most widely-used nonclassicality metrics in the optomechanics community. We do not intend to be thorough—whole theses have been written on such topics [191]!—but only to provide some justification for using the Wigner function (§ 3.1.2) over other possible phase space distributions.

There are many possible ways of associating a quantum state with a phase space distribution [192], but for practical reasons the three most common are the P-function, Wigner function, and Q-function. These correspond to the extreme choices of calculating the characteristic function using normally-ordered expectation values, symmetrically-ordered expectation values, or anti-normally-ordered expectation values, respectively [50].

The definitions of the P-function $P_{\mathrm{GS}}(\alpha)$ [51, 185] and Q-function $Q_{\mathrm{H}}(\alpha)$ [186] are as follows;

$$\hat{\rho} = \int_{-\infty}^{\infty}\mathrm{d}^2\alpha\, P_{\mathrm{GS}}(\alpha)\,|\alpha\rangle\langle\alpha| \tag{3.8a}$$

$$Q_{\mathrm{H}}(\alpha) = \frac{1}{\pi}\langle\alpha|\,\hat{\rho}\,|\alpha\rangle\,. \tag{3.8b}$$

Many nonclassicality metrics rely on the fact that these distributions—much like the Wigner function—

do not always fulfil the requirements of a classical probability density, especially normalisability and non-negativity.

Firstly let us note that the Q-function is always well-behaved, in the sense that it is non-negative and normalisable by definition. The former property holds because of the positivity of the density matrix, and the latter because of the resolution of the identity in terms of coherent states, *viz.*

$$\int \mathrm{d}^2\alpha \, Q_{\mathrm{H}}(\alpha) = \int \frac{\mathrm{d}^2\alpha}{\pi} \, \langle\alpha|\,\hat{\rho}\,|\alpha\rangle = \mathrm{Tr}\{\hat{\rho}\} = 1.$$

However, it does not reproduce the correct marginal distributions, and so cannot be interpreted as a joint probability density under any circumstances. For these reasons we will not consider the Q-function as a useful indicator of nonclassicality, nor employ it in calculations in this thesis.

As noted by many authors (*e.g.* [50]), the non-orthogonality of the coherent states means that P_{GS} is not a genuine probability distribution either. However, unlike the Q-function, for some quantum states the P-function fails to be non-negative and normalisable. In this interpretation, a 'nonclassical' state is one that has a pathological P-function. Physically this means that the state cannot be represented by a statistical mixture of coherent states. The merits of this definition of non-classicality are discussed at length in [191].

Squeezed states are an excellent and experimentally-relevant example of states with pathological P-functions. To see this, note that the variance of the squeezed quadrature is lower than that of the vacuum fluctuations of a coherent state. We would therefore expect the squeezed state's P-function to be narrower than that of a coherent state. This causes a problem; the P-function of a coherent state $|\beta\rangle$, $P_{\mathrm{GS},\beta} = \delta^2(\alpha - \beta)$, cannot be made narrower in any direction. Something has to give, and the full calculation reveals that in this case it is the non-negativity; the P-function of a squeezed state in fact depends on the *derivative* of the Dirac δ, which necessarily has negativity (see App. A.5). On this basis it can be argued that squeezed states are non-classical. This might manifest in experimentally significant ways, such as some amplitude-squeezed states showing nonclassical photon anti-bunching [193].

The above assertion—nonclassicality of the squeezed state on the grounds of pathological $P_{\mathrm{GS}}(\alpha)$—is sometimes rebutted by noting that the Wigner function of the squeezed state (as stated in Tab. 3.2) fulfils nearly all of the requirements of a classical probability density; it is normalised, non-negative, and reproduces the correct marginal distributions [3]. This implies that squeezed states are 'classical', in the sense that one can construct a local hidden variable theory that explains the statistics of quadrature measurements [194]. We are thus led to consider that there may be different 'degrees' of nonclassicality, beginning with ill-behaved P_{GS} and increasing towards the violation of Bell and Bell-type inequalities[4].

Throughout this thesis we will consider negativity of the Wigner function to be a sign of nonclassicality *stronger* than that of the squeezed state. This is a qualitatively useful approach that is often employed in the optomechanics literature. We should note that the use of Wigner negativity as a quantitative nonclassicality metric is justified in many cases [194] but is still poorly understood. Furthermore, divining an operational interpretation of Wigner negativity is notoriously difficult [194–196].

[3] In fact, the Wigner function is a Gaussian convolution of the P function with the vacuum noise [50].

[4] Obviously this requires a multi-mode description.

3.3 Solving equations of motion

As discussed in § 2.1.1, the optomechanical interaction is intrinsically nonlinear. However, in many cases we may readily linearise it. This process of linearisation is ubiquitous in quantum optics, so we will only provide discussion on linear equations of motion in what follows.

3.3.1 Linearised Langevin equations

Consider a Langevin equation of the form

$$\frac{\mathrm{d}\boldsymbol{q}}{\mathrm{d}t} = A\boldsymbol{q}(t) + \boldsymbol{f}(t) \tag{3.9}$$

where $\boldsymbol{q}$ is an n-element vector containing the n-many system operators, A is an $n \times n$ time-independent matrix, and $\boldsymbol{f}(t)$ is a vector of noise operators. Equations of this form—systems of linear first-order ordinary differential equations with additive noise—appear extremely frequently in the optomechanics and quantum optics literature.

There are two typical methods of solving systems in the form of Eqn (3.9); one may diagonalise and solve the time domain problem, or one may use a Fourier transform to find the steady-state properties of the system in the frequency domain. The former is most useful when transient dynamics are important, whilst the latter is more easily connected to experimental measurements made using a spectrum analyser.

Time domain approach

Calculations made in the time domain can be useful when we are interested in transient behaviours, such as how a particular initial state evolves towards the steady-state, or when the system is unstable and frequency domain methods do not converge.

Let us suppose that Eqn (3.9) is non-trivial (A is not proportional to the identity $\mathbb{1}$) and that A is diagonalisable, which is always true for linear, Hamiltonian equations of motion. Then $A = PDP^{-1}$, where D is the diagonal matrix containing the eigenvalues of A, and P is formed from the eigenvectors of A. From this we define a new set of operators $\boldsymbol{b} = P^{-1}\boldsymbol{q}$, such that

$$\frac{\mathrm{d}\boldsymbol{b}}{\mathrm{d}t} = D\boldsymbol{b} + P^{-1}\boldsymbol{f}(t).$$

Employing an integrating factor allows us to write

$$\boldsymbol{b}(t) = \mathrm{e}^{Dt}\boldsymbol{b}(0) + \int_0^t \mathrm{d}t'\, \mathrm{e}^{D(t-t')}P^{-1}\boldsymbol{f}\left(t'\right).$$

Thus if we multiply through from the left by P we obtain

$$\boldsymbol{q}(t) = P\mathrm{e}^{Dt}P^{-1}\boldsymbol{q}(0) + \int_0^t \mathrm{d}t'\, P\mathrm{e}^{D(t-t')}P^{-1}\boldsymbol{f}\left(t'\right),$$

which can be written as

$$\boldsymbol{q}(t) = M(t)\,\boldsymbol{q}(0) + \boldsymbol{F}(t) \tag{3.10}$$

in which the homogeneous component is described by

$$M(t) = P\mathrm{e}^{Dt}P^{-1},$$

and the aggregated noise is

$$\boldsymbol{F}(t) = \int_0^t \mathrm{d}t'\, M\left(t-t'\right)\boldsymbol{f}\left(t'\right). \tag{3.11}$$

Note that, by definition, $M(0) = \mathbb{1}$.

This is an extremely useful result, because it shows that the influence of the noise on the dynamics is described by the *exact* same matrix, M, as the homogeneous part of the evolution. If we know the solution to the homogeneous equations—essentially the classical physics—we may immediately write down the solution to the nonhomogeneous equations. Another important property of Eqn (3.10) is that the initial conditions $\boldsymbol{q}(0)$ explicitly appear. As we will see below, in the frequency domain the initial conditions do not play any role.

If the incoming noise is uncorrelated with the system—the typical case encountered in this thesis—then Eqn (3.10) can be used to calculate the evolution of the covariance matrix according to

$$V(t) = M(t)\,V(0)\,M^{\mathrm{T}}(t) + V_{\mathrm{FF}}(t), \tag{3.12}$$

where we have introduced the covariance matrix of $\boldsymbol{F}$ (Eqn (3.11)), V_{FF}. This is easily found by substituting Eqn (3.10) into Eqn (3.1).

A convenient corollary of Eqn (3.12) is that the system's steady-state—if it exists—may be determined in a relatively straightforward manner. For Gaussian noise and $\det\{M(t)\} < 1$ we obtain the steady-state covariance matrix

$$V_{\mathrm{SS}} = \lim_{\mathrm{t}\to\infty}\int_0^t \mathrm{d}t' \int_0^t \mathrm{d}t''\, M\left(t-t'\right)\left(\frac{\left\langle \boldsymbol{f}(t')\,\boldsymbol{f}^{\mathrm{T}}(t'')\right\rangle + \left\langle \boldsymbol{f}(t'')\,\boldsymbol{f}^{\mathrm{T}}(t')\right\rangle^{\mathrm{T}}}{2}\right) M^{\mathrm{T}}\left(t-t''\right). \tag{3.13}$$

The condition $\det\{M(t)\}$ implies that the homogeneous dynamics are stable.

If the noise is also Markovian we can write

$$\left(\frac{\left\langle \boldsymbol{f}(t')\,\boldsymbol{f}^{\mathrm{T}}(t'')\right\rangle + \left\langle \boldsymbol{f}(t'')\,\boldsymbol{f}^{\mathrm{T}}(t')\right\rangle^{\mathrm{T}}}{2}\right) = \mathscr{N}\boldsymbol{\delta}\left(t'-t''\right),$$

so

$$V_{\mathrm{SS}} = \lim_{\mathrm{t}\to\infty}\int_0^t \mathrm{d}t'\, M\left(t-t'\right)\mathscr{N}\,M^{\mathrm{T}}\left(t-t'\right). \tag{3.14}$$

Frequency-domain approach

In many situations it is beneficial to convert Eqn (3.9) to the frequency domain and consider its behaviour there. This is particularly useful when the time-dependent dynamics are extremely fast, such that any realisable experiment inevitably averages measurement results over several cycles of the system's behaviour. A key example of this is quantum optical experiments, where the optical period is on the order of 10^{-15} s and cannot be resolved by typical measurement devices.

Mathematically, moving to the frequency domain (also called the 'Fourier domain') is achieved by performing a Fourier transform on the equations of motion. For any well-behaved function of time, $f(t)$, there exists a function $\tilde{f}(\omega)$ of (angular) frequency ω that is given by

$$\tilde{f}(\omega) = \int_{-\infty}^{\infty} \mathrm{d}t \ \mathrm{e}^{\mathrm{i}\omega t} f(t) . \tag{3.15}$$

The physical meaning of this is best intuited by considering the inverse transformation, *viz.*

$$f(t) = \frac{1}{2\pi} \int_{-\infty}^{\infty} \mathrm{d}\omega \ \mathrm{e}^{-\mathrm{i}\omega t} \tilde{f}(\omega) . \tag{3.16}$$

Eqn (3.16) makes it clear that $\tilde{f}(\omega)$ contains the phase *and* amplitude information required to reconstruct the function $f(t)$ from the basis of harmonic waves $\mathrm{e}^{-\mathrm{i}\omega t}$.

A number of useful relationships between the time and frequency domain can be drawn; a full list is given in App. A.6. For the purposes of addressing the generic linear Langevin equation (Eqn (3.9)) the most important time–frequency domain relationship is Eqn (A.9c),

$$\frac{\mathrm{d}f}{\mathrm{d}t} \Leftrightarrow -\mathrm{i}\omega \tilde{f}(\omega) ,$$

because we may use it to write

$$\begin{aligned} -(\mathrm{i}\omega \mathbb{1} + A)\, \tilde{\boldsymbol{q}}(\omega) &= \tilde{\boldsymbol{f}}(\omega) \\ \tilde{\boldsymbol{q}}(\omega) &= -(\mathrm{i}\omega \mathbb{1} + A)^{-1} \tilde{\boldsymbol{f}}(\omega) , \end{aligned} \tag{3.17}$$

for all frequencies such that $\mathrm{i}\omega\mathbb{1} + A$ is non-singular. Non-invertibility is generally only an issue when the system has no loss or is strongly amplified *i.e.* has no steady-state.

As can be seen from Eqn (3.17), in the frequency domain we lose track of the initial condition $\boldsymbol{q}(0)$, and thus this description is poor for understanding transient behaviours. However, it does have several important uses, such as calculating variances in the steady-state without having to take explicit long-time limits.

The connection between Eqn (3.17) and measurable quantities, such as variances, is the power spectrum. The power spectrum $S_{ff}[\omega]$ of a fluctuation operator $f(t)$ with stationary statistics may be calculated *via* the Wiener-Khinchin theorem [5], giving

$$S_{ff}[\omega] = \frac{1}{2\pi} \int_{-\infty}^{\infty} \mathrm{d}\omega' \ \left\langle \tilde{f}^{\dagger}(-\omega) \tilde{f}\left(\omega'\right) \right\rangle .$$

If f is a Hermitian operator then $f(t) \in \mathbb{R} \, \forall \, t \ \Leftrightarrow \ \tilde{f}(\omega) = \tilde{f}^{\dagger}(-\omega)$ (*cf.*App. A.6), so[5]

$$S_{ff}[\omega] = \frac{1}{2\pi} \int_{-\infty}^{\infty} \mathrm{d}\omega' \ \left\langle \tilde{f}(\omega) \tilde{f}\left(\omega'\right) \right\rangle . \tag{3.18}$$

This is the form that we will employ throughout this thesis, except as noted. Note that the power spectra of most quantum operators are not symmetric in frequency like their classical counterparts [70].

[5] In general, the Fourier transform of the Hermitian conjugate of an operator is *not* equal to the Hermitian conjugate of the Fourier transform of that operator. We will use $\tilde{f}^{\dagger}$ to refer to the conjugate of the transform.

The steady-state variance of f (because $\langle f \rangle = 0$) is then determined by

$$\langle f^2 \rangle = \frac{1}{2\pi} \int_{-\infty}^{\infty} \mathrm{d}\omega \, S_{ff}[\omega]. \tag{3.19}$$

We note that the Fourier transform can also be used to solve nonlinear equations of motion, but this situation is more complicated and only succeeds under specific conditions. This is because the Fourier transform of a product of functions is related to the convolution of their individual transforms. The time domain solutions are also extremely difficult—if not impossible—to analytically determine in this situation.

Approximation: adiabatic elimination

In quantum optomechanics we may encounter coupling between systems with vastly different characteristic timescales. This is especially true in the unresolved sideband regime, where the cavity decay rate κ is much larger than the mechanical resonance frequency ω_{M}. Under these circumstances it is often expeditious to find an approximate solution to the equations of motion by exploiting the separation of timescales in a procedure known as adiabatic elimination. One 'fast' dynamical variable is 'eliminated' from the equations of motion, leaving the remaining 'slow' variables with new effective equations of motion [197].

To motivate this approximation, let us consider a single cavity mode a_1 that is pumped by an external field $a_{\mathrm{in},1}$. The linewidth of the cavity is κ_1, so excitations decay from the cavity over a timescale of κ_1^{-1}. Suppose we begin in the steady-state with respect to the drive, and then suddenly change the pump intensity. The cavity mode will evolve towards a new steady-state over a timescale of several κ_1^{-1}. This process can be repeated *ad nauseam*. Importantly, the cavity will retain no memory of its previous configurations so long as the time between each sudden change is much longer than the relaxation time κ_1^{-1}. One can then imagine taking the limit in which the abrupt changes tend towards zero but occur arbitrarily frequently, and κ_1 is made sufficiently large that the cavity still reaches steady-state between each change. In this limit the abrupt jumps can be replaced by a slowly-varying smooth function, and the cavity mode can be seen to be approximately in equilibrium with the drive on any timescale relevant to the slow function. This is the essential observation behind adiabatic elimination; the 'fast' degrees of freedom are always approximately in the steady-state with respect to the configuration of the 'slow' degrees of freedom.

To see how to implement the approximation in practice, let us consider the simple case of linearly-coupled optical cavity modes with different linewidths. We will assume that both are pumped on resonance, and move into a frame rotating at the cavity frequency. Thus the equations of motion are

$$\begin{aligned} \dot{a}_1 &= -\kappa_1 a_1 + \sqrt{\kappa_1}\, a_{\mathrm{in},1} + \mathrm{i}g a_2 \\ \dot{a}_2 &= -\kappa_2 a_2 + \sqrt{\kappa_2}\, a_{\mathrm{in},2} + \mathrm{i}g a_1, \end{aligned}$$

where g is the coupling rate. Suppose now that $\kappa_2 \gg \kappa_1$, so that mode two responds very rapidly to any change in mode one. This means that we may eliminate mode two. To do this we set $\dot{a}_2 = 0$ and

solve the resulting algebraic equation to obtain

$$a_2 \approx \frac{1}{\kappa_2}\left(\sqrt{\kappa_2}\, a_{\mathrm{in},2} + \mathrm{i}g a_1\right).$$

This can be back-substituted into our dynamical equation for a_1 to obtain

$$\begin{aligned}\dot{a}_1 &\approx -\kappa_1 a_1 + \sqrt{\kappa_1}\, a_{\mathrm{in},1} + \frac{\mathrm{i}g}{\kappa_2}\left(\sqrt{\kappa_2}\, a_{\mathrm{in},2} + \mathrm{i}g a_1\right) \\ &\approx -\left(\kappa_1 + \frac{g^2}{\kappa_2}\right) a_1 + \sqrt{\kappa_1}\, a_{\mathrm{in},1} + \frac{\mathrm{i}g}{\sqrt{\kappa_2}} a_{\mathrm{in},2}.\end{aligned}$$

Mode two has been 'eliminated' from this description of mode one's dynamics. In this simple model it can be seen that the effect of the coupling to mode two is to increase the effective linewidth[6] of a_1 from κ_1 to $\kappa_1 + g^2/\kappa_2$. Physically we can interpret this as meaning that quanta that couple from a_1 into a_2 are lost from a_2 much more rapidly than they can be returned to a_1 *via* the coupling. This is, in effect, a simplified model of optomechanical cooling.

More complicated outcomes are possible than this toy model, as will be seen in § 4.

3.4 Example: damped harmonic motion

Damped harmonic oscillators are extremely common in nature; key examples include optical and microwave field modes, low-amplitude acoustic oscillations, collective vibrational modes in crystals, and motional degrees of freedom of trapped ions or neutral atoms. With this in mind, let us explore the time domain (§ 3.3.1) and frequency domain (§ 3.3.1) treatments of the damped harmonic oscillator.

The equations of motion of a harmonic oscillator of (angular) frequency ω_{M} subject to momentum-dependent damping at rate Γ are

$$\dot{X} = +\omega_{\mathrm{M}} P, \tag{3.20a}$$

$$\dot{P} = -\omega_{\mathrm{M}} X - \Gamma P + \sqrt{2\Gamma}\, \xi(t), \tag{3.20b}$$

Note that the loss appears only in Eqn. (3.20b), as does the noise operator $\xi(t)$. These equations are typically employed to describe classical systems, but may be readily—if not straightforwardly—quantised (*e.g.* [198]). Note that in general $\xi(t)$ does not commute with the system operators (*cf.* App. A.2).

We can easily identify that in this situation

$$\begin{aligned}\boldsymbol{q} &= (X\ P)^{\mathrm{T}} \\ \boldsymbol{f} &= \sqrt{2\Gamma}\ (0\ \xi(t))^{\mathrm{T}} \\ A &= \begin{pmatrix} 0 & \omega_{\mathrm{M}} \\ -\omega_{\mathrm{M}} & -\Gamma \end{pmatrix}.\end{aligned}$$

[6] As well as renormalising the amplitude and phase of the effective cavity drive field.

In order to find closed-form solutions we will also require some knowledge of the correlation function of the noise operator $\xi(t)$. In the high-temperature, high-Q limit the noise operator becomes Markovian and Gaussian, *viz.*

$$\left\langle \xi(t)\,\xi\left(t'\right)+\xi\left(t'\right)\xi(t)\right\rangle = 2\left(2\bar{n}_{\mathrm{H}}+1\right)\delta\left(t-t'\right), \tag{3.21}$$

where $\bar{n}_{\mathrm{H}}$ is the occupancy of the bath, given by the Bose–Einstein distribution. We shall henceforth restrict our attention to this case, leaving discussion of the more general case to App. A.2.

3.4.1 Damped harmonic motion in the time domain

Following the procedure specified in § 3.3.1 yields

$$M = \mathrm{e}^{-\frac{\Gamma t}{2}}\begin{pmatrix} \cos(\sigma\omega_{\mathrm{M}}t)+\frac{\Gamma}{2\sigma\omega_{\mathrm{M}}}\sin(\sigma\omega_{\mathrm{M}}t) & \frac{1}{\sigma}\sin(\sigma\omega_{\mathrm{M}}t) \\ -\frac{1}{\sigma}\sin(\sigma\omega_{\mathrm{M}}t) & \cos(\sigma\omega_{\mathrm{M}}t)-\frac{\Gamma}{2\sigma\omega_{\mathrm{M}}}\sin(\sigma\omega_{\mathrm{M}}t), \end{pmatrix}$$

in which the damping-modified oscillation frequency is $\sigma\omega_{\mathrm{M}}$ with $\sigma = \left(1-\Gamma^2/4\omega_{\mathrm{M}}^2\right)^{1/2}$, and

$$\boldsymbol{F}(t) = \sqrt{2\Gamma}\int_0^t \mathrm{d}t'\, M\left(t-t'\right)\begin{pmatrix} 0 \\ \xi(t') \end{pmatrix} = \mathrm{e}^{-\Gamma t/2}\begin{pmatrix} \Delta X \\ \Delta P \end{pmatrix}. \tag{3.22}$$

Note that we have assumed that the oscillator is underdamped ($\Gamma < \omega_{\mathrm{M}}/2$) *i.e.* on average an excitation will persist for many mechanical cycles before decaying away. This is the only relevant parameter regime in this thesis.

The properties of the noise operator are listed in App. A.2.

In § 5 and § 6 it will prove useful to have an explicit expression for V_{FF} under this evolution. Using Eqn (3.21),

$$\begin{aligned} V_{\mathrm{FF}} &= \int_0^t \mathrm{d}t' \int_0^t \mathrm{d}t''\, 2\Gamma\left(2\bar{n}_{\mathrm{H}}+1\right)\delta\left(t-t'\right) M\left(t-t'\right)\begin{pmatrix} 0 & 0 \\ 0 & 1 \end{pmatrix} M^{\mathrm{T}}\left(t-t''\right) \\ &= \begin{pmatrix} V_{\mathrm{FF}}^{1,1} & V_{\mathrm{FF}}^{1,1} \\ V_{\mathrm{FF}}^{1,2} & V_{\mathrm{FF}}^{2,2} \end{pmatrix} \end{aligned} \tag{3.23}$$

with

$$V_{\mathrm{FF}}^{1,1} = \left(2\bar{n}_{\mathrm{H}}+1\right)\left[1+\frac{\mathrm{e}^{-\Gamma t}}{\sigma^2}\left(\frac{\Gamma^2\cos(2\sigma\omega_{\mathrm{M}}t)-2\Gamma\sigma\omega_{\mathrm{M}}\sin(2\sigma\omega_{\mathrm{M}}t)}{4\omega_{\mathrm{M}}^2}-1\right)\right] \tag{3.24a}$$

$$V_{\mathrm{FF}}^{2,2} = \left(2\bar{n}_{\mathrm{H}}+1\right)\left[1+\frac{\mathrm{e}^{-\Gamma t}}{\sigma^2}\left(\frac{\Gamma^2\cos(2\sigma\omega_{\mathrm{M}}t)+2\Gamma\sigma\omega_{\mathrm{M}}\sin(2\sigma\omega_{\mathrm{M}}t)}{4\omega_{\mathrm{M}}^2}-1\right)\right] \tag{3.24b}$$

$$V_{\mathrm{FF}}^{1,2} = \left(2\bar{n}_{\mathrm{H}}+1\right)\left[\frac{\Gamma\mathrm{e}^{-\Gamma t}}{\sigma^2\omega_{\mathrm{M}}}\sin^2(\sigma\omega_{\mathrm{M}}t)\right]. \tag{3.24c}$$

The long-time evolution (Eqn (3.14)) yields the steady-state covariance matrix

$$V_{\mathrm{SS}} = \lim_{t\to\infty} V(t) = \left(2\bar{n}_{\mathrm{H}}+1\right)\mathbb{1}, \tag{3.25}$$

which is easily recognisable as a thermal state with occupancy equal to that of the bath.

3.4.2 Damped harmonic motion in the frequency domain

If we instead go to the frequency domain we clearly wish to calculate $-(\mathrm{i}\omega + A)^{-1}$, which for the momentum-damped oscillator gives

$$\tilde{q}(\omega) = \frac{\sqrt{2\Gamma}}{\omega_{\mathrm{M}}^2 - \omega^2 - \mathrm{i}\omega\Gamma} \begin{pmatrix} \Gamma - \mathrm{i}\omega & \omega_{\mathrm{M}} \\ -\omega_{\mathrm{M}} & -\mathrm{i}\omega \end{pmatrix} \begin{pmatrix} 0 \\ \tilde{\xi}(\omega) \end{pmatrix}.$$

Thus the steady-state properties of $\tilde{q}$ are dependent upon filtered versions of the noise operators. The bare properties of the frequency domain noise operator $\tilde{\xi}(\omega)$ are described by the correlator

$$\left\langle \tilde{\xi}(\omega)\tilde{\xi}(\omega') + \tilde{\xi}(\omega')\tilde{\xi}(\omega) \right\rangle = 4\pi(2\bar{n}_{\mathrm{H}} + 1)\delta(\omega + \omega').$$

Thus we have the power spectra[7]

$$S_{XX}[\omega] = 2\Gamma\omega_{\mathrm{M}}^2 M^2 (2\bar{n}_{\mathrm{H}} + 1)|\chi_{\mathrm{M}}|^2 \tag{3.26a}$$

$$S_{PP}[\omega] = 2\Gamma\omega^2 M^2 (2\bar{n}_{\mathrm{H}} + 1)|\chi_{\mathrm{M}}|^2, \tag{3.26b}$$

in which we have introduced the mechanical susceptibility

$$\chi_{\mathrm{M}} = \left[M\left(\omega_{\mathrm{M}}^2 - \omega^2 - \mathrm{i}\omega\Gamma\right)\right]^{-1},$$

where M is the effective mass of the mode. Note that although they appear very similar $S_{XX}[\omega] \neq S_{PP}[\omega]$ except at $\omega = \omega_{\mathrm{M}}$.

The power spectrum of the position operator is experimentally measurable and contains a significant quantity of information about the oscillator. If the noise is approximately white—that is, has a flat spectrum across all relevant frequencies—the power spectrum is proportional to $|\chi_{\mathrm{M}}|^2$. Typically, the susceptibility is Lorentzian; strongly-peaked at $\omega = \omega_{\mathrm{M}}$ with a linewidth of Γ. These characteristics are displayed in Fig. 3.2. Finally, the area under the power spectrum is proportional to the temperature. To see this we make use of the relationships

$$\frac{\pi}{\Gamma\omega_{\mathrm{M}}^2} = \int_{-\infty}^{\infty} \mathrm{d}\omega \, \frac{1}{\left(\omega^2 - \omega_{\mathrm{M}}^2\right)^2 + \Gamma^2\omega^2} \tag{3.27a}$$

$$\frac{\pi}{\Gamma} = \int_{-\infty}^{\infty} \mathrm{d}\omega \, \frac{\omega^2}{\left(\omega^2 - \omega_{\mathrm{M}}^2\right)^2 + \Gamma^2\omega^2} \tag{3.27b}$$

to calculate that $\langle X^2 \rangle = \langle P^2 \rangle = (2\bar{n}_{\mathrm{H}} + 1)$, exactly as expected.

3.5 Experimental tools

Although the majority of the work presented in this thesis is theoretical, we will also detail the experimental characterisation of SiC string properties in § 7. This requires knowledge of heterodyne detection,

[7] Strictly speaking, we have been somewhat cheeky in this calculation, in that we have substituted $\left\langle \tilde{\xi}(\omega)\tilde{\xi}(\omega') \right\rangle = \left\langle \tilde{\xi}(\omega)\tilde{\xi}(\omega') + \tilde{\xi}(\omega')\tilde{\xi}(\omega) \right\rangle/2$, which is not entirely true. However, the correction term is an odd function of frequency that integrates to zero, so we have ignored it from the beginning.

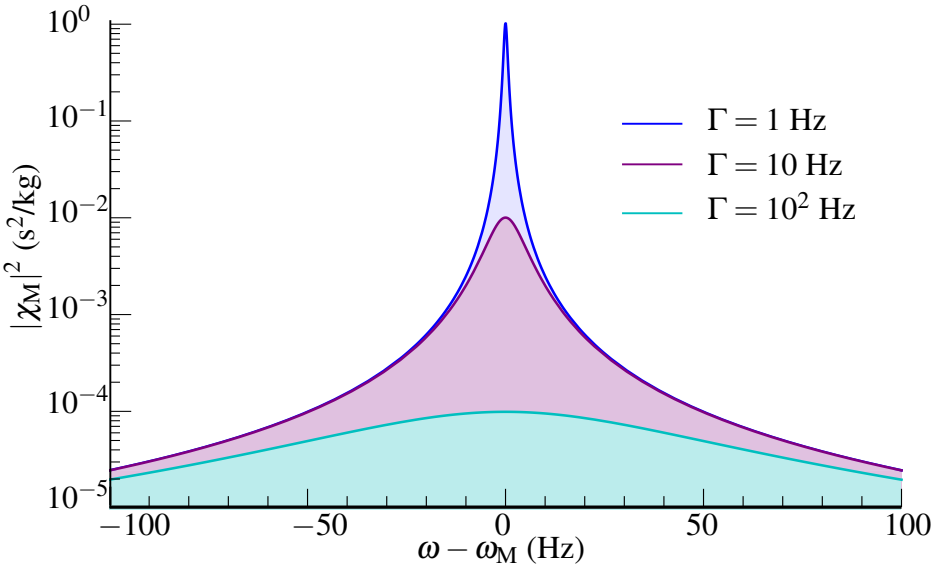

Figure 3.2: Some Lorentzian lineshapes of high-Q mechanical oscillators with $\omega_M = 10^6$ Hz and $M = 1$ ng. To an excellent approximation, the position of the central peak is ω_M and its full width at half-maximum is Γ. If the Q is low then the central peak is located at $\omega_M\sqrt{1-\Gamma^2/2\omega_M^2}$ and the FWHM is $\sigma\Gamma$.

which we will introduce alongside the closely-related homodyne detection scheme. Homodyne and heterodyne measurements of optical fields are widely used in the quantum optics and optomechanics community— they have been described as 'extremely useful and somewhat magic' [199]—which warrants a detailed discussion of their operation.

Both homo- and hetero-dyne are derived from traditional radio frequency (RF) detection technologies and rely on interfering a signal field with a powerful coherent field. The powerful field is called the Local Oscillator (LO), just as in the RF technology. Nonlinear mixing of the signal and LO allows information to be transferred between different spectral domains as required, based on the Fourier duality (*cf.* Eqn (A.9e))

$$f(t)\,e^{i\Omega t} \Leftrightarrow \tilde{f}(\omega+\Omega)\,.$$

This mixing property can be used to shift signals away from undesirable noise sources. In the context of quantum optics the LO and signal field are combined on a beamsplitter—a linear mixing process—and the nonlinearity is introduced when both output modes are detected with photodiodes, which are sensitive to the photon flux (squares of the quadratures). The difference between the photocurrents arising from each diode encodes information about the statistics of the signal field. Importantly, this information is at a frequency that can be processed with conventional RF electronics. A schematic is shown in Fig. 3.3.

Mathematically, let us represent the signal field by its annihilation operator $a = \alpha + \delta a$, and the LO as $b_{LO} = (\beta_{LO} + \delta b_{LO})\,e^{-i\Delta\omega t + i\varphi}$, where $\Delta\omega$ is the frequency offset of the LO from the signal, and φ is their initial phase difference. With this convention in place we may assume $\{\alpha, \beta_{LO}\} \in \mathbb{R}$

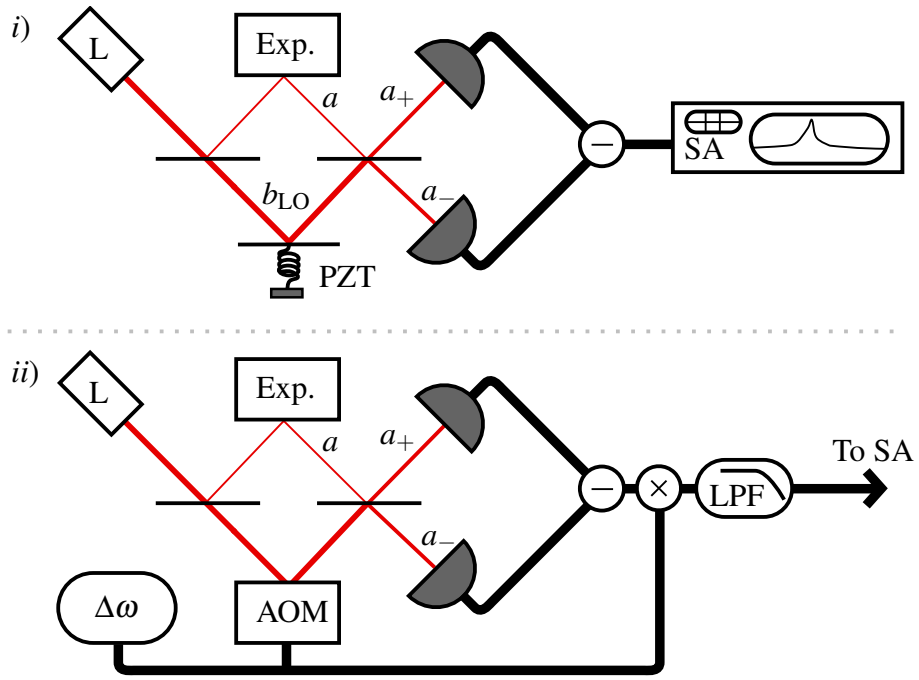

Figure 3.3: Schematics of homodyne and heterodyne detection. A bright coherent field is generated by a laser (L) and split on an asymmetric beamsplitter. The weaker beam a becomes the signal field that interacts with the experimental apparatus (Exp.); the bright field becomes the local oscillator $b_{\rm LO}$. The probe and $b_{\rm LO}$ are combined on a 50:50 beamsplitter and the output modes $a_\pm$ are detected with photodiodes (grey semicircles). Fluctuations of the signal field are encoded on the difference of the photocurrents.
i) For practical homodyne measurements ($\Delta\omega = 0$) the relative path lengths often require stabilisation (*e.g.* by a PZT-controlled mirror).
ii) The frequency shift of the local oscillator in heterodyne can be generated by an acousto-optic modulator (AOM). The photocurrent ($\Delta\omega \neq 0$) is typically 'mixed down' by multiplying with a sinusoid at frequency $\Delta\omega$ and then low-pass filtering (LPF) prior to the spectrum analyser (SA).

with no loss of generality. Letting the beamsplitter be 50:50, the output modes are

$$\begin{aligned} a_\pm &= \frac{1}{\sqrt{2}}\left(b_{\rm LO} \pm a\right) \\ &= \frac{1}{\sqrt{2}}\left(\beta_{\rm LO}\mathrm{e}^{-\mathrm{i}\Delta\omega t+\mathrm{i}\varphi} \pm \alpha\right) \pm \frac{1}{\sqrt{2}}\left(\delta b_{\rm LO}\mathrm{e}^{-\mathrm{i}\Delta\omega t+\mathrm{i}\varphi} \pm \delta a\right). \end{aligned}$$

Upon detection, these fields generate photocurrents $\hat{i}_\pm$ that are proportional to the number of incident photons. In the regime where the linearisation approximation is valid, the difference of these is

$$\begin{aligned} \Delta\hat{i} \;\propto\; & \beta_{\rm LO}\alpha\left(\mathrm{e}^{+\mathrm{i}\Delta\omega t-\mathrm{i}\varphi} + e^{-\mathrm{i}\Delta\omega t+\mathrm{i}\varphi}\right) \\ & + \beta_{\rm LO}\left(\delta a\mathrm{e}^{+\mathrm{i}\Delta\omega t-\mathrm{i}\varphi} + \delta a^\dagger\mathrm{e}^{-\mathrm{i}\Delta\omega t+\mathrm{i}\varphi}\right) \\ & + \alpha\left(\delta b_{\rm LO}\mathrm{e}^{-\mathrm{i}\Delta\omega t+\mathrm{i}\varphi} + \delta b_{\rm LO}^\dagger\mathrm{e}^{+\mathrm{i}\Delta\omega t-\mathrm{i}\varphi}\right). \end{aligned}$$

It is important to note that the signal field's fluctuations are amplified by $\beta_{\rm LO}$, whilst the LO noise is amplified by α. This has two important consequences;

- the desired signal, dependent upon δa, is optically amplified in a phase-sensitive manner; and

- the effect of noise entering from the LO field may be suppressed by choosing $\beta_{\mathrm{LO}} \gg \alpha$.

For these reasons, in typical experiments one aims for $\beta_{\mathrm{LO}}/\alpha \sim 100$ or greater. The final term of $\Delta\hat{i}$ may then safely be dropped, yielding

$$\Delta\hat{i} \propto 2\beta_{\mathrm{LO}}\alpha\cos(\varphi - \Delta\omega t) + \beta_{\mathrm{LO}}\delta X_a(\varphi - \Delta\omega t). \tag{3.28}$$

We have introduced the fluctuation quadrature at angle φ, $\delta X_a(\varphi) = \mathrm{e}^{-\mathrm{i}\varphi}\delta a + \mathrm{e}^{+\mathrm{i}\varphi}\delta a^\dagger$.

3.5.1 Homodyne

'Homodyne' is the name given to the case when the fields have equal carrier frequencies ($\Delta\omega = 0$). In this case the power spectrum of $\Delta\hat{i}$ is (except for a DC term) proportional to the power spectrum of $\delta X_a(\varphi)$. Thus the choice of the LO angle φ sets the quadrature that is being measured, and the measurement is completely insensitive to the orthogonal quadrature.

$$S^{\mathrm{homo}}_{\Delta\hat{i}\Delta\hat{i}}[\omega] \propto S_{\delta X_a(\varphi)\delta X_a(\varphi)}[\omega]. \tag{3.29}$$

In an experiment it is necessary to stabilise the relative phase, otherwise the measurement randomly drifts across phase space and measures different quadratures at different times. This is typically done by deriving the local oscillator and the signal field from the same laser, so that the majority of classical noise—especially laser phase noise—is common-mode. This converts the homodyne apparatus into a form of Mach-Zehnder interferometer, as depicted in Fig. 3.3. It is no surprise then that homodyne also requires active stabilisation of the difference between the path lengths of the LO and signal mode. For these technical reasons it is sometimes more practical to employ heterodyne measurements and forego the quadrature selectivity of homodyne measurements.

3.5.2 Heterodyne

A heterodyne measurement is one with $\Delta\omega \neq 0$. If we rewrite Eqn (3.28) in terms of the quadratures $X_a(\varphi)$ and $P_a(\varphi) = X_a(\varphi + \pi/2)$ we obtain

$$\Delta\hat{i} = 2\beta_{\mathrm{LO}}\alpha\cos(\varphi - \Delta\omega t) + \beta_{\mathrm{LO}}\left[\delta X_a(\varphi)\cos\Delta\omega t - \delta P_a(\varphi)\sin\Delta\omega t\right] \tag{3.30}$$

To extract the quadrature variances from this signal we may mix-down at a frequency of $\Delta\omega$. In an experimental setting this is achieved by mixing the photocurrent with a sinusoidal function, and then filtering out the high-frequency ($\sim 2\Delta\omega$) components. Mathematically, we have

$$\begin{aligned} \Delta i_{\cos} &\sim \alpha\beta_{\mathrm{LO}}\cos\varphi + \frac{1}{2}\beta_{\mathrm{LO}}\delta X_a(\varphi) \\ \Delta i_{\sin} &\sim \alpha\beta_{\mathrm{LO}}\sin\varphi - \frac{1}{2}\beta_{\mathrm{LO}}\delta P_a(\varphi). \end{aligned}$$

Although at first glance this would seem to permit simultaneous determination of both the phase and amplitude quadratures of a light field, this is not the case because the mixing process is done with a

classical photocurrent. It can be shown (*e.g.* Appendix A.3 of [70]) that, prior to amplification, the quantised photocurrent contains sufficient noise to ensure that the Heisenberg uncertainty relation is satisfied. Physically, this can be considered to be a consequence of the vacuum noise at $\pm\Delta\omega$ beating with the LO and the coherent amplitude of the probe.

If one does not care about distinguishing between phase and amplitude quadrature fluctuations, one can consider the spectrum without mixing. This is the route we will employ in § 7. This has the advantage of requiring no control over the relative path length travelled by the LO and signal.

3.5.3 Example: detecting amplitude and phase modulations

We will investigate the specific case of detecting coherent fields with phase or amplitude modulations. These might be deliberately generated by an experimentalist to calibrate a detection system [199] or perform a locking operation [200], or they might be generated by the optomechanical interaction, *etc.*

Let us first calculate the form of the fields involved. For simplicity, throughout this section we will only consider classical fields; this is, of course, an approximation.

An amplitude-modulated (AM) field can be written

$$\alpha_{\mathrm{AM}} = \alpha_0 \left(1 + \Delta A \cos \Omega t\right)$$

where α_0 is the coherent part of the original field, Ω is the modulation frequency, and ΔA is the modulation depth, which we take to be $\Delta A \ll 1$. We will take α_0 to be real without loss of generality. Then we way write

$$\alpha_{\mathrm{AM}} = \alpha_0 \left[1 + \frac{\Delta A}{2}\left(\mathrm{e}^{\mathrm{i}\Omega t} + \mathrm{e}^{-\mathrm{i}\Omega t}\right)\right]. \tag{3.31}$$

It is useful to consider the field as being the sum of three fields at different frequencies. One is at the carrier frequency ($\omega = 0$, because α_0 is here represented in a rotating frame), and the other two are the upper ($+\Omega$) and lower ($-\Omega$) sidebands. For a pure AM field the sidebands begin in phase with each other and the carrier[8].

A phase-modulated (PM) field has the form

$$\alpha_{\mathrm{PM}} = \alpha_0 \mathrm{e}^{\mathrm{i}\Delta\phi \cos \Omega t}$$

where $\Delta\phi$ is the modulation depth of the phase. It is not obvious that this can be represented in a similar way to the AM field; however, if we take $\Delta\phi$ to be small we can make a first-order Maclaurin expansion to find

$$\alpha_{\mathrm{PM}} \approx \alpha_0 \left[1 + \frac{\mathrm{i}\Delta\phi}{2}\left(\mathrm{e}^{\mathrm{i}\Omega t} + \mathrm{e}^{-\mathrm{i}\Omega t}\right)\right]. \tag{3.32}$$

This is extremely similar to Eqn (3.31), in that it may be interpreted as the sum of three fields at frequencies $-\Omega$, 0, and $+\Omega$, but note that the sidebands are now initially $\pi/2$ out of phase with the carrier. Let's write these in a unified form,

$$\alpha_{\mathrm{M}} = \alpha_0 \left(1 + m \cos \Omega t\right),$$

[8] This is strictly true only for cosine modulations.

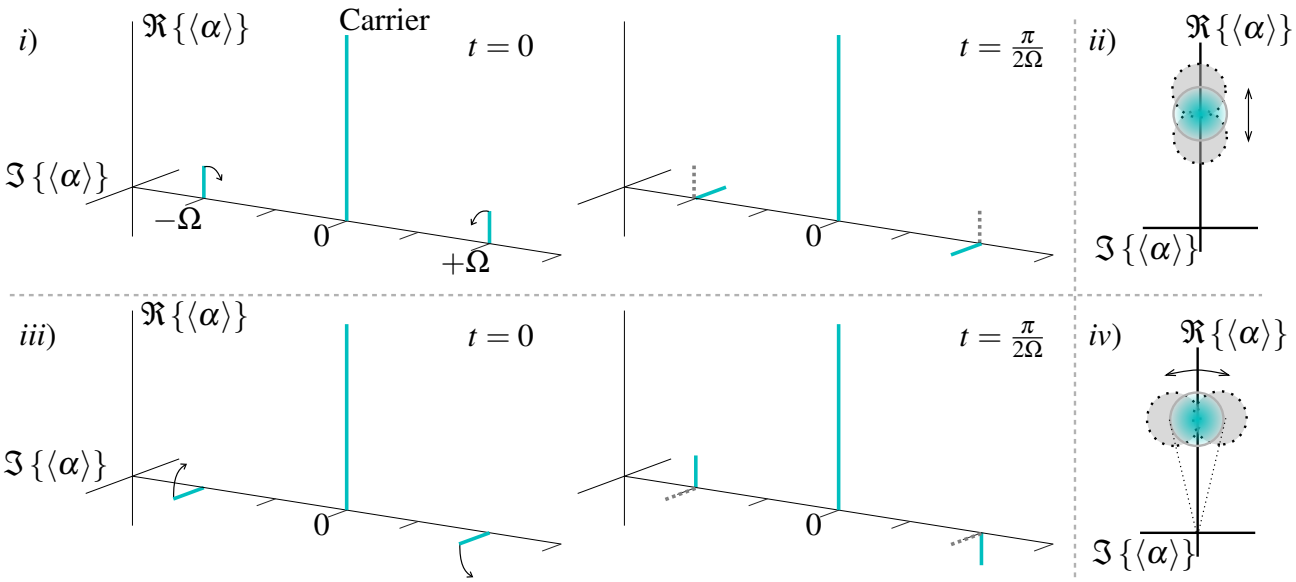

Figure 3.4: Amplitude- and phase-modulated fields represented as sidebands. Each section through the $\Re\{\alpha\},\Im\{\alpha\}$ plane corresponds to a phasor diagram for the component of the field at frequency ω (long axis).
i) An amplitude-modulated field. The sidebands and carrier begin in phase, such that the resultant is larger than the carrier. After a quarter cycle ($t = \pi/2\Omega$) the sidebands, that have rotated in opposite directions, cancel one another. This leads to the ball-and-stick diagram shown in panel *ii*).
ii) Interference of the sidebands in panel *i*) gives a ball-and-stick diagram where the ball of coherent noise is displaced up and down (along the amplitude axis) every Ω.
iii) A phase-modulated field. Just like the AM field, interference between the sidebands encodes the modulation. However, the sidebands now begin a quarter cycle out of phase with the carrier, so that they rotate the resultant away from the $\Re\{\langle\alpha\rangle\}$ axis. A quarter cycle later the sidebands cancel, leading to no change in the field's amplitude to first order in $\Delta\phi$.
iv) The PM field in the ball-and-stick representation. The coherent amplitude does not change length (to first order), but its complex phase is varied periodically.

where $m = \Delta A$ for the AM field and $m = \Delta\phi$ for the PM case. A graphical representation of these fields is given in Fig. 3.4.

Let us now calculate the power spectrum of the quadrature operators. Since we are dealing with classical fields that are not wide-sense stationary we cannot use the Wiener-Khinchin theorem (Eqn (3.18)) given earlier; in this case[9] we instead have $S_{ff}[\omega] = \left|\tilde{f}(\omega)\right|^2$. The φ quadrature of the modulated field is given by

$$X_{\mathrm{M},\varphi} = \alpha_0\left[2\cos\varphi + \left(m\mathrm{e}^{-\mathrm{i}\varphi} + m^*\mathrm{e}^{+\mathrm{i}\varphi}\right)\cos\Omega t\right]$$

and by using Eqn (A.9e) we obtain

$$\tilde{X}_{\mathrm{M},\varphi}(\omega) = 4\pi\alpha_0\cos\varphi\,\delta(\omega) + 2\pi\alpha_0\frac{m\mathrm{e}^{-\mathrm{i}\varphi} + m^*\mathrm{e}^{+\mathrm{i}\varphi}}{2}\left[\delta(\omega+\Omega) + \delta(\omega-\Omega)\right].$$

Calculating the power spectrum requires us to find multiples of Dirac δ distributions, which do not exist. We are saved by the fact that in any real experiment we necessarily measure for only a finite

[9] The use of power spectra in classical *versus* quantum systems does carry some subtleties, which are touched on in Chapters 1 and 3 of [70].

time τ, so the δ terms are broadened into well-behaved functions that can be multiplied. If we use $\check{\delta}_\tau$ to represent a broadened δ function (in this case it is in fact a sinc function) we obtain

$$\begin{aligned} S^{\text{homo}}_{\text{M},\varphi}[\omega] &= (4\pi\alpha_0)^2 \cos^2\varphi \check{\delta}^2_\tau(\omega) + \\ &\quad (2\pi\alpha_0)^2 |m|^2 \cos^2(\varphi-\varphi_m)\left[\check{\delta}^2_\tau(\omega+\Omega)+\check{\delta}^2_\tau(\omega-\Omega)\right] \end{aligned}$$

by using the fact that $\check{\delta}_\tau(\omega)\check{\delta}_\tau(\omega') \approx 0$ for $\omega \neq \omega'$. We have introduced the complex phase of m, φ_m.

In the AM case we obtain the maximum signal for a local oscillator phase $\varphi = 0$, and become completely insensitive to the modulation (to second order in m) when $\varphi = \pi/2$. The situation is reversed for the PM case ($\varphi_m = \pi/2$). This demonstrates that homodyne measurements are phase sensitive.

For a heterodyne measurement we find

$$\begin{aligned} \tilde{X}_{\text{M},\varphi}(\omega) &= 2\pi\alpha_0\left[e^{i\varphi}\delta(\omega-\Delta\omega)+e^{-i\varphi}\delta(\omega+\Delta\omega)\right] + \\ &\quad \pi\alpha_0\left[\begin{array}{c} m^* e^{i\varphi}\delta(\omega+\Omega-\Delta\omega)+m^* e^{i\varphi}\delta(\omega-\Omega-\Delta\omega)+ \\ m e^{-i\varphi}\delta(\omega+\Omega+\Delta\omega)+m e^{-i\varphi}\delta(\omega-\Omega+\Delta\omega) \end{array}\right] \end{aligned}$$

which yields the power spectrum

$$\begin{aligned} S^{\text{het}}_{\text{M},\varphi}[\omega] &= (2\pi\alpha_0)^2\left[\check{\delta}^2_\tau(\omega+\Delta\omega)+\check{\delta}^2_\tau(\omega-\Delta\omega)\right] + \\ &\quad (\pi\alpha_0)^2|m|^2\left[\begin{array}{c} \check{\delta}^2_\tau(\omega+\Omega-\Delta\omega)+\check{\delta}^2_\tau(\omega-\Omega-\Delta\omega)+ \\ \check{\delta}^2_\tau(\omega+\Omega+\Delta\omega)+\check{\delta}^2_\tau(\omega-\Omega+\Delta\omega) \end{array}\right]. \end{aligned}$$

Two key features are immediately evident. Firstly, the information carried by the modulated sidebands now appears as peaks around the large beats at $\omega \pm \Delta\omega$. Secondly, the heterodyne power spectrum is independent of the local oscillator angle, and so one cannot distinguish between AM and PM fields.

Part II

Progress: Theory

Chapter 4

Coherent control and feedback cooling in a remotely-coupled hybrid atom–optomechanical system

The work presented in this chapter has been published by IOP Publishing;
J. S. Bennett, L. S. Madsen, M. Baker, H. Rubinsztein-Dunlop, and W. P. Bowen, Coherent control and feedback cooling in a remotely coupled hybrid atom–optomechanical system, *New Journal of Physics* 16, 083036, 2014.

Cooling to the motional ground state is an important first step in the preparation of nonclassical states of mesoscopic mechanical oscillators. Light-mediated coupling to a remote atomic ensemble has been proposed as a method to reach the ground state for low frequency oscillators. The ground state can also be reached using optical measurement followed by feedback control. Here we investigate the possibility of enhanced cooling by combining these two approaches. The combination, in general, outperforms either individual technique, though atomic ensemble-based cooling and feedback cooling each individually dominate over large regions of parameter space.

Our results are consistent with those of Mahajan *et al.*, who studied a closely-related hybrid optomechanical system in which the atoms and mechanical oscillator are integrated into a single optical cavity [201]. These results were not brought to our attention until recently.

4.1 Introduction

Preparation of mesoscopic mechanical devices in high-purity nonclassical states is a long-standing goal of the opto- and electromechanical communities. In addition to promising applications in fundamental physics research—such as gravitational effects in quantum mechanics and the quantum-to-classical transition [26,202]—mechanical devices provide outstanding opportunities for metrology [31,203,204] and emerging quantum technologies [205–207].

The majority of mechanical quantum state preparation and verification schemes require that the oscillator be initialised very near to the motional ground state [82, 208]. Though this has been achieved in the gigahertz and megahertz regimes [15–17], progress toward cooling low-frequency (ω_{M}) oscillators has been inhibited by the lack of both cryogenic systems capable of freezing out their thermal motion and sufficiently high quality optical cavities to achieve the good cavity (cavity linewidth $\kappa \ll \omega_{\mathrm{M}}$) regime required for resolved sideband cooling.

Both remote coupling to the motional state of a cooled atomic ensemble [6, 150, 151] and optical measurement followed by feedback control [114, 118, 123, 209–211] have been suggested as alternative approaches to cooling that, in principle, overcome these limitations and allow ground state cooling in the bad cavity limit ($\kappa \gg \omega_{\mathrm{M}}$).

In remote atomic ensemble-based cooling, or *sympathetic cooling*, light mediates a swap between the centre of mass motional state of the ensemble and a mode of the mechanical oscillator, which may be separated from the former by a macroscopic distance (~ 1 m) [6, 150, 151]. Proposed remotely-coupled atom–optomechanical systems are theoretically capable of sympathetically cooling their mechanical elements to near the ground state. The directional flow of quantum information from the mechanical element—the 'plant', in control parlance—to the atoms and back allows us to identify the atoms as an irreversible coherent controller (*cf.* [212], pg. 3, and [124, 213]). The controller is necessarily imperfect, as the phase of the output optical field retains knowledge of the mechanical position. The resulting back-action on the momentum hinders the cooling process.

In this article we investigate combining sympathetic cooling with feedback damping based on a phase measurement of the output field (*cf.* Fig. 4.1). The latter retrieves information from the optical field and allows suppression of decoherence. We derive an analytical mechanical power spectrum for such a system, from which the steady-state temperature is found. This reveals a set of criteria specifying when near-ground-state temperatures may be achieved. In general the combined scheme outperforms both individual methods; however, when the optomechanical cooperativity is sufficiently large the cooling is dominated by feedback. Conversely, one may still approach the mechanical ground state with weak optomechanical cooperativity provided that its ensemble–light counterpart (*cf.* Eqn (4.20)) is appropriately large. These statements are made quantitative in § 4.3.2. We also clarify the role of atom–light and optomechanical interactions in performing the atom $\leftrightarrow$ mechanical state swap that underpins sympathetic cooling. In particular, and somewhat counter-intuitively, this swap is possible even when the optomechanical cooperativity is insufficient to permit a complete state transfer between the oscillator and the optical field.

4.2 Model

Consider the device depicted in Fig. 4.1, in which a ring resonator, containing an atomic cloud (*e.g.* as realised by [214]) and a one-sided optomechanical cavity are coupled by a lossless optical transmission line. An optical lattice, formed by interference of the counter-propagating cavity modes, traps the atoms in approximately harmonic wells (*cf.* § 4.2.1). The atomic centre of mass and the optically-coupled

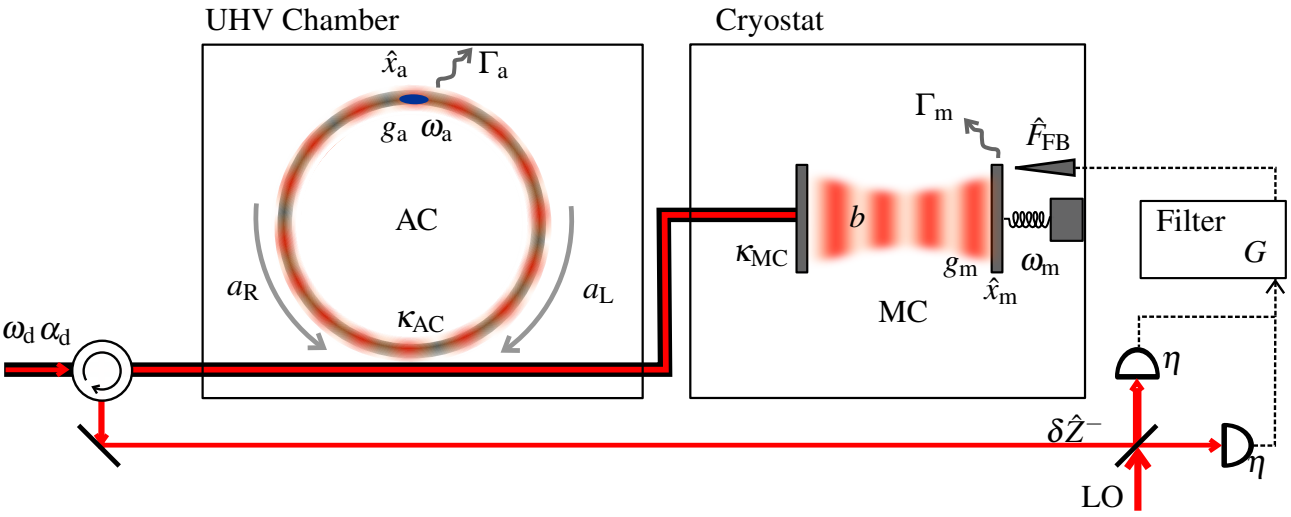

Figure 4.1: A generic remotely-coupled hybrid atom–optomechanical system incorporating continuous measurement and feedback. The counter-propagating optical modes of a ring cavity (AC) are coupled to the motion of an atomic ensemble; similarly, the modes a single-sided cavity (MC) interact with a micromechanical oscillator. The transfer of light between these two subsystems couples the collective motion of the atoms to that of the mechanical element. Light exiting the system may be mixed with a bright local oscillator (LO) in order to measure the (optical phase quadrature) mechanical position, allowing the application of a classical feedback force.

oscillator therefore comprise two harmonic mechanical degrees of freedom.

This class of hybrid atom–optomechanical system (*e.g.* [6, 150, 151] and [140]) is desirable from an immediate experimental perspective, where their key advantage is circumventing the need for close integration of cryogenic and ultra-high vacuum apparatus, and within the context of future quantum networks, where atomic and solid-state processing and memory nodes are anticipated to be interfaced *via* optical photons [179].

Displacement of the atoms relative to the lattice results in an exchange of photons between the left- and right-going optical modes, which modulates the optical power incident upon the mechanical device. Conversely, changing the position of the latter alters the phase of the reflected field (*cf.* § 4.2.2), causing axial translation of the optical lattice. In this way each oscillator is subject to a force that depends on the position of its counterpart [150].

Our model of the atom–mechanical coupling is closely related to that realised by [151, 152]. The primary difference, besides the inclusion of the external measurement-based feedback loop, is the addition of a second optical cavity into which the atoms are loaded. The cavity allows us to employ an intuitive two-mode description of the atom–light interaction and may be experimentally desirable in certain circumstances (*cf.* § 4.2.3).

4.2.1 Atom–light interaction

The heart of the atom trapping apparatus is an optical dipole trap [215] that uses the AC Stark effect to confine N identical two-level atoms of mass m. This trap is incorporated into a ring resonator of quality Q_{AC} which is driven by an input field a_D, with a large coherent amplitude $\alpha_D = \langle a_D \rangle$ at (angular)

frequency ω_{D}. Neglecting internal losses, the linewidth of this cavity is $\kappa_{\mathrm{AC}} \approx \omega_{\mathrm{D}}/Q_{\mathrm{AC}}$ (*i.e.* the resonator is strongly overcoupled to the transmission line). We take the majority of the cavity's modes to be far off resonance with the drive beam, leaving two relevant counter-propagating modes that are lowered by the operators a_{L} and a_{R}, with the subscripts referring to the handedness of circulation depicted in Fig. 4.1.

In practice additional field modes or semiclassical potentials may be required to stably confine the atoms in the plane transverse to the counter-propagating modes introduced above. We will neglect all noise introduced by these fields/potentials in the analysis that follows on the grounds that, to harmonic order, motion in the transverse directions is decoupled from the axial motion.

The Hamiltonian governing the internal (axial) dynamics of the cavity—in a frame rotating at the drive beam frequency ω_{D}—is then

$$\hat{H}_{\mathrm{AC}} = -\hbar\Delta_{\mathrm{AC}}\left(a_{\mathrm{R}}^{\dagger}a_{\mathrm{R}} + a_{\mathrm{L}}^{\dagger}a_{\mathrm{L}}\right) + \hat{H}_{\mathrm{SS}} + \sum_{j=1}^{N}\frac{\hat{p}_j^2}{2m},$$

where Δ_{AC} is the detuning of the drive from the bare cavity resonance, $\hat{p}_j$ is the momentum of the j^{th} atom and $\hat{H}_{\mathrm{SS}}$, the Stark shift operator, models the light–atom interactions.

Following [150] (*cf.* [216]), we will treat all atom–light interactions in the dispersive limit, suppressing any internal structure of the ground and first excited electronic states of the atom. This is a valid approximation for alkali gases provided that the detuning Δ_{t} between the drive and the electronic transition frequency is large compared to the laser linewidth and all other relevant frequency scales [215]. The one-dimensional Hamiltonian describing the atom–light interaction is therefore (neglecting off-resonant terms)

$$\hat{H}_{\mathrm{SS}} = \sum_{j=1}^{N}\frac{\mu^2}{\hbar\Delta_{\mathrm{t}}}\hat{E}^{(-)}\left(\hat{x}_j\right)\hat{E}^{(+)}\left(\hat{x}_j\right), \tag{4.1}$$

where $E^{(+)}$ is the positive frequency component of the electric field and each atom has a transition dipole moment of μ [151].

The positive-frequency part of the cavity electric field may be written

$$\hat{E}^{(+)} = \mathrm{i}\sqrt{\frac{\hbar\omega_{\mathrm{AC}}}{2\varepsilon_0\mathscr{V}}}\left(a_{\mathrm{R}}\mathrm{e}^{-\mathrm{i}kx} + a_{\mathrm{L}}\mathrm{e}^{\mathrm{i}kx}\right),$$

where ω_{AC} is the bare resonance frequency of the atom cavity, k is the optical wavenumber, ε_0 is the permittivity of free space and $\mathscr{V}$ is the cavity mode volume [50]. From this we find *via* Eqn (4.1) that the strength of the single-atom–light interaction is characterised by the coupling rate

$$g_{\mathrm{A}} = \frac{\mu^2\omega_{\mathrm{D}}}{2\hbar\Delta_{\mathrm{t}}\varepsilon_0\mathscr{V}}. \tag{4.2}$$

We have used $\omega_{\mathrm{AC}} \approx \omega_{\mathrm{D}}$. Note that for red detuned light ($\Delta_{\mathrm{t}} < 0$), as we will assume from here onward, g_{A} is negative.

Expanding the annihilation operators $a_{\mathrm{L,R}} \to \alpha_{\mathrm{L,R}} + \delta a_{\mathrm{L,R}}$ about the coherent field amplitudes $\langle a_{\mathrm{L,R}}\rangle = \alpha_{\mathrm{L,R}}$, which we assume are real and satisfy $\alpha_{\mathrm{R}} \approx \alpha_{\mathrm{L}} \gg 1$, and truncating the oscillatory

terms at second order in the Lamb-Dicke parameter [150], we acquire a static shift of the cavity resonance frequency, an effective harmonic trapping potential with frequency

$$\omega_{\mathrm{A}} = 2k\sqrt{\frac{-2\hbar g_{\mathrm{A}}\alpha_{\mathrm{L}}\alpha_{\mathrm{R}}}{m}}$$

and a linearised interaction between the atoms' positions and the optical phase quadrature fluctuations. Finally, setting the bare detuning to $\Delta_{\mathrm{AC}} = -2Ng_{\mathrm{A}}$ brings the cavity onto resonance in the presence of the mean interaction, yielding the Hamiltonian

$$\hat{H}_{\mathrm{AC}} = \sum_{j=1}^{N}\left[\frac{\hat{p}_j^2}{2m} + \frac{m\omega_{\mathrm{A}}^2\hat{x}_j^2}{2} + 2\hbar k g_{\mathrm{A}}\hat{x}_j\left(\alpha_{\mathrm{L}}\delta\hat{P}_{\mathrm{R}} - \alpha_{\mathrm{R}}\delta\hat{P}_{\mathrm{L}}\right)\right] \tag{4.3}$$

where we have introduced the amplitude and phase quadrature fluctuation operators, $\delta\hat{X} = \delta a^\dagger + \delta a$ and $\delta\hat{P} = \mathrm{i}\left(\delta a^\dagger - \delta a\right)$ and neglected contributions of order $\hat{x}_j^2\delta\hat{X}\left(\delta\hat{P}\right)$.

Inspection of Eqn (4.3) reveals that the phase difference of the optical fields couples to the *collective* motion of the atomic cloud, specifically the centre of mass mode. This degree of freedom may be described by a simple harmonic oscillator with coordinate $\hat{x}_{\mathrm{A}} = \frac{1}{N}\sum_{j=1}^{N}\hat{x}_j$, momentum $\hat{p}_{\mathrm{A}} = \sum_{j=1}^{N}\hat{p}_j$ and zero-point extension $x_{\mathrm{ZP,A}} = \sqrt{\hbar/2Nm\omega_{\mathrm{A}}}$ (*cf.* § 4.2.3).

4.2.2 Optomechanical interaction

The canonical cavity optomechanical interaction is most easily understood in the context of a single-sided Fabry-Pérot cavity wherein the input mirror is fixed and the other is harmonically bound (*e.g.* as depicted in Fig. 4.1). Motion of the end mirror changes the cavity length, thereby altering the optical resonance frequency, which in turn modulates the number of photons in the cavity field. Finally, the photon number controls the radiation force experienced by the mirror. This interplay leads to the emergence of a rich variety of well-studied physics [217, 218] even at first-order in $\hat{x}_{\mathrm{M}}$.

A linearly-coupled optomechanical system, whether actuated by radiation pressure or the gradient force [59], may be described by the parametric coupling Hamiltonian [56]

$$\hat{H}_{\mathrm{MC}} = \hbar\left(g_{\mathrm{M}}\hat{x}'_{\mathrm{M}} - \Delta_{\mathrm{MC}}\right)b^\dagger b + \frac{\hat{p}_{\mathrm{M}}^2}{2M} + \frac{1}{2}M\omega_{\mathrm{M}}^2\hat{x}'^2_{\mathrm{M}}$$

in a frame rotating at ω_{D}. The bare detuning of the laser drive to the cavity resonance is Δ_{MC}, $\hat{x}'_{\mathrm{M}}$ is a suitable position coordinate of a vibrational mode with effective mass M and frequency ω_{M}, photons are removed from the cavity field by b and g_{M} is the optomechanical coupling rate (with dimensions of $\mathrm{s}^{-1}\mathrm{m}^{-1}$).

As above, we assume that the internal optical mode is coupled to the drive beam at a rate $\kappa_{\mathrm{MC}} \approx \omega_{\mathrm{D}}/Q_{\mathrm{MC}}$, where Q_{MC} is the Q-factor of the optical resonator, leading to the build-up of a steady-state intracavity amplitude $\beta = 2\alpha_{\mathrm{D}}/\sqrt{\kappa_{\mathrm{MC}}}$. Linearising about this amplitude, introducing a zero-mean position coordinate $\hat{x}_{\mathrm{M}}$ and selecting Δ_{MC} so as to bring the cavity onto resonance in the presence of

the mean interaction[1] yields the effective Hamiltonian

$$\hat{H}_{\mathrm{MC}} = \hbar g_{\mathrm{M}} \hat{x}_{\mathrm{M}} \beta \, \delta\hat{X}_{\mathrm{C}} + \frac{\hat{p}_{\mathrm{M}}^2}{2M} + \frac{1}{2} M \omega_{\mathrm{M}}^2 \hat{x}_{\mathrm{M}}^2, \tag{4.4}$$

with the optical quadrature fluctuation operators within the optomechanical cavity being $\delta\hat{X}_{\mathrm{C}}$ and $\delta\hat{P}_{\mathrm{C}}$.

The ground state position variance of the mechanical resonator is $x_{\mathrm{ZP,M}}^2 = \hbar/2M\omega_{\mathrm{M}}$.

4.2.3 Effective dynamics

Given Eqn (4.3) and Eqn (4.4) we may determine the dynamics of the system in the Heisenberg picture. Under free evolution, neglecting coupling to reservoirs for the moment,

$$Nm\frac{\mathrm{d}^2\hat{x}_{\mathrm{A}}}{\mathrm{d}t^2} = -Nm\omega_{\mathrm{A}}^2\hat{x}_{\mathrm{A}} + 2\hbar N k g_{\mathrm{A}} \left(\alpha_{\mathrm{R}}\delta\hat{P}_{\mathrm{L}} - \alpha_{\mathrm{L}}\delta\hat{P}_{\mathrm{R}}\right), \tag{4.5a}$$

$$M\frac{\mathrm{d}^2\hat{x}_{\mathrm{M}}}{\mathrm{d}t^2} = -M\omega_{\mathrm{M}}^2\hat{x}_{\mathrm{M}} - \hbar g_{\mathrm{M}}\beta\,\delta\hat{X}_{\mathrm{C}}. \tag{4.5b}$$

These equations show, as expected, that the atom–light interaction depends on the optical phase fluctuations, whereas the optomechanical system responds to amplitude noise (*cf.* [6, 151]).

Adiabatic elimination of optical fields

Dramatic simplifications may be made in the optical adiabatic limit, wherein the optical quadrature fluctuations are slaved to the positions of the mechanical and atomic elements. Conveniently, this is also the regime in which the most sensitive measurements of mechanical displacement are achieved [114]. In this limit both optical cavities are strongly overcoupled ($\kappa_{\mathrm{AC}} \gg \left\{\Gamma_{\mathrm{AC}}, -2Nkg_{\mathrm{A}}x_{\mathrm{ZP,A}}, \omega_{\mathrm{A}}\right\}$ and $\kappa_{\mathrm{MC}} \gg \left\{\Gamma_{\mathrm{MC}}, g_{\mathrm{M}}x_{\mathrm{ZP,M}}, \omega_{\mathrm{M}}\right\}$) such that perturbations of the steady-state field amplitudes away from their interaction-free values are negligibly small. Thus we have $\alpha_{\mathrm{L}} = \alpha_{\mathrm{R}} = 2\alpha_{\mathrm{D}}/\sqrt{\kappa_{\mathrm{AC}}}$ and $\beta = 2\alpha_{\mathrm{D}}/\sqrt{\kappa_{\mathrm{MC}}}$.

The Langevin equation describing an optical fluctuation operator δa is [50]

$$\frac{\mathrm{d}\delta a}{\mathrm{d}t} = \frac{1}{\mathrm{i}\hbar}\left[\delta a, \hat{H}\right] + \sqrt{\kappa}\,\delta a_{\mathrm{in}} - \frac{1}{2}\kappa\delta a, \tag{4.6}$$

in which the coupling rate[2] between the resonator and drive mode δa_{in} is κ, and $\hat{H}$ is either Eqn (4.3) or Eqn (4.4) as appropriate. δa_{in} represents the fluctuations of the multi-mode input field.

The fluctuations of the drive mode are given by Eqn (2.7),

[1] For a linear oscillator we may arrive at Eqn (4.4) by introducing $\hat{x}_{\mathrm{M}} = \hat{x}'_{\mathrm{M}} - \langle\hat{x}'_{\mathrm{M}}\rangle$, with $\langle\hat{x}'_{\mathrm{M}}\rangle = \frac{\hbar g_{\mathrm{M}}}{M\omega_{\mathrm{M}}^2}\beta^2$, and detuning from the bare cavity resonance by $\Delta_{\mathrm{MC}} = g_{\mathrm{M}}\langle\hat{x}'_{\mathrm{M}}\rangle$. Alternatively, an external control force may be used to cancel the mean optical force, leaving $\Delta_{\mathrm{MC}} = 0$.

[2] It may be shown that including extraneous losses (*e.g.* scattering into unguided modes and absorption loss) at a rate Γ leads to an amount of additional noise that scales as Γ/κ; we therefore neglect these contributions in the regime $\kappa \gg \Gamma$.

Transfer of information between the two optical cavities is treated using the input-output formalism (Eqn (2.5b)). For the geometry presented in Fig. 4.1 the appropriate input-output relations are

$$\begin{aligned}\delta a_{\mathrm{in,R}} &= \delta a_{\mathrm{D}},\\ \delta b_{\mathrm{in}} &= \sqrt{\kappa_{\mathrm{AC}}}\,\delta a_{\mathrm{R}} - \delta a_{\mathrm{D}},\\ \delta a_{\mathrm{in,L}} &= \sqrt{\kappa_{\mathrm{MC}}}\,\delta b - \delta b_{\mathrm{in}}.\end{aligned}$$

These expressions are valid in the case that the time taken for light to propagate between the two cavities is small compared to the mechanical period(s).

Application of Eqn (4.6) in the adiabatic limit yields

$$\begin{aligned}\delta\hat{X}_{\mathrm{R}} &= \frac{2}{\sqrt{\kappa_{\mathrm{AC}}}}\left(\delta\hat{X}_{\mathrm{D}}^{+} + \frac{4Nkg_{\mathrm{A}}\alpha_{\mathrm{L}}}{\sqrt{\kappa_{\mathrm{AC}}}}\hat{x}_{\mathrm{A}}\right),\\ \delta\hat{P}_{\mathrm{R}} &= \frac{2}{\sqrt{\kappa_{\mathrm{AC}}}}\left(\delta\hat{P}_{\mathrm{D}}\right),\\ \delta\hat{X}_{\mathrm{C}} &= \frac{2}{\sqrt{\kappa_{\mathrm{MC}}}}\left(\delta\hat{X}_{\mathrm{D}} + \frac{8Nkg_{\mathrm{A}}\alpha_{\mathrm{L}}}{\sqrt{\kappa_{\mathrm{AC}}}}\hat{x}_{\mathrm{A}}\right),\\ \delta\hat{P}_{\mathrm{C}} &= \frac{2}{\sqrt{\kappa_{\mathrm{MC}}}}\left(\delta\hat{P}_{\mathrm{D}} - \frac{2g_{\mathrm{M}}\beta}{\sqrt{\kappa_{\mathrm{MC}}}}\hat{x}_{\mathrm{M}}\right),\\ \delta\hat{X}_{\mathrm{L}} &= \frac{2}{\sqrt{\kappa_{\mathrm{AC}}}}\left(\delta\hat{X}_{\mathrm{D}}^{+} + \frac{4Nkg_{\mathrm{A}}\alpha_{\mathrm{L}}}{\sqrt{\kappa_{\mathrm{AC}}}}\hat{x}_{\mathrm{A}}\right),\\ \delta\hat{P}_{\mathrm{L}} &= \frac{2}{\sqrt{\kappa_{\mathrm{AC}}}}\left(\delta\hat{P}_{\mathrm{D}} - \frac{4g_{\mathrm{M}}\beta}{\sqrt{\kappa_{\mathrm{MC}}}}\hat{x}_{\mathrm{M}}\right).\end{aligned}$$

By inspecting these equations we may see that the optomechanical interaction creates phase fluctuations that then perturb the atoms, whilst motion of the atoms modulates the amplitude fluctuations experienced by the micromechanical element.

In this same limit the optical field that exits the system carries the fluctuations

$$\begin{aligned}\delta\hat{X}_{\mathrm{out}} &= \delta\hat{X}_{\mathrm{D}}\\ \delta\hat{P}_{\mathrm{out}} &= \delta\hat{P}_{\mathrm{D}} - \frac{4g_{\mathrm{M}}\beta}{\sqrt{\kappa_{\mathrm{MC}}}}\hat{x}_{\mathrm{M}}.\end{aligned} \tag{4.7}$$

Simplified dynamics and back-action

Substituting the above into the equations of motion (Eqn (4.5a) and Eqn (4.5b)) gives the time evolution of the mechanical elements, Eqn (4.8a) and Eqn (4.8b), under the effect of the coupling (Eqn (4.11)) and the back-action noise

$$\begin{aligned}\hat{F}_{\mathrm{BA,A}} &= 0,\\ \hat{F}_{\mathrm{BA,M}} &= \frac{-4\hbar g_{\mathrm{M}}\alpha_{\mathrm{D}}}{\kappa_{\mathrm{MC}}}\delta\hat{X}_{\mathrm{D}}.\end{aligned}$$

Thus,

$$Nm\frac{\mathrm{d}^2\hat{x}_\mathrm{A}}{\mathrm{d}t^2} = -Nm\omega_\mathrm{A}^2\hat{x}_\mathrm{A} + K\hat{x}_\mathrm{M}, \tag{4.8a}$$

$$M\frac{\mathrm{d}^2\hat{x}_\mathrm{M}}{\mathrm{d}t^2} = -M\omega_\mathrm{M}^2\hat{x}_\mathrm{M} + \hat{F}_\mathrm{BA,M} + K\hat{x}_\mathrm{A}. \tag{4.8b}$$

The spring constant K quantifies—for the moment—the coupling strength, and is given by

$$K = -8^2\hbar N k g_\mathrm{A} g_\mathrm{M}\frac{Q_\mathrm{AC}Q_\mathrm{MC}}{\omega_\mathrm{D}^2}\alpha_\mathrm{D}^2. \tag{4.9}$$

We briefly discuss the result $\tilde{F}_\mathrm{BA,A} = 0$. Complete cancellation of the optical back-action onto the atomic motion is an artefact of our model, arising due to neglect of optical loss and near-field atom–atom interactions. In reality, there will be some amount of heating caused by optical loss, near-field interactions between atoms and spontaneous scattering of photons out of the trap beams.

As noted in § 4.2.3, any optical loss will render the effective oscillator–oscillator interaction asymmetric, and hence non-Hamiltonian. Such losses also introduce vacuum noise on the left-going field that is uncorrelated with that on the right-going, leading to imperfect cancellation of the phase fluctuations appearing in the atomic equation of motion. In the limit that the noise is completely uncorrelated the back-action heating rate is $2\Gamma_\mathrm{A}C_\mathrm{A}$ (where C_A is the atom–optomechanical cooperativity defined in Eqn (4.20)).

Even in the absence of uncorrelated noise, diffusion of the atomic centre of mass occurs due to near-field optically-mediated interactions between atoms: for instance, a sideband photon may be emitted by one atom and absorbed by another. To a first approximation these processes do not alter the optical far-field, which our (one-dimensional) model describes, but do lead to back-action heating of the atomic motion. This effect will be small in the far-detuned limit, and scales weakly with the atom number ($\propto N^{1/3}$) [219], and we therefore neglect it. Experiments with large atom numbers have observed collective scattering effect [153].

The heating rate associated with Gordon-Ashkin (GA) diffusion [220] is also negligible in the regime discussed. To illustrate this, consider the momentum diffusion coefficient $\mathscr{D}_\mathrm{p}$ given by [221]. Since the atoms are trapped near to an antinode of the cavity field there is (to first order) no spatial variation of the electric field amplitude or of the degree of coherence between the atoms' ground and excited states (given by $\langle\sigma\rangle$, where σ is the atomic lowering operator), so the diffusion should be dominated by spontaneous scattering terms. The axial motion of each atom is thus heated at a rate (in the harmonic approximation)

$$\Gamma_\mathrm{GA}\bar{n}_\mathrm{GA} = \frac{\mathscr{D}_\mathrm{p}}{6m\hbar\omega_\mathrm{A}} \approx \frac{\omega_\mathrm{A}\gamma_\mathrm{e}}{8\left|\Delta_\mathrm{t}\right|},$$

where the excited state lifetime is $1/2\gamma_\mathrm{e}$ (on the order of 10 ns for ^{87}Rb [222]), Γ_GA is the coupling rate to the effective bath and $\bar{n}_\mathrm{GA}$ is the phonon number characterising this bath. We may easily satisfy $\Gamma_\mathrm{GA}\bar{n}_\mathrm{GA} \ll \Gamma_\mathrm{A}/2$ because we operate in the far-detuned and bad-cavity limits. Furthermore, independent scattering from each atom results in suppression of the centre of mass diffusion coefficient by a factor of $1/\sqrt{N}$. Heating due to Gordon-Ashkin processes may therefore be safely omitted from our model.

Effective Hamiltonian dynamics

It is natural to divide the optically-mediated interactions into coherent and 'incoherent' processes. The latter is simply the back-action noise. Taken together, Eqn (4.8a) and Eqn (4.8b) imply that the former may be described by an effective direct Hamiltonian interaction between the two oscillators,

$$\begin{aligned}\hat{H}_{\rm eff} &= -\hbar g \frac{\hat{x}_{\rm M}}{x_{\rm ZP,M}} \frac{\hat{x}_{\rm A}}{x_{\rm ZP,A}} \\ &= -\hbar g \left(a_{\rm A}^\dagger a_{\rm M} + a_{\rm M}^\dagger a_{\rm A} + a_{\rm M}^\dagger a_{\rm A}^\dagger + a_{\rm M} a_{\rm A} \right), \end{aligned} \tag{4.10}$$

where the motional annihilation operators are $a_{\rm A}$ (atomic) and $a_{\rm M}$ (mechanical), and g is the atom–mechanical coupling rate [150, 151]. The latter is

$$g = \sqrt{N}\, \frac{g_{\rm M}}{k} \frac{\omega_{\rm A}}{\kappa_{\rm MC}} \sqrt{\frac{m\omega_{\rm A}}{M\omega_{\rm M}}} \tag{4.11}$$

in accordance with the relationship $g = \frac{K}{\hbar} x_{\rm ZP,A} x_{\rm ZP,M}$.

The combined system is stable if

$$g < \frac{1}{2} \frac{1}{1/\omega_{\rm A} + 1/\omega_{\rm M}}; \tag{4.12}$$

at higher coupling rates the harmonic potential experienced by the symmetric mode $\hat{x}_{\rm A} + \hat{x}_{\rm M}$ becomes inverted, anti-trapping this degree of freedom.

Note that if optical losses between (and/or within) the cavities are non-negligible the effective interaction of the oscillators becomes non-Hamiltonian, as discussed in detail by [150].

Our Eqn (4.11) agrees with that derived in [151], which sports a free-space atom trap.

One may be tempted to increase g by choosing $\omega_{\rm A} > \omega_{\rm M}$; however, for our purposes this is counterproductive. Consider Eqn (4.10) in the interaction picture with respect to the free mechanical Hamiltonian ($\hbar\omega_{\rm A} a_{\rm A}^\dagger a_{\rm A} + \hbar\omega_{\rm M} a_{\rm M}^\dagger a_{\rm M}$);

$$\begin{aligned} H_{\rm eff} &= -\hbar g \Big\{ a_{\rm A}^\dagger a_{\rm M} \mathrm{e}^{+\mathrm{i}(\omega_{\rm M}-\omega_{\rm A})t} + a_{\rm M}^\dagger a_{\rm A} \mathrm{e}^{-\mathrm{i}(\omega_{\rm M}-\omega_{\rm A})t} \\ &\qquad + a_{\rm M}^\dagger a_{\rm A}^\dagger \mathrm{e}^{-\mathrm{i}(\omega_{\rm M}+\omega_{\rm A})t} + a_{\rm M} a_{\rm A} \mathrm{e}^{+\mathrm{i}(\omega_{\rm M}+\omega_{\rm A})t} \Big\}, \end{aligned}$$

where the operators are understood to be in the interaction picture. If the mechanical systems are not resonant ($\omega_{\rm A} \neq \omega_{\rm M}$) all four terms have explicit time dependence that, when averaged over many mechanical cycles, degrades the effective interaction strength. Conversely, on resonance ($\omega_{\rm A} = \omega_{\rm M}$) the interaction reduces to an atomic $\leftrightarrow$ mechanical state swap operation (since the 'two-mode squeezing' terms of the lower line are far off-resonant)[3]. Sympathetic cooling leverages this fact by continually swapping the cold motional state of the atoms onto the mechanical device [150]. We will therefore restrict ourselves to the special case of $\omega_{\rm M} = \omega_{\rm A} = \Omega$ in § 4.3.

Note that the atomic $\leftrightarrow$ mechanical state swap that these dynamics perform is *not* composed of consecutive swaps between the mechanical degrees of freedom and the light. A curious corollary is

[3] Physically, the state swap terms correspond to in-phase operations that tend to correlate $\hat{p}_{\rm A}(t)$ and $\hat{p}_{\rm M}(t)$ with time-delayed versions of themselves ($\hat{p}_{\rm A}(t - \pi/\Omega)$ and $\hat{p}_{\rm M}(t - \pi/\Omega)$), whereas the two-mode squeezing terms correspond to in-quadrature operations that lead to correlations between the two oscillators.

that the state transfer may be performed even in a regime where the optomechanical cooperativity is too low to allow an optical $\leftrightarrow$ mechanical swap. The requirements on experimental parameters (for the optomechanical device) are therefore significantly more relaxed than those of resolved sideband cooling (*cf.* § 4.3.2).

Finally, we note that there are experimental advantages to incorporating a ring resonator into an experiment—despite the moderate increase in technical complexity—even though g depends only on $\alpha_{\mathrm{L,R}}$ (*i.e.* on $\alpha_{\mathrm{D}}/\sqrt{\kappa_{\mathrm{AC}}}$). This is especially true if the drive strength α_{D} is limited (*e.g.* by photodetector saturation or absorptive heating). For instance, keeping all other optical parameters constant (*i.e.* fixed detuning, input power and transverse profile), our additional ring cavity yields a $g \propto \sqrt{\mathscr{F}_{\mathrm{AC}}}$ improvement of the coupling rate over that given by a free space trap [151] ($\mathscr{F}_{\mathrm{AC}}$ is the finesse of the ring cavity, and we have imagined scaling $\omega_{\mathrm{M}} \propto \sqrt{\mathscr{F}_{\mathrm{AC}}}$ so as to maintain the $\omega_{\mathrm{A}} = \omega_{\mathrm{M}}$ resonance condition). Including a ring cavity may also permit one to use a larger transverse beam distribution (*e.g.* in a bow-tie resonator), allowing g to be boosted by trapping more atoms simultaneously. Alternatively, the cavity may be used to assist in suppressing heating of the atomic motion due to spontaneous photon scattering [220], which occurs at a rate Γ_{sc}. To see this, note that $\Gamma_{\mathrm{sc}} \propto \alpha_{\mathrm{R}}\alpha_{\mathrm{L}}/\Delta_{\mathrm{t}}^2 \propto \mathscr{F}_{\mathrm{AC}}/\Delta_{\mathrm{t}}^2$ (for fixed α_{D}) [215] whilst $g \propto (\mathscr{F}_{\mathrm{AC}}/\Delta_{\mathrm{t}})^{3/4}$; we may therefore leave g unchanged but suppress Γ_{sc} by a factor of $1/\varepsilon$ by scaling both $\mathscr{F}_{\mathrm{AC}}$ and Δ_{t} by ε (see 4.2.3 for further discussion).

4.2.4 Coupling to reservoirs

Ultimately, the performance of our cooling scheme is limited by noise sources modelled by forming the Langevin equations [198]

$$Nm\frac{\mathrm{d}^2\hat{x}_{\mathrm{A}}}{\mathrm{d}t^2} = -Nm\omega_{\mathrm{A}}^2\hat{x}_{\mathrm{A}} + K\hat{x}_{\mathrm{M}} + \hat{F}_{\mathrm{CB}} - \Gamma_{\mathrm{A}}Nm\frac{\mathrm{d}\hat{x}_{\mathrm{A}}}{\mathrm{d}t}, \tag{4.13a}$$

$$M\frac{\mathrm{d}^2\hat{x}_{\mathrm{M}}}{\mathrm{d}t^2} = -M\omega_{\mathrm{M}}^2\hat{x}_{\mathrm{M}} + \hat{F}_{\mathrm{BA,M}} + K\hat{x}_{\mathrm{A}} + \hat{F}_{\mathrm{TH}} - \Gamma_{\mathrm{M}}M\frac{\mathrm{d}\hat{x}_{\mathrm{M}}}{\mathrm{d}t} + \hat{F}_{\mathrm{FB}}. \tag{4.13b}$$

The atomic motion is damped into a cold bath (*e.g.* by application of laser cooling [61]) at a rate Γ_{A}, which introduces fluctuations $\hat{F}_{\mathrm{CB}}$. We will assume this reservoir to be at zero temperature. Mechanical losses are due to coupling to a hot bath at a rate Γ_{M}, with an associated forcing term $\hat{F}_{\mathrm{TH}}$ consistent with a thermal occupancy $\bar{n}_{\mathrm{M}} \approx k_{\mathrm{B}}T_{\mathrm{B,M}}/\hbar\omega_{\mathrm{M}} \gg 1$ (*cf.* 4.2.6). Optical back-action on the mechanical oscillator is given by $\hat{F}_{\mathrm{BA,M}}$, with the equivalent force on the atomic system vanishing within the realm of validity of our model (*cf.* 4.2.3). Finally, the effects of feedback are encapsulated by $\hat{F}_{\mathrm{FB}}$.

It will be convenient to adopt a frequency domain description of the system for the purposes of treating the feedback circuit; for each time domain operator $\hat{f}(t)$ there is a corresponding frequency domain operator $\tilde{f}(\omega)$ given by the Fourier transform

$$\tilde{f}(\omega) = \int_{-\infty}^{\infty}\mathrm{d}t\ \mathrm{e}^{\mathrm{i}\omega t}\hat{f}(t) \Leftrightarrow \hat{f}(t) = \frac{1}{2\pi}\int_{-\infty}^{\infty}\mathrm{d}\omega\ \mathrm{e}^{-\mathrm{i}\omega t}\tilde{f}(\omega).$$

Taking the transforms of Eqn (4.13a) and Eqn (4.13b) and eliminating $\tilde{x}_{\mathrm{A}}$ yields

$$\tilde{x}_{\mathrm{M}}(\omega) = \frac{1}{\chi_{\mathrm{M}}^{-1}(\omega) - K^2\chi_{\mathrm{A}}(\omega)}\left[\tilde{F}_{\mathrm{TH}} + \tilde{F}_{\mathrm{BA,M}} + \tilde{F}_{\mathrm{FB}} + K\chi_{\mathrm{A}}(\omega)\tilde{F}_{\mathrm{CB}}\right], \tag{4.14}$$

in which the mechanical susceptibility is $\chi_{\rm M}(\omega) = \left[M\left(\omega_{\rm M}^2 - \omega^2 - {\rm i}\omega\Gamma_{\rm M}\right)\right]^{-1}$ and the atomic motion has the transfer function $\chi_{\rm A}(\omega) = \left[Nm\left(\omega_{\rm A}^2 - \omega^2 - {\rm i}\omega\Gamma_{\rm A}\right)\right]^{-1}$.

4.2.5 Modelling cold damping

The fluctuation-dissipation theorem enforces our inability to cool an oscillator by increasing the rate at which it is damped into its thermal bath [116]; however, no such restrictions apply when coupled to a non-thermal environment. One method of engineering such an effective non-equilibrium reservoir is to use an external feedback circuit to apply a force $\hat{F}_{\rm FB} \propto -\hat{p}_{\rm M}$ to the oscillator, which increases its linewidth and introduces a (coloured) fluctuating force determined by noise on measurements of $\hat{p}_{\rm M}$ [119]. The resulting mechanical steady-state is approximately thermal, with an effective temperature that may be less than that of the environment (*cf.* § 4.3.1).

In optomechanical experiments $\hat{p}_{\rm M}$ is typically not directly accessible; instead, one detects the phase quadrature of the output optical field (Eqn (4.7)), which carries information concerning $\hat{x}_{\rm M}$, and feeds this signal through an electrical filter. Balanced homodyne is an appropriate detection method (see § 3.5 for an introduction to homodyne measurement).

The optical field at the output may be found by calculating $\delta a_{\rm out} = \sqrt{\kappa_{\rm AC}}\,\delta a_{\rm L} - \delta a_{\rm in,L}$. Imperfect homodyne detection (efficiency η) is modelled by applying a standard beamsplitter transformation to this field (Eqn (4.7))—that introduces an amount of uncorrelated noise associated with quantum vacuum fluctuations $\delta\hat{X}_{\rm V}\left(\delta\hat{P}_{\rm V}\right)$—and treating the photodetectors as perfectly efficient. The resulting effective detected field is

$$\begin{aligned}
\delta\hat{X}_{\rm det} &= \sqrt{\eta}\,\delta\hat{X}_{\rm D}^{+} + \sqrt{1-\eta}\,\delta\hat{X}_{\rm V}, \\
\delta\hat{P}_{\rm det} &= \sqrt{\eta}\left(\delta\hat{P}_{\rm D} - \frac{4g_{\rm M}\beta}{\sqrt{\kappa_{\rm MC}}}\hat{x}_{\rm M}\right) + \sqrt{1-\eta}\,\delta\hat{P}_{\rm V}.
\end{aligned}$$

The most intuitive filter yielding a force proportional to $-\hat{p}_{\rm M}$ is a low-pass differentiator circuit[4] with bandwidth $\Delta\omega_{\rm FB} \gg \omega_{\rm M}$ [209]; such a filter is near-optimal[5] in the limit that the optomechanical coupling is sufficiently high [6], in that the controlled state asymptotically approaches the ground state for appropriate choice of gain, *cf.* § 4.3.1. The feedback force is

$$\tilde{F}_{\rm FB} = \frac{{\rm i}\omega G\Gamma_{\rm M}M}{1 - {\rm i}\omega/\Delta\omega_{\rm FB}}\tilde{x}_{\rm M} + \tilde{F}_{\rm SN} \tag{4.15}$$

where the contribution due to optical shot noise is

$$\tilde{F}_{\rm SN} = \frac{-{\rm i}\omega G}{1 - {\rm i}\omega/\Delta\omega_{\rm FB}}\frac{M\Gamma_{\rm M}\kappa_{\rm MC}}{8g_{\rm M}\alpha_{\rm D}}\left(\delta\tilde{P}_{\rm D} + \sqrt{\frac{1}{\eta} - 1}\,\delta\tilde{P}_{\rm V}\right).$$

The detection efficiency is $\eta \in [0,1]$ and $\delta\tilde{P}_{\rm V}$ is the uncorrelated vacuum noise coupled in by imperfect detection. We have normalised the filter function such that the overall feedback gain G has a transparent physical interpretation (*cf.* Eqn (4.17)).

[4] In practice one would also include a band-pass filter centred at $\omega_{\rm M}$ so as to isolate the mechanical mode of interest.

[5] For an in-depth discussion of the optimum measurement angle see [223], published after this work was completed. The central claims of this work are unaffected.

[6] Precisely, $C_{\rm M} \gg \bar{n}_{\rm M}$ and $\eta = 1$.

Inserting the feedback force into Eqn (4.14) yields

$$\tilde{x}_{\mathrm{M}}(\omega) = \chi'_{\mathrm{M}}(\omega)\left[\tilde{F}_{\mathrm{TH}} + \tilde{F}_{\mathrm{BA,M}} + \tilde{F}_{\mathrm{SN}} + K\chi_{\mathrm{A}}(\omega)\tilde{F}_{\mathrm{CB}}\right]. \tag{4.16}$$

The effective mechanical susceptibility has been modified to

$$\chi'_{\mathrm{M}}(\omega) = \left[\chi_{\mathrm{M}}^{-1}(\omega) - \frac{\mathrm{i}\omega}{1-\mathrm{i}\omega/\Delta\omega_{\mathrm{FB}}} GM\Gamma_{\mathrm{M}} - K^2\chi_{\mathrm{A}}(\omega)\right]^{-1}. \tag{4.17}$$

In the limit $\omega_{\mathrm{M}} \ll \Delta\omega_{\mathrm{FB}}$ the second term describes a feedback-induced increase in the linewidth of the oscillator, with G being the amount of broadening (so $G = 1$ corresponds to a doubling of the linewidth), whilst the third term is a modification due to the atomic centre of mass motion.

Feedback of the form described here may be implemented in a number of ways. For example, 'electrostatic' actuation may be used to apply a force directly to the mechanical oscillator [117–120], or the feedback force may be generated by imprinting an amplitude modulation onto a bright auxiliary optical field (that does not interact with the atomic system) [116, 121, 122]. Importantly, we note that it is generally possible to arrange the feedback apparatus such that the quantum noise originating from the actuator (*e.g.* the RF or optical field, respectively, for the examples given above) is negligible (*cf.* Eqn (4.16)); this approximation has been extensively employed in the optomechanical feedback literature (*e.g.* [114, 210, 211, 224]).

4.2.6 Position power spectrum

The power spectrum of the position, $S_{x_{\mathrm{M}}x_{\mathrm{M}}}$, is found *via* the Wiener-Khinchin theorem [5] in the limit $\Delta\omega_{\mathrm{FB}} \to \infty$.

$$\begin{aligned} S_{x_{\mathrm{M}}x_{\mathrm{M}}}[\omega] &= \frac{1}{2\pi}\int_{-\infty}^{\infty} \mathrm{d}\omega' \left\langle \tilde{x}_{\mathrm{M}}(\omega)\tilde{x}_{\mathrm{M}}(\omega')\right\rangle \\ &= 2\hbar\left|\chi'_{\mathrm{M}}\right|^2\left[\Gamma_{\mathrm{M}}M\omega_{\mathrm{M}}\left(\frac{1}{2} + \bar{n}_{\mathrm{M}} + C_{\mathrm{M}} + \frac{\omega}{\omega_{\mathrm{M}}}\frac{G}{4} + \frac{\omega^2}{\omega_{\mathrm{M}}^2}\frac{G^2}{4^2\eta C_{\mathrm{M}}}\right)\right. \\ &\qquad \left. + K^2\left|\chi_{\mathrm{A}}\right|^2\Gamma_{\mathrm{A}}Nm\omega_{\mathrm{A}}\left(\frac{1}{2}\right)\right]. \end{aligned} \tag{4.18}$$

The first two terms correspond to vacuum noise $(1/2)$ and phonons entering the mechanics *via* the thermal bath (with occupancy $\bar{n}_{\mathrm{M}}$), whilst the third is the optomechanical cooperativity,

$$C_{\mathrm{M}} = \frac{4\left(g_{\mathrm{M}}x_{\mathrm{ZP,M}}\beta\right)^2}{\Gamma_{\mathrm{M}}\kappa_{\mathrm{MC}}} = \frac{2\hbar}{M\omega_{\mathrm{M}}\Gamma_{\mathrm{M}}}\left(\frac{2g_{\mathrm{M}}\alpha_{\mathrm{D}}}{\kappa_{\mathrm{MC}}}\right)^2, \tag{4.19}$$

corresponding to the effective number of additional bath phonons introduced by optical back-action. As will be seen, C_{M} controls the efficacy of feedback cooling [114] and strongly contributes to the sympathetic cooling performance.

The fourth term of Eqn (4.18) arises from correlations between $\hat{F}_{\mathrm{BA,M}}$ and $\hat{F}_{\mathrm{SN}}$, and the fifth is solely due to the latter (*cf.* 4.2.6).

Finally, noise entering from the zero-temperature bath is filtered by the atomic susceptibility and appears as the sixth term in the power spectrum. It is convenient to define an associated cooperativity

by analogy with $C_{\rm M}$:

$$C_{\rm A} = \frac{2\hbar N}{m\omega_{\rm A}\Gamma_{\rm A}}\left(\frac{4kg_{\rm A}\alpha_{\rm D}}{\kappa_{\rm AC}}\right)^2 = \frac{Nm\omega_{\rm A}^3}{2\hbar\Gamma_{\rm A}}\left(\frac{1}{4k\alpha_{\rm D}}\right)^2. \tag{4.20}$$

Although it does not appear directly in $S_{x_{\rm M}x_{\rm M}}$ (in the above form), $C_{\rm A}$ is important in determining whether sympathetic cooling is capable of reaching the mechanical ground state.

Integrating over the power spectrum yields the steady-state variance of $\hat{x}_{\rm M}$, *viz.*

$$\left\langle \hat{x}_{\rm M}^2 \right\rangle = \frac{1}{2\pi}\int_{-\infty}^{\infty} {\rm d}\omega\, S_{x_{\rm M}x_{\rm M}}[\omega], \tag{4.21}$$

which is the result of interest.

It is generally necessary to evaluate $\left\langle \hat{x}_{\rm M}^2 \right\rangle$ numerically; however, in § 4.3 we also explore several limits in which it is possible to give approximate analytical solutions of Eqn (4.21).

Noise correlation functions

If the typical thermal timescale $\hbar/k_{\rm B}T_{\rm B,M}$ is small compared to the mechanical period it is possible to form the correlator [114]

$$\left\langle \tilde{F}_{\rm TH}(\omega)\tilde{F}_{\rm TH}(\omega')\right\rangle = 4\pi\hbar\Gamma_{\rm M}\omega_{\rm M}M\left(\bar{n}_{\rm M}+\frac{1}{2}\right)\delta(\omega+\omega').$$

$\bar{n}_{\rm M}$ is understood to be the mean number of excitations in the oscillator when in thermal equilibrium with its bath.

When forming the product $\langle \tilde{x}_{\rm M}(\omega)\tilde{x}_{\rm M}(\omega')\rangle$ the following correlators also arise;

$$\begin{aligned}
\left\langle \tilde{F}_{\rm CB}(\omega)\tilde{F}_{\rm CB}(\omega')\right\rangle &= 4\pi\hbar\Gamma_{\rm A}Nm\omega_{\rm A}\frac{1}{2}\,\delta(\omega+\omega'),\\
\left\langle \tilde{F}_{\rm BA,M}(\omega)\tilde{F}_{\rm BA,M}(\omega')\right\rangle &= 4\pi\hbar\Gamma_{\rm M}M\omega_{\rm M}C_{\rm M}\,\delta(\omega+\omega'),\\
\left\langle \tilde{F}_{\rm SN}(\omega)\tilde{F}_{\rm BA,M}(\omega')\right\rangle &= 4\pi\hbar\Gamma_{\rm M}M\omega_{\rm M}\frac{G}{4}\frac{\omega/\omega_{\rm M}}{1-{\rm i}\omega/\Delta\omega_{\rm FB}}\delta(\omega+\omega'),\\
\left\langle \tilde{F}_{\rm SN}(\omega)\tilde{F}_{\rm SN}(\omega')\right\rangle &= -4\pi\hbar\Gamma_{\rm M}\omega_{\rm M}M\left(\frac{G^2}{4^2\eta C_{\rm M}}\right)\times\\
&\qquad \frac{\omega\omega'}{\omega_{\rm M}^2}\frac{\delta(\omega+\omega')}{(1-{\rm i}\omega/\Delta\omega_{\rm FB})(1-{\rm i}\omega'/\Delta\omega_{\rm FB})}.
\end{aligned}$$

It is important to recall that, for any observables $\hat{A}$ and $\hat{B}$, $\left\langle \tilde{A}(\omega)\tilde{B}(\omega')\right\rangle = \left\langle \tilde{B}(-\omega')\tilde{A}(-\omega)\right\rangle^*$. We note also that the commutation relations ensure that for any vacuum field $\left\langle \delta\tilde{X}_{\rm V}(\omega)\,\delta\tilde{P}_{\rm V}(\omega')\right\rangle = +2\pi{\rm i}\delta(\omega+\omega')$.

All correlators not obtained from those above vanish.

4.3 Cooling performance

We are now in a position to calculate the mechanical oscillator's position variance as a function of the system parameters and the applied feedback gain. In the cases examined below the mechanical

steady state is well approximated by a thermal distribution, as confirmed by numerical calculations of its covariance matrix. For this reason $\langle \hat{x}_{\mathrm{M}}^2 \rangle$ serves as an excellent proxy for temperature.

With this in mind, we will refer to the oscillator as 'ground state cooled' if

$$\langle \hat{x}_{\mathrm{M}}^2 \rangle \leq 3 x_{\mathrm{ZP,M}}^2. \tag{4.22}$$

This corresponds to the requirement that the oscillator contain at most one phonon on average ($\langle a_{\mathrm{M}}^\dagger a_{\mathrm{M}} \rangle \leq 1$) [7].

4.3.1 Feedback cooling

Let us first consider the case in which there are no atoms in the trap. We include a brief summary of results (*cf.* sources presented in § 5.1) here for the purposes of comparison with sympathetic cooling.

It is straightforward to extremise Eqn (4.21) with $C_{\mathrm{A}} = 0$ using Eqn (3.27).

This confirms the presence of a global minimum variance of

$$\frac{\langle \hat{x}_{\mathrm{M}}^2 \rangle_{\mathrm{opt}}}{x_{\mathrm{ZP,M}}^2} = \frac{G_{\mathrm{opt}}^{(0)}}{4\eta C_{\mathrm{M}}} \tag{4.23}$$

which is achieved with the feedback gain $G_{\mathrm{opt}}^{(0)} = \sqrt{1+\mathrm{SNR}} - 1$, where the signal-to-noise ratio [117] is given by $\mathrm{SNR} = 16\eta C_{\mathrm{M}}(\bar{n}_{\mathrm{M}} + C_{\mathrm{M}} + 1/2)$.

In the experimentally-relevant regime of $\{\mathrm{SNR}, \bar{n}_{\mathrm{M}}\} \gg 1$ it is straightforward to show that ground state cooling may be realised if

$$\bar{n}_{\mathrm{M}} \lesssim (9\eta - 1) C_{\mathrm{M}} \leq 8 C_{\mathrm{M}}. \tag{4.24}$$

Thus we see that feedback cooling to the ground state is possible when the mechanical noise spectrum is dominated by radiation pressure fluctuations.

4.3.2 Sympathetic cooling

We now consider the capacity of sympathetic cooling alone: our analysis complements and extends those performed by [150] and [151] by explicitly determining the temperature achievable in the regime of hybridised mechanical modes.

Analytical treatments are tractable in both the atomic adiabatic (weak coupling) regime, wherein the atoms are damped heavily compared to the rate of phonon transfer between the oscillators, and the strong coupling (hybridised) regime, in that the coherent interaction (Eqn (4.10)) is dominant. The primary challenge in either case is evaluating $\int_{-\infty}^{\infty} \mathrm{d}\omega \ |\chi_{\mathrm{M}}'|^2$ and $\int_{-\infty}^{\infty} \mathrm{d}\omega \ |\chi_{\mathrm{M}}'|^2 |\chi_{\mathrm{A}}|^2$. These control, respectively, the response to noise acting directly on the mechanics and indirectly *via* the atoms.

[7] We note that this is the same cut-off as implicitly employed in previous works *e.g.* [150, 151]

Weak coupling

In the weak coupling regime ($\Gamma_A \gg g$ & $\Gamma_A > \Gamma_M$) the atomic centre of mass adiabatically follows the motion of the mechanical oscillator, allowing us to expand the atomic susceptibility near the resonance frequency as

$$\chi_A(\omega \approx \Omega) \approx \frac{i}{Nm\omega\Gamma_A} \approx \frac{i}{Nm\Gamma_A\Omega}\left(2 - \frac{\omega}{\Omega}\right).$$

Neglecting the small frequency-independent imaginary term that arises leaves us with the approximate modified mechanical susceptibility

$$\chi'_M(\omega) \approx \frac{1}{M\left[\Omega^2 - \omega^2 - i\Gamma_M\omega(1+c)\right]} \tag{4.25}$$

which describes a simple harmonic oscillator with an enhanced linewidth of $\Gamma_M(1+c)$. Fittingly, the broadening is characterised by the atom–mechanical cooperativity

$$C = \frac{4g^2}{\Gamma_A\Gamma_M} = 4^2 C_A C_M, \tag{4.26}$$

With these approximations $|\chi'_M|^2$ may be readily integrated (*cf.* Eqn (3.27a) & Eqn (3.27b)).

The remaining term, proportional to $\int_{-\infty}^{\infty} d\omega\ |\chi'_M|^2 |\chi_A|^2$, is not evaluated directly. Instead, it may be evaluated by using the fact that the majority of the spectral variance is concentrated near the resonance frequency Ω. We therefore replace $|\chi'_M|^2 |\chi_A|^2$, a product of two approximately Lorentzian functions, with a single (approximate) Lorentzian, the linewidth of which is chosen to give an accurate fit in the region $\omega \approx \Omega$. We find that

$$|\chi'_M|^2 |\chi_A|^2 \approx \left[\frac{1}{NmM\Omega\Gamma_{ser}}\right]^2 \frac{1}{\left(\Omega^2 - \omega^2\right)^2 + \omega^2\Gamma_{par}^2}$$

is a suitable replacement (depicted in Fig. 4.2 panel *ii*)). The linewidth of this function is the 'parallel sum'

$$\Gamma_{par} = \left(\frac{1}{\Gamma_A} + \frac{1}{\Gamma_M(1+C)}\right)^{-1}$$

of the atomic and (enhanced) mechanical motion decay rates, rather than the 'serial sum' $\Gamma_{ser} = [\Gamma_A + \Gamma_M(1+c)]$; this is necessary to obtain the correct behaviour when $\Gamma_M(1+C) \sim \Gamma_A$. Numerical integration confirms that this replacement faithfully reproduces the true value of $\int_{-\infty}^{\infty} d\omega\ |\chi'_M|^2 |\chi_A|^2$, despite decaying more slowly than the true integrand as $\omega \to \infty$.

Using these two approximations we find

$$\frac{\langle \hat{x}_M^2 \rangle}{x_{ZP,M}^2} = \frac{2}{1+c}\left[\bar{n}_M + C_M + \frac{1}{2} + \bar{n}_{a,eff}\right], \tag{4.27}$$

where coupling to the atoms has introduced an effective number of phonons

$$\bar{n}_{a,eff} = \frac{C/2}{1 + \frac{\Gamma_M}{\Gamma_A}(1+C)}.$$

Strong coupling

In the opposite limit, strong coupling ($g \gg \max\{\Gamma_A, \Gamma_M\}$), excitations are hybridised across the two local modes ($\hat{x}_A$ and $\hat{x}_M$), giving rise to a symmetric and an antisymmetric normal mode. In this case $|\chi'_M|^2$ and $|\chi'_M|^2 |\chi_A|^2$ share a similar twin-peaked structure. Splitting of the susceptibility into two peaks, evident in Fig. 4.2 panel *iii*), is a clear signature of hybridisation.

Since the two peaks of the susceptibility account for the majority of the spectral variance we set

$$\left|\chi'_M\right|^2 \approx |\chi_+|^2 + |\chi_-|^2 \tag{4.28}$$

where the symmetric ($+$) and antisymmetric ($-$) modes have susceptibilities

$$\chi_\pm^{-1} = M_\pm \left[\Omega^2 \left(1 \pm \frac{-2g}{\Omega}\right) - \omega^2 - i\omega\Gamma_N\right]. \tag{4.29}$$

Note that when $g \ll \Omega/2$ the splitting between the symmetric and antisymmetric peaks is $2g$. The linewidth Γ_N is the mean of Γ_M and Γ_A, and the effective masses $M_\pm = 2M\left(1 - g^2/\Omega^2\right)$ may be obtained by considering the zero-frequency behaviour of $|\chi'_M|^2$. It is usually possible to ignore the strong suppression of the susceptibility at $\omega \approx \Omega$ (*cf.* Fig. 4.2 panel *iii*), due to interference of the normal modes, without significantly altering the value of the integral.

Noise acting on the atomic local mode appears in $S_{x_M x_M}[\omega]$ as a sharp peak at $\omega \approx \Omega$; fortunately, the aforementioned interference of the normal modes ensures that the product $|\chi_A|^2 |\chi'_M|^2$ remains dominated by the twin-peaked susceptibility, as in Fig. 4.2 panel *iv*). Thus we again note that the majority of the spectral variance lies close to the maxima, motivating the substitution

$$|\chi_A|^2 \left|\chi'_M\right|^2 \approx \frac{|\chi_+|^2 + |\chi_-|^2}{(2Nm\Omega g)^2}. \tag{4.30}$$

The scaling factor $(2Nm\Omega g)^{-2}$ accounts for the different masses of the normal and local modes. This approximate integrand yields quite accurate results, as confirmed by numerical integration.

Combining Eqn (4.28) and Eqn (4.30), we find that the variance is given

$$\frac{\langle \hat{x}_M^2 \rangle}{x_{ZP,M}^2} = \frac{1}{2}\left[\frac{\Gamma_M}{\Gamma_N}(\bar{n}_M + C_M) + 1\right]\left(1 - \frac{g^2}{\Omega^2}\right)^{-2}\left(1 - \frac{4g^2}{\Omega^2}\right)^{-1}. \tag{4.31}$$

Here $\Gamma_N = \frac{1}{2}(\Gamma_A + \Gamma_M)$ is the linewidth of the normal modes of the system.

Comparison with numerics

Our analytical expressions (Eqn (4.27) and Eqn (4.31)) are compared to numerical results in Fig. 4.3. The parameters Ω and Γ_M have been chosen to be representative of a SiN nanostring [225, 226] ($\Omega/2\pi = 220$ kHz, $\Gamma_M = 195$ mHz) held in a dilution refrigerator such that $\bar{n}_M = 2.8 \times 10^4$ (temperature $T_{B,M} = 300$ mK, *cf.* [39]). Optical dipole traps are readily capable of achieving vibrational frequencies on the order of Ω [6, 227]. The remaining independent[8] parameters appearing in the power

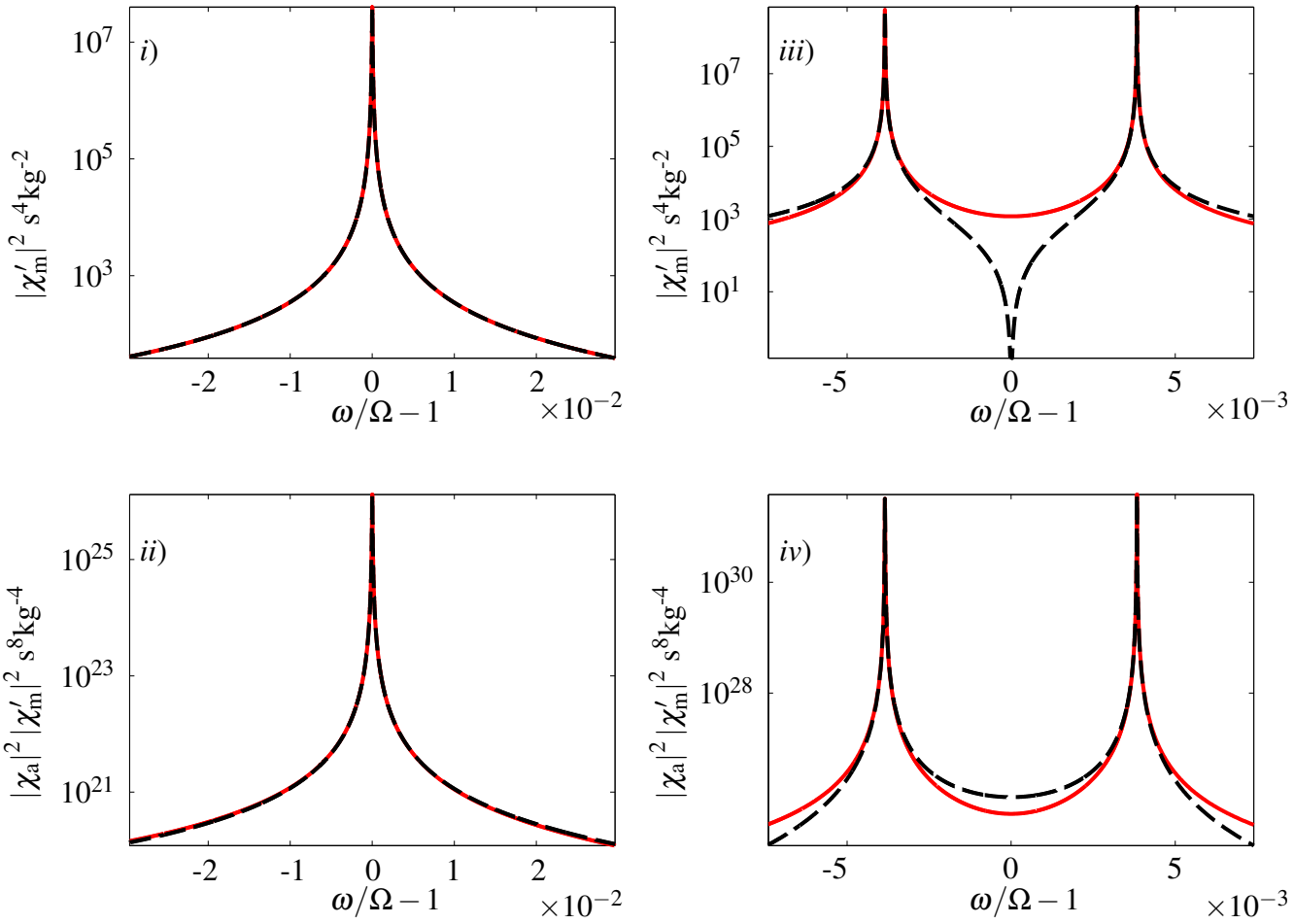

Figure 4.2: Integrands that arise in the calculation of $\langle \hat{x}_{\rm M}^2 \rangle$ in the strong coupling regime. Exact expressions are given in black (dashed) and approximations in red (solid). The coupling rate satisfies $g/\Omega \sim 10^{-3}$ and the frequency scale is normalised and translated such that $\Omega \to 0$. Panels *i*) and *ii*) are calculated with the same parameters as Fig. 4.3 *i*), whilst panels *iii*) and *iv*) draw values from Fig. 4.3 *iii*).

i) In the adiabatic regime the mechanical susceptibility is broadened by the interaction with the atom cloud.

ii) Excitations arriving at the mechanical oscillator through the atomic motion have an approximately Lorentzian spectrum ($|\chi_{\rm A}|^2 |\chi'_{\rm M}|^2$) in the weak coupling limit.

iii) Coherent exchange of excitations between the atoms and mechanics results in the formation of hybrid modes. Their interference suppresses the mechanical response at Ω.

iv) The noise entering the mechanical mode *via* coupling to the atoms is sharply peaked near Ω, but suppression of the mechanical susceptibility in this region (due to interference of the normal modes) ensures that $|\chi_{\rm A}|^2 |\chi'_{\rm M}|^2$ has only two peaks. Our approximation to this integrand is most accurate in the regions with the largest spectral variance.

spectrum are C_A, C_M and Γ_A (with G and η being important when measurement feedback is included). These parameters are discussed further in Table 4.2 and § 4.3.3.

We may now ask whether sympathetic cooling is capable of producing near-ground-state-cooled mechanical oscillators.

Substituting Eqn (4.27) into the ground state criterion (Eqn (4.22)) and using the fact that $\bar{n}_M \gg 1$ yields

$$\bar{n}_M < \left(2+3\frac{\Gamma_M}{\Gamma_A}\right)\bar{n}_{a,\mathrm{eff}} - C_M \tag{4.32}$$

as a sufficient condition for ground state cooling in the adiabatic limit (we have used $c\Gamma_M/\Gamma_A \ll 1$, which holds in this case). Much as the condition $\bar{n}_M < 8C_M$ indicates that the mechanical spectrum must be dominated by radiation pressure fluctuations in order to ground state cool using feedback, Eqn (4.32) shows that *atomic* contributions must dominate in order to sympathetically cool to the ground state.

It is straightforward to show that the region in which Eqn (4.32) is satisfied is a portion of the parameter space where $C > \bar{n}_M$ and $C_A > 1/24$. The condition $C > \bar{n}_M$ is of great importance, as it also dictates whether near-ground-state cooling may be achieved in the strong coupling regime.

Inserting the variance in the hybridised regime (Eqn (4.31)) into the ground state criterion gives an inequality that may only be satisfied if $C = \bar{n}_M$ is reached in the *weak* coupling limit; that is, if near-ground-state cooling is possible in the adiabatic limit then it is also possible in the case of strong coupling[9]. The converse statement is also true; if near-ground-state cooling is *not* possible in the weakly-coupled limit then it is also *not* possible in the hybridised limit (*i.e.* no near-ground cooling if $C = \bar{n}_M$ requires strong coupling).

The physical interpretation of these statements is that the atomic motion must be damped into the zero-temperature bath faster than phonons enter from the hot reservoir, which is entirely consistent with our naïve expectations. Effective steady-state cooling is therefore more difficult to realise in the strongly-coupled case simply because Γ_A is bounded above by $\Omega/2$ (required for stability, *cf.* Eqn (4.12)).

In summary, we have shown that there exist two (slightly overlapping) parameter regimes, summarised in Table 4.1, in which the oscillator is prepared near the quantum ground state.

[8] Of course, the cooperativities *do* depend on the resonance frequency and decay rates: however, it is possible to vary them independently by suitable adjustment of g_A, N, g_M, *etc.*

[9] We imagine tuning between the two regimes by varying C_A and C_M, keeping Γ_A, Γ_M and Ω fixed.

Near-ground cooling	Condition
Sympathetic	$\bar{n}_{\mathrm{M}} < C$ & $1/24 < C_{\mathrm{A}}$ & $\Gamma_{\mathrm{M}}\bar{n}_{\mathrm{M}} \ll \Gamma_{\mathrm{A}}$
Feedback	$\bar{n}_{\mathrm{M}} < (9\eta - 1)\,C_{\mathrm{M}}$
Neither	$\max\{(9\eta - 1)\,C_{\mathrm{M}}, C\} < \bar{n}_{\mathrm{M}}$ or $C_{\mathrm{A}} < 1/24$ or $\Gamma_{\mathrm{A}} \lesssim \Gamma_{\mathrm{M}}\bar{n}_{\mathrm{M}}$

Table 4.1: A summary of the relevant parameter regimes for sympathetic and feedback cooling to near the ground state. In the case that both sympathetic cooling and cold damping are capable of approaching the ground state there exists an overlap region if the feedback efficiency satisfies $1 \geq \eta > \frac{1}{9}\left(1 + \frac{2}{3}\Gamma_{\mathrm{A}}\Gamma_{\mathrm{M}}\bar{n}_{\mathrm{M}}\Omega^{-2}\right)$.

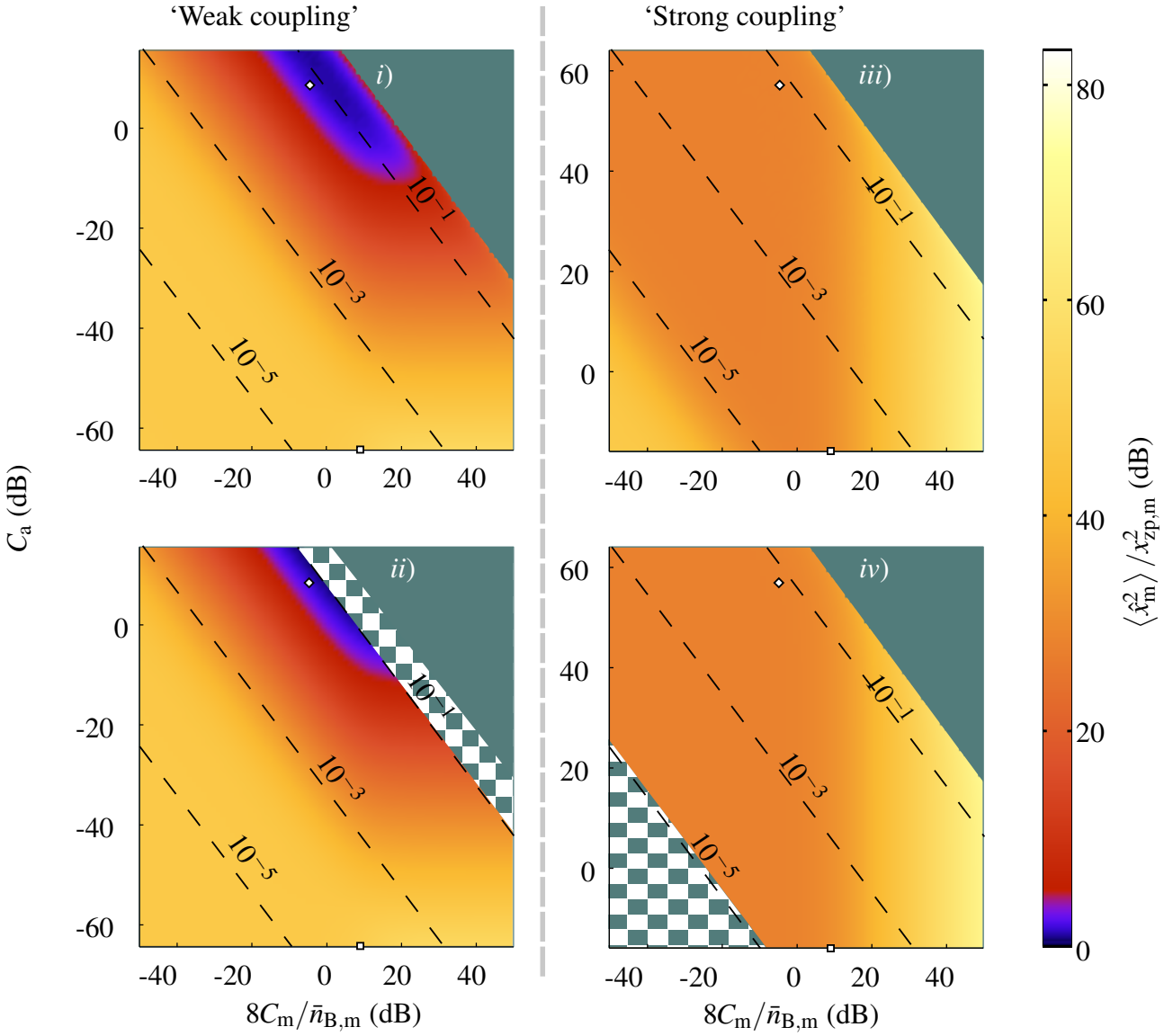

Figure 4.3: The temperature of a micromechanical device sympathetically cooled by coupling to a cold, trapped atomic gas. Purple indicates cooling to near the motional ground state. Contours of equal g/Ω are indicated by dashed lines, and the unstable $g > \Omega/2$ region is coloured teal (*cf.* Eqn (4.12)). The horizontal axis has been normalised (*cf.* Eqn (4.24)). Numerical results are presented in the upper row and the corresponding analytical predictions in the lower. See the text for discussion of the input parameters used. The squares and diamonds indicate feasible experimental parameters (*cf.* Table 4.2).
i) $\Gamma_A = \Omega$. Sympathetic cooling alone is capable of reaching near-ground-state temperatures in the weak coupling regime. Note that the cold 'tongue' protrudes well into the $8C_M > \bar{n}_M$ region in which feedback cooling is also capable of approaching the ground state.
ii) $\Gamma_A = \Omega$. Eqn (4.27) accurately predicts the true steady-state variance in the intended parameter space. In the checked region the system is hybridised *i.e.* strongly coupled.
iii) $\Gamma_A = 1.4 \times 10^{-5}\ \Omega = 10^2\ \Gamma_M$. As discussed in the text, near-ground-state cooling is not possible if the atoms are incapable of dissipating energy faster than it enters from the mechanical system.
iv) $\Gamma_A = 1.4 \times 10^{-5}\ \Omega = 10^2\ \Gamma_M$. A second analytical expression (Eqn (4.31)) is accurate in the strong coupling regime. The equation is invalid in the checked region, which is in fact weakly coupled ($g < \Gamma_A$).

4.3.3 Combined cooling

We now turn our attention to the performance of combined sympathetic and feedback cooling. Both mechanisms act to suppress the leakage of information into the environment; cold damping achieves this explicitly by measurement and feedback, whilst atomic cooling achieves the same effect by diverting a portion of the leakage into the atoms, and thence back to the mechanical system. Our main computational task is therefore to determine the optimum feedback gain to apply for a fixed sympathetic cooling capacity, and to then calculate the new—hopefully reduced—position variance.

The former is typically pushed away from its $C_\mathrm{A} = 0$ value, $G_\mathrm{opt}^{(0)}$, to a new optimum, G_opt. To calculate this gain we analytically differentiate $S_{x_\mathrm{M}x_\mathrm{M}}$ with respect to G, numerically integrate over ω to find $\partial \left\langle x_\mathrm{M}^2 \right\rangle / \partial G$, and apply a numerical root-finding algorithm to determine G_opt.

The results shown in Fig. 4.4 and Fig. 4.5 are calculated in the case of perfect feedback *i.e.* $\eta = 1$: we note that the results with imperfect feedback efficiency are qualitatively the same for $\eta \gtrsim 50\%$ (one essentially need only renormalise the lower axis appropriately), but differ substantially for $\eta \lesssim 15\%$.

These data make it quite clear that, generally speaking, including measurement-based feedback alongside sympathetic cooling significantly decreases the oscillator's temperature. The notable exception to this behaviour is in the parameter space where atoms alone are capable of achieving near-ground-state temperatures ($8C_\mathrm{M} < \bar{n}_\mathrm{M} < C$ & $\Gamma_\mathrm{M}\bar{n}_\mathrm{M} \ll \Gamma_\mathrm{A}$), in which the addition of feedback yields little improvement (~ 0.01 dB improvement). Furthermore, the addition of atoms to the system has negligible impact if feedback cooling to the ground state is possible.

Exemplary experimental parameters are given in Table 4.2; these yield the points denoted by $\square$ and $\diamond$ in Figures 4.3, 4.4 and 4.5.

Ideally, our example mechanical system that operates in the mechanical back-action–dominated regime ($8C_\mathrm{M} > \bar{n}_\mathrm{M}$, left panel of Table 4.2) will reach a final variance of $1.41\,x_\mathrm{ZP,M}^2$ with feedback alone: its thermal variance is $\sim 5 \times 10^4\, x_\mathrm{ZP,M}^2$.

Our suggested hybrid system (right panel of Table 4.2: note that g_M has been adjusted such that $8C_\mathrm{M} < \bar{n}_\mathrm{M}$ *i.e.* cold damping to the ground state is not possible) achieves variances of $1.35\,x_\mathrm{ZP,M}^2$ and $1.33\,x_\mathrm{ZP,M}^2$ in the weakly-coupled regime—with and without feedback, respectively—whilst in the case of strong coupling the (sympathetically-cooled) variance of $603\,x_\mathrm{ZP,M}^2$ may be reduced to a mere $4.79\,x_\mathrm{ZP,M}^2$ by switching on feedback. This is essentially equal to the feedback-only steady-state variance in this regime.

It is encouraging that all of these parameters are within reach of state-of-the-art optomechanical and atomic systems; sympathetic cooling (and/or cold damping) to the mechanical ground state is technically feasible. The experimental challenges lay in combining these heretofore disparate elements and eliminating technical noise (and system-specific noise sources, such as absorptive heating) that we have not considered here.

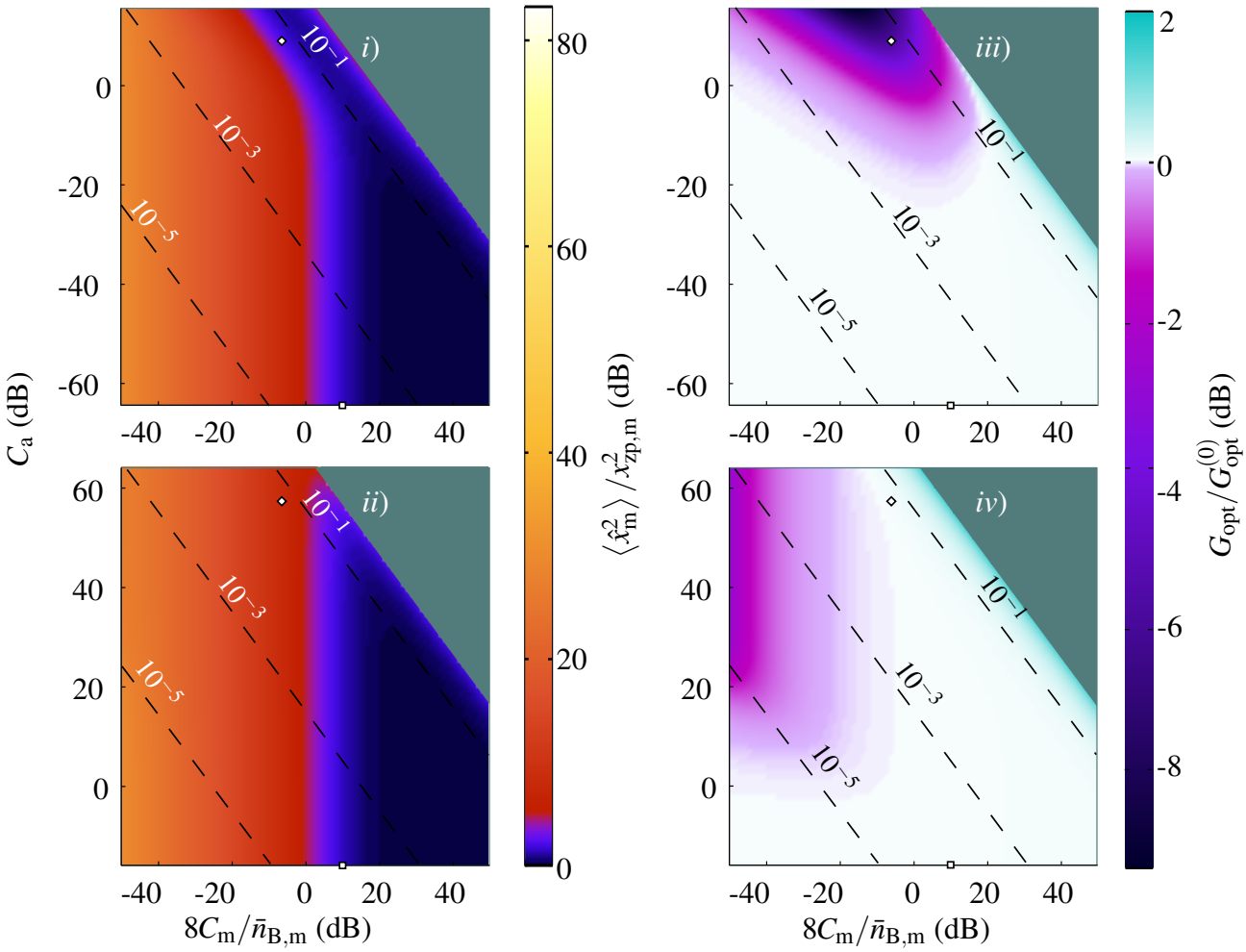

Figure 4.4: The steady-state behaviour of a mechanical device subject to combined sympathetic and feedback cooling ($\eta = 1$). The left column shows numerical calculations of the optimum position variance, and the right displays the corresponding optimised feedback gain ($G_{\rm opt}$) relative to its $C_{\rm A} = 0$ value ($G_{\rm opt}^{(0)}$). Note that the colour scale on panels *i*) and *ii*) matches that of Fig. 4.3, as do the annotations. These results have been truncated near to the instability region because numerical calculations of $\partial \langle \hat{x}_{\rm M}^2 \rangle / \partial G$ become unreliable in this limit. Squares and diamonds indicate achievable experimental parameters, as in Table 4.2.

i) $\Gamma_{\rm A} = \Omega$. Feedback does not significantly alter the optimum temperature in the region where the atoms alone are capable of ground state cooling; however, it is of significant use outside of this area.

ii) $\Gamma_{\rm A} = 1.4 \times 10^{-5}\ \Omega = 10^2\ \Gamma_{\rm M}$. If feedback is introduced in the regime $\Gamma_{\rm M} \sim \Gamma_{\rm A}$ it is possible to reach much smaller variances than with atoms alone.

iii) $\Gamma_{\rm A} = \Omega$. The optimum gain $G_{\rm opt}$ is not appreciably altered from its atom-free value $G_{\rm opt}^{(0)}$ across a wide range of parameters. The dark region in the upper left of the plot indicates that the atoms are dominating cooling in this regime.

iv) $\Gamma_{\rm A} = 1.4 \times 10^{-5}\ \Omega = 10^2\ \Gamma_{\rm M}$. Deviations from $G_{\rm opt}^{(0)}$ occur for low $C_{\rm M}$ because the feedback circuit becomes unable to track the mechanical position with sufficient accuracy. In this regime sympathetic cooling plays an increasingly significant role.

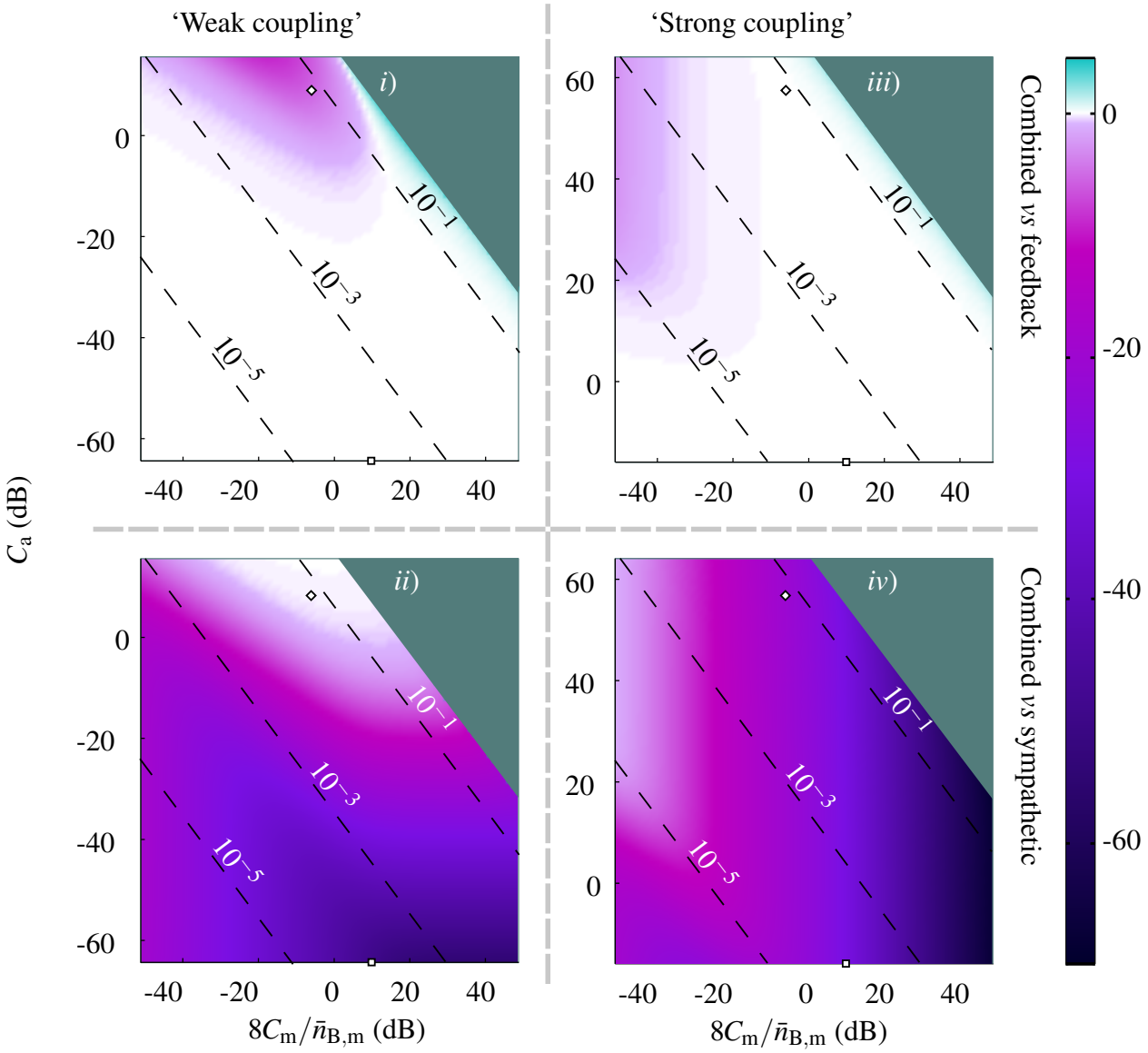

Figure 4.5: A comparison of combined feedback and sympathetic cooling with each mechanism employed individually. The left column shows results in the weakly-coupled regime, with strong on the right. The upper row compares the variance with combined cooling to that with optimised feedback in the absence of atoms (*i.e.* $\left\langle \hat{x}_M^2\left(c, G_{opt}\right)\right\rangle / \left\langle \hat{x}_M^2\left(0, G_{opt}^{(0)}\right)\right\rangle$, in dB), whilst the lower column shows the performance of combined cooling with respect to sympathetic cooling only (*i.e.* $\left\langle \hat{x}_M^2\left(c, G_{opt}\right)\right\rangle / \left\langle \hat{x}_M^2\left(c, 0\right)\right\rangle$, in dB). Feasible experimental parameters (*cf.*Table 4.2) are plotted as squares and diamonds.

i) $\Gamma_A = \Omega$. Addition of atoms in the weakly-coupled regime does allow one to reach temperatures below that achieved by feedback alone, with the greatest impact being for parameter combinations where feedback cooling is incapable of approaching the ground state.

ii) $\Gamma_A = \Omega$. Introducing feedback cooling dramatically reduces the variance everywhere outside of the near-ground-state-cooled area.

iii) $\Gamma_A = 1.4 \times 10^{-5}\ \Omega = 10^2\ \Gamma_M$. The cooling is almost completely dominated by the measurement-based feedback in the strong coupling regime.

iv) $\Gamma_A = 1.4 \times 10^{-5}\ \Omega = 10^2\ \Gamma_M$. The sympathetic damping mechanism contributes most strongly to the combined cooling power of the hybrid system in the low-C_M regime.

Mechanical alone □ *cf.* [226]		Mechanical and atomic ⋄			
$\omega_M/2\pi$	220 kHz	$\omega_M/2\pi$	220 kHz	ω_A	ω_M
$\Gamma_M/2\pi$	31 mHz	$\Gamma_M/2\pi$	31 mHz	Γ_A	$\omega_M\ (10^2\,\Gamma_M)$
M	1.4 ng	M	1.4 ng	m	1.44×10^{-25} kg
κ_{MC}	$20\,\omega_M$	κ_{MC}	$20\,\omega_M$	κ_{AC}	$20\,\omega_M$
α_D	$6.58\times10^6\ \sqrt{\text{Hz}}$	α_D	$6.58\times10^6\ \sqrt{\text{Hz}}$	N	3.1×10^8 [228]
g_m	9.85 MHz/nm	g_m	3.19 MHz/nm	$\Delta_t/2\pi$	-1 GHz [151]
$T_{B,M}$	300 mK [37]	$T_{B,M}$	300 mK [37]	$\mathscr{V}$	2.8×10^{-8} m^3
$8C_M/\bar{n}_M$	9.03 dB	$8C_M/\bar{n}_M$	-4.38 dB	C_A	9.54 (58.1) dB

Table 4.2: Feasible experimental parameters that permit preparation of a mechanical oscillator near its ground state by using sympathetic or feedback cooling.
The mechanical (□) specifications are drawn from the literature concerning evanescently-coupled, high-tension silicon nitride nanostrings (as discussed in § 4.3.2); we have assumed that the damping rate is independent of temperature.
The atomic cavity (⋄) parameters have been chosen to be comparable to those used to construct optical parametric oscillators (*e.g.* cavity length ~ 30 cm, linewidth $\kappa_{AC}/2\pi = 4.4$ MHz). The transverse beam area is drawn from [6] and the detuning estimated according to [151]. We have used the transition wavelength and dipole moment of the ^{87}Rb D2 line *cf.* [151]. Values in parentheses are valid in the small Γ_A limit. It is possible to prepare large numbers of atoms in their motional ground state (*e.g.* using Raman cooling in a three-dimensional optical lattice) [228].
See § 4.3.3 for discussion of the final temperatures achieved using these specifications.

4.4 Conclusion

We have modelled steady-state cooling of a low-frequency mechanical oscillator using the combined effects of optical coupling to a remote atomic ensemble and measurement-based feedback. Combining these two methods is beneficial in all circumstances, although there exist distinct regions of parameter space (*cf.* Table 4.1) in which one technique or the other dominates the cooling. We have also demonstrated that an optically-mediated state swap between the two mechanical degrees of freedom (*i.e.* sympathetic cooling to the ground state) may be performed even in the case that $\bar{n}_M < C_M$, in which a complete mechanical $\leftrightarrow$ optical swap is forbidden. Both sympathetic and feedback cooling to the ground state are feasible with current experimental parameters.

Chapter 5

A quantum optomechanical interface beyond the resolved sideband limit

The work presented in this chapter has been published by IOP Publishing;
J. S. Bennett, K. Khosla, L. S. Madsen, M. R. Vanner, H. Rubinsztein-Dunlop, and W. P. Bowen, A quantum optomechanical interface beyond the resolved sideband limit, *New Journal of Physics* 18, 053030, 2016

Mechanical oscillators that respond to radiation pressure are a promising means of transferring quantum information between light and matter. Optical–mechanical state swaps are a key operation in this setting. Existing proposals for optomechanical arbitrary state swap interfaces are only effective in the resolved sideband limit. Here, we show that it is possible to fully and deterministically exchange mechanical and optical states outside of this limit, in the common case that the cavity linewidth is larger than the mechanical resonance frequency. This high-bandwidth interface opens up a significantly larger region of optomechanical parameter space, allowing generation of non-classical motional states of high-quality, low-frequency mechanical oscillators.

5.1 Introduction

Quantum interfaces are anticipated to form a crucial component of future quantum information networks due to their ability to transfer quantum information between 'flying' carriers—photons—and 'stationary' quantum media [105, 179]. Numerous physical settings lend themselves to creating such interfaces, including both warm and cold neutral atoms [143, 229], quantum dots [230, 231], nitrogen–vacancy (and other) colour centres [232, 233] and trapped ions [234, 235].

Cavity optomechanical systems are a promising platform for novel quantum interfaces because they may be used to couple light to the 'stationary' media listed above, and because existing mechanical oscillators have extremely long decay times (~ 30 s, *e.g.* [226]). In these systems a mechanical degree of freedom with (angular) frequency ω_{M} is parametrically coupled to an optical cavity with linewidth κ. These devices have entered the quantum regime for the first time in recent years (*e.g.* [15–17, 26])

and they are set to find technological and research applications in a variety of capacities. For instance, a mechanical oscillator that is subject to radiation pressure arising from microwave and optical modes simultaneously may be used to couple superconducting circuits to optics [182, 236–240]; the capability to do this at the quantum level would permit construction of quantum information networks that utilise the advantages of both low-loss optical transmission and the exquisite quantum control of superconducting circuits. There are also a wealth of proposals for employing cavity optomechanical coupling to prepare massive mechanical oscillators in non-classical states, which could allow sensitive probing of the quantum-to-classical transition [26] or quantum-enhanced metrology (*e.g.* mass sensing [28], accelerometry [29]).

In many of these applications it is expedient to employ a low-frequency mechanical oscillator (*e.g.* [31]); for instance, devices with material-limited damping rates Γ obey the scaling $\Gamma \propto \omega_{\mathrm{M}}^2$ (due to the Akhiezer effect [32]). Furthermore, large optomechanical coupling rates require small cavity volumes, and the optical linewidth typically scales inversely with its length, so that κ is often unavoidably larger than ω_{M} in micro- and nano-optomechanical devices. This high-bandwidth operating regime, $\kappa \gg \omega_{\mathrm{M}}$, is known as the *unresolved sideband limit* or *bad-cavity limit*, despite the fact that the cavities involved often have large Q factors.

Current technologies make it possible to cool a mechanical oscillator to near its ground state in the unresolved sideband limit using optical measurement-based feedback cooling (*e.g.* [119]), or to perform steady-state cooling using hybrid quantum systems [1, 152, 241], dissipative optomechanics [168], optomechanically-induced transparency [112], and related schemes (*e.g.* [242,243]). Very rapid ground state cooling of the mechanical oscillator is also enabled by varying the optical drive's amplitude and phase dynamically [89, 99, 154, 158, 160]. Alternatively, one may exploit the large cavity bandwidth in the bad-cavity limit to engineer quantum non-demolition (QND) interactions between short optical pulses and a mechanical oscillator (*cf.* (2.19)) [154]. QND interactions are the basis of proposed quantum 'upload' interfaces, which write the state of one input mode onto one output mode [244–246]. Further applications of QND interactions include generation of mechanical geometric phases [160], and cooling by measurement and state tomography [158].

Despite this—and the success of optomechanical interfaces in the 'resolved sideband' ($\kappa \ll \omega_{\mathrm{M}}$), regime (*e.g.* [15, 16, 73, 84, 87, 247])—there are currently no quantum optical–to–mechanical interfaces that permit a state swap in the unresolved sideband limit. Teleportation schemes [248] and the aforementioned quantum 'upload' interfaces [244, 245], which transfer an input state from one degree of freedom to another, are incapable of directly exchanging two input states.

Here we present a *bidirectional* optomechanical interface that can perform a quantum state swap and other operations in the unresolved sideband limit. Our interface is completely deterministic and does not rely on measurement or any form of conditioning or post-selection. Furthermore, the proposed protocol only requires classical open-loop control, which may be performed with very low added noise (*i.e.* below the back-action noise) [156].

We predict that the interface is capable of performing a number of important operations, including mechanical ground state cooling, squeezing, and exploiting non-Gaussian optical inputs to create

Wigner-negative mechanical states, including low-amplitude Schrödinger cat ('kitten') states.

5.2 Pulsed QND interaction

Deep sub-mechanical-period optical pulses can interact with an optomechanical system to generate a quantum non-demolition (QND) interaction between the optical and mechanical components [154]. The theory underpinning this was outlined in § 2.3.4.

For the purposes of this chapter we will require some slight generalisations. We will redefine the amplitude fluctuations operator as

$$\check{X}_{\mathrm{L}}(t) = \frac{\alpha(t)\,\delta a^{\dagger}(t) + \alpha^{*}(t)\,a(t)}{|\alpha(t)|},$$

and the conjugate (phase) fluctuations as

$$\check{P}_{\mathrm{L}}(t) = \mathrm{i}\frac{\alpha(t)\,\delta a^{\dagger}(t) - \alpha^{*}(t)\,a(t)}{|\alpha(t)|}.$$

These zero-mean operators reduce to the definitions given in § 2.3.4 when $\alpha(t) \in \mathbb{R}$. When $\alpha(t)$ is not real these new definitions ensure that $\check{X}_{\mathrm{L}}(t)$ and $\check{P}_{\mathrm{L}}(t)$ retain their physical interpretations as the amplitude and phase fluctuations parallel and perpendicular to the 'stick' in a ball-and-stick diagram. This ensures that the fluctuations transform correctly when the optical state is displaced—as in Fig. 5.1 panel *ii*)—which will be important in our model.

Following the same procedure as outlined in § 2.3.4, we arrive at the standard QND interaction between the mechanical oscillator and the collective quadratures of the optical pulse, reproduced here for convenience;

$$X'_{\mathrm{M}} = X_{\mathrm{M}}, \qquad P'_{\mathrm{M}} = P_{\mathrm{M}} + \chi X_{\mathrm{L}}, \tag{5.1a}$$

$$X'_{\mathrm{L}} = X_{\mathrm{L}}, \qquad P'_{\mathrm{L}} = P_{\mathrm{L}} + \chi X_{\mathrm{M}}. \tag{5.1b}$$

The coupling strength is

$$\chi = \frac{-8g_0\sqrt{N}}{\kappa}$$

where N is the mean number of photons in the pulse envelope. As before, the collective pulse quadratures are the amplitude-weighted averages of the instantaneous cavity quadratures over the duration of the pulse. We have also implicitly included an open-loop displacement operation that cancels the mean impulse on the mechanical oscillator.

5.3 Basic protocol

A QND interaction correlates each oscillator with the other, but only one quadrature at a time; evidently some extra ingredients will be required to perform a complete state swap. We will first show how to use a sequence of QND interactions and local operations to realize a state swap under ideal conditions. Secondly, we will generalise our protocol to allow both state transfer and squeezing.

In our approach the pulse enters and leaves the optomechanical cavity multiple times, with local operations on the pulse and mechanical resonator occurring between the optomechanical interactions. Figure 5.1 summarises the necessary steps, as presented below, graphically. This approach is in the spirit of the proposal of [244, 245]; however, our protocol replaces measurement and feedback with a third QND interaction to achieve a two-way interface.

Firstly, consider the case in which $\chi = -1$ and there are no optical or mechanical decoherence mechanisms. From (2.19) it is clear that a single QND pulse correlates $P'_{\rm M}$ ($P'_{\rm L}$) with $X_{\rm L}$ ($X_{\rm M}$). In order to build the necessary correlations between the other pair of quadratures we must exchange $X'_{\rm M}$ ($X'_{\rm L}$) and $P'_{\rm M}$ ($P'_{\rm L}$). This may be achieved by local $\pi/2$ rotations on each mode.

For definiteness, we can consider the local rotations to be generated in the following manner. Delay the pulse for a quarter of a mechanical period before re-injecting it into the cavity to achieve a mechanical rotation of $\pi/2$. The optical amplitude and phase noise rotations may be generated by *displacing* the optical state in phase space, as demonstrated in Fig. 5.1 (panel *ii*), *e.g.* by interfering the pulse with a very bright, temporally matched pulse on a highly asymmetric beamsplitter (*cf.* Fig. 5.1, panel *iii*). For instance, consider the special case of a displacement sending the mean amplitude α to $\mathrm{i}\alpha$; this yields the transformation

$$\begin{aligned} X_{\rm L} &\rightarrow P_{\rm L}, \\ P_{\rm L} &\rightarrow -X_{\rm L}, \end{aligned}$$

which is precisely a $\pi/2$ *rotation* of the noise (by contrast, a rotation of the optical field leaves the noise unchanged, because the fluctuations are also rotated). Given that the noise associated with this operation may be made arbitrarily small in principle (by selecting an extreme asymmetry and applying a more powerful displacement pulse) we will neglect it, or else absorb it into the total efficiency $\eta_{\rm L}$ defined in § 5.4.1.

If we apply these rotations and then allow the pulse and oscillator to interact for a second time the quadratures have been transformed according to

$$X'_{\rm M} = P_{\rm M} - X_{\rm L}, \qquad P'_{\rm M} = -P_{\rm L}, \tag{5.2a}$$

$$X'_{\rm L} = P_{\rm L} - X_{\rm M}, \qquad P'_{\rm L} = -P_{\rm M}. \tag{5.2b}$$

The momentum quadratures have been entirely swapped, as desired, because the contribution of the initial mechanical position to $P'_{\rm M}$ due to free evolution has been coherently cancelled by the contribution of $X'_{\rm L}$ (which depends on the initial position) from the QND interaction. However, it is clear that $X'_{\rm M}$ ($X'_{\rm L}$) still retains some 'memory' of the initial momentum $P_{\rm M}$ ($P_{\rm L}$) of the mechanical (optical) oscillator; this needs to be erased for the swap to be completed. Fortunately, this can be achieved by a second pair of $\pi/2$ rotations and a third QND interaction, *viz.*

$$X'_{\rm M} = -P_{\rm L}, \qquad P'_{\rm M} = X_{\rm L}, \tag{5.3a}$$

$$X'_{\rm L} = -P_{\rm M}, \qquad P'_{\rm L} = X_{\rm M}. \tag{5.3b}$$

This is a perfect state swap, up to local rotations (which we shall not consider), because the mechanical system now carries only fluctuations from the initial optical state, and *vice versa*.

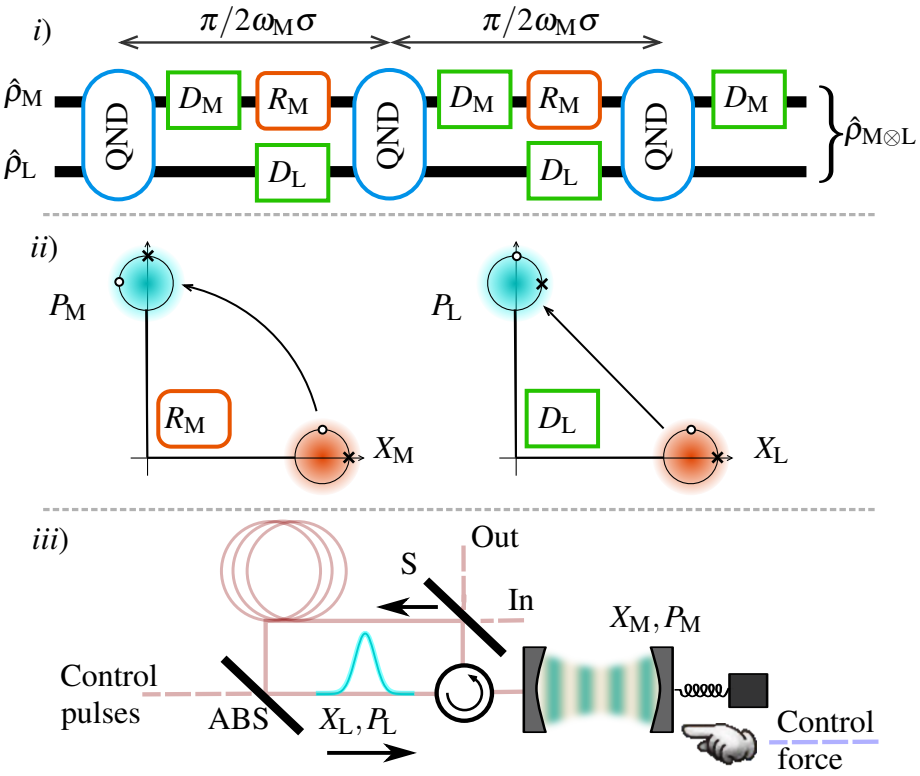

Figure 5.1: Schematic of our pulsed optomechanical interface.
i) Quantum circuit representation (operations proceeding from left to right). The input density operator is separable, $\hat{\rho} = \hat{\rho}_M \otimes \hat{\rho}_L$. An open-loop mechanical displacement (D_M) negates the classical momentum kick imparted by the mean amplitude of the pulse during the quantum non-demolition (QND) interaction. R_M denotes a $\pi/2$ mechanical rotation (under free evolution) and D_L is the matching optical displacement (noise rotation). Immediately before the second QND interaction the state of each oscillator is correlated with both inputs ($\hat{\rho}_M$ & $\hat{\rho}_L$). In the ideal case the final QND interaction separates the output into the form $\hat{\rho} = \hat{\rho}_L \otimes \hat{\rho}_M$, but in general the output state need not be separable.
ii) Illustration of the effect of R_M and D_L on Gaussian states. Each 'ball & stick' represents a noise ellipse of the state's Wigner function. R_M rotates the entire state (shown with non-zero mean amplitude for clarity). D_L is a displacement of the optical state; note, however, that it effectively rotates the noise quadratures relative to the mean amplitude. The initial amplitude quadrature is marked by a cross, and the initial phase quadrature by a circle.
iii) A potential physical architecture for the interface. The pulse carrying the initial optical quadratures is injected at the switch (upper right, S) and circulates counter-clockwise. After a QND interaction with the optomechanical cavity (centre) it is coupled into a delay arm via the switch and held for a quarter of a mechanical period. The pulse then encounters a bright, temporally-matched coherent pulse at the asymmetric beamsplitter (ABS, lower left), which perform a displacement of the pulse (rotation of the optical noise). This process repeats. After the final QND interaction the switch is opened and the output pulse leaves the interface.

5.4 Decoherence mechanisms

The fundamental limits on the interface's performance are imposed by optical loss and thermomechanical noise.

5.4.1 Optical loss

Optical losses due to inefficiencies within the recirculating loop may be partially compensated by altering the magnitude and phase angle of the displacement pulse, but contamination of the fluctuation quadratures by vacuum noise cannot be reversed. Losses may be modelled by coupling the circulating pulse to a vacuum bath on a beamsplitter with efficiency $\eta_{\rm L}$ (unity for perfect operation). The resulting nonhomogeneous evolution is

$$X_{\rm L} \rightarrow \sqrt{\eta_{\rm L}}\, X_{\rm L} + \sqrt{1-\eta_{\rm L}}\, X_{\rm V},$$

where $X_{\rm V}$ is vacuum noise. An analogous relation holds for $P_{\rm L}$. The properties of the vacuum mode are $\langle X_{\rm V}^2 \rangle = \langle P_{\rm V}^2 \rangle = 1$ and $\langle X_{\rm V} P_{\rm V} \rangle_{\rm S} = 0$. Here we have introduced the symmetrised expectation value, $\langle X_{\rm V} P_{\rm V} \rangle_{\rm S} = \frac{1}{2} \langle X_{\rm V} P_{\rm V} + P_{\rm V} X_{\rm V} \rangle = \Re \{ \langle X_{\rm V} P_{\rm V} \rangle \}$.

5.4.2 Damped mechanical evolution (rotation)

Mechanical decoherence is induced by two intimately related mechanisms: loss of energy from the oscillator into a heat bath, and random excitation of the oscillator by the bath. These processes may be described by the Langevin equations for the damped evolution (*cf.* [249]),

$$\dot{X}_{\rm M} = +\omega_{\rm M} P_{\rm M} \tag{5.4a}$$

$$\dot{P}_{\rm M} = -\omega_{\rm M} X_{\rm M} + \sqrt{2\Gamma}\, \hat{\xi} - \Gamma P_{\rm M}. \tag{5.4b}$$

Momentum-dependent damping occurs at a rate Γ whilst excitations enter via the random force $\hat{\xi}$ at a rate of $\Gamma \times (\bar{n}_{\rm H} + 1/2)$, where $\bar{n}_{\rm H}$ is the equilibrium occupancy of the oscillator, related to the bath temperature T through the Bose-Einstein distribution (hence $\bar{n}_{\rm H} \approx k_{\rm B} T / \hbar \omega_{\rm M}$ for large temperatures).

A full treatment of these equations is given in § 3.4.1.

Position and momentum after a quarter cycle

When evaluated after a quarter of a mechanical cycle ($X_{\rm M}$ and $P_{\rm M}$ in the following expressions are implicitly evaluated at time zero; $X'_{\rm M}$, $P'_{\rm M}$, $\Delta X_{\rm M}$ and $\Delta P_{\rm M}$ are evaluated at time $t = \pi / 2\omega_{\rm M}\sigma$) we obtain

$$X'_{\rm M} = \sqrt{\eta_{\rm M}} \left[\varepsilon X_{\rm M} + \frac{1}{\sigma} P_{\rm M} + \Delta X_{\rm M} \right],$$

$$P'_{\rm M} = \sqrt{\eta_{\rm M}} \left[-\varepsilon P_{\rm M} - \frac{1}{\sigma} X_{\rm M} + \Delta P_{\rm M} \right].$$

The noise increments $\Delta X_{\rm M}$ and $\Delta P_{\rm M}$ are defined by Eqn (3.22). Non-zero mechanical damping has reduced the mechanical resonance frequency to $\omega_{\rm M}\sigma$, where

$$\sigma = \sqrt{1 - (\Gamma / 2\omega_{\rm M})^2}$$

$$= \left(1 + \varepsilon^2\right)^{-1/2} \leq 1,$$

with $\varepsilon = \Gamma / 2\omega_{\rm M}\sigma$ (we assume that the oscillator is underdamped throughout) being a small parameter in the high-$Q_{\rm M}$ limit ($Q_{\rm M} \approx \omega_{\rm M}/\Gamma \gg 1$ in typical optomechanics experiments).

The following commutators apply;

$$\begin{aligned}
[\Delta X_{\rm M}, \Delta P_{\rm M}] &= 2{\rm i}\left(\eta_{\rm M}^{-1} - 1\right), \\
[X_{\rm M}, \Delta X_{\rm M}] &= [X_{\rm M}, \Delta P_{\rm M}] = 0, \\
[P_{\rm M}, \Delta X_{\rm M}] &= +2{\rm i}\varepsilon, \\
[P_{\rm M}, \Delta P_{\rm M}] &= -2{\rm i}\sigma\varepsilon^2.
\end{aligned}$$

The efficiency $\eta_{\rm M} = \exp\{-\pi\varepsilon\}$ is approximately the amount by which a coherent excitation of the oscillator decays over the course of one quarter mechanical period: for an initial coherent excitation amplitude β we have $|\beta|^2 \rightarrow \eta_{\rm M}\left(1/\sigma^2 + \varepsilon^2\right)|\beta|^2 = \eta_{\rm M}\left(1 + 2\varepsilon^2\right)|\beta|^2$, which is approximately $\eta_{\rm M}|\beta|^2$ for high-$Q_{\rm M}$ oscillators.

5.4.3 Pulse absorption

We close this section with some remarks about achieving $\chi = -1$ in the face of experimental imperfections and decoherence. Firstly, we wish to emphasise that many recent pulsed optomechanics experiments have entered a closely-related regime where the optomechanical cooperativity (see Eqn (5.13)) exceeds $\bar{n}_{\rm H}$ (*e.g.* [93, 183]). The essential difference is that our scheme simultaneously requires $\kappa \sim g_0\sqrt{N}$ to be satisfied, implying that $g_0\sqrt{N} \gg \omega_{\rm M}$. This necessitates the use of a very large number of pulse photons, because we are by assumption operating with $g_0 \ll \omega_{\rm M}$ and $\omega_{\rm M} \ll \kappa$. Such high-$N$ pulses could be readily generated by acousto-optic or electro-optic (*e.g.* [158]) modulation of a pump beam over the timescales relevant to our scheme. For example, a pulse lasting 1% of a mechanical period at $\omega_{\rm M}/2\pi = 100.2$ kHz requires an average power of ~ 10 mW to reach $N \sim 10^9$ (*cf.* example experimental parameters given in Table 5.1). The chief technical issue expected to be encountered in this large N limit is heating due to optical absorption, which is often a problem in continuous-wave optomechanics experiments.

Here we show that our scheme does not suffer from significant heating due to absorption (see § 5.4) by considering an explicit potential realisation. We model a microstring mechanical resonator of thickness $t_{\rm R} = 54$ nm, width $w_{\rm R} = 10$ μm and length $\ell_{\rm R} = 1$ mm; such devices may be fabricated from silicon nitride (*cf.* Table 5.1) [165]. Note that all of the parameters below have been realised in existing experiments.

Using the formula for the absorption of a dielectric plate given by [250] (Eqn (3.7) thereof) and the measured imaginary refractive index of SiN [251] we estimate that the fraction of incident power absorbed by the oscillator is $f \sim 10^{-5}$. The energy deposited into the resonator by a single pulse is therefore $E \approx \hbar\omega_{\rm p} f N 2\mathscr{F}/\pi$, where $\mathscr{F}$ is the cavity finesse (*cf.* [151]) and $\omega_{\rm p}$ is the pulse's central frequency. We have taken the energy of a pulse photon to be $\hbar\omega_{\rm p}$, ignoring its spectral width.

It takes a characteristic time for thermal energy deposited at the centre of the string to leave, given by $\omega_{\rm th}^{-1} = \rho_{\rm R} c_{\rm R} \ell_{\rm R}^2/\kappa_{\rm th}$, where $\rho_{\rm R}$ is the device's mass density, $c_{\rm R}$ is its specific heat capacity and $\kappa_{\rm th}$ is its thermal conductivity. We take $\rho_{\rm R} = 3.18 \times 10^3$ kg m^{-3}, $c_{\rm R} = 711$ J kg^{-1} K^{-1} and $\kappa_{\rm th} = 150$ W m^{-1} K^{-1} (values for Si_3N_4 taken from [252], tables 40, 88 and 104). Given the geometry

Table 5.1: Exemplary parameters for use with the three-pulse protocol, taken from existing experiments. The mechanical frequency $\omega_{\rm M}$, zero-point coupling rate g_0 and optical linewidth κ are taken from silicon nitride microstring resonators evanescently coupled to silica microsphere whispering gallery modes [165]; the decay rate Γ of comparable oscillators has previously been observed to be as low $2\pi \times 31$ mHz [160, 226]. With these specifications and a bath temperature of 4 K the oscillator may be ground state cooled ($\langle \hat{n}'_{\rm M} \rangle = 0.606$). Reducing the bath temperature to 50 mK (*e.g.* [253]) would permit $\langle \hat{n}'_{\rm M} \rangle = 0.008$ and preparation of the $|1\rangle$ motional state with infidelity $1 - \mathscr{F} = 2.3\%$.

Mechanical frequency	$\omega_{\rm M}/2\pi$	100.2 kHz	Mechanical decay	$\Gamma/2\pi$	31 mHz
Cavity linewidth	$\kappa/2\pi$	25.6 MHz	Optomechanical coupling	$g_0/2\pi$	75 Hz
Photon number	N	7.28×10^9	Cooperativity	C	7.72×10^5
Bath temperature	T	$\begin{cases} 4\text{ K} \\ 50\text{ mK} \end{cases}$	Bath occupancy	$\bar{n}_{\rm H}$	$\begin{cases} 8.32 \times 10^5 \\ 1.04 \times 10^4 \end{cases}$

described here, $\omega_{\rm M} \gg \omega_{\rm th} \approx 260$ Hz. This means that we may treat the dynamics of the heat distribution as very slow compared to the mechanical motion of interest.

During the full protocol time of half a mechanical period, thermal energy deposited at the centre of the string has propagated a distance (root-mean-squared) of $L = \sqrt{2\pi\kappa_{\rm th}/\rho_{\rm R} c_{\rm R} \omega_{\rm M}}$. Thus the volume of heated material may be approximated as $V_{\rm R} \approx t_{\rm R} w_{\rm R} L$. The resulting change in temperature of the material over this volume is $\delta T = E/\pi\rho_{\rm R} c_{\rm R} V_{\rm R}$. As a consequence, the occupancy of the bath seen by the mechanical mode changes by (at worst)

$$\begin{aligned} \delta\bar{n}_{\rm H} &= 3k_{\rm B}\delta T/\hbar\omega_{\rm M} \\ &= 3\frac{2fk_{\rm B}\omega_{\rm p}\mathscr{F}}{\pi^2\omega_{\rm M}\rho_{\rm R}c_{\rm R}V_{\rm R}}N. \end{aligned}$$

The overall factor of three accounts for the fact that there are three pulses.

If we employ a pulse with photons at a central wavelength of 1559 nm [165] we obtain $\delta\bar{n}_{\rm H} \approx 10^{-9} \times \mathscr{F}N$. Thus for a finesse of 100 and photon number as in Table 5.1 the change in the effective bath occupancy is approximately 10% at 50 mK.

This result is in many ways a worst-case scenario. Firstly, the change in temperature seen by the mode of interest is likely to be lower than calculated here because the mode extends over a larger region of the string. Secondly, alternative resonator geometries (which are not long and thin) can permit much lower $\delta\bar{n}_{\rm H}$ because of their larger volume and faster thermal diffusion times. We are therefore confident that heating will not (in principle) prevent one from achieving $\chi = -1$.

5.5 Extended model

The three-pulse protocol introduced above may easily be generalised to the case in which the pulses have unequal interaction strengths, which we shall denote by $\chi^{(j)}$ where $j = 1, 2, 3$ labels each pulse. This could be arranged by using the control (displacement) pulses to alter the mean number of envelope photons $N^{(j)}$ between QND interactions.

A single QND interaction (including open loop displacement of the mechanics) may be written as

$$\boldsymbol{X} \to M^{(j)}_{\rm QND}\boldsymbol{X}$$

with

$$M_{\mathrm{QND}}^{(j)} = \begin{pmatrix} 1 & 0 & 0 & 0 \\ 0 & 1 & \chi^{(j)} & 0 \\ 0 & 0 & 1 & 0 \\ \chi^{(j)} & 0 & 0 & 1 \end{pmatrix},$$

and $\boldsymbol{X} = (X_{\mathrm{M}}, P_{\mathrm{M}}, X_{\mathrm{L}}, P_{\mathrm{L}})^{\mathrm{T}}$.

The evolution induced by a single pulse–displace–delay cycle may then be expressed as a nonhomogeneous linear equation

$$\boldsymbol{X} \to M^{(j)}\boldsymbol{X} + \boldsymbol{F}^{(j)}$$

where $M^{(j)}$ is a square matrix characterised by the interaction strength $\chi^{(j)} = \frac{-8g_0\sqrt{N^{(j)}}}{\kappa}$ and the efficiencies η_{L} and η_{M};

$$M^{(j)} = \begin{pmatrix} \varepsilon\sqrt{\eta_{\mathrm{M}}} & \sqrt{\eta_{\mathrm{M}}}/\sigma & \sqrt{\eta_{\mathrm{M}}}\,\chi^{(j)}/\sigma & 0 \\ -\sqrt{\eta_{\mathrm{M}}}/\sigma & -\varepsilon\sqrt{\eta_{\mathrm{M}}} & -\varepsilon\chi^{(j)}\sqrt{\eta_{\mathrm{M}}} & 0 \\ \sqrt{\eta_{\mathrm{L}}}\,\chi^{(j)} & 0 & 0 & \sqrt{\eta_{\mathrm{L}}} \\ 0 & 0 & -\sqrt{\eta_{\mathrm{L}}} & 0 \end{pmatrix}.$$

The inhomogeneous term corresponds to thermal and vacuum noises; $\boldsymbol{F}^{(j)} = \boldsymbol{f}^{(j)} + (1-\eta_{\mathrm{L}})\,\boldsymbol{v}^{(j)}$ where

$$\boldsymbol{f}^{(j)} = \sqrt{\eta_{\mathrm{M}}}\,\left(\Delta X_{\mathrm{M}}^{(j)},\, \Delta P_{\mathrm{M}}^{(j)},\, 0,\, 0\right)^{\mathrm{T}}$$

and

$$\boldsymbol{v}^{(j)} = \left(0,\, 0,\, X_{\mathrm{V}}^{(j)},\, P_{\mathrm{V}}^{(j)}\right)^{\mathrm{T}}$$

in which $X_{\mathrm{V}}^{(j)}$ ($P_{\mathrm{V}}^{(j)}$) are vacuum noise operators and $\Delta X_{\mathrm{M}}^{(j)}$ and $\Delta P_{\mathrm{M}}^{(j)}$ are evaluated at $t = \pi/2\omega_{\mathrm{M}}\sigma$ (*i.e.* at one-quarter mechanical period).

The noise has the following covariance, with other terms vanishing;

$$\begin{aligned}
\left\langle \Delta X_{\mathrm{M}}^{(j)} \Delta X_{\mathrm{M}}^{(k)} \right\rangle &= \left\langle \Delta P_{\mathrm{M}}^{(j)} \Delta P_{\mathrm{M}}^{(k)} \right\rangle \\
&= \delta_{\mathrm{j,k}}\,(2\bar{n}_{\mathrm{H}}+1)\left(\frac{1}{\eta_{\mathrm{M}}} - 1 - 2\varepsilon^2\right), \\
\left\langle \Delta X_{\mathrm{M}}^{(j)} \Delta P_{\mathrm{M}}^{(k)} \right\rangle_{\mathrm{S}} &= 4\delta_{\mathrm{j,k}}\,(2\bar{n}_{\mathrm{H}}+1)\,\frac{\varepsilon}{\sigma}, \\
\left\langle X_{\mathrm{V}}^{(j)} X_{\mathrm{V}}^{(k)} \right\rangle &= \left\langle P_{\mathrm{V}}^{(j)} P_{\mathrm{V}}^{(k)} \right\rangle \\
&= \delta_{\mathrm{j,k}}, \\
\left\langle X_{\mathrm{V}}^{(j)} P_{\mathrm{V}}^{(k)} \right\rangle_{\mathrm{S}} &= 0.
\end{aligned}$$

$\delta_{\mathrm{j,k}}$ is the Kronecker delta.

The complete transformation between initial and final quadratures is found by chaining the above operations together (remembering that the final pulsed interaction is not followed by a rotation & optical displacement). The resulting nonhomogeneous linear map is

$$\boldsymbol{X}' = M\boldsymbol{X} + \boldsymbol{F}, \tag{5.5}$$

where the explicit matrix form of $M = M^{(3)}_{\rm QND}\, M^{(2)}\, M^{(1)}$ is

$$\begin{pmatrix} \mu^{(1)} - \eta_{\rm M} & 0 & 0 & -\mu^{(2)} \\ \varepsilon\sigma\left[\mu^{(3)} - \mu^{(1)}\right] & \mu^{(3)} - \eta_{\rm M} & \frac{1}{\mu^{(2)}}\left[\eta_{\rm L}\mu^{(3)} + \mu^{(1)}\left(\eta_{\rm M} - \mu^{(3)}\right)\right] & \mu^{(2)}\varepsilon\sigma \\ -\mu^{(2)}\varepsilon\sigma & -\mu^{(2)} & \mu^{(1)} - \eta_{\rm L} & 0 \\ \frac{1}{\mu^{(2)}}\left[\eta_{\rm M}\mu^{(3)} + \mu^{(1)}\left(\eta_{\rm L} - \mu^{(3)}\right)\right] & 0 & 0 & \mu^{(3)} - \eta_{\rm L} \end{pmatrix}, \tag{5.6}$$

and

$$\boldsymbol{F} = M^{(3)}_{\rm QND}\left[M^{(2)}\,\boldsymbol{F}^{(1)} + \boldsymbol{F}^{(2)}\right].$$

Here we have introduced the 'pulse strengths' $\mu^{(j)}$, which take into account the level of decoherence present; they are given by

$$\begin{aligned} \mu^{(1)} &= -\chi^{(1)}\,\mu^{(2)}, \\ \mu^{(2)} &= -\sqrt{\eta_{\rm L}\eta_{\rm M}}\;\chi^{(2)}/\sigma, \\ \mu^{(3)} &= -\chi^{(3)}\,\mu^{(2)}. \end{aligned}$$

Note that in the absence of decoherence the perfect state swap is achieved when $\mu^{(j)} = 1\ \forall\ j$. This makes the anti-diagonal elements of M equal to ± 1, whilst simultaneously setting the diagonal blocks—which determine how incomplete the swap is—to zero.

In what follows we will restrict ourselves to the case in which the optical and mechanical modes are initially separable and zero-mean ($\langle \boldsymbol{X} \rangle = \boldsymbol{0}$). Note that the latter may always be arranged by local operations on the input states, and that the mean amplitudes are unchanged by the interface.

Before continuing, it is instructive to consider the form of M in some ideal cases.

State swap

Setting $\mu^{(j)} = 1$ with no decoherence ($\varepsilon = 0$, $\eta_{\rm M} = \eta_{\rm L} = 1$) yields

$$M = \begin{pmatrix} 0 & 0 & 0 & -1 \\ 0 & 0 & 1 & 0 \\ 0 & -1 & 0 & 0 \\ 1 & 0 & 0 & 0 \end{pmatrix}. \tag{5.7}$$

Squeezed state swap

Setting $\mu^{(1,3)} = 1$ with no decoherence gives

$$M = \begin{pmatrix} 0 & 0 & 0 & -\mu^{(2)} \\ 0 & 0 & 1/\mu^{(2)} & 0 \\ 0 & -\mu^{(2)} & 0 & 0 \\ 1/\mu^{(2)} & 0 & 0 & 0 \end{pmatrix}.$$

This may be factorised into a state swap (as given above) followed by the application of the two local squeezing operations

$$\begin{aligned} S &= \exp\left\{\frac{1}{2}\xi^* a^2 - \frac{1}{2}\xi a^{\dagger 2}\right\} \exp\left\{\frac{1}{2}\xi^* b^2 - \frac{1}{2}\xi b^{\dagger 2}\right\} \\ &\rightarrow \begin{pmatrix} \mu^{(2)} & 0 & 0 & 0 \\ 0 & 1/\mu^{(2)} & 0 & 0 \\ 0 & 0 & \mu^{(2)} & 0 \\ 0 & 0 & 0 & 1/\mu^{(2)} \end{pmatrix}, \end{aligned}$$

which have equal squeezing parameters $\xi = -\ln \mu^{(2)}$. This possibility will be examined in § 5.8.

5.6 Ground state cooling

Ground state cooling is a convenient starting point for several schemes that aim to generate non-classical states of motion [26, 82], fundamental tests of quantum mechanics and many quantum information processing protocols (*e.g.* see [254]). We shall refer to systems with average occupancies less than one ($\langle \hat{n}'_{\rm M} \rangle < 1$) as 'ground state cooled' or 'near ground state cooled'. Examples include [15–17].

Clearly the three-pulse state swap protocol introduced here can achieve optomechanical cooling in the bad-cavity limit; a coherent optical pulse carries only vacuum (zero temperature) noise, which can be swapped onto the mechanical system. In order to formulate a ground state cooling criterion we calculate the evolution of the mechanics–light covariance matrix.

With the assumption that the noise operator $\boldsymbol{F}$ is uncorrelated with the initial state, it is straightforward to show that the output covariance matrix V' is related to the input by (*cf.* Eqn (5.5))

$$V' = MV\,M^{\rm T} + V_{\rm FF}.$$

The first diagonal block of V' corresponds to the output mechanical covariance matrix, the second represents the output optical state, and the antidiagonal blocks describe correlations between the two subsystems.

In the high-$Q_{\rm M}$ limit we may expand this result about $\varepsilon = 0$ and determine the final mechanical

variances.

$$\begin{aligned}
\left\langle {X'_{\rm M}}^2 \right\rangle &= \langle X_{\rm M}^2 \rangle \left(\mu^{(1)} - 1\right)\left(\mu^{(1)} + 2\pi\varepsilon - 1\right) \\
&\quad + \langle P_{\rm L}^2 \rangle \, {\mu^{(2)}}^2 + 2\pi\varepsilon\,(2\bar{n}_{\rm H} + 1) \\
&\quad + \left(\frac{1}{\eta_{\rm L}} - 1\right) {\mu^{(2)}}^2, \qquad (5.8a) \\
\left\langle {P'_{\rm M}}^2 \right\rangle &= \langle P_{\rm M}^2 \rangle \left(\mu^{(3)} - 1\right)\left(\mu^{(3)} + 2\pi\varepsilon - 1\right) \\
&\quad + \langle X_{\rm M} P_{\rm M} \rangle_{\rm S} \, 2\varepsilon \left(\mu^{(3)} - 1\right)\left(\mu^{(3)} - \mu^{(1)}\right) \\
&\quad + \langle X_{\rm L} P_{\rm L} \rangle_{\rm S} \, 2\varepsilon \left(\mu^{(1)} + \mu^{(3)}\,\eta_{\rm L} - \mu^{(1)}\,\mu^{(3)}\right) \\
&\quad + \langle X_{\rm L}^2 \rangle \, {\mu^{(2)}}^{-2} \left\{\mu^{(1)}\left(\mu^{(3)} - 1\right) - \eta_{\rm L}\,\mu^{(3)}\right\} \\
&\quad \times \left\{\mu^{(1)}\left(\mu^{(3)} + 2\pi\varepsilon - 1\right) - \eta_{\rm L}\,\mu^{(3)}\right\} \\
&\quad + \pi\varepsilon\,(2\bar{n}_{\rm H} + 1)\left\{2 - \mu^{(3)}\left(2 - \mu^{(3)}\right)\right\} \\
&\quad + \left(\frac{\mu^{(3)}}{\mu^{(2)}}\right)^2 \left(1 - \eta_{\rm L}^2\right). \qquad (5.8b)
\end{aligned}$$

It is safe to assume that the initial mechanical state is thermal, *viz.*

$$\langle X_{\rm M}^2 \rangle = \langle P_{\rm M}^2 \rangle = 2\bar{n}_{\rm H} + 1, \; \langle X_{\rm M} P_{\rm M} \rangle_{\rm S} = 0,$$

and because a coherent pulse carries only vacuum noise we have

$$\langle X_{\rm L}^2 \rangle = \langle P_{\rm L}^2 \rangle = 1, \; \langle X_{\rm L} P_{\rm L} \rangle_{\rm S} = 0.$$

The final occupancy of the mechanical oscillator is then readily calculated using

$$\langle \hat{n}'_{\rm M} \rangle = \frac{1}{4}\left[\left\langle {X'_{\rm M}}^2 \right\rangle + \left\langle {P'_{\rm M}}^2 \right\rangle - 2\right]. \qquad (5.9)$$

This yields

$$\begin{aligned}
4\langle \hat{n}'_{\rm M} \rangle &= (2\bar{n}_{\rm H} + 1)\left[\left(\mu^{(1)} - 1\right)\left(\mu^{(1)} + 2\pi\varepsilon - 1\right)\right. \qquad (5.10) \\
&\quad + \left(\mu^{(3)} - 1\right)\left(\mu^{(3)} + 2\pi\varepsilon - 1\right) \\
&\quad \left. + \pi\varepsilon\left(4 - \mu^{(3)}\left(2 - \mu^{(3)}\right)\right)\right] \\
&\quad + \frac{1}{{\mu^{(2)}}^2}\left[{\mu^{(3)}}^2 - 2\eta_{\rm L}\,\mu^{(1)}\,\mu^{(3)}\left(\mu^{(3)} + \pi\varepsilon - 1\right)\right. \\
&\quad \left. + {\mu^{(1)}}^2\left(\mu^{(3)} - 1\right)\left(\mu^{(3)} + 2\pi\varepsilon - 1\right)\right] \\
&\quad + \frac{{\mu^{(2)}}^2}{\eta_{\rm L}} - 2.
\end{aligned}$$

To minimise this, note that $\langle \hat{n}'_{\rm M} \rangle$ may be divided into a term proportional to $(2\bar{n}_{\rm H} + 1)$ and a term independent of the thermal bath. The former is dependent only upon $\mu^{(1)}$ and $\mu^{(3)}$, whilst the latter

depends on all three strengths. We therefore choose to approximately minimise the occupancy by minimising the two terms separately.

Minimising the bath-dependent term yields, to first order in ε,

$$\mu^{(1,3)} \approx 1 - \pi\varepsilon \approx \eta_{\mathrm{M}}.$$

We then substitute these into the remaining noise contribution and select $\mu^{(2)}$ accordingly. Thus for optimum cooling we require

$$\begin{aligned} \mu^{(1)} &\approx \eta_{\mathrm{M}} \\ \mu^{(2)} &\approx \frac{1+\eta_{\mathrm{M}}}{2}\eta_{\mathrm{L}}^{1/4} \\ \mu^{(3)} &\approx \eta_{\mathrm{M}}. \end{aligned}$$

As η_{M} & η_{L} approach 1 we obtain $\mu^{(j)} = 1$ to a very good approximation, as stated previously.

Evaluated at $\mu^{(j)} = 1$, the final occupancy is

$$\left\langle \hat{n}'_{\mathrm{M}} \right\rangle_{\min} \approx \frac{\pi\varepsilon}{4}\left\{3\left(2\bar{n}_{\mathrm{H}}+1\right) - 2\eta_{\mathrm{L}}\right\} + \frac{1}{4}\left\{\frac{1}{\eta_{\mathrm{L}}} - 1\right\}. \tag{5.11}$$

If the decoherence is dominated by thermomechanical noise, which is the case in the regime of interest (assuming $\bar{n}_{\mathrm{H}} \gg 1$), we may insert Eqn (5.11) into the ground state criterion $\langle \hat{n}'_{\mathrm{M}} \rangle < 1$ to show that ground state cooling is possible only when the additional criteria

$$\bar{n}_{\mathrm{H}} < \frac{4\omega_{\mathrm{M}}}{3\pi\Gamma} \tag{5.12a}$$

$$\eta_{\mathrm{L}} > 1/5 \tag{5.12b}$$

are satisfied. As discussed in § 5.4 (*cf.* Table 5.1), meeting the requirement $\mu^{(j)} \approx 1$ is experimentally tractable. The further condition Eqn (5.12a) is essentially a requirement of quantum coherent oscillation (*i.e.* less than one phonon entering the oscillator per mechanical period). Many experimental systems boast Q_{M} large enough to satisfy this at temperatures achievable with conventional refrigeration technologies (*e.g.* [226]). Recent devices may permit this regime to even be reached at room temperature ($Q_{\mathrm{M}} \sim 10^8$ at $\omega_{\mathrm{M}}/2\pi \sim 150$ kHz) [255].

Other strategies for optomechanical cooling, such as resolved sideband cooling or cold damping, typically express their criteria for ground state cooling in terms of the optomechanical cooperativity C. We will therefore recast Eqn (5.12a) into a requirement on the cooperativity.

C is a dimensionless parameter describes how strongly the quantum back-action of the optomechanical coupling (due to amplitude noise) perturbs the dynamics of the mechanical oscillator: in the steady state

$$C = \frac{4g_0^2|\alpha|^2}{\Gamma\kappa} \text{ (steady state)}.$$

A natural quantity to use in the pulsed setting is the instantaneous cooperativity time-averaged over the entire three-pulse sequence; thus

$$\begin{aligned} C &= \frac{4g_0^2}{\Gamma\kappa} \times \frac{\sigma\omega_{\mathrm{M}}}{\pi} \int_0^{\pi/\sigma\omega_{\mathrm{M}}} \mathrm{d}t \ |\alpha(t)|^2 \\ &= \frac{1}{8\pi\varepsilon}\left(\frac{{\mu^{(1)}}^2 + {\mu^{(3)}}^2}{{\mu^{(2)}}^2} + \frac{\sigma^2\,{\mu^{(2)}}^2}{\eta_{\mathrm{L}}\eta_{\mathrm{M}}}\right) \end{aligned} \tag{5.13}$$

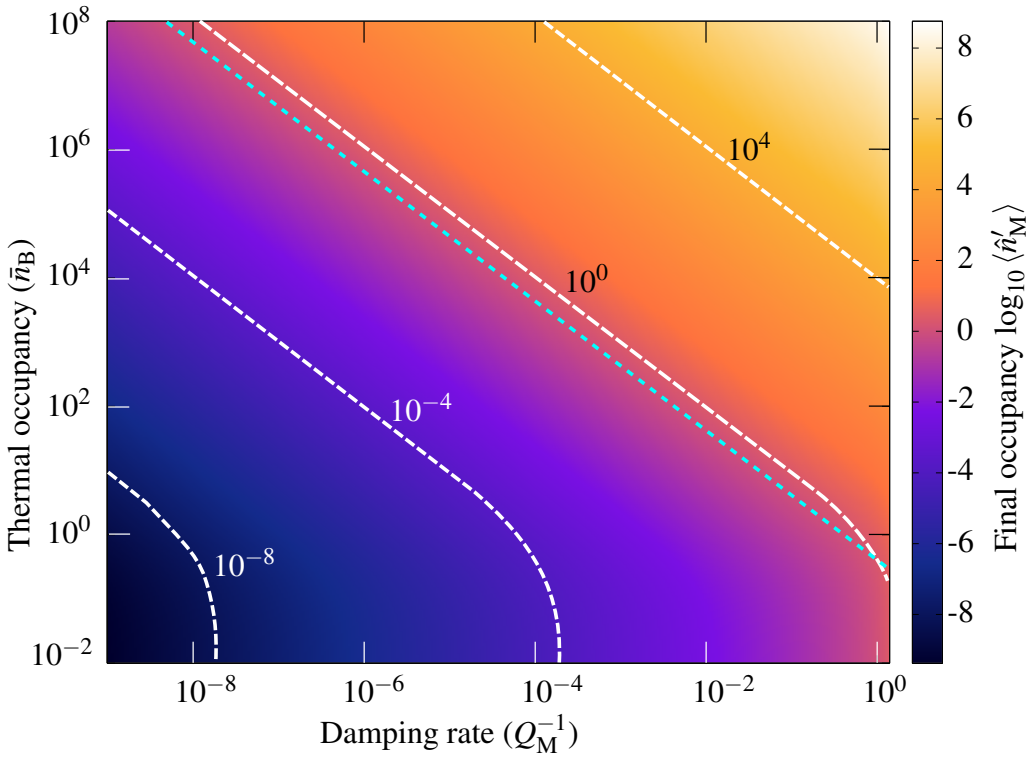

Figure 5.2: Final occupancy of the mechanical oscillator after a complete three-pulse cooling sequence as a function of damping rate Γ and bath occupancy $\bar{n}_H$. White contours show lines of equal (normalised) heating rates $(\Gamma(\bar{n}_H + 1/2)/\omega_M)$; the shoulder at low n_H is where vacuum fluctuations begin to dominate over thermal noise. The cyan dashed line demarcates the zone where ground state cooling ($\langle\hat{n}'_M\rangle \leq 1$) is possible, as given by Eqn (5.14). We have assumed $\mu^{(j)} = 1$.

where in the first line $\alpha(t)$ includes contributions from all three pulses.

Substituting this definition into Eqn (5.12a) and noting that $\mu^{(j)} \approx 1 \; \forall \; j$ for optimum cooling yields

$$\bar{n}_H < \frac{16}{3\left(2+\eta_L^{-1}\right)} C \leq \left(\frac{4}{3}\right)^2 C. \tag{5.14}$$

Thus, although operating in a pulsed manner and in a fundamentally different regime, our interface's ground state cooling criterion is remarkably similar to that of resolved sideband cooling ($\bar{n}_H < C$), the current 'gold standard' for optomechanical cooling [84]. We note also that it also resembles the criterion for feedback cooling to near the ground state in the bad-cavity regime, namely $\bar{n}_H < 8C$ [1]. However, it must be remembered that in Eqn (5.14) the cooperativity must be evaluated with $\mu^{(j)} \approx 1$ because a near-perfect state swap is only possible in this regime: merely having a large cooperativity does not guarantee near ground state cooling using the three-pulse protocol.

In the case that the pulse strengths are not equal to unity we find that significant cooling is still possible so long as the deviation in μ is less than a threshold value that scales inversely with $\sqrt{Q_M}$ (*cf.* Fig. 5.3, § 5.6.1).

The validity of Eqn (5.14) is confirmed by numerical calculations of the final phonon occupancy for a variety of $\mu^{(j)}$, Γ and $\bar{n}_H$, as shown in Fig. 5.2 (and Fig. 5.3). In all figures we have set $\eta_L = 1$.

Fig. 5.2 shows the expected trend of decreasing final occupancy as the oscillator Q_M is increased and the initial temperature is decreased. The analytical threshold for near-ground-state cooling

(Eqn (5.14)) is in excellent agreement with the calculations. Note that the lines of equal heating rate are curved because there is a non-zero incoming noise contribution from the mechanical bath even when the ambient temperature is zero.

Near ground state cooling can be realised using the three–pulse protocol with achievable experimental parameters, as shown in Table 5.1. This cooling will persist for a time proportional to $(\Gamma\bar{n}_{\mathrm{H}})^{-1}$ after the conclusion of the protocol. We note that these same parameters also permit non-classical state transfer, as discussed below (§ 5.7).

5.6.1 Tolerance to pulse strength variations

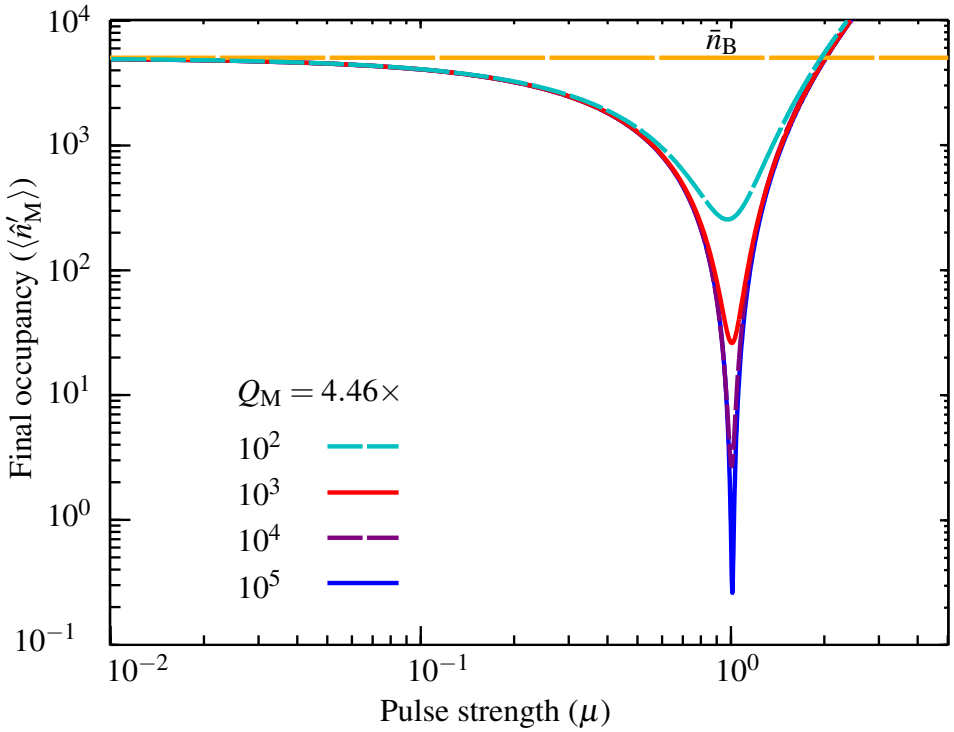

Figure 5.3: Final mechanical occupancy $\langle\hat{n}'_{\mathrm{M}}\rangle$ as a function of pulse strength $\mu^{(j)} = \mu$ for different mechanical quality factors. The bath occupancy is fixed at 5000, corresponding to a temperature of approximately 24 mK for $\omega_{\mathrm{M}}/2\pi = 100.2$ kHz (*cf.* Table 5.1).

It is clear from Fig. 5.3 that the system becomes less tolerant to variations in $\mu^{(j)}$ for very high-Q_{M} oscillators, which means that the mean number of photons in the coherent envelope of each pulse must be controlled to a very high degree when attempting to reach the mechanical ground state.

To quantify this we consider the case where all pulse strengths are equal (denoted by μ with no superscript). We first find the two values of μ for which

$$\langle\hat{n}'_{\mathrm{M}}\rangle = 2\,\langle\hat{n}'_{\mathrm{M}}\rangle_{\mathrm{min}}\,.$$

The difference of these values is used as a proxy for the width of the cooling dip (*cf.* Fig. 5.3). If $\bar{n}_{\mathrm{H}} \gg 1$ and $\eta_{\mathrm{L}} \gtrsim 0.1$ this reduces to

$$\text{width} \approx \sqrt{6\pi\varepsilon}\,.$$

Thus the tolerance of the protocol to imperfections in the pulse strengths scales as $\varepsilon^{1/2}$. This is a very strong dependence in the high-Q_{M} limit; for instance, a mechanical Q_{M} of 10^6 would require the value of μ to be stabilised to approximately one part in a thousand.

To translate this into terms of photon number, note that width $\approx \Delta\mu \approx -\Delta\chi$, where $\Delta\mu$ ($\Delta\chi$) is the tolerance of the protocol to μ (χ). Then we may expand the definition of χ to see that

$$\Delta\chi \approx \frac{-8g_0}{\kappa}\sqrt{N}\left(\frac{\Delta N}{2N}\right),$$

which becomes $\Delta\chi \approx -\Delta N/2N$ in the case that $\chi \approx -1$. Thus $\Delta N/N \approx 2\sqrt{6\pi\varepsilon}$ is the tolerable fractional variation of the pulse photon number amplitude. For Q_{M} of 10^6 the fractional variation needs to be less than approximately 0.6%.

This $\sqrt{\varepsilon}$ scaling may be explained by considering the two ways in which the thermal bath contributes to the final mechanical temperature. Firstly, there is noise entering the system during the protocol; this component is reasonably weakly dependent on μ, and tends to set the minimum attainable final temperature. The second contribution is from the initial thermal state of the oscillator. The amount of this noise that is swapped out of the mechanical system depends strongly on μ, and tends to set the shape of the $\langle \hat{n}'_{\mathrm{M}}(\mu)\rangle$ curve (*cf.* Fig. 5.3). If the former dominates then the strong μ dependence of the second term is washed out.

5.7 Fock state preparation

For more complicated quantum states the covariance matrix ceases to be a full description, so we now move to considering the evolution of the system's Wigner function. The Wigner function is a quasiprobability distribution that is permitted to be negative over parts of phase space; negativity is considered to be a 'smoking gun' for non-classical states (see § 3.2 for discussion). The definition of the Wigner function, the associated characteristic function, and some of their properties, are given in § 3.1.2. Generalisation to multi-mode systems is provided in App. A.4; the reader is encouraged to peruse this before continuing.

5.7.1 Lossy evolution

It will prove useful to work in the reciprocal domain ($\boldsymbol{\beta}$) for the calculations that follow. The output characteristic function may be written (according to its definition in the Heisenberg picture, for a linear system) as

$$\begin{aligned}
\chi'(\boldsymbol{\beta}) &= \mathrm{Tr}\left\{\hat{\rho}\exp\left[\mathrm{i}\boldsymbol{X}'\cdot\Omega\boldsymbol{\beta}\right]\right\} \\
&= \mathrm{Tr}\left\{\hat{\rho}\exp\left[\mathrm{i}\left(M\boldsymbol{X}+\boldsymbol{F}\right)\cdot\Omega\boldsymbol{\beta}\right]\right\} \\
&= \mathrm{Tr}\left\{\hat{\rho}\exp\left[\mathrm{i}\,\boldsymbol{\beta}^{\mathrm{T}}\,\Omega^{\mathrm{T}}M\boldsymbol{X}\right]\exp\left[\mathrm{i}\boldsymbol{F}\cdot\Omega\boldsymbol{\beta}\right]\right\} \\
&= \mathrm{Tr}\left\{\hat{\rho}\exp\left[\mathrm{i}\,\boldsymbol{\beta}^{\mathrm{T}}\,\Omega^{\mathrm{T}}M\boldsymbol{X}\right]\right\}\mathrm{Tr}\left\{\hat{\rho}\exp\left[\mathrm{i}\boldsymbol{F}\cdot\Omega\boldsymbol{\beta}\right]\right\}.
\end{aligned}$$

In going from line two to line three we used the Baker–Campbell–Haussdorff lemma, and to arrive at line four we noted that expectation values of system and noise operators factorise under the approximations used here.

If we define a vector $\boldsymbol{\gamma} = \Omega\, M^{\mathrm{T}}\, \Omega\boldsymbol{\beta}$ then it is clear that the exponent of the first trace above becomes

$$\begin{aligned}
\boldsymbol{\beta}^{\mathrm{T}}\, \Omega^{\mathrm{T}} M \boldsymbol{X} &= -\,\boldsymbol{\beta}^{\mathrm{T}}\, \Omega^{\mathrm{T}} M \Omega\, \Omega^{\mathrm{T}}\, \boldsymbol{X} \\
&= \boldsymbol{\beta}^{\mathrm{T}} \left(-\,\Omega^{\mathrm{T}} M \Omega\right) \Omega^{\mathrm{T}}\, \boldsymbol{X} \\
&= \boldsymbol{\beta}^{\mathrm{T}} \left(\Omega M \Omega\right) \Omega^{\mathrm{T}}\, \boldsymbol{X} \\
&= \boldsymbol{\gamma}^{\mathrm{T}}\, \Omega^{\mathrm{T}}\, \boldsymbol{X},
\end{aligned}$$

whence

$$\chi'\left(\boldsymbol{\beta}\right) = \mathrm{Tr}\left\{\hat{\rho}\exp\left[\mathrm{i}\boldsymbol{X}\cdot\Omega\boldsymbol{\gamma}\right]\right\}\mathrm{Tr}\left\{\hat{\rho}\exp\left[\mathrm{i}\boldsymbol{F}\cdot\Omega\boldsymbol{\beta}\right]\right\}.$$

We now recognise the term on the left as being simply the input characteristic function with its arguments rescaled to $\boldsymbol{\gamma}$, *viz.*

$$\chi\left(\boldsymbol{\beta}\right) \rightarrow \chi\left(\Omega\, M^{\mathrm{T}}\, \Omega\boldsymbol{\beta}\right)\mathrm{Tr}\left\{\hat{\rho}\exp\left[\mathrm{i}\boldsymbol{F}\cdot\Omega\boldsymbol{\beta}\right]\right\}.$$

Since we are already aware of the general form of a Gaussian characteristic function (*cf.* Tab. 3.2) we may simply use this formula to find the kernel induced by Gaussian noise, *viz.*

$$\begin{aligned}
\chi_{\mathrm{F}}\left(\boldsymbol{\beta}\right) &= \mathrm{Tr}\left\{\hat{\rho}\exp\left[\mathrm{i}\boldsymbol{F}\cdot\Omega\boldsymbol{\beta}\right]\right\} \\
&= \exp\left\{-\frac{1}{2}\,\boldsymbol{\beta}^{\mathrm{T}}\, \Omega^{\mathrm{T}} V_{\mathrm{FF}} \Omega\boldsymbol{\beta}\right\},
\end{aligned}$$

where $V_{\mathrm{FF}} = \Re\left\{\left\langle \boldsymbol{F}\, \boldsymbol{F}^{\mathrm{T}}\right\rangle\right\}$.

Let us now consider a two mode system. If the density matrix is separable (*i.e.* $\hat{\rho} = \hat{\rho}_{\mathrm{M}} \otimes \hat{\rho}_{\mathrm{L}}$), as we have assumed, the input characteristic function factorises into the form

$$\chi\left(\boldsymbol{\beta}\right) = \chi_{\mathrm{M}}\left(\boldsymbol{\beta}_{\mathrm{M}}\right)\chi_{\mathrm{L}}\left(\boldsymbol{\beta}_{\mathrm{L}}\right)$$

where

$$\boldsymbol{\beta} = \begin{pmatrix} \boldsymbol{\beta}_{\mathrm{M}} \\ \boldsymbol{\beta}_{\mathrm{L}} \end{pmatrix}$$

Let us define the matrices

$$E_{\mathrm{M}} = \begin{pmatrix} 1 & 0 & 0 & 0 \\ 0 & 1 & 0 & 0 \end{pmatrix},$$

$$E_{\mathrm{L}} = \begin{pmatrix} 0 & 0 & 1 & 0 \\ 0 & 0 & 0 & 1 \end{pmatrix}.$$

With these we may write $\boldsymbol{\beta}_{\mathrm{M,L}} = E_{\mathrm{M,L}}\boldsymbol{\beta}$. Thus, from the evolution above we can find that

$$\chi\left(\Omega\, M^{\mathrm{T}}\, \Omega\boldsymbol{\beta}\right) = \chi_{\mathrm{M}}\left(E_{\mathrm{M}}\Omega\, M^{\mathrm{T}}\, \Omega\boldsymbol{\beta}\right)\chi_{\mathrm{L}}\left(E_{\mathrm{L}}\Omega\, M^{\mathrm{T}}\, \Omega\boldsymbol{\beta}\right)$$

This allows us to write the transformation between input and output characteristic functions as

$$\chi_{\mathrm{M}}(\boldsymbol{\beta})\,\chi_{\mathrm{L}}(\boldsymbol{\beta}) \rightarrow \chi_{\mathrm{M}}\left(E_{\mathrm{M}}\Omega\, M^{\mathrm{T}}\,\Omega\boldsymbol{\beta}\right)\chi_{\mathrm{L}}\left(E_{\mathrm{L}}\Omega\, M^{\mathrm{T}}\,\Omega\boldsymbol{\beta}\right)\chi_{\mathrm{F}}(\boldsymbol{\beta})$$

The final Wigner function of the mechanical oscillator is obtained by evaluating this at $\boldsymbol{\beta}^{\mathrm{T}} = (\Re\{\beta_{\mathrm{M}}\},\Im\{\beta_{\mathrm{M}}\},0,0)$ and applying the appropriate transformation (Eqn (3.5)).

Note that this calculation is equivalent to determining the Wigner function by propagating the reduced density matrix of the mechanical mode in the Schrödinger picture.

5.7.2 Fock state transfer

Our interface uses only linear interactions and therefore cannot generate Wigner negativity. It can, however, *transfer* negativity from one system to another. We demonstrate this numerically by considering the preparation of a single phonon Fock state (Appendix 5.7). Fock states have definite energy but completely undefined phase, and as such are highly nonclassical. As may be seen in Fig. 5.4 (panels *i–iii*), transfer of a single-photon state onto the mechanical oscillator is possible with realistic mechanical parameters (*cf.* Table 5.1). Note that the state becomes rotationally asymmetric when the noise entering from the thermal bath is significant, and that increasing the heating rate leads to degradation of the Wigner negativity. This is consistent with thermalisation of the system during the protocol.

Higher-number mechanical Fock states may also be prepared. We show the infidelity (1-$\mathscr{F}$, where $\mathscr{F}$ is the Schumacher fidelity (*cf.* Eqn (3.7)) of this operation in Fig. 5.5 (panel *i*). Note that higher-n Fock states are more difficult to prepare because of their intrinsically larger susceptibility to environmental noise.

5.8 Squeezed transfer

The interface may be made to perform additional non-trivial operations on the states involved. Here we consider fixing $\mu^{(1,3)} = 1$ and allowing $\mu^{(2)}$ to take on non-unit values. In this case Eqn (5.6) becomes (setting $\eta_{\mathrm{L}} = \eta_{\mathrm{M}} = 1$)

$$M\left(\mu^{(2)}\right) = \begin{pmatrix} 0 & 0 & 0 & -\mu^{(2)} \\ 0 & 0 & 1/\,\mu^{(2)} & 0 \\ 0 & -\mu^{(2)} & 0 & 0 \\ 1/\,\mu^{(2)} & 0 & 0 & 0 \end{pmatrix}, \tag{5.15}$$

which may be decomposed into a state transfer, *à la* Eqn (5.3), followed by local squeezing operations (one on each output) with equal squeezing parameters $\xi = -\ln\mu^{(2)}$. Thus $\mu^{(2)} < 1$ yields position-squeezed output states, and momentum-squeezed outputs may be prepared with $\mu^{(2)} > 1$.

In principle, it is then straightforward to generate unconditionally squeezed motion by transferring the noise of a coherent pulse onto the oscillator with $\mu^{(2)} \neq 1$.

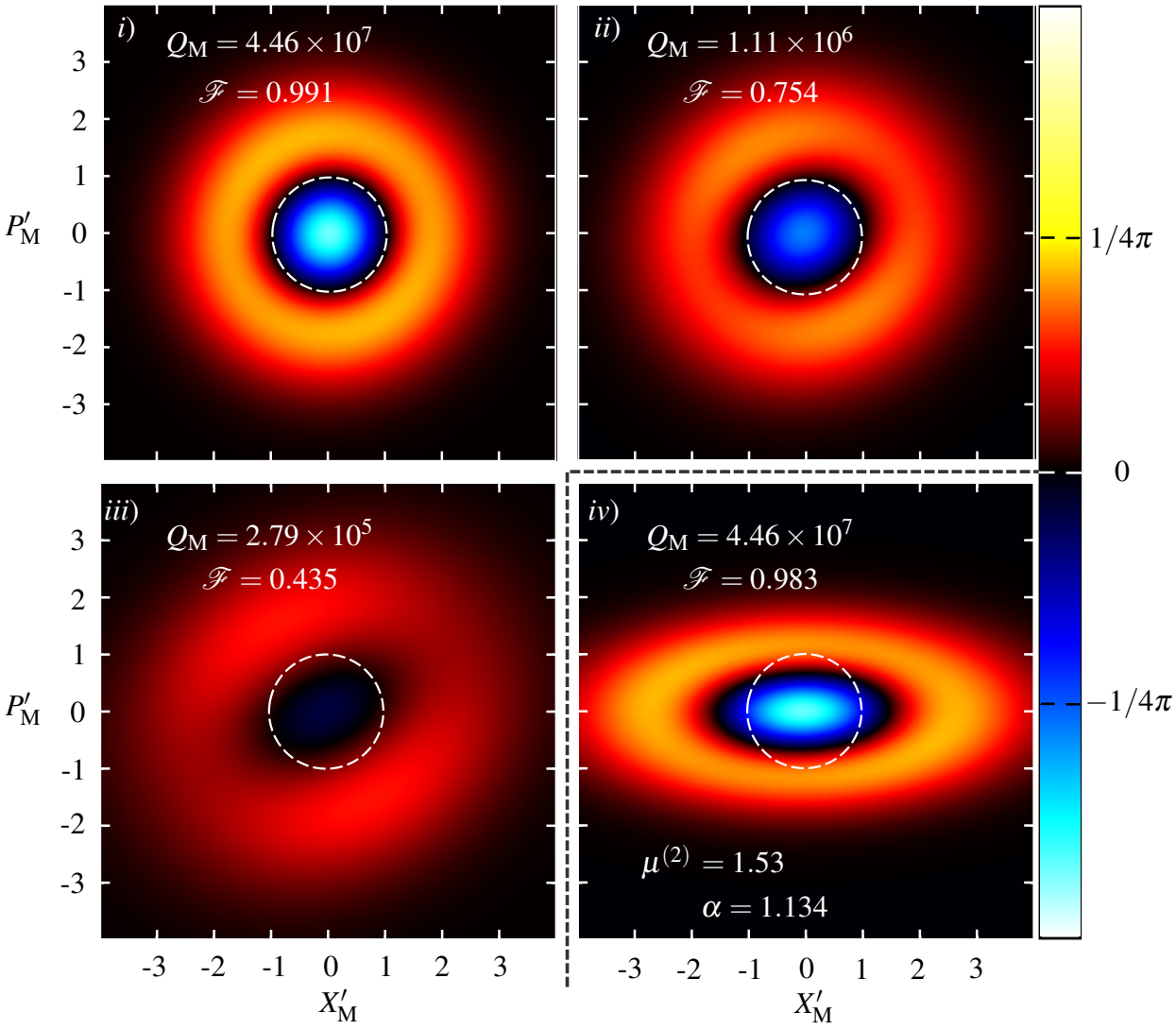

Figure 5.4: *i*), *ii*) & *iii*): calculated output mechanical Wigner functions after transfer of an optical Fock state $|1\rangle$ in the presence of decoherence ($Q_M = \omega_M/\Gamma$) with $\mu^{(j)} = 1$ for all pulses. These parameters are experimentally feasible. The mechanical state is initially thermal with 10 phonons on average, simulating the result of a cooling pulse sequence, and the bath occupancy is fixed at $\bar{n}_H = 5 \times 10^4$. Blue tones denote negative regions of the Wigner function and positive regions are red, passing through black at zero. The unit circle in white is the uncertainty contour of a vacuum state, shown for reference. Note that as the decoherence increases the output state becomes rotationally asymmetric and the Wigner negativity washes out. Due to the large optical bandwidth used in this scheme, it may be possible to transfer single photons generated using heralded spontaneous parametric down-conversion, which are naturally broad-band.
iv) A 'Schrödinger kitten' state generated by squeezed transfer of a $|1\rangle$ state onto the mechanical oscillator. The bath conditions are the same as above, and $\mu^{(1)} = \mu^{(3)} = 1$. The target odd cat state amplitude is α.

A more intriguing application of this squeezed transfer is generation of small-amplitude mechanical Schrödinger cat states (coherent state superpositions), termed 'kitten' states. As has been demonstrated in optical systems, these may be 'bred' into large-amplitude cat states by a number of schemes [256–258]; this could result in a macroscopic superposition of a massive object. Creating such a state is a research goal of foundational interest [26], and is also sufficient to allow universal quantum

computation [259, 260] with phonons.

Any state of the form

$$\left|\Psi^{(-)}\right\rangle = \frac{|\alpha\rangle - |-\alpha\rangle}{\sqrt{2\left(1-\mathrm{e}^{-2|\alpha|^2}\right)}},$$

is an odd cat state. Taking α to be small and real, we have

$$\begin{aligned}\left|\Psi^{(-)}\right\rangle &= \frac{|\alpha\rangle - |-\alpha\rangle}{\sqrt{2\left(1-\mathrm{e}^{-2|\alpha|^2}\right)}} \\ &= \sqrt{\frac{2}{\mathrm{e}^{+|\alpha|^2}-\mathrm{e}^{-|\alpha|^2}}}\sum_{\mathrm{j}\in\mathrm{odd}}^{\infty}\frac{\alpha^j}{\sqrt{j!}}|j\rangle \\ &\approx \frac{\alpha}{|\alpha|}\left(|1\rangle + \frac{\alpha^2}{\sqrt{6}}|3\rangle + \mathscr{O}\left(\alpha^4\right)\right).\end{aligned}$$

Note that this contains only odd Fock state contributions.

A squeezer generates correlated pairs of photons; it follows that weakly squeezing $|1\rangle$ could give an approximation to an odd kitten state (*cf.* [261]). For small squeezing parameters ξ,

$$\begin{aligned}S(\xi)|1\rangle &= \exp\left\{\frac{1}{2}\left(\xi^* a^2 - \xi\, a^{\dagger\,2}\right)\right\}|1\rangle \\ &= \sum_{\mathrm{j}=0}^{\infty}\left(\frac{1}{2}\right)^j\frac{\left(\xi^* a^2 - \xi\, a^{\dagger\,2}\right)^j}{j!}|1\rangle \\ &\to |1\rangle - \xi\sqrt{\frac{3}{2}}\,|3\rangle + \mathscr{O}\left(\xi^2\right).\end{aligned}$$

By comparing these we see that the approximate kitten state has an amplitude given by $\xi = -\frac{\alpha^2}{3}$. Thus we obtain $\mu^{(2)} = \exp\left\{\alpha^2/3\right\}$.

The Wigner function of such a state is given in Table 3.2 and shown with mild decoherence in Fig. 5.4 (panel *iv*). It is important to note that the Wigner function contains two positive lobes along the X'_{M} axis ('alive' and 'dead') separated by a region of quantum interference exhibiting Wigner negativity, proving that coherence between the lobes persists [82]. Again, note that these parameters are experimentally realisable (although requiring very large N to achieve the squeezing shown in Fig. 5.4, panel *iv*).

The degree to which the decohering squeezed single phonon state approximates a true cat state is shown in Fig. 5.5 (panel *ii*). It is evident that large cat states cannot be produced directly in this manner, as the minimum infidelity rises monotonically with $|\alpha|$; this is not due to imperfections in our interface, but from the approximate equality of an odd cat state and a squeezed single phonon state. Environmental noise clearly degrades the preparation process, both through decreasing the purity of the initial mechanical state and through destroying the phonon pair correlations required for squeezing. Even so, it is possible to push the infidelity to low values with realistic parameters (*cf.* Table 5.1). We also note that other non-Gaussian quantum states of light can be transferred to the mechanics by our interface thus providing several routes for motional state engineering.

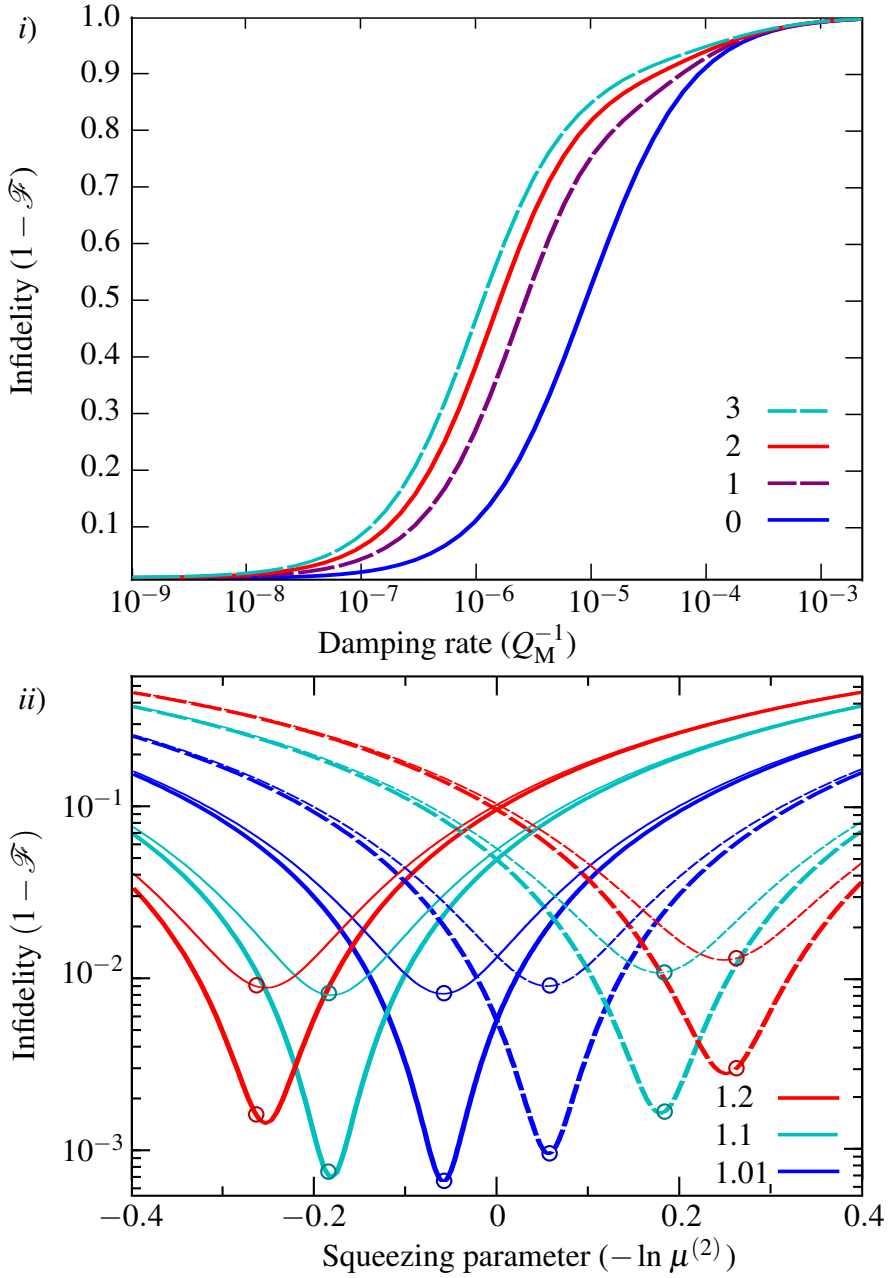

Figure 5.5: *i*) The infidelity of mechanical Fock state preparation via pulsed optomechanical state transfer. The target states are $|n\rangle$ as indicated. All pulse strengths are fixed at unity and parameters are experimentally realisable. The initial mechanical state in all cases is thermal, containing 10 phonons (with a bath of $\bar{n}_{\mathrm{H}} = 5 \times 10^4$). *ii*) Calculation of the infidelity of mechanical kitten state preparation using pulsed optomechanical state transfer with squeezing. Each colour corresponds to a given mean number of phonons in the target kitten, as indicated, with dashes corresponding to target states with imaginary α and solid lines indicating $\alpha \in \mathbb{R}$. Thick lines show the decoherence-free case ($\Gamma/\omega_{\mathrm{M}} = 0$, initial mechanical state $|0\rangle$), and results with the small but achievable ratio $\Gamma/\omega_{\mathrm{M}} = 2.24 \times 10^{-7}$ are shown as thin lines (initially thermal with 10 phonons, $\bar{n}_{\mathrm{H}} = 5 \times 10^3$). $\xi = -\ln \mu^{(2)}$ is the magnitude of the squeezing induced by the transfer (with $\mu^{(1)} = \mu^{(3)} = 1$). Circles indicate the naïve analytical estimates for optimum overlap with each target kitten state, $\xi = -\alpha^2/3$. The asymmetry is due to thermal noise being mixed into the output state differently for different values of $\mu^{(2)}$.

5.9 Conclusion

We have shown how open–loop rotations and displacements plus repeated QND interactions may be used to construct an optomechanical interface that operates in the high-bandwidth ($\kappa \gg \omega_{\mathrm{M}}$) limit of optomechanics, a natural operating regime for many devices. Our calculations predict that such an interface is within reach of current experimental parameters (*cf.* Table 5.1). Furthermore, we have shown how our three-pulse protocol may be extended to performing more complicated operations, including optical–mechanical state transfer with squeezing of the final modes; we note that it is also possible to perform a partial state swap that entangles the final modes, though we have not modelled that process here.

These results show that optomechanical systems in the unresolved sideband limit are capable of performing an optomechanical state-swap, and may prove important in the construction of quantum networks and studies of macroscopic quantum mechanics. Finally, we note that this three-pulse protocol could directly be applied in other circumstances where QND interactions with light are available, such as in spin ensembles.

Chapter 6

Quantum thermodynamics beyond the rotating wave approximation

The work presented in this chapter has been submitted for publication and is available on the arXiv; **J. S. Bennett**, L S. Madsen, H. Rubinsztein-Dunlop, and W. P. Bowen. Quantum thermodynamics beyond the rotating wave approximation, *arXiv* quant-ph 1705.09174, 2017.

* * *

We consider a thermodynamic system in which the working fluid is a quantised harmonic oscillator subjected to periodic squeezing operations at a rate much larger than its resonance frequency. When the oscillator–bath coupling is treated with the conventional rotating wave approximation (RWA) we find that the system can behave as a heat pump. Without the RWA a much richer picture emerges, including refrigeration and heat engine behaviours, and a new method of parametric cooling of the oscillator. This shows the emergence of quantum thermodynamical phenomena beyond those permitted in the RWA.

This work is an important contribution to the physics of optomechanics in the unresolved sideband regime for three reasons. Firstly, in this work we consider the short-time dynamics of the oscillator (times $t \ll \omega_{\mathrm{M}}^{-1}$), which may be experimentally accessible in low-frequency oscillators probed using optomechanical techniques. Secondly, we highlight key differences between two Markovian Langevin equations that are often employed in the optomechanics literature (for a condensed discussion, see App. A.10). Finally, as part of this study we outline how to produce an extremely rapid mechanical squeezing operation using pulsed optomechanics in the unresolved sideband regime (§ 6.8).

6.1 Introduction

The union of thermodynamics and quantum mechanics has proved extremely fruitful since its earliest days. Recent years have seen a rapid acceleration of this progress [262, 263], including important developments such as the generalisation of the second law of thermodynamics to the quantum realm

[264], as well as the first general proof of the third law of thermodynamics [265]. Tools from quantum information theory [266] have also clarified the role of information in thermodynamical processes, as demonstrated by, for example, the quantum Szilard thermodynamic engine [267].

Quantum systems with engineered Hamiltonians and system–bath interactions—such as atoms in optical cavities, superconducting circuits, and opto- or electro-mechanical devices [70]—are promising tools with which to experimentally study quantum thermodynamics [66, 268–273]. These systems are frequently modelled using the Born–Markov master equation (BMME), or its equivalent Langevin equations. The BMME provides a convenient description of the system's behaviour as it interacts with its environment over timescales comparable to or greater than a characteristic internal time (τ_S); however, it fails to capture shorter timescales correctly [70]. This inadequacy may be traced to the treatment of the heat bath in the BMME. If one begins with an independent oscillator model of the environment—the most general microscopic model of a linear, passive heat bath [274, 275]—one obtains the BMME by making the rotating-wave approximation (RWA) [1] (see § 2.2.3). Essentially, this consists of neglecting non-energy-conserving terms in the Hamiltonian, the absence of which 'washes out' dynamics faster than τ_S^{-1}. It is well-known in many branches of quantum mechanics that the RWA can mask interesting physical phenomena [276–279], or introduce non-physical artefacts into the theoretical description of a system [280–284].

In this chapter we study the influence of the RWA on predictions in quantum thermodynamics. Specifically, we consider an oscillator subjected to a periodic train of impulsive squeezing operations at a rate much larger than its natural oscillation frequency. The oscillator couples to a hot bath between squeezers, whilst imperfect squeezing operations provide a cold bath. We prove that within the approximation of the BMME the oscillator can only operate as a heat pump. However, without the RWA we find consistently richer behaviours, including additional refrigerator and heat engine regimes. Thus we predict the existence of thermodynamic cycles not permitted by the RWA. Our scheme also provides an alternative to standards techniques of cooling the oscillator such as optomechanical sideband cooling [285], distinguished by its ability to cool below the cold bath temperature. Together, these phenomena indicate the emergence of non-trivial thermodynamical behaviour beyond the RWA.

6.2 Damped harmonic motion with and without the RWA

For concreteness we will consider a mechanical oscillator, such as a micro- or nano-mechanical resonator. Such devices have been reported to have Q factors up to $(9.8 \pm 0.2) \times 10^7$ [255], with $Q > 10^5$ being readily achieved in many materials and resonator geometries [5]. As such, they are weakly coupled to their thermal environment and generally amenable to treatment using the Markovian limit of the independent oscillator model. Similar conclusions may be drawn for analogous systems *e.g.* electronic circuits [286] or optical cavities.

The equations of motion derived from the independent oscillator model (*cf.* Eqn (3.20) & App. A.3)

[1] The bare resonance frequency must also be renormalised.

are reproduced here for convenience.

$$\dot{X} = +\omega_{\mathrm{M}} P, \tag{6.1a}$$

$$\dot{P} = -\omega_{\mathrm{M}} X - \Gamma P + \sqrt{2\Gamma}\,\xi(t), \tag{6.1b}$$

where X and P are the dimensionless position and momentum operators obeying $[X,P] = 2\mathrm{i}$, ω_{M} is the resonance frequency, and $\Gamma = \omega_{\mathrm{M}}/Q$ is the decay rate. Note that these equations are asymmetric under rotations in phase space because the loss ($-\Gamma P$) and thermal noise ($\xi(t)$) terms couple only to P. This is in contradistinction to the BMME (here written as the equivalent Langevin equations)

$$\dot{X} = +\omega_{\mathrm{M}} P - \frac{\Gamma}{2} X + \sqrt{\Gamma}\, X_{\mathrm{in}}(t), \tag{6.2a}$$

$$\dot{P} = -\omega_{\mathrm{M}} X - \frac{\Gamma}{2} P + \sqrt{\Gamma}\, P_{\mathrm{in}}(t), \tag{6.2b}$$

where loss and noise affect X and P equally.

Full solutions to Eqn (6.1) are given in § 3.4.

The asymmetry of Eqn (6.1) is strongly manifest in the short-time behaviour of the system. This is most plainly seen from the covariance matrix, which we introduced in § 3.1.1. For all times $t \geq 0$, V is related to its initial value V_0 by a linear transformation $V = M(t) V_0 M^{\mathrm{T}}(t) + V_{\mathrm{FF}}(t)$, where $M(t)$ is a square matrix encoding the homogeneous part of the dynamics (*cf.* § 3.4). The aggregated effect of thermal noise is described by the added noise covariance matrix $V_{\mathrm{FF}}(t)$, which is given by Eqn (3.24). For short evolution times ($t \ll \omega_{\mathrm{M}}^{-1}$) this added noise varies as

$$V_{\mathrm{FF}} = (2\bar{n}_{\mathrm{H}} + 1) \begin{pmatrix} \frac{2}{3}\Gamma\omega_{\mathrm{M}}^2 t^3 & \Gamma\omega_{\mathrm{M}} t^2 \\ \Gamma\omega_{\mathrm{M}} t^2 & 2\Gamma t \end{pmatrix} \tag{6.3}$$

to leading non-trivial order in each matrix element. The first (second) diagonal element describes the noise added to X (P). Thus, over short timescales the noise introduced by the environment is 'squeezed', in the sense that the diagonal elements of V_{FF} are markedly unequal (see Fig. 6.1 *ii*)). Strikingly, this phenomenon is absent in the BMME prediction, where, again taking $t \ll \omega_{\mathrm{M}}^{-1}$, $V_{\mathrm{FF}}^{(\mathrm{RWA})} = (2\bar{n}_{\mathrm{H}} + 1)\Gamma t \mathbb{1}$, with $\mathbb{1}$ being the identity matrix.

6.2.1 Born–Markov master equation

It is instructive to consider the oscillator's dynamics under the BMME. The reader is encouraged to compare this section with § 3.3.1.

Solving Eqn (6.2) requires knowledge of the noise correlation functions. Since Eqn (6.2) is in fact equivalent to Eqn (2.5a) we may use our knowledge of the correlation functions Eqn (2.8)

$$\left\langle X_{\mathrm{in}}(t)^2 \right\rangle = (2\bar{n}_{\mathrm{H}} + 1)\,\delta\left(t - t'\right),$$

$$\left\langle P_{\mathrm{in}}(t)^2 \right\rangle = (2\bar{n}_{\mathrm{H}} + 1)\,\delta\left(t - t'\right),$$

$$\Re\left\{\langle X_{\mathrm{in}} P_{\mathrm{in}} \rangle\right\} = 0.$$

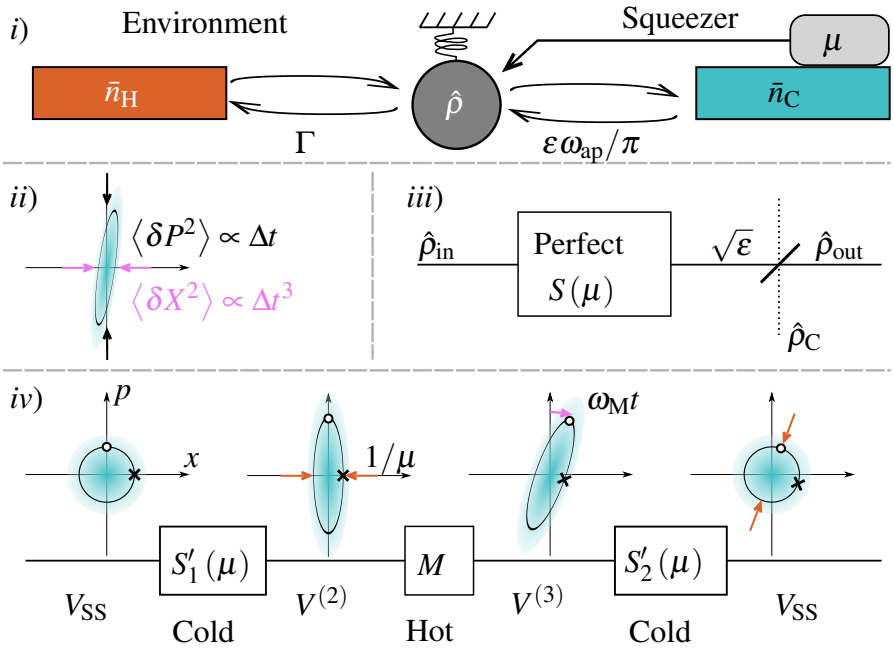

Figure 6.1: A thermodynamic system utilising quantum squeezing.
i) System schematic. A harmonic oscillator (grey circle) in state $\hat{\rho}$ is coupled to a hot bath ($\bar{n}_H$, orange). A work reservoir (μ) performs perfect squeezing operations on the oscillator. Imperfections in the squeezers couple the oscillator to a cold bath ($\bar{n}_C$, blue).
ii) Wigner representation of the noise added during interaction with the hot bath (V_{FF}).
iii) Model of imperfect squeezing operation S'_j.
iv) Diagram of a single step of the squeeze–rotate–squeeze protocol. Time flows to the right.

Using these yields the evolution of the covariance matrix, which is entirely analogous to Supp. Eqn (3.12) except that

$$M^{(\mathrm{RWA})} = \mathrm{e}^{-\Gamma t/2} R\left(\omega_M t\right)$$

and

$$V_{FF}^{(\mathrm{RWA})} = \left(2\bar{n}_H + 1\right)\left(1 - \mathrm{e}^{-\Gamma t}\right)\mathbb{1},$$

where $R\left(\omega_M t\right)$ is a rotation through an angle of $\omega_M t$, and $\mathbb{1}$ is the identity matrix. Note that $V_{FF}^{(\mathrm{RWA})}$ is proportional to the identity matrix, and at short times both diagonal elements of $V_{FF}^{(\mathrm{RWA})}$ grow at first order in t; this is very different behaviour from the independent oscillator model, where $V_{FF}^{(1,1)}$ initially only increases at third order in t.

Despite this, the long-time behaviour in the RWA is identical to the independent oscillator model, *viz.*

$$V_{SS}^{(\mathrm{RWA})} = \lim_{t\to\infty} V\left(t\right) = \left(2\bar{n}_H + 1\right)\mathbb{1} = V_{SS}^{(\mathrm{IO})}.$$

6.3 A squeezing-driven thermodynamic device

In § 6.2 we made observations that indicate that there is a link between the short-time behaviour of Eqn (6.1) and squeezing. We will therefore consider the possibility of manipulating the dissipative dynamics using squeezing operations that are applied much more frequently than ω_M.

6.3.1 Squeeze–rotate–squeeze engine

Our proposed protocol is divided into three broad steps (see Fig. 6.1 *i*) & *iv*)): an initial imperfect squeezing operation S_1', a short time of evolution whilst in contact with the hot bath, and a second imperfect squeezer S_2'. This sequence is repeated at a rate of $\omega_{\rm ap} = 2\pi/t$.

As seen in Fig. 6.1 *iii*), each imperfect squeezer S_j' $(j = 1,2)$ is modelled by subdividing it into two further steps. The first is a unitary squeezing operation S_j, distinguished by the lack of prime. The second is a beamsplitter interaction between the system and a thermal state of covariance $V_{\rm C} = (2\bar{n}_{\rm C}+1)\,\mathbb{1}$, with transmissivity $1-\varepsilon$ and effective thermal occupancy $\bar{n}_{\rm C} < \bar{n}_{\rm H}$. We did investigate a more advanced squeezing model, as discussed in App. A.7, but in most regimes it predicts behaviour similar to that obtained with this simple model.

We select the first squeezer (S_1) such that it performs the operation $X \to \mu^{-1}X$ & $P \to \mu P$, where μ is the squeezing strength. The momentum becomes antisqueezed for $\mu > 1$ and squeezed for $\mu < 1$. S_2 is then chosen to be $S_2 = RS_1^{-1}R^{\rm T}$ where R is a rotation matrix with angle $\omega_{\rm M}t$. This choice ensures that if the oscillator is decoupled from both hot and cold baths ($\Gamma = 0$, $\varepsilon = 0$, under which conditions $M = R$) the evolution induced by the protocol is completely passive, with the state effectively experiencing only free evolution.

6.3.2 History of quantum thermodynamic engines

Let us briefly acknowledge the history of quantum thermodynamic engines modelled using open quantum systems approaches (*e.g.* [287, 288]). The first detailed studies of quantum heat engines operating in finite time were carried out by [289–295], followed by investigations of quantum heat pumps [289, 292], and later studies of quantum refrigerators [294, 296, 297]. Some of these devices operate in a cyclical fashion, like most classical thermodynamic devices, whilst others operate continuously.

6.4 The periodic 'steady-state'

A typical thermodynamic device (engine, pump, or refrigerator) operates by performing a cyclical process in which the working fluid is returned to the same state at the end of each cycle. We will refer to this as the 'steady-state'. Repeated application of our squeezing protocol will gradually force any initial state towards a zero-mean Gaussian 'steady-state' with covariance $V_{\rm SS}$ [2] defined by the self-consistency condition

$$V_{\rm SS} = M_{\rm hom} V_{\rm SS}\, M_{\rm hom}^{\rm T} + V_{\rm add}. \tag{6.4}$$

The matrix $M_{\rm hom} = (1-\varepsilon)\,S_2 M(t)\,S_1$ is the homogeneous component of the evolution, and

$$\begin{aligned} V_{\rm add} \;&=\; (1-\varepsilon)\,S_2 V_{\rm FF} S_2^{\rm T} \\ &\quad + \varepsilon\left[\mathbb{1} + (1-\varepsilon)\,S_2 M M^{\rm T} S_2^{\rm T}\right] V_{\rm C} \end{aligned}$$

[2] This approach to steady-state is guaranteed because $\det\{M_{\rm hom}\} < 1$.

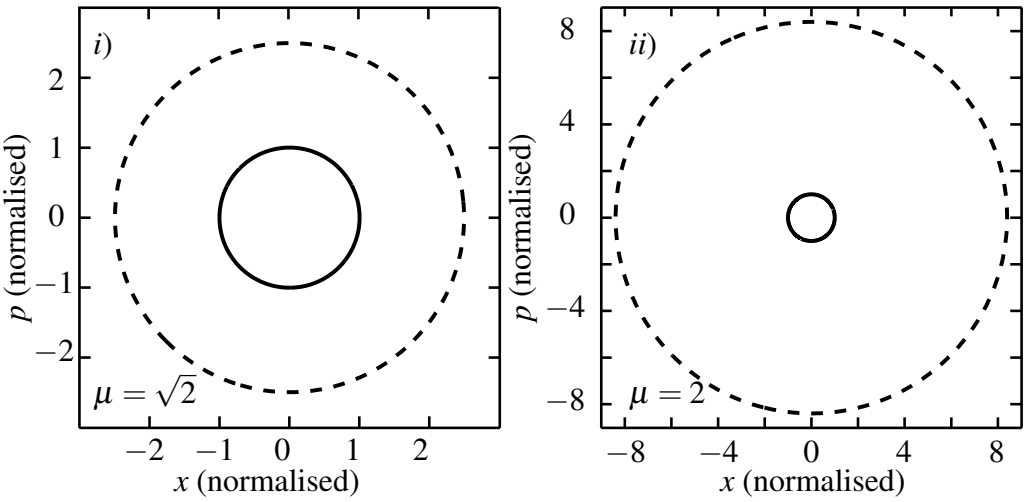

Figure 6.2: Comparison of steady-state Wigner function contours calculated using momentum-dependent damping (solid lines) and in the RWA (dashed). The axes in each panel have been normalised such that the maximum eigenvalue of $V_{\rm SS}$ (without the RWA) is equal to unity. The system parameters are $\omega_{\rm M} = 10^6$ Hz, $Q = 10^6$, $\bar{n}_{\rm H} = 4\times10^4$, $\bar{n}_{\rm C} = 10^2$, and $\varepsilon = \pi\times10^{-9}$, with the squeezing parameters indicated in each panel. Small squeezing strengths have been chosen because the relative size of $V_{\rm SS}^{(\rm RWA)}$ grows rapidly with μ.

is the aggregate effect of the noise entering from the baths. It is critical to note that $V_{\rm FF}$ and $\varepsilon V_{\rm C}$ are strongly modified by S_2. This allows us to manipulate the squeezing of $V_{\rm add}$ by adjusting the evolution time t and squeezing strength μ.

Eqn (6.4) can be recognised as a Sylvester equation, which is readily solved using standard numerical techniques. Solutions show that the steady-state is very well approximated by the thermal state $V_{\rm SS} = (2\bar{n}_{\rm SS}+1)\,\mathbb{1}$, where $\bar{n}_{\rm SS}$ is the effective occupancy. Two examples are given in Fig. 6.2.

Representative calculations of $\bar{n}_{\rm SS}$ as a function of the squeezing strength μ and the squeezing application rate $\omega_{\rm ap} = 2\pi/t$ are given in Fig. 6.3 *i*) & *ii*). We use $\omega_{\rm M} = 1$ MHz & $Q = 10^6$—as might be expected for SiN or SiC microstrings [4]—and $\bar{n}_{\rm H} = 4\times10^4$ ($T_{\rm H} \approx 300$ mK, achievable in a 3-He cryostat), and will continue to use these parameters throughout this chapter unless otherwise stated.

Fig. 6.3 clearly shows that the squeeze–rotate–squeeze protocol can reduce the temperature of the oscillator to well below $\bar{n}_{\rm H}$, opening up a new method of cooling mechanical oscillators to study their quantum behaviour, and as a preparatory step for quantum sensing and information processing protocols [70].

6.4.1 Analytical approximation for steady-state occupancy

To understand the cooling effect of our protocol we cast Eqn (6.4) in the typical form of a Sylvester equation by noting that $M_{\rm hom}^{-1}$ does exist for any non-negative, finite time t. Thus

$$M_{\rm hom}^{-1} V_{\rm SS} - V_{\rm SS}\, M_{\rm hom}^{\rm T} = M_{\rm hom}^{-1} V_{\rm add}. \tag{6.5}$$

This can be solved analytically, in principle. The general solution to Supp. Eqn (6.5) is [298]

$$\mathrm{vec}\{V_{\rm SS}\} = \left(\mathbb{1}\otimes\left(M_{\rm hom}^{-1}\right) - M_{\rm hom}\otimes\mathbb{1}\right)^{-1} \mathrm{vec}\left\{M_{\rm hom}^{-1} V_{\rm add}\right\},$$

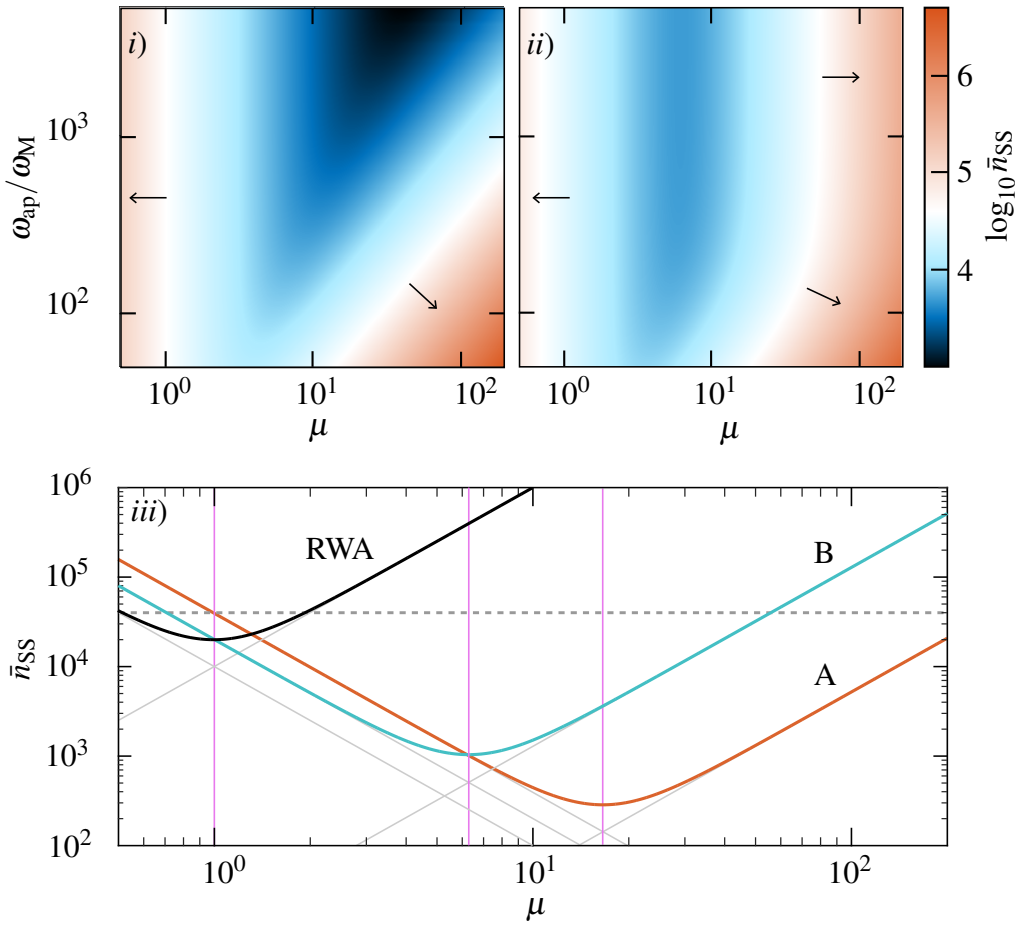

Figure 6.3: Steady-state temperature of the oscillator.
i) Effective steady-state occupancy $\bar{n}_{SS}$ of the oscillator subject to perfect squeezing ($\varepsilon = 0$; no cold bath) of magnitude μ at a rate of ω_{ap}. White indicates $\bar{n}_{SS} = \bar{n}_H$. Arrows indicate the directions of increasing $\bar{n}_{SS}$. Other parameters given in text.
ii) $\bar{n}_{SS}$ with imperfect squeezing. The cold bath occupancy is $\bar{n}_C = 10^2$, and ε has been adjusted at each ω_{ap} such that the effective Q is held constant (*i.e.* $\pi\omega_M/\varepsilon\omega_{ap} = \omega_M/\gamma = 10^6$).
iii) Cross sections through parts *a* (A, orange) and *b* (B, blue) at $\omega_{ap}/\omega_M = 10^3$. The RWA result is given in black. Numerical results are indistinguishable from the analytical approximation on this scale. The optimum values of μ are shown as pink vertical lines. Solid grey lines show the expected $\bar{n}_{SS} \propto \mu^{-2}$ scaling for $\mu < \mu_{opt}$, and the $\bar{n}_{SS} \propto \mu^2$ scaling for $\mu > \mu_{opt}$; the dashed grey line indicates the hot bath occupancy $\bar{n}_H$.

where $\otimes$ is the Kronecker product and $\mathrm{vec}\{\cdots\}$ is the vectorisation operation (defined in App. A.8).

As seen in Fig. 6.2, the steady-state Wigner function is essentially symmetrical between position and momentum. Therefore, the state is thermal and characterised by an effective occupancy

$$\bar{n}_{\mathrm{SS}} = \frac{\sqrt{\det\{V_{\mathrm{SS}}\}} - 1}{2}.$$

$\bar{n}_{\mathrm{SS}}$ can in principle be calculated entirely analytically, but the resulting expression is immensely unwieldy. Instead, we will find an approximate expression that is accurate in the region of interest ($\{Q, \bar{n}_{\mathrm{H}}\} \gg 1$, $\{\varepsilon, \varepsilon\bar{n}_{\mathrm{C}}, \omega_{\mathrm{M}}t\} \ll 1$).

For simplicity, let us first consider the perfect squeezing ($\varepsilon = 0$) case. Each matrix may be calculated analytically. We then expand $\mathrm{vec}\{V_{\mathrm{SS}}\}$ to second order in t, calculate the determinant, and truncate the result at $\mathscr{O}(t^2)$ and $\mathscr{O}(\Gamma)$. Discarding small terms (which are not boosted by μ) then gives

$$\bar{n}_{\mathrm{SS}}|_{\varepsilon=0} \approx \bar{n}_{\mathrm{H}} \left(\frac{1}{\mu^2} + \frac{4\pi^2\omega_{\mathrm{M}}^2}{3\omega_{\mathrm{ap}}^2}\mu^2 \right). \tag{6.6}$$

Consider the coefficient of μ^2 in Eqn (6.6). This can in fact be related directly to properties of the added noise. To see this, let us ask which value of μ minimises the energy contained by the added noise V_{add}. In this case ($\varepsilon = 0$) we have $V_{\mathrm{add}} = S_2 V_{\mathrm{FF}} S_2^{\mathrm{T}}$; thus we wish to select the value of μ that minimises $\mathrm{Tr}\left\{S_2^{\mathrm{T}} S_2 V_{\mathrm{FF}}\right\}$. Calculating this yields

$$\mu_{\mathrm{opt}}^4\big|_{\varepsilon=0} = \frac{3\omega_{\mathrm{ap}}^2}{4\pi^2\omega_{\mathrm{M}}^2},$$

which is the inverse of the coefficient of μ^2 in Eqn (6.6).

Similarly, consider the $\mu = 1$ value of $\bar{n}_{\mathrm{SS}}|_{\varepsilon=0}$, which is approximately $\bar{n}_{\mathrm{H}}$.

If we rewrite $\bar{n}_{\mathrm{SS}}$ as

$$\bar{n}_{\mathrm{SS}}|_{\varepsilon=0} = \left(\bar{n}_{\mathrm{SS}}|_{\mu=1}\right) \left(\frac{1}{\mu^2} + \frac{\mu^2}{\mu_{\mathrm{opt}}^4|_{\varepsilon=0}} \right)$$

then—guided by our numerical calculations—we can make the educated guess that the same form holds when the squeezers become imperfect.

The first factor $\bar{n}_{\mathrm{SS}}|_{\mu=1}$ needs to be generalised to there being two baths. The most likely estimate is the typical equilibrium occupancy expected from detailed balance[3], *viz.*

$$\bar{n}_{\mathrm{SS}}|_{\mu=1} \to \frac{\Gamma\bar{n}_{\mathrm{H}} + \gamma\bar{n}_{\mathrm{C}}}{\Gamma + \gamma}.$$

The effective coupling rate to the cold bath is γ, which is taken to be $\gamma = 2\varepsilon/t = \varepsilon\omega_{\mathrm{ap}}/\pi$ because the loss of 2ε occurs over every timestep t.

[3] Note the similarity between this and Eqn (2.12).

Secondly, we replace $\mu_{\rm opt}|_{\varepsilon=0}$ with the value of μ that minimises the trace of $V_{\rm add}$ *including* noise from the cold bath. This may be analytically found to be

$$\mu_{\rm opt} = \left(\frac{\left[\begin{array}{c} (2\bar{n}_{\rm H}+1-\varepsilon(2\bar{n}_{\rm C}+1))\left(4\omega_{\rm M}-4\omega_{\rm M}\left(1-\sigma^2\right)\cos 2\omega_{\rm M}\sigma t \right. \\ \left. -2\Gamma\sin 2\omega_{\rm M}\sigma t+\Gamma(1-\sigma)\sin 4\omega_{\rm M}\sigma t)-4\omega_{\rm M}{\rm e}^{\Gamma t}(2\bar{n}_{\rm H}+1)\sigma^2 \right] }{\left[\begin{array}{c} (2\bar{n}_{\rm H}+1-\varepsilon(2\bar{n}_{\rm C}+1))\left(4\omega_{\rm M}-4\omega_{\rm M}\left(1-\sigma^2\right)\cos 2\omega_{\rm M}\sigma t \right. \\ \left. +2\Gamma\sin 2\omega_{\rm M}\sigma t-\Gamma(1-\sigma)\sin 4\omega_{\rm M}\sigma t)-4\omega_{\rm M}{\rm e}^{\Gamma t}(2\bar{n}_{\rm H}+1)\sigma^2 \right] } \right)^{1/4},$$

which simplifies (for small t and ε) to

$$\mu_{\rm opt} \approx \left(\frac{1-{\rm e}^{-\Gamma t}\left(1-\varepsilon\frac{2\bar{n}_{\rm C}+1}{2\bar{n}_{\rm H}+1}\right)\left(1-\frac{\Gamma}{2\omega_{\rm M}}\sin 2\omega_{\rm M}t\right)}{1-{\rm e}^{-\Gamma t}\left(1-\varepsilon\frac{2\bar{n}_{\rm C}+1}{2\bar{n}_{\rm H}+1}\right)\left(1+\frac{\Gamma}{2\omega_{\rm M}}\sin 2\omega_{\rm M}t\right)} \right)^{1/4}. \tag{6.7}$$

Thus

$$\bar{n}_{\rm SS} \approx \frac{\Gamma\bar{n}_{\rm H}+\gamma\bar{n}_{\rm C}}{\Gamma+\gamma}\left(\frac{1}{\mu^2}+\frac{\mu^2}{\mu_{\rm opt}^4}\right). \tag{6.8}$$

This is an excellent approximation, as seen in Fig. 6.3 panel *iii*).

The functional form of Eqn (6.8) is reminiscent of that of the standard quantum limit for position measurement on a free mass, where an optimal interaction strength exists that balances measurement noise with quantum back-action noise [70]. In this case the balance is between attenuating the noise added to P and amplifying the noise added to X during each timestep. These processes can be linked to the μ^{-2} and $\mu^2/\mu_{\rm opt}^4$ terms of Eqn 6.8 respectively. When the squeezing strength reaches $\mu_{\rm opt}$ the noises added to X and P are equal, and the total noise energy is minimised. Increasing the squeezing beyond this point begins to increase the noise energy, as S_2 amplifies the noise entering on X to the point that it dominates.

It should be noted that in the limiting case of $\bar{n}_{\rm C} \gg 1$ and $\bar{n}_{\rm H} \gg \bar{n}_{\rm C}$, $\mu_{\rm opt}$ reduces to a simple ratio of heating rates, *viz.* $\mu_{\rm opt} \approx \sqrt{2}\,(\Gamma T_{\rm H}/\gamma T_{\rm C})^{1/4}$, so that

$$\bar{n}_{\rm SS}|_{\mu=\mu_{\rm opt}} \approx \frac{\sqrt{\Gamma\gamma\bar{n}_{\rm C}\bar{n}_{\rm H}}}{\Gamma+\gamma}.$$

This shows that the oscillator may be made arbitrarily cold—even colder than $\bar{n}_{\rm C}$—as $\gamma \to 0$ or $\Gamma \to 0$. The full numerical calculations support this conclusion, as seen in Fig. 6.4. As we shall see, the mechanism underlying this behaviour is essentially 'heat pumping' into the bath with the largest decay rate. Of course, this is an asymptotic limit, as the cooling rate also falls under these conditions in accordance with the Third Law of Thermodynamics.

Steady-state occupancy in the RWA

Repeating the same exercise in the RWA yields

$$\bar{n}_{\rm SS}^{\rm RWA} \approx \frac{1}{2}\frac{\Gamma\bar{n}_{\rm H}+\gamma\bar{n}_{\rm C}}{\Gamma+\gamma}\left(\frac{1}{\mu^2}+\mu^2\right). \tag{6.9}$$

which is never less than the simple detailed-balance equilibrium value of

$$\bar{n}_{\rm SS}|_{\mu=1} \approx \bar{n}_{\rm SS}^{\rm RWA}|_{\mu=1} = (\Gamma\bar{n}_{\rm H}+\gamma\bar{n}_{\rm C})(\Gamma+\gamma)^{-1}.$$

Thus in the RWA it is never possible to achieve $\bar{n}_{\rm SS} < n_{\rm C}$.

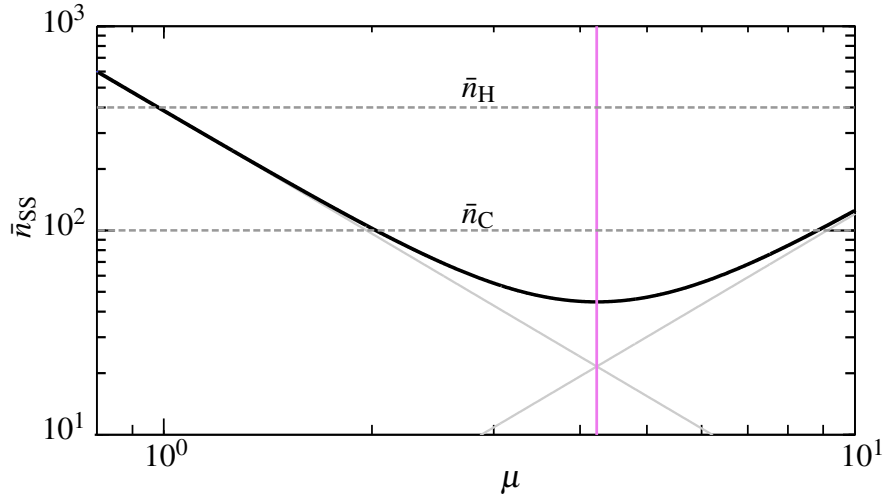

Figure 6.4: Numerical calculations showing that the oscillator can be colder than the cold bath occupancy $\bar{n}_{\rm C}$ (lower grey dashed line). Parameters: $\bar{n}_{\rm H} = 4\times10^2$, $\bar{n}_{\rm C} = 10^2$, $\omega_{\rm ap}/\omega_{\rm M} = 5\times10^3$, $Q = 10^6$, $\omega_{\rm M} = 10^6$ Hz, & $\varepsilon = \pi\times10^{-11}$.

6.5 Thermodynamic cycles

As clearly shown in Fig. 6.3 *i*), $\bar{n}_{\rm SS}$ can be reduced well below $\bar{n}_{\rm H}$ even when $\varepsilon = 0$. The second law of thermodynamics implies that this must be accompanied by a net heat flux *into* the hot bath, because otherwise the system would extract work from a single thermal bath and reduce the entropy of the universe. The system is acting as a heat pump, taking work from the squeezers and pushing it into the hot bath.

In order to determine if this behaviour persists with imperfect squeezers we calculate the work (W), heat from the cold bath ($Q_{\rm C}$), and heat from the hot bath ($Q_{\rm H}$) during a cycle of evolution in the steady-state. A positive number indicates an influx of energy to the oscillator, normalised to units of mechanical quanta. It is clear that because the perfect squeezers S_j are unitary (isentropic) they are associated with W, with the other operations corresponding to heat exchange. Thus

$$W = \frac{1}{4}\mathrm{Tr}\left\{SV_{\rm SS}S^{\rm T} - V_{\rm SS} + S_2V^{(3)}S_2^{\rm T} - V^{(3)}\right\} \tag{6.10a}$$

$$Q_{\rm H} = \frac{1}{4}\mathrm{Tr}\left\{V^{(3)} - V^{(2)}\right\}, \tag{6.10b}$$

where $V^{(2)}$ and $V^{(3)}$ are the covariance matrices immediately after S_1' and immediately before S_2' respectively (*cf.* Fig. 6.1 *iv*)). Given that the process is cyclical, the heat transferred to the cold bath is $Q_{\rm C} = -(W + Q_{\rm H})$.

The system can indeed act as a heat pump when the cold bath is present, fulfilling $Q_{\rm H} < 0$ & $W > 0$. It can also act as a heat engine ($Q_{\rm H} > 0$ & $W < 0$); or as a refrigerator ($Q_{\rm C} > 0$ & $W > 0$). These regimes are shown in Fig. 6.5. There is also a fourth region in which the work performed on the system is positive but insufficient to reverse the flow of heat from the hot bath to the oscillator. Together, these form a 'phase diagram' that is vastly richer than the RWA predicts.

The heat pump behaviour is straightforward to understand by considering the limit as the time between squeezers (t) tends to zero. The damping rate of the system into the hot bath then becomes

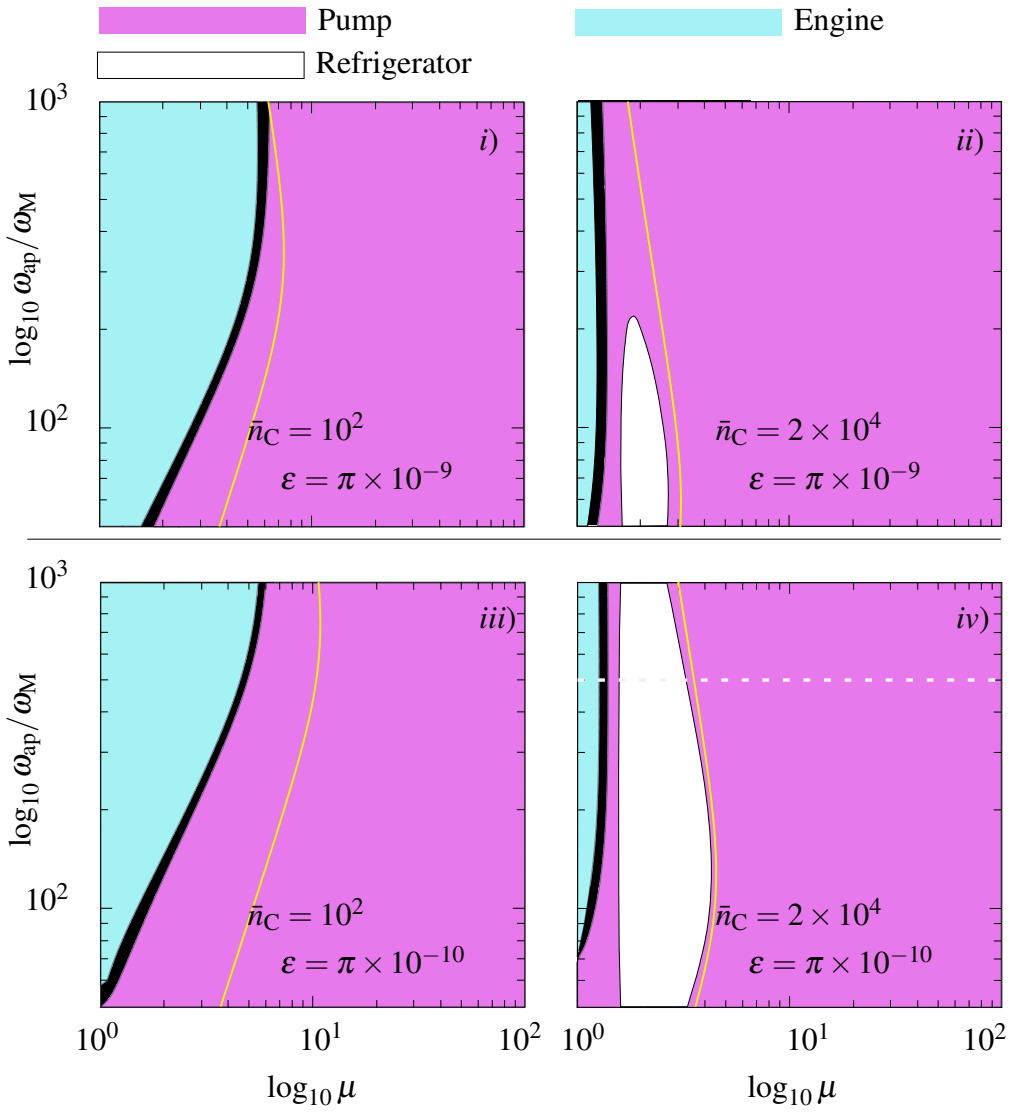

Figure 6.5: Approximate operating regimes of the squeeze–rotate–squeeze protocol for different cold bath occupancies $\bar{n}_{\rm C}$ and coupling constants ε. In the black region energy flows from hot to cold even with the application of work. Panels *i*) and *ii*) correspond to $\omega_{\rm M}/\gamma = 10^6$, whilst *iii*) and *iv*) have $\omega_{\rm M}/\gamma = 10^7$. Note that if $\varepsilon = 0$ (no cold bath) the system never exhibits refrigeration or heat engine behaviour. Other parameters given in text. The white dashed line in *iv*) indicates the cross-section plotted in Fig. 6.6, and the yellow lines show $\mu_{\rm opt}$.

$2\Gamma\langle P^2\rangle$, where $\langle P^2\rangle$ is boosted above its 'steady-state' value by a factor of $(1-\varepsilon)\mu^2$ during the first squeezing interaction. Thus heat pumping occurs whenever this boosted loss rate overwhelms the noise coming in from the bath. This phenomenon is also behind the remarkable fact that the oscillator may be cooled to temperatures lower than that of the cold bath, unlike with other cooling techniques such as sideband cooling (see Fig. 6.4 and [102]).

In the heat engine region the system is extracting work from the hot bath and dumping entropy into the cold bath. This occurs when the state $V^{(3)}$ is more squeezed than $V^{(2)}$. The momentum-damped Langevin equations (Eqn (3.20)) permit this if

$$2\bar{n}_{\mathrm{H}}+1>(1-\varepsilon)\,(2\bar{n}_{\mathrm{SS}}+1)\,\mu^2+\varepsilon\,(2\bar{n}_{\mathrm{C}}+1)\,. \tag{6.11}$$

When $\{\varepsilon,\varepsilon\bar{n}_{\mathrm{C}}\}\ll 1\ll\bar{n}_{\mathrm{H}}$ this becomes $n_{\mathrm{H}}>\bar{n}_{\mathrm{SS}}\mu^2$ *i.e.* the 'apparent occupancy' of the momentum must be less than the hot bath occupancy, such that more heat flows from the bath to the oscillator than in the reverse direction. A derivation of this criterion is given in § 6.6.1.

Refrigeration—removing heat from the cold bath—only occurs when $\bar{n}_{\mathrm{C}}$ is sufficiently large. The sign of Q_{C} may be determined by considering the two loss steps involving the cold bath, as shown in § 6.6.2. For small ε we find the condition for refrigeration is

$$\bar{n}_{\mathrm{C}}>\frac{\bar{n}_{\mathrm{SS}}}{2}\left(1+\frac{\mu^2+\mu^{-2}}{2}\right). \tag{6.12}$$

By explicitly calculating the steady-state covariance matrix in the RWA we were able to derive no-go theorems (§ 6.7) that show that the heat engine and refrigerator phases of operation are forbidden in the RWA. The former proof is valid in all parameter regimes satisfying basic requirements of physicality, whilst the latter is valid in the $\varepsilon\ll 1$ and $\Gamma\ll\omega_{\mathrm{M}}\ll\omega_{\mathrm{ap}}$ regime considered throughout this chapter.

Finally, we can consider the performance of the available thermodynamic cycles. The relevant coefficients of performance (COP) are defined by

$$\mathrm{COP}_{\mathrm{pump}} = |Q_{\mathrm{H}}/W|\leq\eta^{-1} \tag{6.13a}$$

$$\mathrm{COP}_{\mathrm{engine}} = |W/Q_{\mathrm{H}}|\leq\eta \tag{6.13b}$$

$$\mathrm{COP}_{\mathrm{fridge}} = |Q_{\mathrm{C}}/W|\leq(1-\eta)/\eta, \tag{6.13c}$$

where the thermodynamic limits (inequalities) are expressed in terms of the Carnot efficiency $\eta=1-T_{\mathrm{C}}/T_{\mathrm{H}}$. These describe how much of the desired result (numerator) is obtained per input energy (denominator); for example, the heat pump is desired to use input work to force heat into the hot bath, so we take the ratio of Q_{H} (desired result) to W (input energy). Conversely, a refrigerator is desired to remove heat from the cold bath as a result of input work, requiring that the numerator be Q_{C}.

A representative calculation is provided for a cross-section through Fig. 6.5 *iv*), as shown in Fig. 6.6 *i*). This demonstrates that (for these parameters) the peak engine efficiency is approximately one third of the Carnot limit. It also confirms that the heat pumping efficiency is maximised when the squeezing strength μ is below the value μ_{opt} that minimises the steady-state occupancy. Conversely, in the RWA

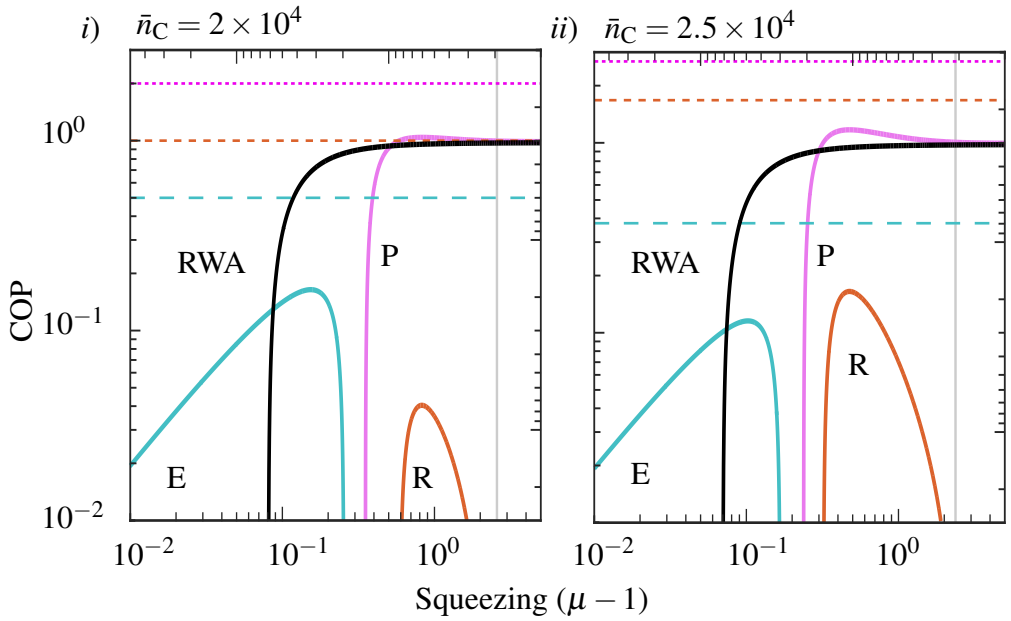

Figure 6.6: Coefficients of performance when operating as a heat pump (pink, P), heat engine (blue, E), or refrigerator (orange, R). The black line shows the RWA prediction for the heat pump phase; note that it does not exceed one for any μ. Thermodynamic bounds are shown as dashed lines (E, P, and R in order of increasing dash length). Panel *i*) shows a cross-section through Fig. 6.5 *iv*). Other system parameters: $\omega_{ap} = 500\omega_M$, $\varepsilon = \pi \times 10^{-10}$, and as given in text.

case the heat pump efficiency improves monotonically with μ. This difference arises because the RWA has only a heat pump phase, as we prove in § 6.7. Calculations for different bath temperatures (*e.g.* Fig. 6.6 *ii*)) show the expected trends: namely that the heat engine becomes less efficient as $\bar{n}_C$ increases, whereas $\mathrm{COP}_{\mathrm{fridge}}$ improves with $\bar{n}_C$.

6.6 Bounds on the existence of thermodynamic cycles

Consider a complete cycle of the squeeze–rotate–squeeze protocol with lossy squeezing as described in the main text. For clarity, let us divide up the protocol into the following steps (*cf.* Fig. 6.1 and Eqn (6.10)):

$$\begin{aligned} V^{(1)} &= S_1 V_{SS} \, {S_1}^{\mathrm{T}} \\ V^{(2)} &= (1-\varepsilon) V^{(1)} + \varepsilon \, (2\bar{n}_C + 1) \, \mathbb{1} \\ V^{(3)} &= M V^{(2)} \, M^{\mathrm{T}} \\ V^{(4)} &= S_2 V^{(2)} \, {S_2}^{\mathrm{T}} \\ V_{SS} &= (1-\varepsilon) V^{(4)} + \varepsilon \, (2\bar{n}_C + 1) \, \mathbb{1}. \end{aligned}$$

The squeezing steps perform work, allowing us to identify the total work (in units of quanta) as

$$W = \frac{1}{4} \mathrm{Tr} \left\{ V^{(4)} - V^{(3)} + V^{(1)} - V_{SS} \right\}.$$

Similarly,

$$\begin{aligned} Q_{\mathrm{H}} &= \frac{1}{4}\mathrm{Tr}\left\{V^{(3)} - V^{(2)}\right\}, \\ Q_{\mathrm{C}} &= \frac{1}{4}\mathrm{Tr}\left\{V_{\mathrm{SS}} - V^{(4)} + V^{(2)} - V^{(1)}\right\}. \end{aligned}$$

We will use these and the approximation $V_{\mathrm{SS}} = (2\bar{n}_{\mathrm{SS}} + 1)\,\mathbb{1}$ to derive bounds on that parameter regimes permit particular thermodynamic cycles. Note that none of these results depend on the specific form of $\bar{n}_{\mathrm{SS}}$ *i.e.* they do not rely on Eqn (6.8) being accurate.

6.6.1 Criterion for heat engine phase

The system behaves as a heat engine if it receives heat from the hot bath ($Q_{\mathrm{H}} > 0$) and produces output work ($W < 0$). Any excess entropy is dumped into the cold bath.

Our numerical calculations show that the engine phase overlaps very well with the parameter regime where $V^{(3)}$ is more squeezed than $V^{(2)}$ *i.e.* where the asymmetry of the lossy evolution step is strong enough to actually *increase* the asymmetry of the Wigner function over a short timestep.

Firstly, let us establish that the degree of squeezing present in an arbitrary (single mode, 2×2) covariance matrix can be expressed as the ratio of its eigenvalues, κ. For a vacuum state operated on by $S_j(\mu)$ we have $\kappa = \langle P^2 \rangle / \langle X^2 \rangle = \mu^4$. It is easily seen that κ is in fact a function of

$$K = \frac{\mathrm{Tr}\{V\}}{\sqrt{|V|}},$$

which is directly proportional to the product of the energy ($\propto \mathrm{Tr}\{V\}$) and purity $|V|^{-1/2}$ of the state. Thus we can use K as a proxy for the level of squeezing.

To simplify the calculation of $K^{(2)}$ and $K^{(3)}$ we will consider the high-Q limit and set $\sigma = \sqrt{1 - \Gamma^2/4\omega_{\mathrm{M}}^2} \to 1$. We expand the resulting inequality around small t to first order, yielding

$$(2\bar{n}_{\mathrm{H}} + 1)\left(V_{\mathrm{XP}}^{(2)\,2} + V_{\mathrm{XX}}^{(2)\,2} - |V|\right) < \left(V_{\mathrm{XX}}^{(2)} - V_{\mathrm{PP}}^{(2)}\right)|V|,$$

where the diagonal elements of V are V_{XX} and V_{PP}, and the off-diagonal elements are both V_{XP}. Since $V^{(2)}$ is position squeezed the right hand side of this inequality is a negative number. Thus we get

$$(2\bar{n}_{\mathrm{H}} + 1) > \frac{V_{\mathrm{PP}}^{(2)} - V_{\mathrm{XX}}^{(2)}}{1 - V_{\mathrm{XX}}^{(2)\,2}/|V|},$$

where we used the fact that $V_{\mathrm{XP}}^{(2)} = 0$. Now we can write $V^{(2)} = \sqrt{|V|}\,\mathrm{diag}\{\eta^{-2}, \eta^2\}$, where η is the squeezing parameter after being degraded by the cold bath. Then we obtain

$$(2\bar{n}_{\mathrm{H}} + 1) > \sqrt{|V|}\,\eta^2 = \sqrt{V_{\mathrm{XX}}^{(2)}\,V_{\mathrm{PP}}^{(2)}}\left(\frac{V_{\mathrm{PP}}^{(2)\,2}}{V_{\mathrm{XX}}^{(2)\,2}}\right)^{1/4} = V_{\mathrm{PP}}^{(2)}.$$

Substituting the explicit form of the variance yields (as given in Eqn (6.11))

$$(2\bar{n}_{\mathrm{H}} + 1) > (1 - \varepsilon)(2\bar{n}_{\mathrm{SS}} + 1)\,\mu^2 + \varepsilon(2\bar{n}_{\mathrm{C}} + 1),$$

which in most cases of interest ($\{\varepsilon, \varepsilon\bar{n}_{\mathrm{C}}\} < 1 \ll \bar{n}_{\mathrm{H}}$) can be replaced by the simplified condition

$$\bar{n}_{\mathrm{H}} > \mu^2 \bar{n}_{\mathrm{SS}}.$$

6.6.2 Criterion for refrigeration phase

In the refrigeration regime, the resonator uses input work ($W > 0$) to extract heat from the cold reservoir ($Q_{\mathrm{C}} > 0$) and push it into the hot reservoir ($Q_{\mathrm{H}} < 0$).

Consider $Q_{\mathrm{C}} > 0$. Thus

$$\mathrm{Tr}\left\{V_{\mathrm{SS}} - V^{(4)} + V^{(2)} - V^{(1)}\right\} > 0.$$

By rearranging $V_{\mathrm{SS}} = (1-\varepsilon)V^{(4)} + \varepsilon(2\bar{n}_{\mathrm{C}}+1)\mathbb{1}$ this can be written entirely in terms of S_1 and V_{SS}, *viz.*

$$\left(1 - \frac{1}{1-\varepsilon}\right)\mathrm{Tr}\{V_{\mathrm{SS}}\} - \varepsilon\mathrm{Tr}\left\{S_1^2 V_{\mathrm{SS}}\right\} + 2\varepsilon\left(\frac{1}{1-\varepsilon}+1\right)(2\bar{n}_{\mathrm{C}}+1) > 0.$$

Using the fact that $V_{\mathrm{SS}} = (2\bar{n}_{\mathrm{SS}}+1)\mathbb{1}$, we obtain

$$\frac{2-\varepsilon}{1-\varepsilon}(2\bar{n}_{\mathrm{C}}+1) > \left(\frac{1}{1-\varepsilon} + \frac{\mu^2+\mu^{-2}}{2}\right)(2\bar{n}_{\mathrm{SS}}+1).$$

In the limit that $\varepsilon \ll 1$ this becomes equal to Eqn (6.12).

6.7 No-go theorems in the RWA

The following no-go theorems are based on the complete analytical result for the steady-state covariance matrix in the RWA, not on the approximate expression Eqn 6.9.

6.7.1 No-go theorem for heat engines

We calculated the exact criterion for heat engine function in the RWA using Wolfram Mathematica. The expression $W^{(\mathrm{RWA})} < 0$ factorises into a form involving three factors, two of which are always positive. The final factor is only negative when

$$\mu^4 + B\mu^2 + 1 < 0, \tag{6.14}$$

where

$$B = \frac{a(2\bar{n}_{\mathrm{H}}+1) + b(2\bar{n}_{\mathrm{C}}+1)}{c(2\bar{n}_{\mathrm{H}}+1) + d(2\bar{n}_{\mathrm{C}}+1)},$$

with a, b, c, and d being functions of ε, t, Γ, and ω_{M}, *viz.*

$$\begin{aligned}
a &= \left(e^{\Gamma t}-1\right)\left(e^{\Gamma t} - (1-\varepsilon)^2\right)\left(e^{\Gamma t} + (1-\varepsilon)^3 - (1-\varepsilon)\left(1 + e^{\Gamma t} - \varepsilon\right)\cos 2\omega_{\mathrm{M}} t\right)\csc^2\omega_{\mathrm{M}} t \\
b &= \varepsilon\left[\begin{array}{c} e^{3\Gamma t} - 2(1-\varepsilon)^5 + e^{2\Gamma t}\varepsilon + e^{\Gamma t}(1-\varepsilon)^2(1-\varepsilon(3-\varepsilon)) - \\ (1-\varepsilon)\left(e^{2\Gamma t}(3-2\varepsilon) - (1-\varepsilon)^3 + e^{\Gamma t}(\varepsilon(5-3\varepsilon)-2)\cos 2\omega_{\mathrm{M}} t\right) \end{array}\right]\csc^2\omega_{\mathrm{M}} t \\
c &= \left(e^{\Gamma t}-1\right)(1-\varepsilon)\left(e^{\Gamma t} + (1-\varepsilon)^2\right)\left(e^{\Gamma t} + \varepsilon - 1\right) \\
d &= \varepsilon(1-\varepsilon)\left(e^{\Gamma t} + (1-\varepsilon)^2\right)\left(e^{\Gamma t} + \varepsilon - 1\right).
\end{aligned}$$

Clearly c and d are non-negative. Let us now consider the signs of a and b.

The factor a is positive if

$$e^{\Gamma t} + (1-\varepsilon)^3 > (1-\varepsilon)\left(1 + e^{\Gamma t} - \varepsilon\right)\cos 2\omega_M t. \tag{6.15}$$

The right hand side of this inequality is never larger than $(1-\varepsilon)\left(1+e^{\Gamma t}-\varepsilon\right)$ (*i.e.* set $\cos 2\omega_M t = 1$); thus if we can satisfy $e^{\Gamma t} + (1-\varepsilon)^3 > (1-\varepsilon)\left(1+e^{\Gamma t}-\varepsilon\right)$ we can always satisfy Eqn (6.15). Rearranging $e^{\Gamma t} + (1-\varepsilon)^3 > (1-\varepsilon)\left(1+e^{\Gamma t}-\varepsilon\right)$ yields

$$e^{\Gamma t} > (1-\varepsilon)^2,$$

which is always true. This means that Eqn (6.15) is always satisfied, and a is always positive.

The remaining coefficient b is positive when the term in square brackets is positive, *viz.*

$$\left[\begin{array}{c} e^{3\Gamma t} - 2(1-\varepsilon)^5 + \varepsilon e^{2\Gamma t} + e^{\Gamma t}(1-\varepsilon)^2(1-\varepsilon(3-\varepsilon)) - \\ (1-\varepsilon)\left\{e^{2\Gamma t}(3-2\varepsilon) - (1-\varepsilon)^3 + e^{\Gamma t}(\varepsilon(5-3\varepsilon)-2)\right\}\cos 2\omega_M t \end{array}\right] > 0. \tag{6.16}$$

We begin by noting that the term in braces (in Eqn (6.16)) is always positive. This may be proven as follows:

- Convert the term $(e^{2\Gamma t}(3-2\varepsilon) - (1-\varepsilon)^3 + e^{\Gamma t}(\varepsilon(5-3\varepsilon)-2))$ into a quadratic in $\lambda = e^{\Gamma t}$.
- Solve for the roots of the quadratic. The largest root is

$$\lambda_R = \frac{1-\varepsilon}{6-4\varepsilon}\left[2 - 3\varepsilon - \sqrt{16 - 32\varepsilon + 17\varepsilon^2}\right].$$

- Consider the inequality $\lambda_R > 1$. It simplifies to $\varepsilon^2 - 6\varepsilon + 6 < 0$.
- Calculate the roots of this quadratic, which are $\varepsilon = 3 \pm \sqrt{3}$, both of which are larger than 1.
- Conclude that the quadratic condition on ε is never satisfied for physical values of ε; thereby see that $\lambda_R < 1 \;\forall\; \varepsilon \in (0,1)$.
- Use the definition of λ to see that $\lambda > 1$ for all Γt of interest, and thus this λ_R is not physical.
- Conclude that the term in Supp. Eqn (6.16) is always positive.

With this we can see that

$$\begin{array}{c} (1-\varepsilon)\left\{e^{2\Gamma t}(3-2\varepsilon) - (1-\varepsilon)^3 + e^{\Gamma t}(\varepsilon(5-3\varepsilon)-2)\right\} > \\ (1-\varepsilon)\left\{e^{2\Gamma t}(3-2\varepsilon) - (1-\varepsilon)^3 + e^{\Gamma t}(\varepsilon(5-3\varepsilon)-2)\right\}\cos 2\omega_M t \end{array},$$

which prompts us to consider the simpler inequality

$$\begin{array}{c} e^{3\Gamma t} - 2(1-\varepsilon)^5 + \varepsilon e^{2\Gamma t} + e^{\Gamma t}(1-\varepsilon)^2(1-\varepsilon(3-\varepsilon)) > \\ (1-\varepsilon)\left\{e^{2\Gamma t}(3-2\varepsilon) - (1-\varepsilon)^3 + e^{\Gamma t}(\varepsilon(5-3\varepsilon)-2)\right\} \end{array}, \tag{6.17}$$

equivalent to considering the right hand side with $\cos 2\omega_M t = 1$. This new condition factorises rather straightforwardly, yielding

$$\left(e^{\Gamma t} - (1-\varepsilon)^2\right)^2\left(e^{\Gamma t} + 2\varepsilon - 1\right) > 0,$$

which is obviously satisfied. Thus we conclude that $b > 0$ always.

Since we have established that a, b, c, and d are all positive we know B is positive. Consider then Eqn (6.14), which is quadratic in μ^2. There are only solutions to Eqn (6.14) when the determinant of the left hand side, $B^2 - 4$, is non-negative. This gives $B \geq 2$. Rearranging this yields the condition

$$e^{2\Gamma t} + (1-\varepsilon)^4 - 2e^{\Gamma t}(1-\varepsilon)^2 \cos 2\omega_M t > 0$$

which is seen to be quadratic in $\lambda = e^{\Gamma t}$. The determinant of the left hand side is negative, thus there are no real roots. This means that this conditions is always satisfied, and B is always at least 2.

We may thus calculate that $\mu^4 + B\mu^2 + 1 < 0$ is satisfied when

$$\frac{-1}{2}\left(\sqrt{B^2-4} + B\right) < \mu^2 < \frac{1}{2}\left(\sqrt{B^2-4} - B\right). \tag{6.18}$$

This clearly has no solution for real μ because both the upper and lower limits of Eqn (6.18) are negative. This implies $W^{(\mathrm{RWA})} < 0$ cannot be satisfied, and hence that there is no heat engine phase in the RWA.

Note that we have not taken any limits during this derivation, nor have we approximated V_{SS} as diagonal, so our no-go theorem holds for arbitrary $\varepsilon \in (0,1)$ and any positive $\Gamma < \omega_M/2$.

6.7.2 No-go theorem for refrigeration

Consider the criterion for refrigeration, namely $\mathrm{Tr}\{V_{\mathrm{SS}} - V_4 + V_2 - V_1\} > 0$. Substituting the appropriate covariance matrices and using the cyclical property of the trace gives

$$2\frac{2-\varepsilon}{1-\varepsilon}(2\bar{n}_C + 1) > \mathrm{Tr}\left\{\begin{pmatrix} \mu^{-2} + \frac{1}{1-\varepsilon} & 0 \\ 0 & \mu^2 + \frac{1}{1-\varepsilon} \end{pmatrix} V_{\mathrm{SS}}\right\}.$$

This can be re-written

$$\frac{2\bar{n}_C + 1}{2\bar{n}_H + 1}\alpha < \beta. \tag{6.19}$$

The coefficients α and β are relatively high-order polynomials in ε and λ, so we will consider the limit of small $\omega_M t$ and ε. Then

$$\begin{aligned} \alpha &= 4\varepsilon^5\mu^4(2-\varepsilon)^4\left[2\varepsilon\left(\mu^2-1\right)^2 + \Gamma t\left(5 - 14\mu^2 + 5\mu^4 + \varepsilon\left(1+\mu^2\right)^2\right)\right] \\ \beta &= 2\varepsilon^5\mu^4(2-\varepsilon)^4\Gamma t\left[\varepsilon\left(1+6\mu^2+\mu^4\right) - 2\left(1+\mu^2\right)^2\right]. \end{aligned}$$

The sign of each coefficient is controlled by the terms in square brackets.

α does have real zeros, but these only occur for negative values of μ^2, which are unphysical. Thus $\alpha > 0$ for all $\mu > 1$.

The (square) bracketed term in β is quadratic in μ^2. Calculating its determinant makes it clear that $\beta < 0$ for all physical μ.

This means that the left hand side of Supp. Eqn (6.19) is always positive, whilst the right is always negative, thereby ensuring that the condition cannot be met. We conclude that there is no refrigeration in the RWA (at least in the small ε, high-Q regime). Our numerical calculations support this conclusion.

6.8 Potential scheme for a fast squeezer using pulsed optomechanics

We have approximated all squeezing interactions as occurring instantaneously, rather than the conventional case of parametric amplification over many mechanical periods (*e.g.* [299]). The extremely rapid mechanical squeezing operations needed by this protocol could potentially be realised by combining the pulsed optomechanics interface of [2] with the arbitrary-quadrature pulsed optomechanical interaction of [71], using a squeezed optical state as an ancilla. In this section we will provide a brief outline of how this can be achieved. We stress that this particular realisation of a fast squeezer has not been used to generate any of the results in other sections of this chapter.

6.8.1 Generating an approximate squeezer with QND interactions

Let us begin by considering two types of QND interactions between mechanical (M) and optical (L) modes: X–X couplings and P–P couplings, so named because of the form of their Hamiltonians. The former yields the transformation

$$X'_{\mathrm{M}} = X_{\mathrm{M}}, \qquad P'_{\mathrm{M}} = P_{\mathrm{M}} + \chi X_{\mathrm{L}}, \tag{6.20a}$$

$$X'_{\mathrm{L}} = X_{\mathrm{L}}, \qquad P'_{\mathrm{L}} = P_{\mathrm{L}} + \chi X_{\mathrm{M}}, \tag{6.20b}$$

where primed quadratures are the outputs. This is easily recognised as the QND interaction generated by pulsed optomechanics encountered in Chapter 5. The P–P coupling yields

$$X'_{\mathrm{M}} = X_{\mathrm{M}} + \chi P_{\mathrm{L}}, \qquad P'_{\mathrm{M}} = P_{\mathrm{M}}, \tag{6.21a}$$

$$X'_{\mathrm{L}} = X_{\mathrm{L}} + \chi P_{\mathrm{M}}, \qquad P'_{\mathrm{L}} = P_{\mathrm{L}}. \tag{6.21b}$$

Note that now $P_{\mathrm{M,L}}$ are the QND variables, with all of the back-action appearing on the position and amplitude operators. As before, χ are the interaction strengths. In matrix form we have

$$\mathscr{M}_{\mathrm{XX}} = \begin{pmatrix} 1 & 0 & 0 & 0 \\ 0 & 1 & \chi & 0 \\ 0 & 0 & 1 & 0 \\ \chi & 0 & 0 & 1 \end{pmatrix}, \tag{6.22a}$$

$$\mathscr{M}_{\mathrm{PP}} = \begin{pmatrix} 1 & 0 & 0 & \chi \\ 0 & 1 & 0 & 0 \\ 0 & \chi & 1 & 0 \\ 0 & 0 & 0 & 1 \end{pmatrix}. \tag{6.22b}$$

The column vector on which these act is $\boldsymbol{X} = (X_{\mathrm{M}}\, P_{\mathrm{M}}\, X_{\mathrm{L}}\, P_{\mathrm{L}})^{\mathrm{T}}$.

Imagine chaining three QND interactions together; X–X, then P–P, then a second X–X. Let these have interaction strengths $\chi^{(j)}$ where $j \in \{1,2,3\}$. The total evolution is then

$$\begin{aligned} \mathscr{M} &= \mathscr{M}_{\mathrm{XX}}^{(3)}\, \mathscr{M}_{\mathrm{PP}}^{(2)}\, \mathscr{M}_{\mathrm{XX}}^{(1)}, \\ &= \begin{pmatrix} \mathscr{D} & \mathscr{A} \\ \mathscr{A} & \mathscr{D} \end{pmatrix}, \end{aligned}$$

where the diagonal blocks are

$$\mathscr{D} = \begin{pmatrix} 1+\chi^{(1)}\,\chi^{(2)} & 0 \\ 0 & 1+\chi^{(2)}\,\chi^{(3)} \end{pmatrix}$$

and the antidiagonals are

$$\mathscr{A} = \begin{pmatrix} 0 & \chi^{(2)} \\ \chi^{(1)}+\chi^{(3)}\left(1+\chi^{(1)}\,\chi^{(2)}\right) & 0 \end{pmatrix}.$$

State swap

As an interesting aside, if we select $\chi^{(1)} = \chi^{(3)} = -\chi^{(2)} = -1$ then

$$\mathscr{M} = \begin{pmatrix} 0 & 0 & 0 & 1 \\ 0 & 0 & -1 & 0 \\ 0 & 1 & 0 & 0 \\ -1 & 0 & 0 & 0 \end{pmatrix},$$

This is a unitary state swap, plus a pair of local rotations. Note that this is precisely the operation used in our pulsed optomechanical state swap interface (Eqn (5.7)), since a P–P QND interaction can be constructed from $\pi/2$ rotations on both modes before and after an X–X interaction.

Effectively unitary squeezer

Now consider the case that $\chi^{(1)}+\chi^{(3)}\left(1+\chi^{(1)}\,\chi^{(2)}\right) = 0$. This can be achieved by setting

$$\chi^{(2)} = -\left(\chi^{(1)\,-1} + \chi^{(3)\,-1}\right).$$

In this situation

$$\mathscr{M} = \begin{pmatrix} -\chi^{(1)}/\chi^{(3)} & 0 & 0 & -\left(\chi^{(1)\,-1}+\chi^{(3)\,-1}\right) \\ 0 & -\chi^{(3)}/\chi^{(1)} & 0 & 0 \\ 0 & -\left(\chi^{(1)\,-1}+\chi^{(3)\,-1}\right) & -\chi^{(1)}/\chi^{(3)} & 0 \\ 0 & 0 & 0 & -\chi^{(3)}/\chi^{(1)} \end{pmatrix}.$$

Note that the diagonal blocks are local squeezing operations. To perform an effective squeezer on mode M it is possible to select an initial optical state that is highly phase-squeezed; the non-zero upper right element of $\mathscr{M}$ does not contribute significantly in this case, and not at all in the limit that the

squeezing becomes infinite. Mathematically, this is very similar to feedforward squeezing in optical systems [300]. The input–output relations for a broadband squeezed state are given in App. A.9.

To position squeeze the mechanical oscillator we require $\left|\chi^{(3)}\right| > \left|\chi^{(1)}\right|$. In this case the ancillary mode is also position squeezed; thus a fresh ancilla mode is required for each application of the 'squeezer'.

Thus we have established that it is possible to construct an effectively unitary local squeezing operation on mode M by using a strongly squeezed ancilla and three QND interactions. However, it is not obvious how to implement this sequence because pulsed optomechanics gives rise to an X–X coupling only. We will need to settle for an *approximate* sequence instead.

6.8.2 Constructing a P–P QND interaction with the optomechanical toolbox

We will permit the following operations;

- X–X QND interactions;
- arbitrary local rotations on the optical mode; and
- small local rotations on the mechanical mode (because we wish the squeezer to be fast).

The aim is to approximate the sequence $\mathscr{M}_{\mathrm{XX}}\mathscr{M}_{\mathrm{PP}}\mathscr{M}_{\mathrm{XX}}$.

Approximate P–X interaction

In [71] it is shown that an effective P–X coupling (*i.e.* Hamiltonian of the form $P_{\mathrm{M}}X_{\mathrm{L}}$) can be generated by chaining together an X–X QND, a local mechanical rotation and a second X–X interaction.

Mathematically,

$$\begin{aligned}\mathscr{M}_{\overline{\mathrm{PX}}} &= \mathscr{M}_{\mathrm{XX}}\left(\lambda^{(2)}\right) R_{\mathrm{M}}(\varphi)\, \mathscr{M}_{\mathrm{XX}}\left(\lambda^{(1)}\right) \\ &= \begin{pmatrix} \cos\varphi & \sin\varphi & \lambda^{(1)}\sin\varphi & 0 \\ -\sin\varphi & \cos\varphi & \lambda^{(2)}+\lambda^{(1)}\cos\varphi & 0 \\ 0 & 0 & 1 & 0 \\ \lambda^{(1)}+\lambda^{(2)}\cos\varphi & \lambda^{(2)}\sin\varphi & \lambda^{(1)}\,\lambda^{(2)}\sin\varphi & 1 \end{pmatrix}\end{aligned}$$

where we have used an over-line on the subscript to denote an approximate interaction.

If we factorise out a mechanical rotation by φ we are left with

$$R(-\varphi)\,\mathscr{M}_{\overline{\mathrm{PX}}} = \begin{pmatrix} 1 & 0 & -\lambda^{(2)}\sin\varphi & 0 \\ 0 & 1 & \lambda^{(1)}+\lambda^{(2)}\cos\varphi & 0 \\ 0 & 0 & 1 & 0 \\ \lambda^{(1)}+\lambda^{(2)}\cos\varphi & \lambda^{(2)}\sin\varphi & \lambda^{(1)}\,\lambda^{(2)}\sin\varphi & 1 \end{pmatrix}.$$

Comparing this with a true P–X interaction,

$$\mathscr{M}_{\mathrm{PX}} = \begin{pmatrix} 1 & 0 & \chi & 0 \\ 0 & 1 & 0 & 0 \\ 0 & 0 & 1 & 0 \\ 0 & -\chi & 0 & 1 \end{pmatrix},$$

we see that (up to a rotation) $\mathscr{M}_{\overline{\mathrm{PX}}}$ looks similar to $\mathscr{M}_{\mathrm{PX}}\left(\chi = -\lambda^{(3)}\sin\varphi\right)$.

To create a closer approximation, we set $\lambda^{(1)} = -\lambda^{(2)}\cos\varphi$, yielding

$$R(-\varphi)\mathscr{M}_{\overline{\mathrm{PX}}} = \begin{pmatrix} 1 & 0 & -\lambda^{(2)}\sin\varphi & 0 \\ 0 & 1 & 0 & 0 \\ 0 & 0 & 1 & 0 \\ 0 & \lambda^{(2)}\sin\varphi & -\frac{1}{2}{\lambda^{(2)}}^2\sin 2\varphi & 1 \end{pmatrix}.$$

This has the form of a P–X QND interaction followed by a Kerr interaction with a Hamiltonian of the form X_{L}^2 (or indeed preceded by, because the operators commute).

Approximate P–P QND

Note that a P–X QND may easily be turned into a P–P interaction by local optical rotations, *viz.*

$$\mathscr{M}_{\mathrm{PP}}(\chi) = R_{\mathrm{L}}(-\pi/2)\mathscr{M}_{\mathrm{PX}}(\chi)R_{\mathrm{L}}(+\pi/2).$$

We might therefore be tempted to construct an approximate P–P QND by rotating $\mathscr{M}_{\overline{\mathrm{PX}}}$ in the same way. However, this leads to the Kerr term becoming mixed into the amplitude quadrature, and thereby onto the mechanical oscillator after a further QND interaction.

This unwanted interaction can be mitigated by perform *unequal* rotations on the optical mode before and after $\mathscr{M}_{\overline{\mathrm{PX}}}$. Suppose

$$\mathscr{M}_{\overline{\mathrm{PP}}} = R_{\mathrm{L}}(-\pi/2)R_{\mathrm{L}}(\psi)\mathscr{M}_{\overline{\mathrm{PX}}}R_{\mathrm{L}}(+\pi/2).$$

The angle ψ may then be selected such that it rotates the Kerr term from P_{L} onto X_{L}. From there $R_{\mathrm{L}}(-\pi/2)$ will rotate it back onto P_{L}, leaving X_{L} (which participates in a later X–X QND interaction) free of any influence of the Kerr term.

By inspecting this expression, we see that ψ obeys

$$\tan\psi = -\frac{1}{2}{\lambda^{(2)}}^2\sin 2\phi.$$

6.8.3 Complete transformation

The final transformation is

$$\mathscr{M} = \mathscr{M}_{\mathrm{XX}}\left(\chi^{(3)}\right)\mathscr{M}_{\overline{\mathrm{PP}}}\left(\lambda^{(2)}\right)\mathscr{M}_{\mathrm{XX}}\left(\chi^{(1)}\right).$$

It is again instructive to factorise out a mechanical rotation. If we do so and then extract the upper left 2×2 block we obtain

$$\begin{pmatrix} 1-\lambda^{(2)}\,\chi^{(1)}\sin\varphi & \frac{2\lambda^{(2)}\,\chi^{(3)}\sin^2\varphi}{\sqrt{4+\lambda^{(2)\,3}\sin^2 2\varphi}} \\ 0 & 1-\frac{\lambda^{(2)}\,\chi^{(3)}\cos\varphi\sin\varphi}{\sqrt{1+\lambda^{(2)\,4}\cos^2\varphi\sin^2\varphi}} \end{pmatrix}$$

This can be brought into the form of an approximate mechanical squeezer by selecting the diagonal elements to be inverses of one another. This may be enforced by fixing

$$\chi^{(3)} = \frac{\chi^{(1)}\sec\varphi\sqrt{1+\lambda^{(2)\,4}\cos^2\varphi\sin^2\varphi}}{\lambda^{(2)}\,\chi^{(1)}\sin\varphi-1}.$$

This yields

$$\begin{pmatrix} 1-\lambda^{(2)}\,\chi^{(1)}\sin\varphi & \frac{\lambda^{(2)}\,\chi^{(1)}\sin\varphi\tan\varphi}{\lambda^{(2)}\,\chi^{(1)}\sin\varphi-1} \\ 0 & \frac{1}{1-\lambda^{(2)}\,\chi^{(1)}\sin\varphi} \end{pmatrix}.$$

It also brings the upper right block into the form

$$\begin{pmatrix} \chi^{(1)}\tan\varphi & -\lambda^{(2)}\sin\varphi \\ 0 & 0 \end{pmatrix}.$$

Note that only one quadrature of the initial optical noise is being mapped onto the mechanical output state; it is $X_{\rm L}(\theta_{\rm S}) = X_{\rm L}\cos\theta_{\rm S} + P_{\rm L}\sin\theta_{\rm S}$ where $\tan\theta_{\rm S} = -\lambda^{(2)}\cos\varphi/\chi^{(1)}$. The gain of the coupled quadrature is

$$\mathscr{G} = \sin\varphi\sqrt{\lambda^{(2)\,2}+\frac{\chi^{(1)\,2}}{\cos^2\varphi}}\,.$$

We may suppress the optical contributions to the final output state by strongly squeezing the input optical fluctuations along the direction $\theta_{\rm S}$ (*i.e.* choosing $r_{\rm S}$ such that $\mathrm{e}^{2r_{\rm S}} \gg \mathscr{G}$).

The full sequence is displayed in Fig. 6.7.

Linearised interaction

Expanding $\mathscr{M}$ about $\varphi = 0$ gives the total transformation (including the mechanical rotation previously factorised out)

$$\begin{pmatrix} 1-\lambda^{(2)}\,\chi^{(1)}\,\varphi & \varphi & \chi^{(1)}\,\varphi & -\lambda^{(2)}\,\varphi \\ -\left(1-\lambda^{(2)}\,\chi^{(1)}\,\varphi\right)\varphi & \frac{1}{1-\lambda^{(2)}\,\chi^{(1)}\,\varphi} & 0 & 0 \\ 0 & -\lambda^{(2)}\,\varphi & 1-\lambda^{(2)}\,\chi^{(1)}\,\varphi & 0 \\ 0 & -\frac{\varphi\chi^{(1)}}{1-\lambda^{(2)}\,\chi^{(1)}\,\varphi} & \varphi\frac{\lambda^{(2)\,2}-\chi^{(1)\,2}}{1-\lambda^{(2)}\,\chi^{(1)}\,\varphi} & \frac{1}{1-\lambda^{(2)}\,\chi^{(1)}\,\varphi} \end{pmatrix}.$$

Implementing this transformation would be extremely technically challenging, but these calculations nevertheless show that an arbitrarily fast squeezing operation can be constructed from the 'standard' pulsed optomechanical toolbox.

A full consideration of the noise introduced by imperfect squeezing has not been performed.

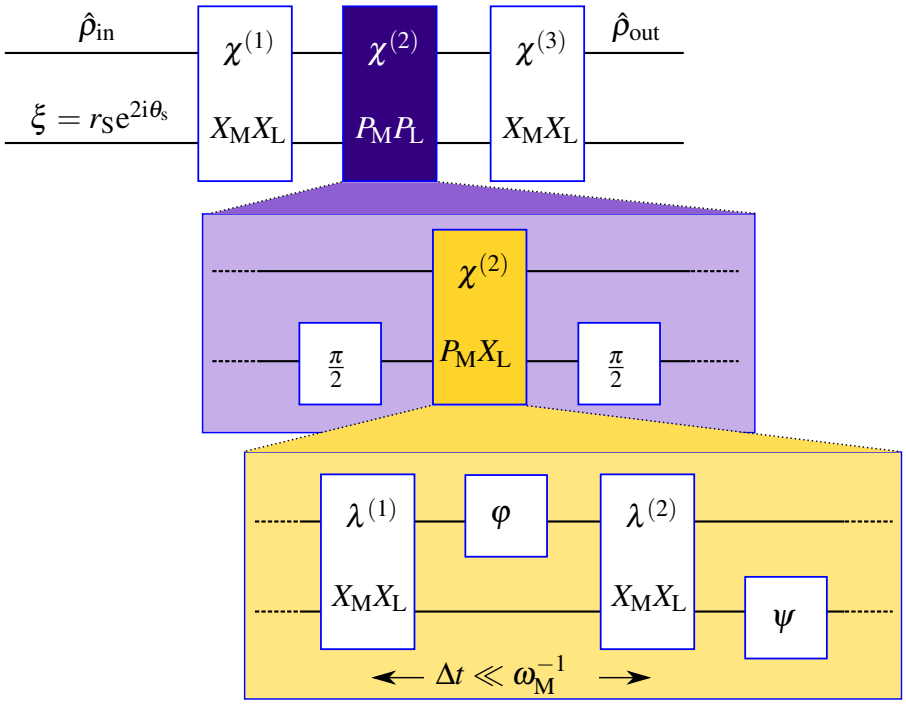

Figure 6.7: Pulse sequence to implement a fast squeezer. The purple box shows how the $P_{\rm M}P_{\rm L}$ interaction can be expressed in terms of a $P_{\rm M}X_{\rm L}$ QND interaction, and the yellow box shows how the latter can be approximated using optomechanical pulsed interactions. Parameters are discussed in the main text.

6.9 Conclusion

It is worthwhile to briefly identify the limitations of the theories employed in this study. Eqns (3.20) are not of Lindblad form, and so are not guaranteed to be completely positive for all initial states and (hot) bath temperatures [287, 301]; however, they are valid in the high-Q and $\bar{n}_{\rm H} \gg 1$ regime considered throughout this chapter ($\bar{n}_{\rm H} \geq 10^2$). No such restriction exists for the cold bath temperature in our model. For further discussion, see App. A.10.

We have proposed and modelled a thermodynamic system based on a momentum-damped mechanical oscillator subjected to rapid squeezing operations. Our calculations indicate that such a system can operate as a heat pump, a refrigerator, or a heat engine. Importantly, if lossy evolution is modelled by the BMME the latter two effects vanish. This indicates the emergence of rich—and potentially useful—quantum thermodynamical phenomena beyond the RWA.

Part III

Progress: Device design

Chapter 7

Epitaxial silicon carbide resonators for quantum optomechanics

Portions of the work presented in this chapter have been published by Wiley Online Library;
A. R. Kermany, **J. S. Bennett**, V. M. Valenzuela, W. P. Bowen, and F. Iacopi. Potential of epitaxial silicon carbide microbeam resonators for chemical sensing, *Physica Status Solidi A* 214 (4), 1600437, 2016;
and also by the American Institute of Physics Publishing;
A. R. Kermany, **J. S. Bennett**, G. A. Brawley, W. P. Bowen, and F. Iacopi, Factors affecting the $f \times Q$ product of 3C-SiC microstrings: What is the upper limit for sensitivity?, *Journal of Applied Physics* 119, 055304, 2016.

* * *

Epitaxial silicon carbide (SiC) is a promising material for optomechanical device fabrication because of its excellent mechanical and thermal properties. In this chapter we will introduce the properties of SiC, provide a brief literature survey of SiC resonators, and detail our experimental efforts towards creating the next generation of high-Q micromechanical SiC devices. Our SiC string resonators have extremely large (room temperature) $Q \times f$ products (§ 2.1.4), which means that they are well-isolated from their thermal environments, and their typical resonant frequencies place them in the unresolved cavity regime for most optical cavities to which they could practically be coupled. Furthermore, their electrical, chemical, and biochemical properties make them suitable for practical optomechanical sensor applications in biological systems or other harsh environments.

7.1 Introduction

Currently, microelectromechanical systems (MEMS) technology plays an important role in sensing, energy harvesting, signal processing, atomic force microscopy, and precision measurements [302].

Microresonators fabricated from wide-bandgap semiconductors are excellent candidates for the construction of sensors, actuators, and optomechanical devices [303–305] that are capable of higher performance than those of silicon alone.

In the classical regime semiconductor microresonators have been used to detect volatile organics [306], explosives [307, 308], glucose [309, 310], DNA hybridisation [311], and bacteria and viruses [312] with unparalleled sensitivities. From a quantum standpoint, they promise large $Q \times f$ products at room temperature, which makes them desirable candidates for testing macroscopic quantum optomechanics (as explained in Chapter 2), or for quantum-enhanced sensing applications.

7.2 Material properties of SiC

Many wide bandgap materials—including silicon carbide (SiC), silicon oxide (SiO_2), silicon nitride (αSiN), gallium nitride (GaN), gallium arsenide (GaAs), and diamond—have been investigated for MEMS resonator fabrication, due to their excellent mechanical properties and chemical stability. Their properties—including structure, bandgap (E_g), lattice constants (lattice a and c), Young modulus (E), density (ρ), Poisson's ratio (ν), thermal expansion coefficient (α), thermal conductivity (κ), melting sublimation temperature (T_m), specific heat capacity at constant volume (c_V), and hardness (Mohs hardness)—are summarised in Table 7.1 [302–304, 313–319].

SiC has many crystal structures with different stacking sequences. The most common polytypes are hexagonal (2H, 4H, and 6H-SiC), rhombohedral (15R and 21R-SiC), and cubic (3C-SiC). Among them, 3C-SiC is the only thermodynamically stable polytype that can be heteroepitaxially grown on a Si substrate, and thus it is widely used for MEMS applications, where it is easy to micromachine, and can be produced with a larger surface area and lower cost than bulk SiC substrates [321–323].

Epitaxial SiC has great potential for MEMS applications in harsh environments because of its high Young-modulus-to-density ratio, high hardness, and large thermal conductivity. It also has high electrical stability, high resistance to radiation, and is biocompatible [303,323–326]. Although diamond nominally has superior material properties to epitaxial SiC, these are not accessible in single-crystalline epitaxial films. Additionally, fabrication of diamond is expensive and complicated [327].

Table 7.1: Material properties of wide bandgap semiconductors applied in MEMS [302–304,313–320].

material	SiC(100)	SiC(100)	SiC(111)	SiO_2	αSiN	GaN	GaAs	diamond
structure	cubic	cubic	cubic	amorphous	amorphous	wurtzite	cubic	cubic
E_g eV	1.12	2.4	2.4	9	5	3.4	1.43	5.5
lattice constant a (Å)	5.43	4.36	4.36	–	–	3.2	5.65	3.57
lattice constant c (Å)	–	–	–	–	–	5.2	–	–
E (GPa)	130	330	400	70	250	330	85	1220
ρ (kg·m^{-3})	2300	3200	3200	2200	3200	6100	5300	3500
ν	0.28	0.267	0.235	0.17	0.27	0.2	0.31	0.2
α (10^{-6} K^{-1})	2.6	3	3	0.5	3	5.5	5.73	1
κ (W/mK)	130–150	70–360	70–360	1	8	130	55	2000
T_m (K)	1690	3103	3103	1970	2170	2400	1510	4270
c_V (MJ·m^{-3}·K^{-1}	1.6	3	3	1.5	3	3	3.5	1.8
Mohs hardness	6–7	9–9.5	9–9.5	6–7	8.5	–	4–5	10

One significant downside of epitaxial SiC for some applications—but not necessarily for optomechanics—is that at high temperatures the SiC–Si interface can electrically short the two layers. This can happen either upon film growth or during subsequent high temperature processing [328].

7.2.1 Epitaxial growth and residual stress

Epitaxial growth of SiC is performed through techniques including chemical vapour deposition (CVD) [329, 330], liquid phase epitaxy [331], and molecular beam epitaxy [332]. CVD is the most commonly used growth method and involves three general steps: (*i*) hydrogen surface etching to remove any native oxide; (*ii*) a carbonisation process to form a buffer (sealing) layer; and (*iii*) the supply of gases to grow the 3C-SiC layer [333]. Optimisation of the CVD growth parameters—such as temperature, deposition rate, and pressure—can lead to the production of very high quality monocrystalline films [334].

Despite that, the formation of defects such as misfit dislocation and stacking faults within the SiC crystal is inevitable due to the differing thermal expansion coefficients ($\sim 8\%$ during the cool down) and lattice constants ($\sim 20\%$) of Si and 3C-SiC [322, 335–337].

The large mismatch between the lattice constants of Si and SiC generates significant residual stress within the SiC film. The stress profile $\sigma(z)$ varies across the thickness of the SiC film; z is the coordinate perpendicular to the plane of the film. It is often useful to decompose the stress into its mean value—

$$\sigma = \frac{1}{t}\int_0^t \mathrm{d}z\, \sigma(z)\,,$$

where t is the film's thickness—and the gradient stress,

$$\Delta\sigma = \sigma|_{z=t} - \sigma|_{z=0}\,.$$

Many studies have focused on understanding the residual stress behaviour, as the impact of the mean stress could be beneficial or disadvantageous depending on the application [338–341]. As we will see, in string resonators it leads to a beneficial increase in the mechanical $Q \times f$ product (§ 7.3.2) due to 'dissipation dilution'. The gradient stress is of less interest in this scenario. It does, however, control the static morphology of cantilevers and free-free beams, as shown in § 7.8.

It is known that the orientation of the silicon substrate has a marked effect on the σ that can be achieved in a heteroepitaxial SiC film. From Table 7.2, we can observe that tensile stress values as high as 1500 MPa can be achieved using the (111) orientation, with $Q \times f_1$ products exceeding state-of-the-art αSiN microstrings (5.3×10^{11} Hz [225]).

7.3 Mechanical properties of string resonators

Each resonator structure has multiple vibrational modes, where each mode has its specific displacement pattern (mode function), frequency, and Q factor. Each vibrational mode is named and numbered according to its vibration pattern and number of antinodes, respectively [342]. The lowest frequency

Table 7.2: Literature study on the mechanical behaviour of MEMS bridges in vacuum. The length, width, thickness and mean stress are listed (L, w, t, σ), along with the operating pressure P, fundamental mode frequency f_1, and quality Q. The $Q \times f_1$ product is a key figure of merit for sensors and optomechanical devices (*cf.* § 7.4). The $Q \times R$ ($R =$ surface area to volume ratio) is important for mass and chemo-sensing applications. In both cases, larger is better, for reasons that will be expanded on in § 7.4.

ref.	material	L (μm)	w (μm)	t (nm)	σ (MPa)	P (mbar)	f_1 (kHz)	Q	$Q \times f_1$ (Hz)	$Q \times R$ (nm^{-1})
[321]	SiC(111)	1000	4	255	750	2×10^{-7}	220	8×10^5	1.8×10^{11}	6.7×10^3
[321]	SiC(111)	930	4	255	1500	10^{-6}	280.5	3×10^6	8.4×10^{11}	2.5×10^4
[225]	αSiN	1553	4	177	190	10^{-5}	78.7	2×10^6	1.6×10^{11}	2.4×10^4
[225]	αSiN	1553	4	157	890	10^{-5}	176	3×10^6	5.3×10^{11}	4.0×10^4
[344]	GaAs	37	10	200	0	–	1230	1800	2.2×10^9	18.4
[344]	GaAs	53	10	200	**	–	2900	2×10^3	5.5×10^{10}	20.4
[345]	Al	5	3	10	0	$< 10^{-3}$	1320	720	9.5×10^8	144
[345]	Al	5	3	10	13.5	$< 10^{-3}$	1370	1.4×10^3	1.9×10^9	281

mode is called the fundamental mode. We will identify the fundamental with a subscripted '1'. Modes with higher frequencies are called overtones; examples are shown in Fig. 7.1 [343] (experimental measurements of mode shapes are displayed in Fig. 7.10).

Microresonator structures can be broadly divided into beams, diaphragms, and combinations thereof. Beam resonators appear in two shapes; single-clamped (s-c) or 'cantilever' resonators; and double-clamped (d-c) or 'bridge' devices [342]. These are shown in Fig. 7.1. Long and narrow bridges are known as string resonators in the literature.

In this section we will focus on string resonators, and many of the equations given will be peculiar to this geometry; however, the physical mechanisms underpinning them are common to the other resonator geometries that we will encounter. A literature survey of typical mechanical parameters is given in Table 7.2.

7.3.1 Frequency

The out-of-plane flexural resonant frequencies of a rectangular microbeam consisting of a uniform material with thickness t, width w, and length L are described by Euler–Bernoulli beam theory [346], yielding

$$f_n = \frac{\kappa_n^2}{2\pi}\sqrt{\frac{k}{m}} = \frac{\kappa_n^2}{4\pi\sqrt{3}}\frac{t}{L^2}\sqrt{\frac{E}{\rho}}, \tag{7.1}$$

where m and k are the beam's mass and spring constant. The term $\kappa_n^2/4\pi\sqrt{3}$ is known as the clamping coefficient, and κ_n is the n^{th} eigenvalue of the bending equation. For bridges $\kappa_n = (n+1/2)\,\pi$, and for cantilever resonators $\kappa_n = (n-1/2)\,\pi$. Thus, the clamping coefficient of the fundamental mode is 1.03 for the bridge and 0.162 for the cantilever. For extremely thin beams, where the width w satisfies $w \geq 5t$, it is necessary to replace the Young modulus E with $E\left(1-\nu^2\right)^{-1}$, where ν is the Poisson ratio that characterises the material's tendency to couple strains along different axes. Overall, we see that the mechanical frequency of a flexural beam is influenced by the geometry, mode number, and material properties.

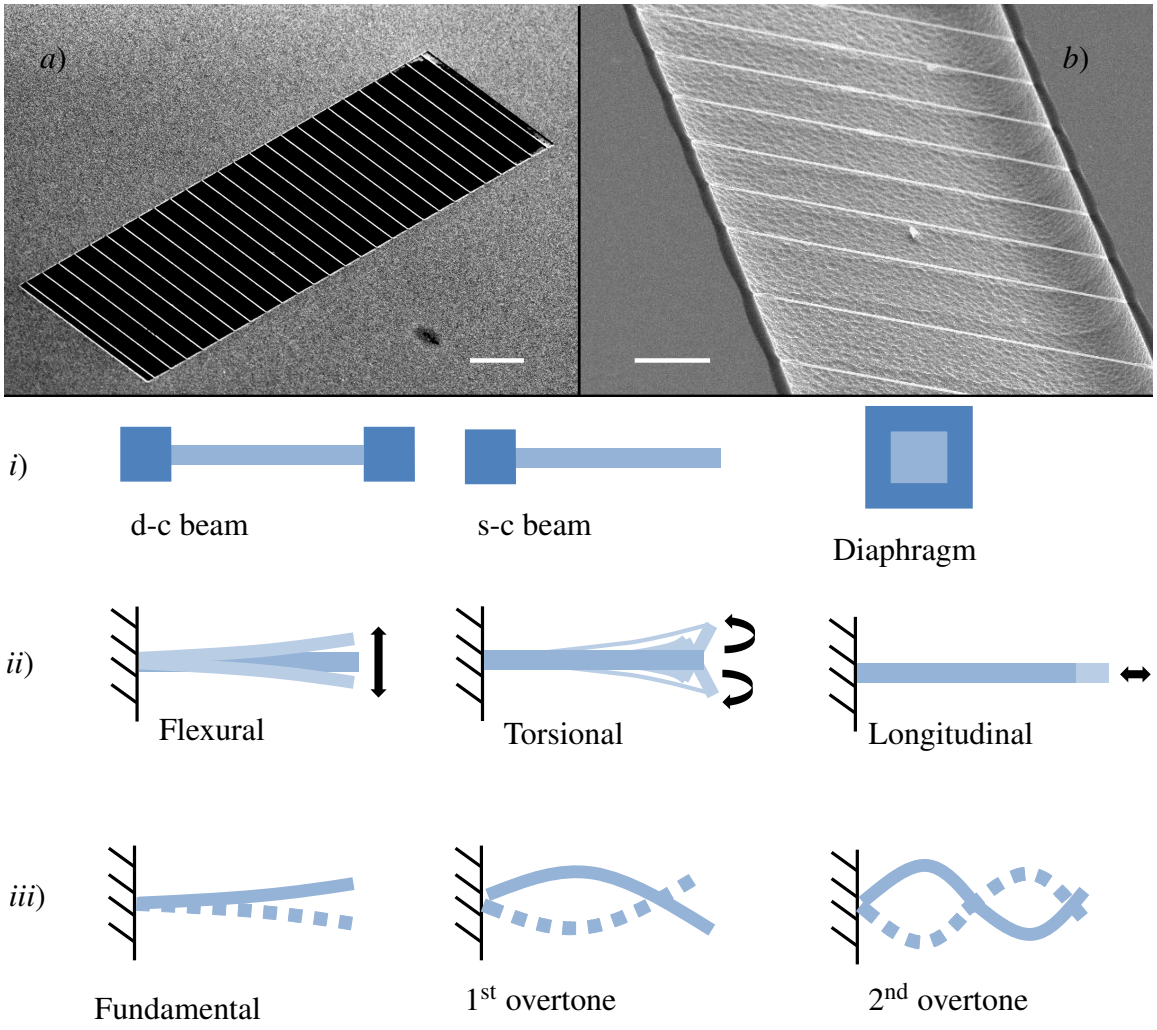

Figure 7.1: Examples of SiC double-clamped 'string' resonator arrays fabricated photolithographically from 3C-SiC grown on Si. The scale bars in images *a*) and *b*) both show 100 μm lengths. Micrographs supplied by Atieh R. Kermany.
Schematic of mechanical modes.
i) resonator types; anchors and resonators are shown in dark and light blue colours, respectively.
ii) vibration displacement patterns (mode types); and
iii) the first three higher-order modes of out-of-plane flexural vibrations of a cantilever. A new vibrational node is added at each order.

A strain-dependent correction of the Euler–Bernoulli theory becomes important in the presence of residual mean (tensile) stress within the resonator material, as we have seen exists for 3C-SiC films (§ 7.2.1). The out-of-plane flexural mode of a string microresonator is modified from Eqn (7.1) to [326]

$$f_n = \frac{\kappa_n^2 t}{4\pi\sqrt{3}\,L^2}\sqrt{\frac{E}{\rho}}\left(1+\gamma_n\frac{\sigma L^2}{Et^2}\right)^{1/2}. \tag{7.2}$$

Here γ_n is a mode-dependent coefficient obeying

$$\gamma_n = \frac{12\,(\kappa_n - 2)}{\kappa_n^3}$$

and σ is the film's mean tensile stress.

By inspecting Eqn (7.2) and Table 7.1 we can see that for 3C-SiC films $\gamma_n\sigma L^2/Et^2 \gg 1$, so that the frequency is mainly a function of tensile stress and length, *viz.*

$$f_{\text{hetero}} \propto \frac{1}{L}\sqrt{\frac{\sigma}{\rho}}\,. \tag{7.3}$$

The frequency is not a function of thickness, and so thinner and lighter resonators may be fabricated. This is the opposite of bulk or homoepitaxial resonators, which typically have (*cf.* Eqn (7.1))

$$f_{\text{homo}} \propto \frac{t}{L^2}\sqrt{\frac{E}{\rho}}\,,$$

i.e. lower frequencies for thinner resonators. As we will see, this allows high-tensile strings to display higher mass sensitivities and lower clamping loss than stress-free resonators.

Torsional Modes

The torsional frequencies of a beam resonator are obtained from (7.4) [347].

$$f_n^{\text{torsion}} = \frac{2n-1}{4L}\sqrt{\frac{E}{1+\nu}\frac{\xi_{\text{tor}}}{\rho}\frac{6}{tw^3+wt^3}}\,, \tag{7.4}$$

where

$$\xi_{\text{tor}} = \frac{t^4}{3}\left(\frac{w}{t} - \frac{192}{\pi^5}\sum_{j=1}^{\infty}\frac{1}{j^5}\tanh\left(\frac{j\pi w}{2t}\right)\right).$$

Torsional modes are difficult to detect using the method described in § 7.6, but they do have a measurable effect on the spectrum of the out-of-plane flexural modes. Finite element method (FEM) modelling performed by Atieh R. Kermany indicates that the torsional modes hybridise with the flexural modes, which can be measured as a frequency splitting in the mechanical spectrum. This is evident in Fig. 7.10.

7.3.2 Quality factor

The Q factor is defined as the ratio of the energy stored in an oscillator to the energy lost during a single cycle of vibration. For high-Q devices this is given by $Q = \omega_{\text{M}}/\Gamma$ (*cf.* § 2.1.4).

A resonator's Q can be obtained obtained by measuring the centre (ω_{M}) and width (Γ) of its thermomechanical power spectrum, as shown in Fig. 3.2). Alternatively, in the free decay method, Q is quantified from the time constant (τ_{d}) of the resonator's exponentially-decaying amplitude during a ring-down process [348], *viz.*

$$Q = \pi \tau_{\mathrm{d}} f. \tag{7.5}$$

It is desirable for a resonator to have a high quality factor. This reduces the mechanical coupling to the surrounding environment, which further results in high accuracy, high resolution and spectral purity, and long-term stability [349, 350]. Also, less drive energy is required to maintain a given amplitude of vibration in high-Q oscillators [351, 352]. Furthermore, thermal isolation is a key ingredient for the majority of quantum optomechanical protocols (as in § 2.1.4).

7.3.3 Damping mechanisms

The following sections describe the influence of damping mechanisms on a microbeam resonator's frequency and quality factor. It also includes an overview of the methods that can be used to improve the sensitivity/thermal isolation parameter ($Q \times f$) of epitaxial SiC microbeam resonators.

It should be noted that all the models shown in this section are for the flexural out-of-plane movements of a bridge microresonator.

The magnitude of damping is influence by many parameters including the resonator type, geometry, clamping, mode of vibration, and material (chemistry, defects, residual stress, crystallinity, surface quality, and the presence of material interfaces). The damping of a resonator is also influenced by temperature, pressure, and even transduction technique [302]. In general, damping is classified into medium damping (Q_{medium}), which is related to the environment of the resonator structure; clamping loss (Q_{clamp}), which is related to the energy dissipation through the resonator's anchors; material damping (Q_{mat}), which is related to the resonator material; and other losses (Q_{other}) [304, 342]. These add 'in parallel', thus

$$Q = \left[\left(\sum \frac{1}{Q_{\mathrm{medium}}} \right) + \left(\sum \frac{1}{Q_{\mathrm{clamp}}} \right) + \left(\sum \frac{1}{Q_{\mathrm{mat}}} \right) + \left(\sum \frac{1}{Q_{\mathrm{other}}} \right) \right]^{-1}, \tag{7.6}$$

where the major losses control the overall Q. In typical MEMS the material damping becomes important only after eliminating or minimising the extrinsic losses [304], particularly clamping and medium losses.

Gas damping

Gas damping is the only form of medium damping relevant to this thesis.

Newell was the first to analyse the effect of air damping on the Q [353]. He divided the pressure range from ambient pressure to vacuum into three regions: the viscous, molecular (fine vacuum), and intrinsic (high vacuum) regions. In the viscous regime gas damping is the dominant loss mechanisms, whilst in the intrinsic region the pressure is sufficiently low that the Q is approximately independent of the pressure.

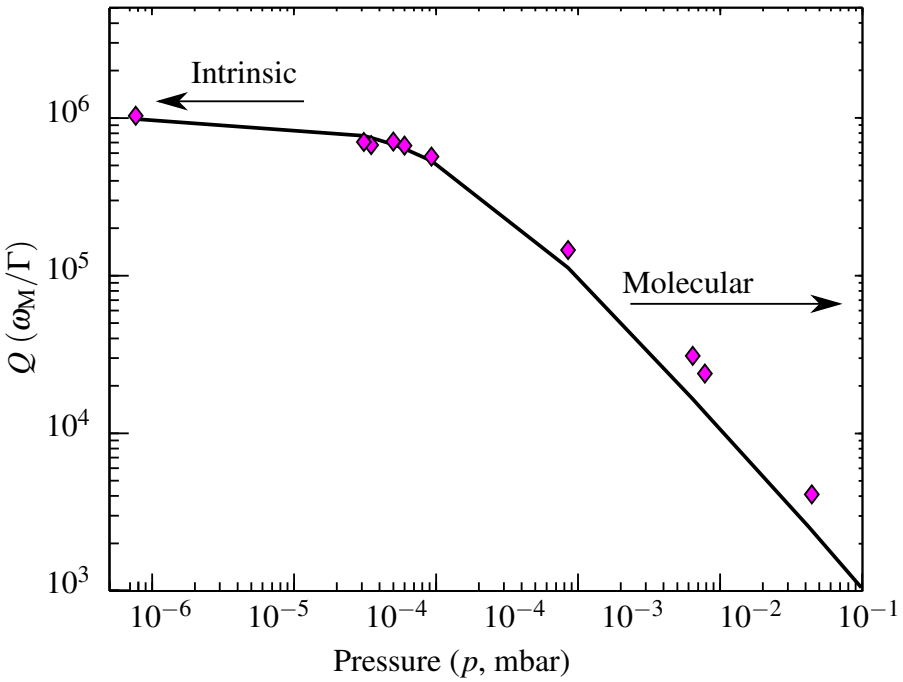

Figure 7.2: Environmental pressure effect on the Q for a 3C-SiC(111) string with 2600 μm length, 4 μm width, and 50 nm thickness. Experimental points are shown as magenta diamonds; the black line is a fit according to Eqn 7.7.

To find the upper boundary of the intrinsic region experimentally the resonator needs to be operated at different pressures. The function

$$Q = \left(\frac{1}{Q_0} + \alpha P\right)^{-1} \tag{7.7}$$

can then be used for analysis; Q_0 is the intrinsic Q factor and α is a fitting factor. The device is operating in the intrinsic region when the αP factor is smaller than Q_0 [4].

At higher pressure, the air molecules are still too far apart to interact but they do significantly damp the oscillator by colliding with it. In this molecular case it is predicted that $Q \propto 1/P$ [354].

Fig.7.2 shows results from an experiment where we measured the Q factor of a string resonator as a function of pressure. It clearly shows the intrinsic and molecular regimes. The measurements were made as detailed in § 7.6.

Clamping loss

When operating in a high vacuum, the viscous damping from the environment can be eliminated. This can make the clamping loss (Q_{clamp}) one of the dominant dissipation factors. Clamping loss results from energy radiating from the beam resonator anchors into the substrate [355]. As such, it is strongly geometry dependent.

There are multiple models of clamping loss available in the literature, but they do not all agree with one another or with experiments [356]. For our purposes it will be sufficient to know that they do concur that t/L is a crucial parameter. For instance, the two-dimensional model of Cross and Lifshitz [357]

and the three-dimensional model of Photiadis and Judge [358] both find that perfect-clamped beam resonators obey

$$Q_{\text{clamp}}^{-1} \propto t/L \tag{7.8}$$

for their out-of-plane flexural modes.

Note that Eqn (7.8) and Eqn (7.2) together indicate that we can achieve larger $Q \times f$ products by employing thin, highly-stressed strings.

More generally, Q_{clamp}^{-1} can be reduced through the minimisation of chip and substrate contact, vibration isolators [359], and acoustic reflectors [360]; alternatively more complicated structures such as free-free beams (where anchors are connected to the beam nodal points) [361] or phononic crystals [362, 363] can assist in reducing Q_{clamp}^{-1}.

Thermoelastic dissipation

One of the ultimate limits to microresonator performance is thermoelastic dissipation (TED) [1]. It is the result of coupling between the resonator's strain field and the local temperature [352, 364]. As the resonator vibrates, regions under compression will become warmer, while regions under expansion will be cooled. This results in the formation of a temperature gradient across the thickness of the resonator. Spontaneous heat flow down the gradient results in irreversible energy loss [365], which sets a fundamental limit on the Q of MEMS devices. Following Liftshitz and Roukes [366],

$$\begin{aligned} Q_{\text{TED}} &= \frac{c_{\text{V}}}{ET\alpha^2}\left(\frac{6}{\xi_{\text{TED}}^2} - \frac{6}{\xi_{\text{TED}}^3}\frac{\sinh\xi_{\text{TED}} + \sin\xi_{\text{TED}}}{\cosh\xi_{\text{TED}} + \cos\xi_{\text{TED}}}\right)^{-1} \\ \xi_{\text{TED}} &= t\sqrt{\frac{2\pi f_n c_{\text{V}}}{2\kappa}}, \end{aligned} \tag{7.9}$$

where T is the temperature (typically 300 K). Note that Q_{TED} reduces with thickness (much like Q_{clamp}). Eqn (7.9) makes it possible to determine how closely a given string is operating to the thermoelastic limit. Values of the appropriate material properties for most of the semiconductor materials used in MEMS, including epitaxial SiC films, are shown in Table 7.1.

7.4 Figures of merit for optomechanics and sensing

We will focus on two figures of merit; the $Q \times f$ product, and the product of the Q and the surface-area-to-volume ratio, $Q \times R$. The first of these arises naturally in optomechanics when one considers mechanical displacement sensing, mass sensing, and quantum protocols such as entanglement generation, whilst the latter is important for mass detection and chemo-sensing. As such, we will consider mass sensing as an exemplary scenario.

For a d-c beam sensor we wish to detect a change in its resonance frequency that occurs when its mass and/or stiffness are altered by the adsorption of a material [313]. The resonant frequency shift

[1] If phonons scatter more rapidly than the vibrational period of a lattice distortion induced by a local strain then the Akhiezer effect becomes important in addition to TED [33]. For bending-mode MEMS devices TED is dominant.

is dominated by the added mass when the molecules are adsorbed at the high vibrational amplitude points, while adsorption at nodal or clamping points predominately alters the stiffness [367]. Thus, it can be important to control the position of the molecular adsorption through a surface functionalisation process.

Generally, the resonator natural frequency reduces as the resonator mass increases [368, 369]. An explicit relationship that shows this can be simply established under the approximation that the stiffness of the resonator is unchanged by the added mass. This approximation is appropriate when the molecules adsorb at or near the points of high vibrational amplitude on the resonator. The resonance frequency shift (Δf_n) can then be straightforwardly determined using the relationship $k_n = m_{\text{eff}} f_n^2$ between the spring constant, effective mass (m_{eff}), and frequency of the resonator mode (f_n). In the case where the fractional change in the effective mass ($\Delta m_n / m_{\text{eff}}$) is small, it is straightforward to show that

$$\frac{\Delta f_n}{f_n} = -\frac{\Delta m_n}{2m_{\text{eff}}}, \tag{7.10}$$

where it is natural to define the mass sensitivity $S_{\text{m}} = \Delta f_n / \Delta m_n = f_n / 2m_{\text{eff}}$ [304].

It is important to note that the effective mass m_{eff} of a resonator mode is not equal to the total mass m_{tot} of the resonator; rather, the effective mass is a fraction of m_{tot} determined by the mode shape. For instance, for a bridge resonator

$$m_{\text{eff}} = 0.735 \times m_{\text{tot}} = 0.735 \times Ltw\rho, \tag{7.11}$$

where the constant value of 0.735 represents the decreased contribution of mass near the clamping points [370]. Similarly, the change in effective mass Δm_n is a fraction of the total particle mass, depending on where the mass is added to the resonator. The change in effective mass only equals the total added mass if the mass is added at the position of peak amplitude of vibration.

7.4.1 Minimum resolvable mass

As discussed above, mass sensing is a common use of beam microresonators (Fig. 7.3), where the sensing is performed by measuring the frequency shift following adsorption [371,372]. The uncertainty in this frequency shift measurement determines the resolution of the sensor. Two common strategies are used to perform precise measurements of the resonance frequency of micromechanical resonators.

In the first technique, the motion of the resonator is detected, delayed, amplified, and fed-back onto the resonator *via* an applied force [373]. With correct choice of the delay, the applied force reinforces the velocity of the resonator providing a gain process that competes with its intrinsic damping. With sufficient amplification, this results in regenerative oscillation of the motion of the resonator, closely analogous to laser oscillation. The oscillation occurs at the mechanical resonance frequency, thereby allowing its precise determination.

In the second technique, the motion of the resonator is driven by a set oscillatory force. The response to the force is maximised at the mechanical resonance frequency, or more generally, at each mechanical resonance frequency of the device. The phase of the response to the force varies linearly

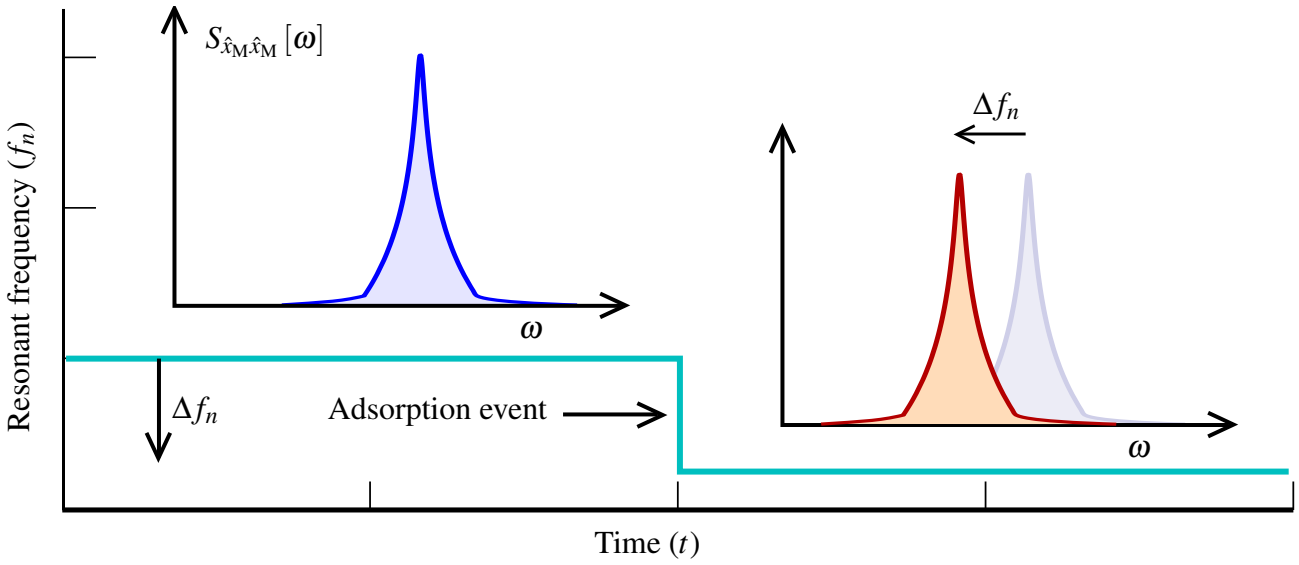

Figure 7.3: Schematic of a mass detection mechanism using a microresonator. The adsorption of an added mass causes a frequency shift Δf_n which can be detected using a phase-locked loop or parametric amplification. Indicative mechanical power spectra are shown before and after the adsorption event (marked).

across the mechanical resonance. Tracking this phase within a phase-locked loop provides an accurate method to characterise the mechanical resonance frequency [373].

To date, these detection mechanisms have made possible the detection of a single cell [312], single virus [374], single deoxyribonucleic acid (DNA) molecule [375], single protein [368], and masses down to the small zeptogram scale [376–378].

Both techniques have the same fundamental noise floor, which is determined by the thermally driven motion of the resonator. This noise floor results in a minimum detectable mass, or mass resolution, well approximated by [376]

$$\frac{\Delta m_n}{2m_{\text{eff}}} \approx \sqrt{\frac{E_{\text{th}}}{E_{\text{osc}}}} \sqrt{\frac{1}{\tau}} \sqrt{\frac{1}{Q \times f_n}}, \tag{7.12}$$

where $E_{\text{th}} = k_{\text{B}} T$ is the thermal energy of the resonator (with k_{B} being Boltzmann's constant and T the temperature), E_{osc} is the energy of the coherent oscillation of the resonator mode, and τ is the total measurement time. It is clear from (7.12) that the mass resolution can be improved both by reducing the effective mass of the resonator and by increasing its $Q \times f_n$ product. However, reducing the size of a resonator both reduces the total adsorption area, and usually results in a decreased Q. Therefore, it is useful to consider two figures of merit to evaluate the sensor performance; $Q \times f_n$ (Hz) and $Q \times R$ (nm^{-1}), where R is the resonator's surface-to-volume ratio [382].

Fig. 7.4 shows a survey of values of these figures of merit drawn from the literature on double-clamped beams. Every device represented was operated in vacuum conditions, such that medium damping is negligible. It is clear that the upper right corner, being the region of high $Q \times R$ and $Q \times f_1$, is dominated by large (∼mm length scale) SiC and SiN bridges. Cryogenic devices, such as the AlN bridge [381], can enjoy higher absolute mass resolution due to their much smaller mass, but with the added complication of integrating vacuum and cryogenic conditions.

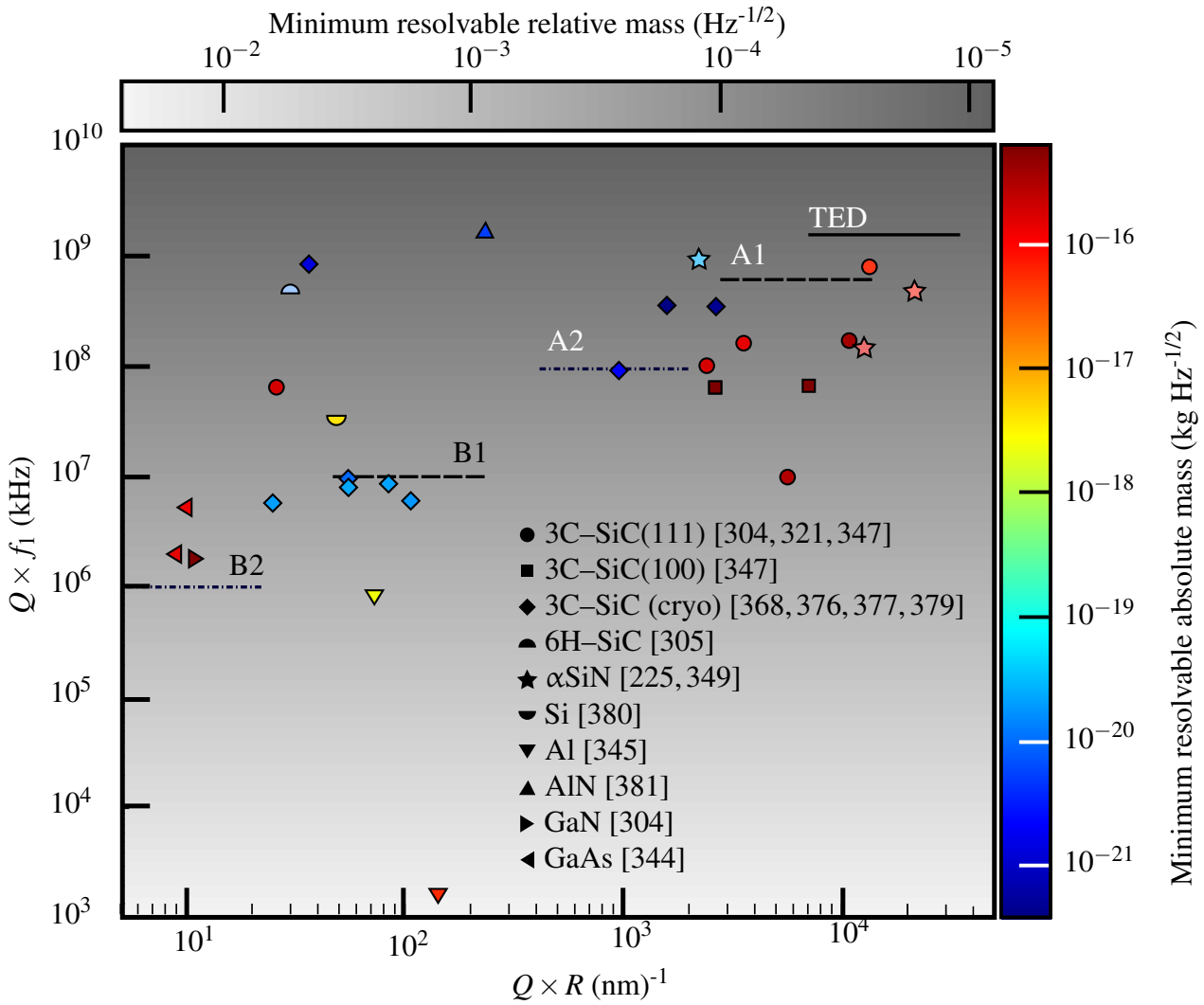

Figure 7.4: Literature survey of doubly-clamped beam resonators. Each point in the $Q \times R$–$Q \times f_1$ plane is experimental data. The table includes resonators of 3C-SiC(111) [304, 321, 347], 3C-SiC(100) [347], 3C-SiC (cryo) [368, 376, 377, 379], 6H–SiC [305], αSiN [225, 349], Si [380], Al (aluminium) [345], AlN (aluminium nitride) [381], GaN [304], and GaAs [344]. Points are coloured (right-hand colour bar) according to the (theoretical) minimum resolvable mass (within a measurement time of one second), assuming that the device is operated under conditions of regenerative oscillation (Eqn (7.12)) with $E_{\rm osc}/E_{\rm th} = 10^3$. The upper colour bar corresponds to the background greyscale gradient; the minimum detectable mass as a fraction of the mode mass. The lines TED, A1, A2, B1, and B2 are theoretical calculations of the properties of 3C-SiC resonators for different lengths, widths, and substrate thicknesses. We have included thermoelastic dissipation and clamping loss. Each line corresponds to sweeping the beam length from 200 μm (left end) to 1000 μm (right end). TED=thermoelastic dissipation limit, which is approximately independent of width; A=substrate thickness 25 μm, B=substrate thickness 2.5 μm; 1=4 μm width, 2=40 μm width. The beam thickness is fixed at 250 nm.

We also show theoretical limits on the figures of merit in Fig. 7.4; they are indicated by lines. These are calculated assuming SiC resonators with a fixed thickness of 250 nm. In the upper right is the thermoelastic limit for devices (with intrinsic stress 1.5 GPa) of lengths ranging from 200 μm (left end) to 1000 μm (right end). Note that this confirms that the resonators reported in [321] are operating close to their material limit. Note also that the extensive presence of crystalline defects needs to be factored in for such heteroepitaxial SiC films. The remaining lines correspond to calculations incorporating clamping losses according to [356] for four combinations of resonator width and substrate thickness. These indicate, yet again, that the beam should be thin and the substrate thick to maximise $Q \times R$ and $Q \times f_1$.

Influence of mean stress on mass sensitivity

From the preceding discussion we can see that out-of-plane flexural string modes (in their intrinsic limit) obey $Q \times f \propto \sigma$. This makes the mean stress an extremely important parameter for device fabrication. Physically, this corresponds to the dissipation being 'diluted' by the mechanical energy stored in the mean tensile stress [382].

7.5 3C-SiC beam resonator fabrication process

SiC on Si beam resonators can be fabricated using Si surface micromachining through four stages of:

- photolithography;
- SiC anisotropic etching;
- Si isotropic etching; and
- photoresist removal.

Resonators fabricated in this manner have suspended and floating anchors as the result of isotropic etching (Fig. 7.5 panel *a*)). To overcome this and create perfect-clamped resonators, two photolithography steps can be used [321]. The first lithography step is used to pattern the microresonator structures on the surface of the SiC film and the second step (Fig. 7.5, panel *i*)) is used to cover the anchors prior to the isotropic Si etching in order to prevent them from being overetched. This is a much faster and easier approach than the backside bulk micromachining method previously reported in the literature [225]. The scanning electron microscopy (SEM) images in Fig. 7.5 show a comparison between beam resonators with suspended anchors (panel *i*) and perfect-clamped beams (panel *ii*).

Fabrication of the SiC resonators used in our experiment (§ 7.6) was performed by Atieh R. Kermany. She fabricated a range of epitaxial 3C-SiC microstrings deposited on on-axis Si(100) and Si(111) with lengths of up to 2600 μm, thicknesses of 50 nm and 255 nm, and widths of 4-12 μm through the four stages of; photolithography, SiC anisotropic etching using hydrogen chloride (HCl), Si isotropic etching using xenon difluoride (XeF_2), and photoresist removal through oxygen plasma (Tegal 915). As described above, an intermediate photolithography step was used to cover the anchors and ensure that the strings are perfectly-clamped.

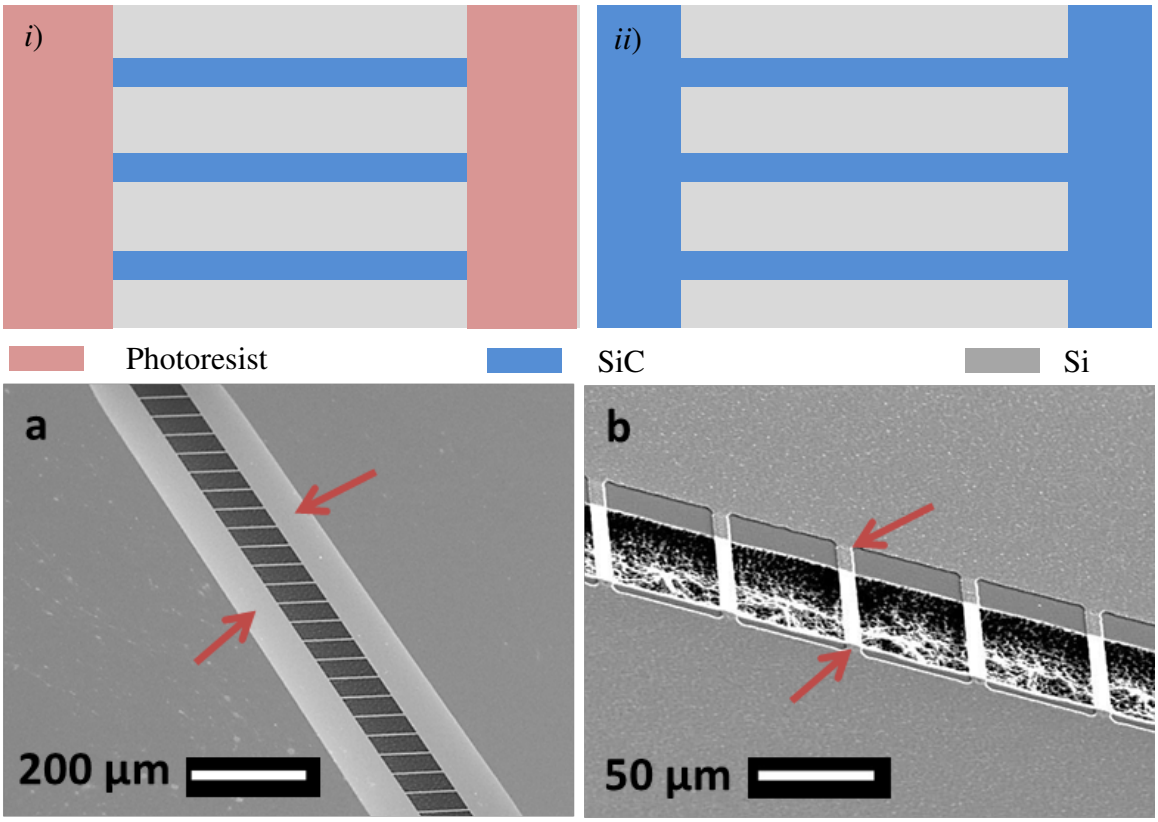

Figure 7.5: Schematic of additional photolithography step required for perfect clamping, and SEM images of resulting bridge resonators. Figured reused and modified with permission of Atieh R. Kermany.
i) Top-down view of second mask patterning (rectangle shapes covering the anchors) prior to the Si isotropic etching to protect the anchors; and
ii) perfect-clamped resonators after the Si etching and photoresist removal.
a) Bridge resonators with suspended anchors. Arrows indicate where the bridge resonators are all connected as the result of the SiC being overetched.
b) Perfect-clamped bridge resonators. The red arrows show where the anchors have been protected as the result of the second lithography step.

An equivalent set of perfect-clamped strings were also fabricated, but with photoresist residues deliberately left behind on the clamping points. This allowed us to determine how sensitive the strings' properties are to this common fabrication imperfection.

7.6 Experimental characterisation of SiC resonators

Measurement of the fundamental out-of-plane mode f_n and Q of the strings was made using all-fibre Mach-Zehnder optical interferometry. The Q factors were obtained using the free ring-down method (Eqn (7.5)) with piezoelectric actuation. All measurements were performed at room temperature, and most were under uniform high vacuum of 7.7×10^{-7} mbar.

7.6.1 Measurement apparatus

A measurement is performed as follows. A resonator is placed inside the vacuum chamber and excited piezoelectrically. Light is directed onto the oscillator and a portion of the reflected beam is collected and measured using balanced heterodyne detection (see § 3.5.2). Vibrations of the oscillator induce a phase modulation that is visible as a peak in the power spectrum of the photocurrent. As the amplitude of vibration decays the height of this peak decreases until it reaches its thermal value (which may be lower than the noise floor of the measurement). The oscillator's decay rate is given by the decay time according to Eqn (7.5).

Further details of the apparatus are given below.

Vacuum chamber

Our vacuum chamber was designed by George Brawley and built in-house. It achieves a base pressure of approximately 7.7×10^{-7} mbar with no bakeout (measured with an Edwards wide range gauge WRG-S). Imaging access is provided by two quartz windows, electronic feedthroughs for the micropositioning stages are standard LEMO connectors, and the optical fibre is fed into the chamber through a Teflon plug as reported by [383]. The chamber is evacuated using a conventional roughing pump plus molecular turbopump arrangement (we have used an Edwards EST-75DX turbopump and XDD1 diaphragm roughing pump).

Due to the unusual specifications of the chamber several flanges have been fitted with Teflon o-rings, rather than the usual Klein flange (elastomeric o-ring sealed against flat surfaces) or copper flange (knife-edge seal in soft metal) arrangements. There were initially worries that viscous deformation of the o-rings—a known property of Teflon—would lead to a loss of sealing capability over time, but there has been no observable degradation over approximately two years. Our o-rings were fabricated by the UQ Physics Workshop.

A schematic of the chamber and the micropositioning stages (SLC-24 by SmarAct GmbH) that are mounted inside it is given in Fig. 7.6. Stage fittings were fabricated by the UQ Physics Workshop, based on designs by George Brawley and James Bennett.

Optics

As briefly discussed above, a house-built heterodyne detection scheme was employed to measure the resonance frequencies and Q factors of SiC strings. For a refresher on heterodyne measurements see § 3.5.2.

The key components of the apparatus are shown in Fig. 7.7.

The probe and local oscillator (LO) beams are derived from a single beam (SOLSTIS TiS laser by M Squared, $\lambda \approx 780$ nm) passed through an AOM that is driven at 68.8 MHz. The first diffracted order is employed as the LO, and the undiffracted light becomes the probe. A half-silvered mirror is used to separate the beams, which do not have parallel propagation vectors after the AOM because of the momentum transferred to the diffracted beam by the absorption of an acoustic phonon. Both beams

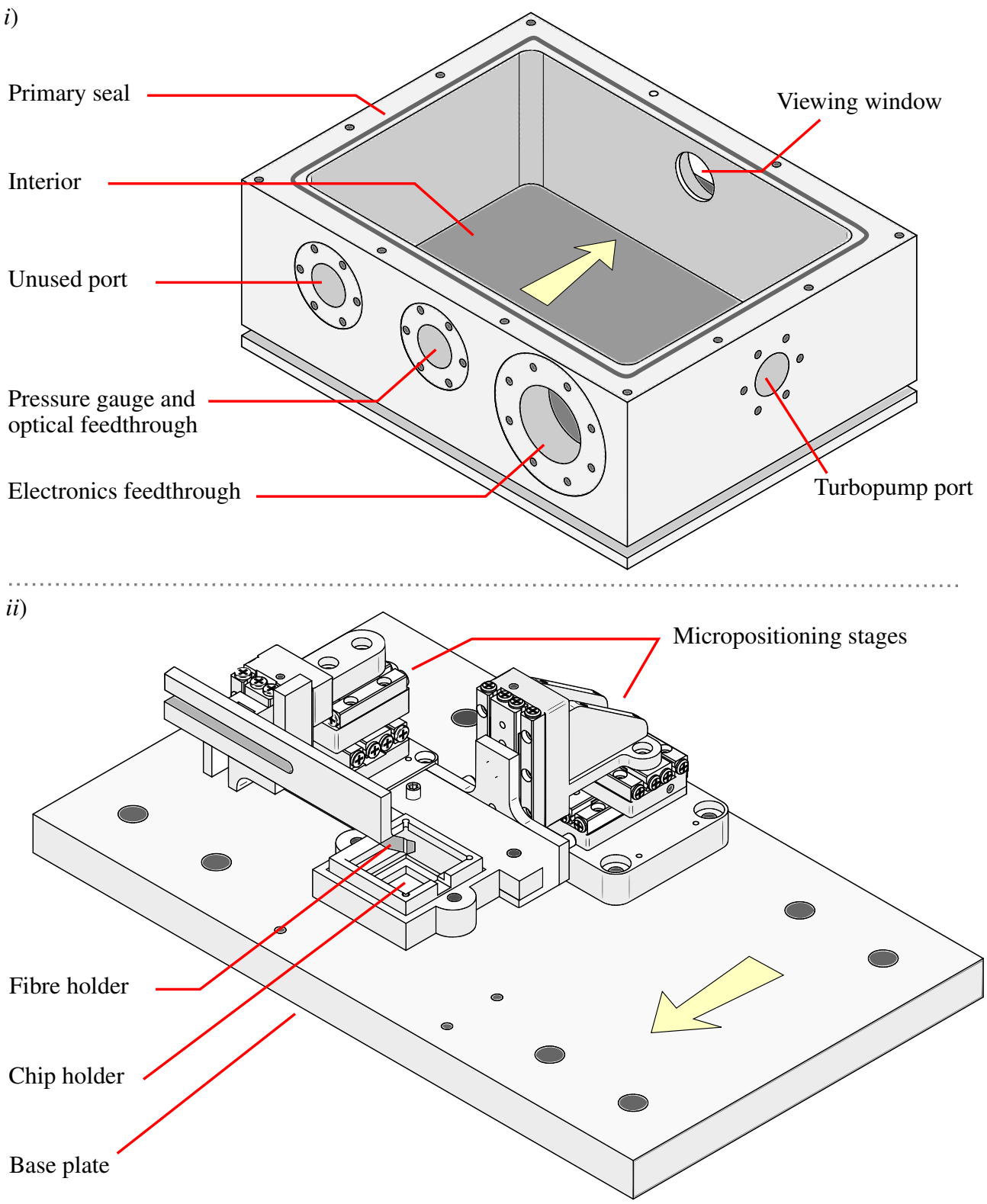

Figure 7.6: Schematic of vacuum chamber and micropositioning stages. The yellow arrows show relative orientation when the base plate is inserted into the chamber.
i) Vacuum chamber *sans* fittings and lid. The unused port could be fitted with an ion pump for future experiments.
ii) Plate holding micropositioning stages for insertion into vacuum chamber. This gives three-axis control for both the resonator position and fibre position. In this configuration—used for the isolated trampoline resonators and drums—the fibre points downwards towards the device. For the microstrings it was more convenient to mount the chip in the vertical plane and hold the fibre horizontally instead (not shown).

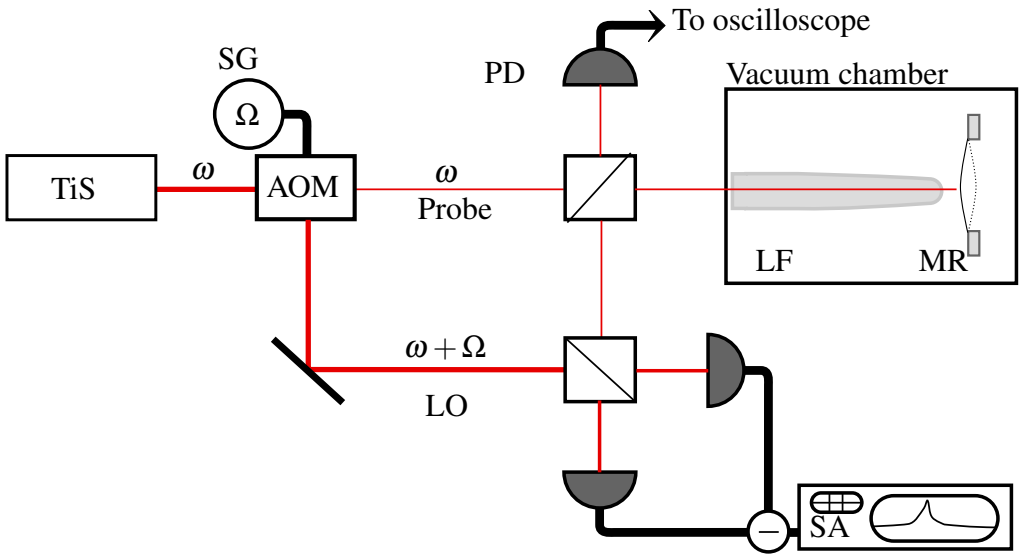

Figure 7.7: Simplified diagram of experimental apparatus (not to scale). A signal generator (SG) drives an AOM at $\Omega = 68.8$ MHz; the 0^{th} and 1^{st} diffracted orders form the probe and LO beams. Probe light is passed into the vacuum chamber and focussed onto the mechanical resonator (MR) by a lensed fibre (LF). Retroreflected light is collected by the fibre and mixed on a beamsplitter with the LO to allow balanced homodyne detection of the mechanical motion. The extra photodiode (PD) was used to monitor the amount of light entering the vacuum chamber.

are then coupled into single-mode fibre (SMF); this has several advantages, including full polarisation control, ease of mode-matching, and eliminating the need for free-space optical elements within the vacuum chamber.

The probe beam is split on a balanced beamsplitter, allowing the incident power to be monitored. The remaining probe light is then passed into the vacuum chamber *via* a Teflon fibre feedthrough [383]. It is there coupled into free space by a tapered lensed fibre. We have employed a Nanonics lensed fibre with a hemispherical lens, a nominal beam spot of 1.5 μm, and a working distance of approximately 5 μm. This was fixed to the aluminium arm indicated in Fig. 7.6.

A fraction of the light retroreflected from the microstring is collected by the same lensed fibre and mixed with the LO on a second balanced beamsplitter. Both optical outputs are then sent to a balanced photodetector (New Focus 1807 Balanced Photoreceiver), and the resulting photocurrent viewed using a spectrum analyser (N9010a Agilent). During experiments we did not mix down the photocurrent; it is sufficient to observe the sidebands of the probe–carrier beat note at ± 68.8 MHz.

We have used up to approximately 50 μW of light in the probe beam during detection. The LO power was chosen to allow approximately 8 dB of clearance between the electronic noise and the quantum noise. These settings satisfy the $|\alpha| \ll |\beta_{\text{LO}}|$ requirement to be insensitive to the LO noise (§ 3.5), and also avoided saturating the balanced photodetector.

7.6.2 Ringdown measurements

The mechanical modes of SiC string resonators are generally narrow enough that they cannot be resolved by a spectrum analyser; it overestimates their linewidth. Thus, it is not possible to determine

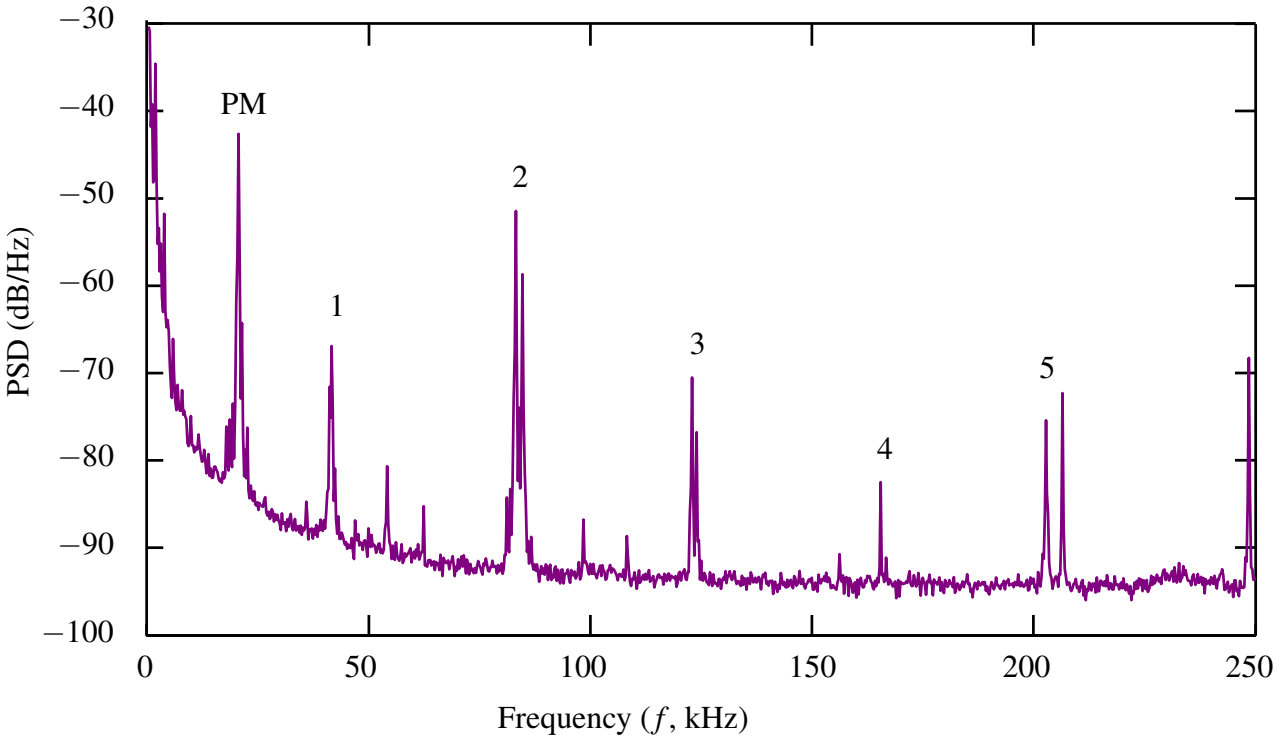

Figure 7.8: A typical power spectrum of showing the modes of a SiC string resonator. The peaks corresponding to each flexural mode (out-of-plane) are labelled. A resolution bandwidth of 100 Hz was used to record these data, which correspond to a cross-section through Fig. 7.10 (at approximately 1 mm from the end of the string). The phase modulation (PM) is generated within the TiS laser and used to lock the wavelength to an internal cavity: it is not due to a mechanical vibration. The vertical axis is scaled such that the beat between the LO and carrier of the probe has magnitude 0 dB.

Γ by directly measuring the apparent linewidth of a mechanical peak. Instead, we have opted to use the free ringdown method.

We begin by locating a mechanical mode. For high-Q strings the thermally-excited modes can be seen above the classical laser noise, as shown in the power spectrum (PSD) Fig. 7.8. One then sets the spectrum analyser to operate in zero-span mode. In this mode the output trace is given by the integral of the power spectrum over a window centred at the resonance frequency, with a width equal to the resolution bandwidth of the analyser. By considering Eqn (3.19) and Fig. 3.2 we can see that this is essentially a measurement of the energy contained by that mode of oscillation.

To create a highly-excited state we rapidly[2] displace the oscillator's centre of mass over 1–2 μm. This is usually sufficient to excite an oscillation that achieves a signal-to-noise ratio (SNR) in excess of 10 dB: we routinely see SNRs of 40 dB. An example of this sudden increase in signal is seen in Fig. 7.9. We then track the decay of the oscillator until the signal vanishes into the noise floor once more. Note that it is common for the noise floors before and after the ringdown to be different, as is evident in Fig. 7.9. This effect can be understood by noting that the mode-matching between the lensed fibre and the reflected light depends on the mean position of the resonator.

To calculate the Q factor we perform a linear fit to the logarithm of the measured integrated power

[2]The exact timescale is determined by the stepping rate of the micropositioning stages, which is sub-millisecond.

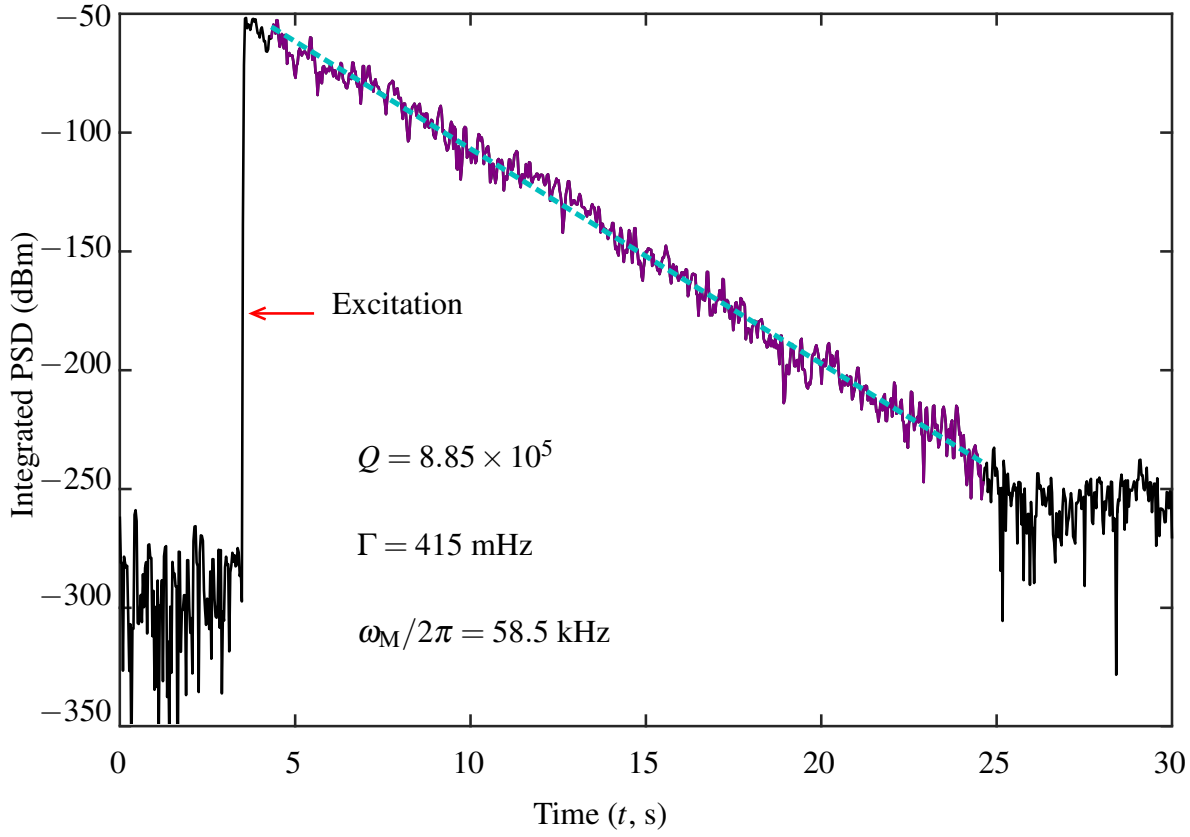

Figure 7.9: Typical ringdown trace of SiC string resonator. The mechanical signal rapidly climbs above the noise floor at the time of excitation (marked with red arrow) and then slowly rings back into a new noise floor (far right). The fitted region is shown in purple and the linear fit is cyan. This trace was obtained from the fundamental mode of a 2 mm long string of 4 μm width and 250 nm thickness. A resolution bandwidth of 20 Hz was used. Note that longer strings typically have larger Q.

over the region where the decaying signal exceeds the noise. The slope of this fit, s, then gives the Q according to

$$Q = \frac{10\omega_M}{-s \ln 10}.$$

It is worth noting that this gives a conservative estimate of the Q, because the logarithmic scaling effectively weights low-power points more strongly than the high-power ones.

7.7 Experimental results

A summary of results is given in Table 7.3. The measured fundamental modes were within 10% of numerical predictions supplied by Atieh R. Kermany (discussed in detail in [321]).

7.7.1 Material properties and string geometry

We can observe from Table 7.3 that the string f_n is directly proportional to $\sigma^{1/2}$, so that for similar L–w geometries we have

$$\frac{f_n^{(1)}}{f_n^{(2)}} \approx \sqrt{\frac{\sigma^{(1)}}{\sigma^{(2)}}}.$$

Table 7.3: Measured mechanical behaviour values for 4 μm wide microstrings.

L (μm)	Material	σ (MPa)	t (nm)	f_n (kHz)	Q	$Q \times f_n$ (Hz)	$Q \times R$ (nm^{-1})	Q_{TED}
2600	SiC(111)	650	255	77	2.4×10^6	1.8×10^{11}	20025	2.1×10^7
	SiC(111)	230	50	42.1	2.6×10^5	1.1×10^{10}	10530	9.8×10^8
	SiC(100)	250	255	45	1.6×10^6	7.2×10^{10}	13350	4.3×10^7
1000	SiC(111)	650	255	202	5.5×10^5	1.1×10^{11}	4590	7.8×10^6
	SiC(100)	250	255	118	6×10^5	7.1×10^{10}	5007	1.6×10^7

As explained in § 7.3.1, this is because the mean stress dominates over the Young's modulus and thickness (*cf.* Eqn (7.3)). This is manifest in our experimental results, with resonators fabricated from SiC(111) (50 nm thickness) and SiC(100) (255 nm thickness) having comparable resonance frequencies despite a five-fold difference in thickness.

At the same time, from Table 7.3 we observe that—for similar geometries and film thicknesses—SiC(111) and SiC(100) strings have comparable Q values. This is remarkable because the SiC(100) strings have considerably lower mean stress (250 MPa) than SiC(111) strings (650 MPa). This outcome can be attributed to the difference in defect densities between the two films; SiC(100) films have an overall better crystal quality than SiC(111) films, thanks to a faster stress relaxation rate [317, 384]. It is therefore expected that SiC(100) films would have less defect-driven internal friction. The reduced mean stress is thus compensated for by the superior film quality, resulting in comparable Q factors.

It is remarkable that as the thickness of SiC(111) resonators reduces from 255 nm to 50 nm (with fixed L and w) the Q drops by almost an order of magnitude: from 2.4×10^6 to 2.6×10^5. The reason for this reduction is two-fold. Firstly, the mean stress drops from 650 MPa to 230 MPa. Secondly, the 50 nm thick devices are comprised of the defect-heavy portion of the 3C-SiC film nearest to the SiC–Si interface [336]. This results in high internal friction that substantially lowers the Q. Further measurements are required to confirm these hypotheses.

Note that in terms of Q factors alone, the SiC(100) strings could potentially perform as well as the SiC(111) bridges, thanks to their higher crystal quality; however, their substantially lower residual stress drastically limits their $Q \times f_n$ performance. Finally, we can observe that both $Q \times f_n$ and $Q \times R$ increase as the strings' lengths increase, due to a substantial increase of Q, able to compensate for the reduction in natural resonant frequencies.

Nearing the thermoelastic dissipation limit

We can conclude from Tables 7.3 and 7.4 that SiC(111) with 1500 MPa mean stress has the closest Q factor (3×10^6) to the thermoelastic limit $Q_{\mathrm{TED}} = 5.6 \times 10^6$, calculated from Eqn (7.9). We calculated the $Q \times f_n$ of this string to be 8.4×10^{11} Hz, approximately only a factor of two away from its upper limit ($Q \times f_n = 1.6 \times 10^{12}$ Hz). Reaching the TED limit will require a reduction in the defect density of the SiC thin film and an increase in the residual tensile stress. This would allow the fabrication of longer strings with large $Q \times f_n$ and $Q \times R$ products.

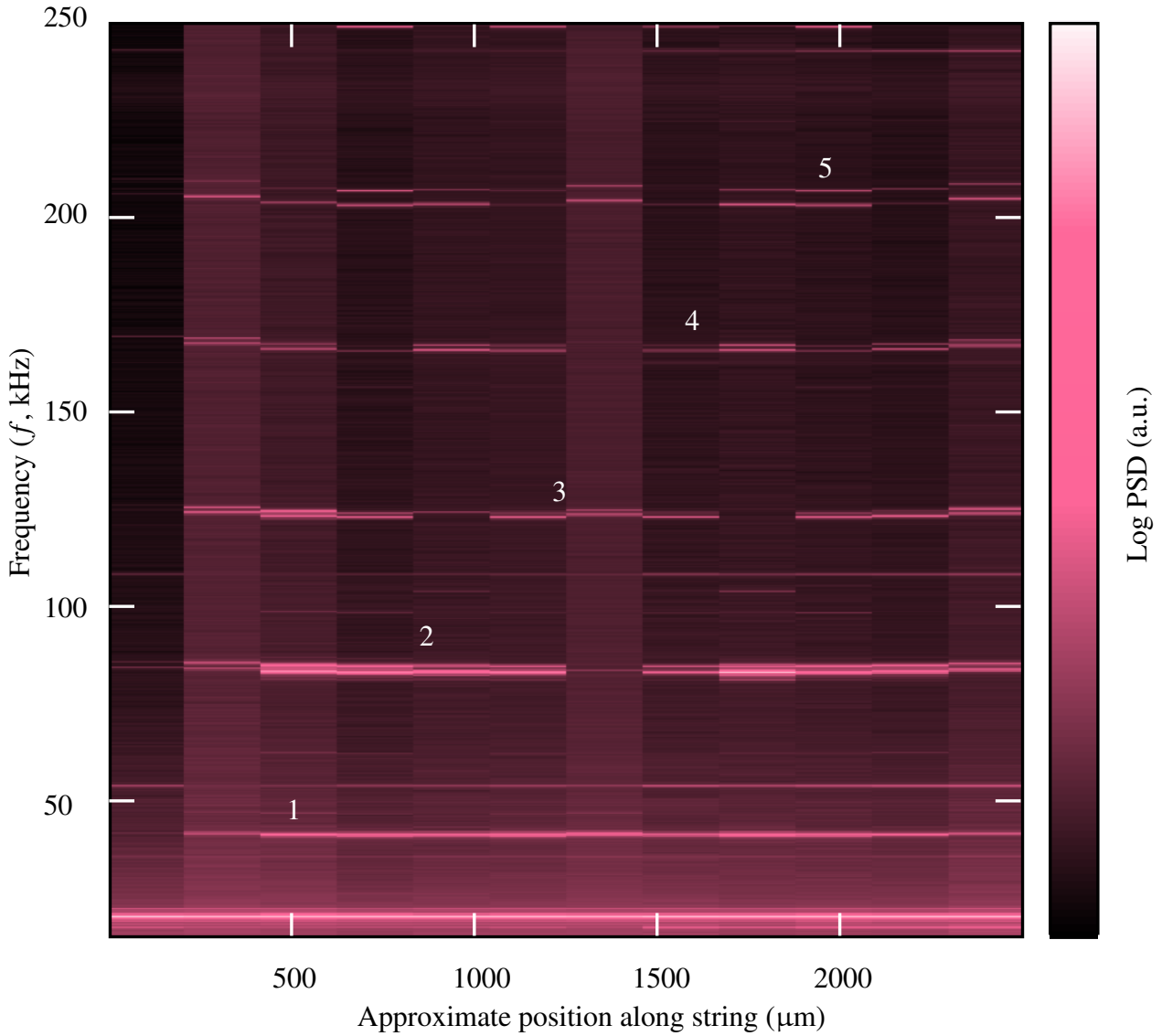

Figure 7.10: Experimental demonstration of the mode structure of a SiC string. Modes appear as peaks in the power spectrum (PSD). The out-of-plane flexural modes are labelled by their mode numbers, corresponding to the number of antinodes displayed along the string. Note that each mode is split into two; numerics indicate that this is due to hybridisation of the flexural and torsional modes. The uniform peak along the bottom of the plot (at 20.3 kHz) corresponds to a phase modulation used to lock the laser's wavelength; each trace has been normalised such that this peak has constant height. These data were collected as detailed in § 7.6. The resonator was a 2.6 mm long string with $Q \sim 10^6$.

7.7.2 Mode functions

We experimentally determined the mode structure of a SiC string and showed that it matches the theoretical expectation (*cf.* Fig. 7.1). The data shown in Fig. 7.10 were collected by collecting multiple power spectra of the mechanical motion as the lensed fibre was stepped along the length of the fibre. The spectrum shown in Fig. 7.8 is a cross-section through Fig. 7.10.

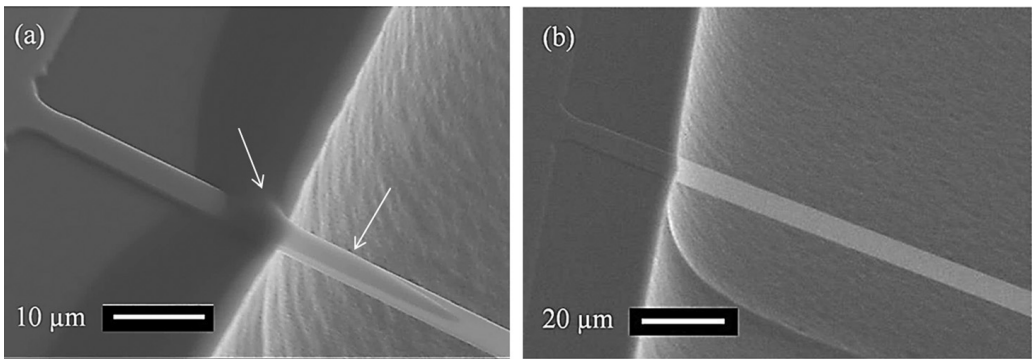

Figure 7.11: SEM of a microstring with residual photoresist on its anchors (*a*), and a completely clean microstring (*b*), used for the comparison in Table 7.4. The photoresist residues in (*a*) are highlighted by arrows. Figure supplied by Atieh R. Kermany.

Table 7.4: Measured Q factors for microstrings without residues (Q_1) and with photoresist residues on their anchors (Q_2). The values are an average out of five measurements. Strings have $w = 4$ µm and $t = 255$ nm.

L (µm)	Q_1 (clean)	Q_2 (resist)
2600	2.4×10^6	9×10^4
1000	5.5×10^5	2.7×10^4

7.7.3 String clamping condition

To analyse the effect of the clamping conditions on Q, we have fabricated and compared the resonant frequencies and corresponding Q factors of two equivalent sets of resonators made of SiC(111) with the dimensions mentioned in Table 7.4. One set had clean anchors, and one set were left imperfect (see § 7.5).

Our comparison indicates similar f_n values for both clamping conditions (with and without residues); however, the Q decreases by more than one order of magnitude when photoresist residue is present, as shown in Table 7.4. The extra oxygen plasma cleaning step is clearly worth the effort.

7.7.4 Influence of environmental pressure

In addition to the above, we also took a single data set studying the effects of pressure on the mechanical Q. The results, plotted in Fig. 7.2, lead us to conclude that a pressure of about 10^{-4} mbar represents the boundary between the intrinsic and molecular regimes for these devices. This also means that below 10^4 mbar variations in pressure will have only a small effects on the Q factor.

7.8 Other resonator geometries

Our optically-detected ringdown apparatus has been—and will continue to be—used for measurements of other SiC resonator designs. Key examples include large drum resonators, up to 3 mm across; free-free beams, which are suspended by tethers at their nodal points; and nested trampoline resonators.

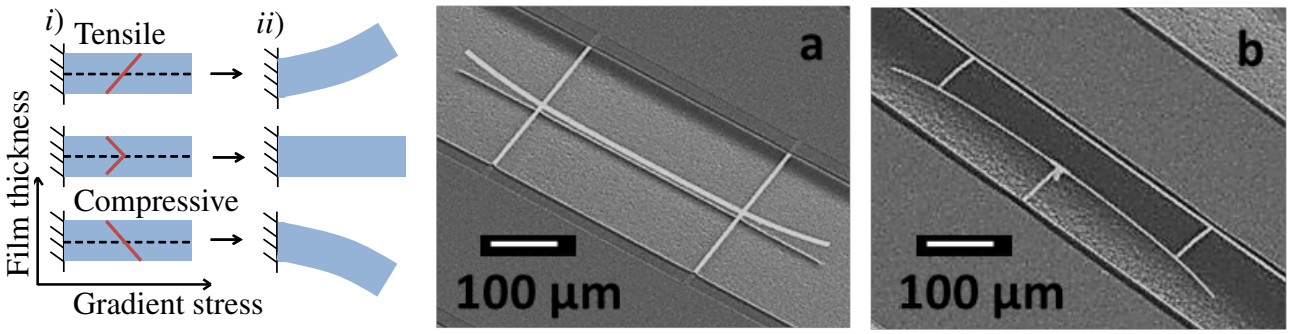

Figure 7.12: Intrinsic bending of free-free beam resonators. Figure reused and modified with permission of Atieh R. Kermany.
i) Stress gradients within the epitaxial film (red line) and *ii*) intrinsic bending behaviours of released cantilevers as the result of gradient stresses. For simplicity a linear gradient is assumed.
a) A 250 nm thickness SiC(111) free-free beam showing the effect of tensile gradient stress.
b) An equivalent device fabricated in SiC(100), showing compressive gradient stress.

The drum studies were intended to determine the effects of depositing a graphene layer onto the SiC layer. This conductive, but extremely light, material can in principle allow electrostatic actuation and readout without metallisation of the drum, which generally reduces its Q by at least an order of magnitude. Unfortunately, the results were inconclusive because of a large variance in the drum etching outcomes. This meant that no systemic degradation of the Q could be detected. Typical devices tested as part of this study had $f_1 \sim 10^5$ Hz and $Q \sim 10^3$. An example is shown in Fig. 7.13 panel *i*).

Free-free beams can in principle provide high-Q by isolating the resonator from its environment. This is achieved by suspending the beam from tethers that attach at the nodal points of the fundamental free-free vibration (which has two nodes along the beam), as seen in Fig. 7.12. Unfortunately, the design of free-free beams in epitaxial SiC films is greatly complicated by the gradient stress, which causes the beams to curl. Furthermore, the mean stress makes it difficult to predict where the true nodal points of the fundamental mode will lie, such that naïvely-placed tethers are often not in the correct location. A selection of free-free beams were fabricated by Atieh R. Kermany and tested by us, but the combination of the above factors limited their Q factors to only 10^3–10^4. This could be improved with further numerical modelling to improve the tether placement design.

The final variety of resonator that has been examined with our apparatus is the isolated trampoline resonator designed by Warwick P. Bowen, Victor M. Valenzuela, Atieh R. Kermany, and Eric Romero-Sánchez. This aims to increase the Q of a trampoline resonator [385] fabricated from SiC by isolating its substrate from the rest of the Si chip [386]. To achieve this, a portion of the silicon chip, on which the trampoline resides, is etched out of the surrounding chip and suspended by only eight SiC tethers. This can be seen in Fig. 7.13 panel *ii*). Design and testing of these devices is ongoing, but preliminary measurements indicate that the Q is of the order of 10^6, with isolated results hinting at Q factors up to 10^8.

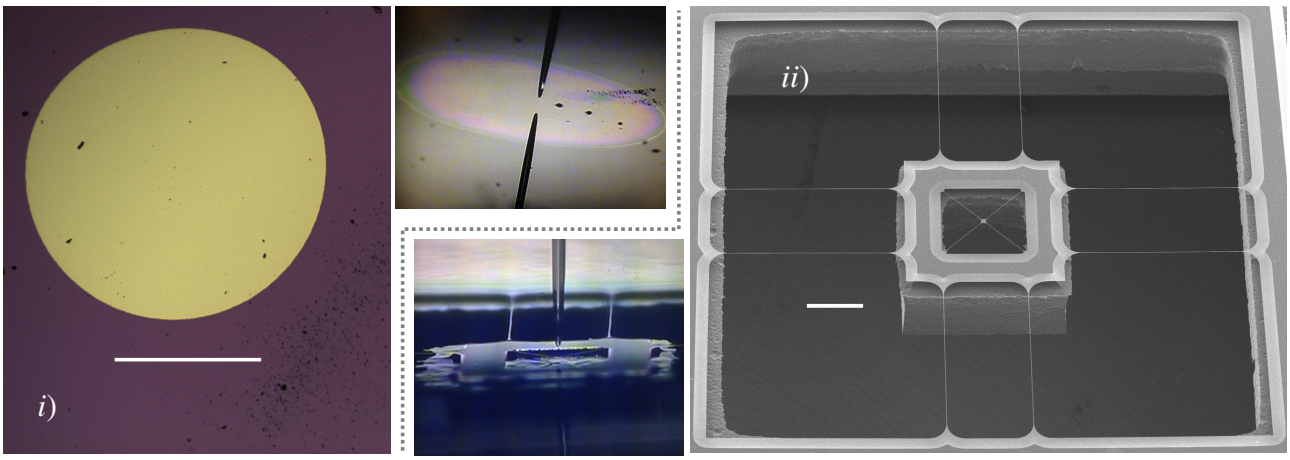

Figure 7.13: SiC drum and trampoline resonators characterised by our optically-detected ringdown apparatus. The scale bars are 500 μm across in both panels.
i) Drum resonators fabricated by Zulfiqar Khan (Griffith University). Graphene was deposited on several of these drums to examine its effects on the Q factor, but results were inconclusive. Micrographs were provided by Christopher Baker. The inset shows the fibre taper in position to measure a drum's Q.
ii) Isolated trampoline resonators designed and fabricated by Warwick P. Bowen, Victor M. Valenzuela, Atieh R. Kermany, and Eric Romero-Sánchez (The University of Queensland). These aim to increase the mechanical Q of the central trampoline resonator by isolating it from the substrate. This is achieved by suspending a block of the substrate. SEM images supplied.

7.9 Conclusion

We reviewed the factors that control the frequency, damping parameters, and material properties of epitaxial SiC, and showed how these affect the use of SiC strings in optomechanics and/or mass sensing applications. Our experimental measurements found that SiC strings can exhibit an $Q \times f_1$ product of 10^{12} Hz, establishing a new state-of-the-art for micromechanical strings [3] and opening new frontiers for mass sensing applications. Theoretical models indicate that our result is approximately a factor two lower than the thermoelastic dissipation limit. Additional improvement is potentially achievable through the use of;

- a high vacuum environment;
- perfect-clamped anchors, clean from any residues;
- using films with high residual tensile stress;
- improved SiC crystalline quality; and
- strings with tailored geometry, *i.e.* high length-to-width ratios.

We have also begun characterising alternative resonator geometries using our apparatus, including isolated trampoline resonators that have the potential to reach extremely high Q factors ($> 10^8$).

[3] Tsaturyan *et al.* have reported a record $Q \times f$ product of $> 10^{14}$ Hz at room temperature in a phononic band-gap isolated resonator [363]. The bandgap allows soft clamping conditions which suppress mode curvature, thereby dramatically reduces the loss induced by bending in the vicinity of the clamping points.

Further work will be required to determine the optomechanical coupling rates which may be achieved with heteroepitaxial SiC resonators. This could be performed by evanescently coupling them to a whispering-gallery mode resonator.

Chapter 8

Conclusion

In this thesis we have presented our research work—theoretical and experimental—that will advance the field of optomechanics in the unresolved sideband regime. This has the potential to couple optomechanical devices to cold atoms for enhanced quantum control; to permit rapid state-swaps between vibrational and electromagnetic degrees of freedom; and to allow optomechanical studies with nonclassical states in material-damping-limited mechanical devices with extremely high Q factors, or with large masses, for tests of fundamental physics.

8.1 Summary

In Chapter 1 we introduced an archetypical optomechanical device and described a selection of the quantum physics that can be accessed by it (§ 1.1). This chapter also provided a formal introduction to the language of quantum optics (§ 1.3), including defining the Fock, coherent, and squeezed states.

Part 1—The State of the Art

Chapter 2 provided a brief overview of the dynamics of quantum optomechanics (§ 2.1.1 & § 2.1.3), including the cooling and entangling operations that can be accessed in the resolved sideband limit (§ 2.2). With this context in mind we turned to the unresolved sideband regime and surveyed some of the proposals for advancing the capabilities of quantum optomechanics in this area (§ 2.3). In particular, we examined the existing literature for hybrid atom–optomechanics (§ 2.3.3) and pulsed optomechanics (§ 2.3.4) which are highly-relevant to the novel research presented in this thesis.

More advanced theory was introduced in Chapter 3. Covariance matrices (§ 3.1.1), Wigner functions (§ 3.1.2), and explicit solutions to linear Langevin equations (§ 3.3.1) were discussed, and compilations of useful results provided. We hope that the reader might also find these tools beneficial in their research efforts. Finally, homo- and heterodyne measurements were introduced and discussed (§ 3.5). We hope this will assist those looking to 'bridge the gap' between theory and experiment.

Part 2—Progress: Theory

Our research that combined a hybrid atom–optomechanical device with measurement-based feedback cooling was presented in Chapter 4. Our calculations revealed that combining the two approaches does improve the device's cooling power significantly in many parameter regimes, and never degrades it. However, the quantum ground state was only reached when either the feedback cooling or the atoms dominated the cooling, depending upon their respective cooperativities. This scheme could be realised with existing experimental parameters.

In Chapter 5 we returned to pulsed optomechanics and presented an interface that can perform a rapid optical–mechanical state swap with arbitrary initial states. Our protocol was shown to be capable of ground state cooling (§ 5.6), and producing nonclassical motional states from nonclassical optical pulses (§ 5.7.2). We saw that it is also possible to implement squeezing of both modes during the operation (§ 5.8). The results presented in this chapter can also be extended to analogous systems in which pulsed light–matter QND interactions are achieved, such as cold atom spin ensembles.

The final theoretical offering in this thesis is Chapter 6, in which we presented our calculations regarding a squeezer-powered thermodynamic device that operates in a regime beyond the validity of the RWA. This device can act as a heat engine, a heat pump, or a refrigerator (§ 2.1.4). Remarkably, if one makes the RWA on the equations of motion this rich behaviour vanishes, leaving only a heat pump regime. We provided no-go theorems to this effect (§ 6.7), and argued that this indicates that interesting and potentially useful thermodynamical behaviours may be accessible beyond the RWA. We also provided an outline of how the rapid squeezing operations (deep-sub-period) required in our protocol could be generated using pulsed optomechanics (§ 6.8).

Part 3—Progress: Device Design

Our experimental characterisation of SiC string resonators is presented in Chapter 7. SiC micromechanical oscillators are promising for achieving high $Q \times f$ products, indicating that they are well-isolated from their thermal environment (§ 7.4). They are also relatively low frequency, so appropriate for use in the unresolved sideband regime. We measured strings and other SiC resonators (§ 7.8) using optically-detected ringdown (§ 7.6.2). A peak room temperature $Q \times f$ product of 10^{12} Hz was recorded, exceeding the previous state-of-the-art αSiN microstring resonators (§ 7.7).

8.2 Future research directions

Of course, one never has enough time to follow every interesting question that arises during research. In this final section we will list some interesting unanswered questions that we encountered and were unable to address.

On the theoretical side of Chapter 4, it would be interesting to investigate whether there is a formal link between the cold atomic system and a dissipative optomechanical device (one which modulates the linewidth of its cavity, rather than the frequency, as a function of position). This line of thought was inspired by the observation that the forward-scattered power in Fig. 4.1 is controlled by the atomic centre-of-mass position. It is also interesting to consider whether squeezed light can improve the

system's performance, whether synchronisation of the atomic motion in the ring cavity could play a role in the atom–optomechanical interaction [153, 387], or whether their diabolical points [388] can be harnessed for quantum operations. We are also curious to see if it is possible—or useful—to establish a coupling between a mechanical oscillator and the phase coherence of two degenerate atomic clouds (Bose–Einstein condensates), as this has not yet been considered in the literature. If, for example, the tunnelling rate of a bosonic Josephson junction [389] could be modulated by a mechanical device it may give access to new nonlinearities.

Experimental implementation of a remotely-coupled hybrid atom–optomechanical interface with a tapered nanofibre trap [227] was hindered by the emergence of a mechanical instability in the motion of the fibre taper. Lars Madsen is developing an understanding of this phenomenon and how it might be mitigated or exploited. Estimates of the required tolerances on the feedback loop (*e.g.* allowable delay, excess noise, uncertainty in gain, *etc.*) would also be useful to know in this context.

It would be interesting to revisit our interface scheme (Chapter 5) in light of the results of Khosla *et al.* [71], which promise to allow our pulsed state-swap interface to operate much more rapidly than even half a mechanical period. If we do so, it may be appropriate to use the Wigner negativity as a metric for how successful the state swap is, as this is in principle extremely sensitive to perturbation (more so than the infidelity for the states we have considered). It would be very interesting to examine the possibility of entanglement creation through our interface.

Our outline of how to achieve a fast squeezer in Chapter 6 is just that: an outline. A full analysis of the added noise and other performance metrics would be interesting and potentially useful. The first step towards realising this proposal would be demonstrating thermal squeezing of a classical oscillator using our scheme.

Finally, although we have demonstrated excellent $Q \times f$ products in SiC strings, their optomechanical coupling rates are still unknown. Closely-related αSiN strings achieve $g_0 \sim 100$ Hz [165] when coupled to a microsphere whispering-gallery mode resonator. Our homodyne measurement apparatus could be converted to measure this property relatively straightforwardly.

Bibliography

[1] J. S. Bennett, L. S. Madsen, M. Baker, H. Rubinsztein-Dunlop, and W. P. Bowen. Coherent control and feedback cooling in a remotely coupled hybrid atom optomechanical system. *New Journal of Physics*, 16:083036, 2014.

[2] J. S. Bennett, K. Khosla, L. S. Madsen, M. R. Vanner, H. Rubinsztein-dunlop, and W. P. Bowen. A quantum optomechanical interface beyond the resolved sideband limit. *New Journal of Physics*, 18:053030, 2016.

[3] A. R. Kermany, J. S. Bennett, V. M. Valenzuela, W. P. Bowen, and F. Iacopi. Potential of epitaxial silicon carbide microbeam resonators for chemical sensing. *Physica Status Solidi A*, 214 (4):1600437, 2017.

[4] A. R. Kermany, J. S. Bennett, G. A. Brawley, W. P. Bowen, and F. Iacopi. Factors affecting the $f \times Q$ product of 3C-SiC microstrings: What is the upper limit for sensitivity? *Journal of Applied Physics*, 119:055304, 2016.

[5] M. Aspelmeyer, T. J. Kippenberg, and F. Marquardt. Cavity Optomechanics. *Reviews of Modern Physics*, 86 (4):1391–1452, 2014.

[6] S. Camerer, M. Korppi, A. Jöckel, D. Hunger, T. W. Hänsch, and P. Treutlein. Realization of an optomechanical interface between ultracold atoms and a membrane. *Physical Review Letters*, 107:223001, 2011.

[7] P. Lebedew. Untersuchungen uber die Druckkrufte des Lichtes. *Annalen der Physik*, 311 (11):433–458, 1901.

[8] E. F. Nichols and G. F. Hull. The Pressure Due to Radiation. *Proceedings of the American Academy of Arts and Sciences*, 38 (20):559–599, 1903.

[9] O. D. Aguiar. Past, present and future of the Resonant-Mass gravitational wave detectors. *Research in Astronomy and Astrophysics*, 11 (1):1–42, 2011.

[10] V. B. Braginsky, A. B. Manukin, and W. O. Hamilton. Measurement of Weak Forces in Physics Experiments. *Physics Today*, 31 (2):51–52, 1978.

[11] C. M. Caves. Quantum-Mechanical Radiation-Pressure Fluctuations in an Interferometer. *Physical Review Letters*, 45 (2):75–79, 1980.

[12] C. M. Caves. Quantum-mechanical noise in an interferometer. *Physical Review D*, 28 (8):1693–1708, 1981.

[13] A. F. Pace, M. J. Collett, and D. F. Walls. Quantum limits in interferometric detection of gravitational radiation. *Physical Review A*, 47 (4):3173–3189, 1993.

[14] V. B. Braginsky, Y. I. Vorontsov, and K. S. Thorne. Quantum Nondemolition Measurements. *Science*, 209 (4456):547–557, 1980.

[15] J. Chan, T. P. Mayer Alegre, A. H. Safavi-Naeini, J. T. Hill, A. Krause, S. Gröblacher, M. Aspelmeyer, and O. Painter. Laser cooling of a nanomechanical oscillator into its quantum ground state. *Nature*, 478:89–92, 2011.

[16] J. D. Teufel, T. Donner, D. Li, J. W. Harlow, M. S. Allman, K. Cicak, A. J. Sirois, J. D. Whittaker, K. W. Lehnert, and R. W. Simmonds. Sideband cooling of micromechanical motion to the quantum ground state. *Nature*, 475:359–363, 2011.

[17] A. D. O'Connell, M. Hofheinz, M. Ansmann, R. C. Bialczak, M. Lenander, E. Lucero, M. Neeley, D. Sank, H. Wang, M. Weides, J. Wenner, J. M. Martinis, and A. N. Cleland. Quantum ground state and single-phonon control of a mechanical resonator. *Nature*, 464:697–703, 2010.

[18] A. H. Safavi-Naeini, J. Chan, J. T. Hill, T. P. Mayer Alegre, A. Krause, and O. Painter. Observation of Quantum Motion of a Nanomechanical Resonator. *Physical Review Letters*, 108:033602, 2012.

[19] D. W. C. Brooks, T. Botter, S. Schreppler, T. P. Purdy, N. Brahms, and D. M. Stamper-Kurn. Nonclassical light generated by quantum-noise-driven cavity optomechanics. *Nature*, 488:476–480, 2012.

[20] T. P. Purdy, P.-L. Yu, R. W. Peterson, N. S. Kampel, and C. A. Regal. Strong Optomechanical Squeezing of Light. *Physical Review X*, 3:031012, 2013.

[21] W. H. P. R. Nielsen, Y. Tsaturyan, C. Bo Møller, E. S. Polzik, and A. Schliesser. Multimode optomechanical system in the quantum regime. *Proceedings of the National Academy of Science of the USA*, 114 (1):62–66, 2016.

[22] E. E. Wollman, C. U. Lei, A. J. Weinstein, J. Suh, A. Kronwald, F. Marquardt, A. A. Clerk, and K. C. Schwab. Quantum squeezing of motion in a mechanical resonator. *Science*, 349 (952):952–953, 2015.

[23] T. P. Purdy, R. W. Peterson, and C. A. Regal. Observation of Radiation Pressure Shot Noise on a Macroscopic Object. *Science*, 339 (801):1231282, 2013.

[24] J. D. Teufel, F. Lecocq, and R. W. Simmonds. Overwhelming Thermomechanical Motion with Microwave Radiation Pressure Shot Noise. *Physical Review Letters*, 116:013602, 2016.

[25] T. P. Purdy, K. E. Grutter, K. Srinivasan, and J. M. Taylor. Quantum correlations from a room-temperature optomechanical cavity. *Science*, 356:1265–1268, 2017.

[26] Y. Chen. Macroscopic quantum mechanics: theory and experimental concepts of optomechanics. *Journal of Physics B: Atomic, Molecular and Optical Physics*, 46:104001, 2013.

[27] H. Kerdoncuff, U. B. Hoff, G. I. Harris, W. P. Bowen, and U. L. Andersen. Squeezing-enhanced measurement sensitivity in a cavity optomechanical system. *Annalen der Physik*, 527 (1-2):107–114, 2015.

[28] F. Liu, S. Alaie, Z. C. Leseman, and M. Hossein-Zadeh. Sub-pg mass sensing and measurement with an optomechanical oscillator. *Optics Express*, 21 (17):19555–19567, 2013.

[29] A. G. Krause, M. Winger, T. D. Blasius, Q. Lin, and O. Painter. A high-resolution microchip optomechanical accelerometer. *Nature Photonics*, 6:768–772, 2012.

[30] B. P. Abbott *et al.* (LIGO scientific collaboration and VIRGO collaboration). Observation of Gravitational Waves from a Binary Black Hole Merger. *Physical Review Letters*, 116:061102, 2016.

[31] G. J. Milburn and M. J. Woolley. An Introduction to Quantum Optomechanics. *Acta Physica Slovaca*, 61 (5):483–601, 2011.

[32] S. A. Chandorkar, M. Agarwal, R. Melamud, R. N. Candler, K. E. Goodson, and T. W. Kenny. Limits of quality factor in bulk-mode micromechanical resonators. *Proceedings of IEEE MEMS*, Tucson, Arizona, 74–77, 2008.

[33] S. Ghaffari, S. A. Chandorkar, S. Wang, E. J. Ng, C. H. Ahn, V. Hong, Y. Yang, and T. W. Kenny. Quantum Limit of Quality Factor in Silicon Micro and Nano Mechanical Resonators. *Scientific Reports*, 3:3244, 2013.

[34] L. Greuter, S. Starosielec, D. Najer, A. Ludwig, L. Duempelmann, D. Rohner, and R. J. Warburton. A small mode volume tunable microcavity: Development and characterization. *Applied Physics Letters*, 105:121105, 2014.

[35] K. Schneider and P. Seidler. Strong optomechanical coupling in a slotted photonic crystal nanobeam cavity with an ultrahigh quality factor-to-mode volume ratio. *Optics Express*, 24 (13):13850, 2016.

[36] A. Schliesser, G. Anetsberger, R. Rivière, O. Arcizet, and T. J. Kippenberg. High-sensitivity monitoring of micromechanical vibration using optical whispering gallery mode resonators. *New Journal of Physics*, 10:095015, 2008.

[37] M. Blencowe. Quantum electromechanical systems. *Physics Reports*, 395:159 – 222, 2004.

[38] E. Romero-Sánchez, W. P. Bowen, M. R. Vanner, K. Xia, and J. Twamley. Quantum magnetomechanics: towards the ultra-strong coupling regime. *arXiv*, [cond-mat.mess-hall] 1701.08482v1, 2017.

[39] J. D. Thompson, B. M. Zwickl, A. M. Jayich, F. Marquardt, S. M. Girvin, and J. G. E. Harris. Strong dispersive coupling of a high-finesse cavity to a micromechanical membrane. *Nature*, 452 (6):06715, 2008.

[40] A. M. Jayich, J. C. Sankey, B. M. Zwickl, C. Yang, J. D. Thompson, S. M. Girvin, A. A. Clerk, F. Marquardt, and J. G. E. Harris. Dispersive optomechanics: a membrane inside a cavity. *New Journal of Physics*, 10:095008, 2008.

[41] Z.-Q. Yin, A. A. Geraci, and T. Li. Optomechanics of levitated dielectric particles. *International Journal of Modern Physics B*, 27 (26):1330018, 2013.

[42] G. I. Harris. *Cavity Optomechanics with Feedback and Fluids*. Ph.D. thesis, The University of Queensland, 2014.

[43] M. Bhattacharya, A. N. Vamivakas, and P. Barker. Levitated optomechanics: introduction. *Journal of the Optical Society of America B*, 34 (6):L01–L02, 2017.

[44] B. Julsgaard, A. Kozhekin, and E. S. Polzik. Experimental long-lived entanglement of two macroscopic objects. *Nature*, 413:400–403, 2001.

[45] J. F. Sherson, H. Krauter, R. K. Olsson, B. Julsgaard, K. Hammerer, I. Cirac, and E. S. Polzik. Quantum teleportation between light and matter. *Nature*, 443 (5):557–560, 2006.

[46] N. Brahms and D. M. Stamper-Kurn. Spin optodynamics analog of cavity optomechanics. *Physical Review A*, 82:041804(R), 2010.

[47] T. P. Purdy, D. W. C. Brooks, T. Botter, N. Brahms, Z.-Y. Ma, and D. M. Stamper-Kurn. Tunable Cavity Optomechanics with Ultracold Atoms. *Physical Review Letters*, 105:133602, 2010.

[48] P. Meystre. A short walk through quantum optomechanics. *Annalen der Physik*, 525 (3):215–233, 2013.

[49] N. Brahms, T. Botter, S. Schreppler, D. W. C. Brooks, and D. M. Stamper-Kurn. Optical Detection of the Quantization of Collective Atomic Motion. *Physical Review Letters*, 108:133601, 2012.

[50] G. J. Milburn. *Quantum Optics*, 2nd edition. Springer, Berlin, 2008.

[51] R. Glauber. The Quantum Theory of Optical Coherence. *Physical Review*, 130 (6):2529–2539, 1963.

[52] D. A. Steck. *Quantum and Atom Optics*. Department of Physics, University of Oregon, 2007.

[53] J. F. Mulligan. Who were Fabry and Pérot? *American Journal of Physics*, 66 (9):797–802, 1998.

[54] P. D. Nation, J. Suh, and M. P. Blencowe. Ultrastrong optomechanics incorporating the dynamical Casimir effect. *Physical Review A*, 93:022510, 2016.

[55] V. Macri, A. Ridolfo, O. Di Stefano, A. F. Kockum, F. Nori, and S. Savasta. Non-perturbative Dynamical Casimir Effect in Optomechanical Systems: Vacuum Casimir-Rabi Splittings. *arXiv*, [quant-ph] 1706.0413v1, 2017.

[56] C. K. Law. Interaction between a moving mirror and radiation pressure: A Hamiltonian formulation. *Physical Review A*, 51 (3):2537–2541, 1995.

[57] K. Karrai, I. Favero, and C. Metzger. Doppler Optomechanics of a Photonic Crystal. *Physical Review Letters*, 100:240801, 2008.

[58] A. Schliesser and T. J. Kippenberg. Cavity optomechanics with whispering-gallery mode optical micro-resonators. *Advances in Atomic, Molecular and Optical Physics*, 58:207–323, 2010.

[59] D. V. Thourhout and J. Roels. Optomechanical device actuation through the optical gradient force. *Nature Photonics*, 4:211–217, 2010.

[60] N. Kiesel, F. Blaser, U. Deli, D. Grass, R. Kaltenbaek, and M. Aspelmeyer. Cavity cooling of an optically levitated submicron particle. *Proceedings of the National Academy of Science of the USA*, 110 (35):14180–14185, 2013.

[61] W. D. Phillips. Laser cooling and trapping of neutral atoms. *Reviews of Modern Physics*, 70 (3):721–741, 1998.

[62] J. Chan, A. H. Safavi-Naeini, J. T. Hill, S. Meenehan, and O. Painter. Optimized optomechanical crystal cavity with acoustic radiation shield. *Applied Physics Letters*, 101:081115, 2012.

[63] G. Bahl, M. Tomes, F. Marquardt, and T. Carmon. Observation of spontaneous Brillouin cooling. *Nature Physics*, 8 (3):203–207, 2012.

[64] R. Van Laer, R. Baets, and D. V. Thourhout. Unifying Brillouin scattering and cavity optomechanics. *Physical Review A*, 93:053828, 2016.

[65] C. W. Gardiner and M. J. Collett. Input and output in damped quantum systems: Quantum stochastic differential equations and the master equation. *Physical Review A*, 31 (6):3761–3774, 1985.

[66] K. Zhang, F. Bariani, and P. Meystre. Quantum Optomechanical Heat Engine. *Physical Review Letters*, 112:150602, 2014.

[67] K. Zhang, F. Bariani, and P. Meystre. Theory of an optomechanical quantum heat engine. *Physical Review A*, 90:023819, 2014.

[68] J. S. Bennett, L. S. Madsen, H. Rubinsztein-Dunlop, and W. P. Bowen. Quantum Thermodynamics Beyond the Rotating Wave Approximation. *arXiv*, [quant-ph] 1705.09174v1, 2017.

[69] G. Anetsberger, E. M. Weig, J. P. Kotthaus, and T. J. Kippenberg. Cavity optomechanics and cooling nanomechanical oscillators using microresonator enhanced evanescent near-field coupling. *Comptes Rendus Physique*, 12:800–816, 2011.

[70] W. P. Bowen and G. J. Milburn. *Quantum Optomechanics*. CRC Press, 2016.

[71] K. Khosla, G. A. Brawley, M. R. Vanner, and W. P. Bowen. Quantum optomechanics beyond the quantum coherent oscillation regime. *arXiv*, [quant-ph] 1704.07032v1, 2017.

[72] M. Aspelmeyer, T. J. Kippenberg, and F. Marquardt, editors. *Cavity Optomechanics*. Springer-Verlag, Berlin, 2014.

[73] S. G. Hofer, W. Wieczorek, M. Aspelmeyer, and K. Hammerer. Quantum entanglement and teleportation in pulsed cavity optomechanics. *Physical Review A*, 84:052327, 2011.

[74] J. M. Dobrindt, I. Wilson-Rae, and T. J. Kippenberg. Parametric Normal-Mode Splitting in Cavity Optomechanics. *Physical Review Letters*, 101:263602, 2008.

[75] S. Gröblacher, K. Hammerer, M. R. Vanner, and M. Aspelmeyer. Observation of strong coupling between a micromechanical resonator and an optical cavity field. *Nature*, 460:724–727, 2009.

[76] A. B. Bhattacherjee. Cavity quantum optomechanics of ultracold atoms in an optical lattice: Normal-mode splitting. *Physical Review A*, 80:043607, 2009.

[77] J. D. Teufel, D. Li, M. S. Allman, K. Cicak, A. J. Sirois, J. D. Whittaker, and R. W. Simmonds. Circuit cavity electromechanics in the strong-coupling regime. *Nature*, 471:204–208, 2011.

[78] E. Verhagen, S. Deleglise, S. Weis, A. Schliesser, and T. J. Kippenberg. Quantum-coherent coupling of a mechanical oscillator to an optical cavity mode. *Nature*, 482:63–67, 2012.

[79] T. Niemczyk, F. Deppe, H. Huebl, E. P. Menzel, F. Hocke, M. J. Schwarz, J. J. Garcia-Ripoll, D. Zueco, T. Hümmer, E. Solano, A. Marx, and R. Gross. Circuit quantum electrodynamics in the ultrastrong-coupling regime. *Nature Physics*, 6:772–776, 2010.

[80] D. Hu, S.-Y. Huang, J.-Q. Liao, L. Tian, and H.-S. Goan. Quantum coherence in ultrastrong optomechanics. *Physical Review A*, 91:013812, 2015.

[81] F. Brennecke, S. Ritter, T. Donner, and T. Esslinger. Cavity Optomechanics with a Bose-Einstein Condensate. *Science*, 322:235–239, 2008.

[82] D. Kleckner, I. Pikovski, E. Jeffrey, L. Ament, E. Eliel, J. van den Brink, and D. Bouwmeester. Creating and verifying a quantum superposition in a micro-optomechanical system. *New Journal of Physics*, 10:095020, 2008.

[83] M. Yuan, V. Singh, Y. M. Blanter, and G. A. Steele. Large cooperativity and microkelvin cooling with a three-dimensional optomechanical cavity. *Nature Communications*, 6:8491, 2015.

[84] F. Marquardt, J. P. Chen, A. A. Clerk, and S. M. Girvin. Quantum Theory of Cavity-Assisted Sideband Cooling of Mechanical Motion. *Physical Review Letters*, 99:093902, 2007.

[85] F. Marquardt, A. A. Clerk, and S. M. Girvin. Quantum theory of optomechanical cooling. *Journal of Modern Optics*, 55 (19-20):3329–3338, 2008.

[86] V. Fiore, Y. Yang, M. C. Kuzyk, R. Barbour, L. Tian, and H. Wang. Storing Optical Information as a Mechanical Excitation in a Silica Optomechanical Resonator. *Physical Review Letters*, 107:133601, 2011.

[87] T. A. Palomaki, J. W. Harlow, J. D. Teufel, R. W. Simmonds, and K. W. Lehnert. Coherent state transfer between itinerant microwave fields and a mechanical oscillator. *Nature*, 495:210–214, 2013.

[88] J.-Q. Liao and C. K. Law. Cooling of a mirror in cavity optomechanics with a chirped pulse. *Physical Review A*, 84:053838, 2011.

[89] X. Wang, S. Vinjanampathy, F. W. Strauch, and K. Jacobs. Ultraefficient Cooling of Resonators: Beating Sideband Cooling with Quantum Control. *Physical Review Letters*, 107:177204, 2011.

[90] J. B. Hertzberg, T. Rocheleau, T. Ndukum, M. Savva, A. A. Clerk, and K. C. Schwab. Back-action-evading measurements of nanomechanical motion. *Nature Physics*, 6:213–217, 2009.

[91] Q. Lin, B. He, R. Ghobadi, and C. Simon. Fully quantum approach to optomechanical entanglement. *Physical Review A*, 90:022309, 2014.

[92] Q. Lin and B. He. Optomechanical entanglement under pulse drive. *Optics Express*, 23 (19):24497–24507, 2015.

[93] T. A. Palomaki, J. D. Teufel, R. W. Simmonds, and K. W. Lehnert. Entangling Mechanical Motion with Microwave Fields. *Science*, 342:710–713, 2013.

[94] S. Mancini, V. Giovannetti, D. Vitali, and P. Tombesi. Entangling Macroscopic Oscillators Exploiting Radiation Pressure. *Physical Review Letters*, 88 (12):120401, 2002.

[95] J. Aasi *et al.* (LIGO scientific collaboration). Advanced LIGO. *Classical and Quantum Gravity*, 32:074001, 2015.

[96] J. B. Clark, F. Lecocq, R. W. Simmonds, J. Aumentado, and J. D. Teufel. Sideband cooling beyond the quantum backaction limit with squeezed light. *Nature*, 541:191–195, 2017.

[97] L. Yong-Chun, H. Yu-Wen, W. C. Wei, and X. Yun-Feng. Review of cavity optomechanical cooling. *Chinese Physics B*, 22 (11):114213, 2013.

[98] S. Machnes, M. B. Plenio, B. Reznik, A. M. Steane, and A. Retzker. Superfast Laser Cooling. *Physical Review Letters*, 104:183001, 2010.

[99] S. Machnes, J. Cerrillo, M. Aspelmeyer, W. Wieczorek, M. B. Plenio, and A. Retzker. Pulsed Laser Cooling for Cavity Optomechanical Resonators. *Physical Review Letters*, 108:153601, 2012.

[100] Y. Li, L.-A. Wu, and Z. D. Wang. Fast ground-state cooling of mechanical resonators with time-dependent optical cavities. *Physical Review A*, 83:043804, 2011.

[101] A. Farace and V. Giovannetti. Enhancing quantum effects via periodic modulations in optomechanical systems. *Physical Review A*, 86:013820, 2012.

[102] L. Zhang, C. Yang, and W. Zhang. Deeper Cooling of Micromechanical Motion by Quadrature Squeezing Beyond the Resolved Sideband Limit. *arXiv*, [quant-ph] 1705.04936v1, 2017.

[103] B. T. Gard, K. Jacobs, R. McDermott, and M. Saffman. Microwave-to-optical frequency conversion using a cesium atom coupled to a superconducting resonator. *arXiv*, [quant-ph] 1705.05700v2, 2017.

[104] L. Yan, J.-Q. Zhang, S. Zhang, and M. Feng. Fast optical cooling of a nanomechanical cantilever by a dynamical Stark-shift gate. *Scientific Reports*, 5:14977, 2015.

[105] M. Wallquist, K. Hammerer, P. Rabl, M. Lukin, and P. Zoller. Hybrid quantum devices and quantum engineering. *Physica Scripta*, T137:014001, 2009.

[106] B. Rogers, N. Lo Gullo, G. De Chiara, G. M. Palma, and M. Paternostro. Hybrid Optomechanics for Quantum Technologies. *Quantum Measurements and Quantum Metrology*, 2:11–43, 2014.

[107] S. Weis, R. Rivière, S. Deléglise, E. Gavartin, O. Arcizet, A. Schliesser, and T. J. Kippenberg. Optomechanically Induced Transparency. *Science*, 330:1520–1524, 2010.

[108] A. H. Safavi-Naeini, T. P. Mayer Alegre, J. Chan, M. Eichenfield, M. Winger, Q. Lin, J. T. Hill, D. E. Chang, and O. Painter. Electromagnetically induced transparency and slow light with optomechanics. *Nature*, 472:69–73, 2011.

[109] V. Fiore, C. Dong, M. C. Kuzyk, and H. Wang. Optomechanical light storage in a silica microresonator. *Physical Review A*, 87:023812, 2013.

[110] C. Dong, J. Zhang, V. Fiore, and H. Wang. Optomechanically induced transparency and self-induced oscillations with Bogoliubov mechanical modes. *Optica*, 1 (6):425–427, 2014.

[111] B. P. Hou, L. F. Wei, and S. J. Wang. Optomechanically induced transparency and absorption in hybridized optomechanical systems. *Physical Review A*, 92:033829, 2015.

[112] T. Ojanen and K. Børkje. Ground-state cooling of mechanical motion in the unresolved sideband regime by use of optomechanically induced transparency. *Physical Review A*, 90:013824, 2014.

[113] L. Yong-Chun, X. Yun-Feng, L. Xing-Sheng, and W. Chee Wei. Optomechanically-induced-transparency cooling of massive mechanical resonators to the quantum ground state. *Science China: Physics, Mechanics and Astronomy*, 58 (5):050305, 2015.

[114] C. Genes, D. Vitali, P. Tombesi, S. Gigan, and M. Aspelmeyer. Ground-state cooling of a micromechanical oscillator: Comparing cold damping and cavity-assisted cooling schemes. *Physical Review A*, 77:033804, 2008.

[115] P. F. Cohadon, A. Heidmann, and M. Pinard. Cooling of a Mirror by Radiation Pressure. *Physical Review Letters*, 83 (16):3174–3177, 1999.

[116] M. Pinard, P. F. Cohadon, T. Briant, and A. Heidmann. Full mechanical characterization of a cold damped mirror. *Physical Review A*, 63:013808, 2000.

[117] K. H. Lee, T. G. McRae, G. I. Harris, J. Knittel, and W. P. Bowen. Cooling and Control of a Cavity Optoelectromechanical System. *Physical Review Letters*, 104:123604, 2010.

[118] A. Hopkins, K. Jacobs, S. Habib, and K. Schwab. Feedback cooling of a nanomechanical resonator. *Physical Review B*, 68:235328, 2003.

[119] M. Poggio, C. L. Degen, H. J. Mamin, and D. Rugar. Feedback Cooling of a Cantilever's Fundamental Mode below 5 mK. *Physical Review Letters*, 99:017201, 2007.

[120] S. Sridaran and S. A. Bhave. Electrostatic actuation of silicon optomechanical resonators. *Optics Express*, 19 (10):9020–9026, 2011.

[121] D. Kleckner and D. Bouwmeester. Sub-kelvin optical cooling of a micromechanical resonator. *Nature*, 444:75–78, 2006.

[122] B. Abbott *et al.* (LIGO scientific collaboration). Observation of a kilogram-scale oscillator near its quantum ground state. *New Journal of Physics*, 11:073032, 2009.

[123] D. Vitali, S. Mancini, L. Ribichini, and P. Tombesi. Mirror quiescence and high-sensitivity position measurements with feedback. *Physical Review A*, 65:063803, 2002.

[124] S. Lloyd. Coherent quantum feedback. *Physical Review A*, 62:022108, 2000.

[125] J. Restrepo, C. Ciuti, and I. Favero. Single-Polariton Optomechanics. *Physical Review Letters*, 11:013601, 2014.

[126] H. Wang, X. Gu, Y.-X. Liu, A. Miranowicz, and F. Nori. Tunable photon blockade in a hybrid system consisting of an optomechanical device coupled to a two-level system. *Physical Review A*, 92:033806, 2015.

[127] D.-Y. Wang, C.-H. Bai, H.-G. Wang, A.-D. Zhu, and S. Zhang. Steady-state mechanical squeezing in a hybrid atom-optomechanical system with a highly dissipative cavity. *Scientific Reports*, 6:24421, 2016.

[128] J. Restrepo, I. Favero, and C. Ciuti. Fully coupled hybrid cavity optomechanics: Quantum interferences and correlations. *Physical Review A*, 95:023832, 2017.

[129] C. Genes, H. Ritsch, M. Drewsen, and A. Dantan. Atom-membrane cooling and entanglement using cavity electromagnetically induced transparency. *Physical Review A*, 84:051801(R), 2011.

[130] F. Bariani, S. Singh, L. F. Buchmann, M. Vengalattore, and P. Meystre. Hybrid optomechanical cooling by atomic Λ systems. *Physical Review A*, 90 (3):033838, 2014.

[131] S. Zhang, J.-Q. Zhang, J. Zhang, C.-W. Wu, W. Wu, and P.-X. Chen. Ground state cooling of an optomechanical resonator assisted by a Λ-type atom. *Optics Express*, 22 (23):1520–1523, 2014.

[132] Y. Han, W.-Z. Zhang, J. Cheng, and L. Zhou. Enhanced cooling of micromechanical oscillator in the atom-assisted optomechanical cavity. *International Journal of Quantum Information*, 12 (1):1450005, 2014.

[133] Z. Yi, G.-X. Li, S.-P. Wu, and Y.-P. Yang. Ground-state cooling of an oscillator in a hybrid atom-optomechanical system. *Optics Express*, 22 (17):359–363, 2014.

[134] J. Zhang, T. Zhang, A. Xuereb, D. Vitali, and J. Li. More nonlocality with less entanglement in a tripartite atom-optomechanical system. *Annalen der Physik*, 527 (1-2):147–155, 2015.

[135] A. Dorsel, J. D. McCullen, P. Meystre, E. Vignes, and H. Walther. Optical Bistability and Mirror Confinement Induced by Radiation Pressure. *Physical Review Letters*, 51 (17):1550–1553, 1983.

[136] Y. Zhang, A. Sohail, and C.-S. Yu. Perfect photon absorption in hybrid atom-optomechanical system. *Europhysics Letters*, 115:64002, 2016.

[137] C. Genes, D. Vitali, and P. Tombesi. Emergence of atom-light-mirror entanglement inside an optical cavity. *Physical Review A*, 77:050307(R), 2008.

[138] H. Zhong, G. Fläschner, A. Schwarz, R. Wiesendanger, P. Christoph, T. Wagner, A. Bick, C. Staarmann, B. Abeln, K. Sengstock, and C. Becker. A millikelvin all-fiber cavity optomechanical apparatus for merging with ultra-cold atoms in a hybrid quantum system. *Review of Scientific Instruments*, 88:023115, 2017.

[139] A. Dantan, B. Nair, G. Pupillo, and C. Genes. Hybrid cavity mechanics with doped systems. *Physical Review A*, 90:033820, 2014.

[140] K. Hammerer, M. Aspelmeyer, E. S. Polzik, and P. Zoller. Establishing Einstein-Poldosky-Rosen Channels between Nanomechanics and Atomic Ensembles. *Physical Review Letters*, 102:020501, 2009.

[141] B. Vogell, T. Kampschulte, M. T. Rakher, A. Faber, P. Treutlein, K. Hammerer, and P. Zoller. Long distance coupling of a quantum mechanical oscillator to the internal states of an atomic ensemble. *New Journal of Physics*, 17:043044, 2015.

[142] C. B. Møller, R. A. Thomas, G. Vasilakis, E. Zeuthen, Y. Tsaturyan, K. Jensen, A. Schliesser, K. Hammerer, and E. S. Polzik. Quantum back action evading measurement of motion in a negative mass reference frame. *arXiv*, [quant-ph] 1608.03613v2, 2017.

[143] K. Hammerer, A. S. Sorenson, and E. S. Polzik. Quantum interface between light and atomic ensembles. *Reviews of Modern Physics*, 82 (2):1041–1093, 2010.

[144] A. Einstein, B. Podolsky, and N. Rosen. Can Quantum Mechanical Descriptions of Reality be Considered Complete?. *Physical Review*, 47:777–780, 1935.

[145] M. Tsang and C. Caves. Evading Quantum Mechanics: Engineering a Classical Subsystem within a Quantum Environment. *Physical Review X*, 2 (3):031016, Sept. 2012.

[146] A. Sanz-Mora, A. Eisfeld, S. Wuster, and J.-M. Rost. Coupling of a nanomechanical oscillator and an atomic three-level medium. *Physical Review A*, 93:023816, 2016.

[147] S. Singh, H. Jing, E. M. Wright, and P. Meystre. Quantum-state transfer between a Bose-Einstein condensate and an optomechanical mirror. *Physical Review A*, 86:021801, 2012.

[148] K. Hammerer, M. Wallquist, C. Genes, M. Ludwig, F. Marquardt, P. Treutlein, P. Zoller, J. Ye, and H. J. Kimble. Strong Coupling of a Mechanical Oscillator and a Single Atom. *Physical Review Letters*, 103:063005, 2009.

[149] D. Meiser and P. Meystre. Coupled dynamics of atoms and radiation-pressure-driven interferometers. *Physical Review A*, 73:033417, 2006.

[150] K. Hammerer, K. Stannigel, C. Genes, P. Zoller, P. Treutlein, S. Camerer, D. Hunger, and T. W. Hänsch. Optical lattices with micromechanical mirrors. *Physical Review A*, 82:021803(R), 2010.

[151] B. Vogell, K. Stannigel, P. Zoller, K. Hammerer, M. T. Rakher, M. Korppi, A. Jöckel, and P. Treutlein. Cavity-Enhanced Long-Distance Coupling of an Atomic Ensemble to a Micromechanical Membrane. *Physical Review A*, 87:023816, 2013.

[152] A. Jöckel, A. Faber, T. Kampschulte, M. Korppi, M. T. Rakher, and P. Treutlein. Sympathetic cooling of a membrane oscillator in a hybrid mechanical atomic system. *Nature Nanotechnology*, 10:55–59, 2015.

[153] A. Vochezer, T. Kampschulte, K. Hammerer, and P. Treutlein. Light-mediated collective atomic motion in a hybrid atom-optomechanical system. *arXiv*, [quant-ph] 1705.10098v1, 2017.

[154] M. R. Vanner, I. Pikovski, G. D. Cole, M. S. Kim, Č. Brukner, K. Hammerer, G. J. Milburn, and M. Aspelmeyer. Pulsed quantum optomechanics. *Proceedings of the National Academy of Science of the USA*, 108 (39):16182–16187, 2011.

[155] D. Malz and A. Nunnenkamp. Optomechanical dual-beam backaction-evading measurement beyond the rotating-wave approximation. *Physical Review A*, 94:053820, 2016.

[156] G. I. Harris, U. L. Andersen, J. Knittel, and W. P. Bowen. Feedback-enhanced sensitivity in optomechanics: Surpassing the parametric instability barrier. *Physical Review A*, 85:061802(R), 2012.

[157] A. I. Lvovsky and M. G. Raymer. Continuous-variable optical quantum-state tomography. *Reviews of Modern Physics*, 81:299–332, 2009.

[158] M. R. Vanner, J. Hofer, G. D. Cole, and M. Aspelmeyer. Cooling-by-measurement and mechanical state tomography via pulsed optomechanics. *Nature Communications*, 4:1–8, 2013.

[159] I. Pikovski, M. R. Vanner, M. Aspelmeyer, M. S. Kim, and Č. Brukner. Probing Planck-scale physics with quantum optics. *Nature Physics*, 8:393–398, 2012.

[160] K. E. Khosla, M. R. Vanner, W. P. Bowen, and G. J. Milburn. Quantum state preparation of a mechanical resonator using an optomechanical geometric phase. *New Journal of Physics*, 15:043025, 2013.

[161] N. Vostrosablin, A. A. Rakhubovsky, and R. Filip. Pulsed quantum interaction between two distant mechanical oscillators. *Physical Review A*, 94:063801, 2016.

[162] N. Vostrosablin, A. A. Rakhubovsky, and R. Filip. Pulsed quantum continuous-variable opto-electromechanical transducer. *arXiv*, [quant-ph] 1704.01784v2, 2017.

[163] A. K. Huttel, G. A. Steele, B. Witkamp, M. Poot, L. P. Kouwenhoven, and H. S. J. van der Zant. Carbon Nanotubes as Ultrahigh Quality Factor Mechanical Resonators. *Nano Letters*, 9 (7):2537–2552, 2009.

[164] M. Vanner. Selective Linear or Quadratic Optomechanical Coupling via Measurement. *Physical Review X*, 1:021011, 2011.

[165] G. A. Brawley, M. R. Vanner, P. E. Larsen, S. Schmid, A. Boisen, and W. P. Bowen. Nonlinear optomechanical measurement of mechanical motion. *Nature Communications*, 7:10988, 2016.

[166] H.-K. Li, Y.-C. Liu, X. Yi, C.-L. Zou, X.-X. Ren, and Y.-F. Xiao. Proposal for a near-field optomechanical system with enhanced linear and quadratic coupling. *Physical Review A*, 85:053832, 2012.

[167] H. Seok and E. M. Wright. Antibunching in an optomechanical oscillator. *Physical Review A*, 95:053844, 2017.

[168] F. Elste, S. M. Girvin, and A. A. Clerk. Quantum Noise Interference and Backaction Cooling in Cavity Nanomechanics. *Physical Review Letters*, 102:207209, 2009.

[169] F. Elste, A. A. Clerk, and S. M. Girvin. Erratum: Quantum Noise Interference and Backaction Cooling in Cavity Nanomechanics. *Physical Review Letters*, 102:207209, 2009.

[170] T. Weiss, C. Bruder, and A. Nunnenkamp. Strong-coupling effects in dissipatively coupled optomechanical systems. *New Journal of Physics*, 15:045017, 2013.

[171] A. Xuereb, R. Schnabel, and K. Hammerer. Dissipative Optomechanics in a Michelson-Sagnac Interferometer. *Physical Review Letters*, 107:213604, 2011.

[172] M. Wu, A. C. Hryciw, C. Healey, D. P. Lake, H. Jayakumar, M. R. Freeman, J. P. Davis, and P. E. Barclay. Dissipative and Dispersive Optomechanics in a Nanocavity Torque Sensor. *Physical Review X*, 4:021052, 2014.

[173] A. Kronwald, F. Marquardt, and A. A. Clerk. Dissipative optomechanical squeezing of light. *New Journal of Physics*, 16:063058, 2014.

[174] A. Sawadsky, H. Kaufer, R. M. Nia, S. P. Tarabrin, F. Y. Khalili, K. Hammerer, and R. Schnabel. Observation of Generalized Optomechanical Coupling and Cooling on Cavity Resonance. *Physical Review Letters*, 114:043601, 2015.

[175] M. Abdi and A. R. Bahrampour. Improving the optomechanical entanglement and cooling by photothermal force. *Physical Review A*, 85:063839, 2012.

[176] K. Usami, A. Næsby, T. Bagci, B. Melholt Nielsen, J. Liu, S. Stobbe, P. Lodahl, and E. S. Polzik. Optical cavity cooling of mechanical modes of a semiconductor nanomembrane. *Nature Physics*, 8:168–172, 2012.

[177] G. I. Harris, D. L. Mcauslan, E. Sheridan, Y. Sachkou, C. Baker, and W. P. Bowen. Laser cooling and control of excitations in superfluid helium. *Nature Physics*, 12:788–793, 2016.

[178] C. G. Baker, G. I. Harris, D. L. McAuslan, Y. Sachkou, X. He, and W. P. Bowen. Theoretical framework for thin film superfluid optomechanics: towards the quantum regime. *New Journal of Physics*, 18:123025, 2016.

[179] H. J. Kimble. The quantum internet. *Nature*, 453:1023–1030, 2008.

[180] T. G. McRae, K. H. Lee, G. I. Harris, J. Knittel, and W. P. Bowen. Cavity optoelectromechanical system combining strong electrical actuation with ultrasensitive transduction. *Physical Review A*, 82:023825, 2010.

[181] C. A. Regal and K. W. Lehnert. From cavity electromechanics to cavity optomechanics - 22nd International Conference on Atomic Physics. *Journal of Physics: Conference Series*, 264:012025, 2011.

[182] L. Tian. Optoelectromechanical transducer: Reversible conversion between microwave and optical photons. *Annalen der Physik*, 527(1–2):1–14, 2015.

[183] R. W. Andrews, A. P. Reed, K. Cicak, J. D. Teufel, and K. W. Lehnert. Quantum-enabled temporal and spectral mode conversion of microwave signals. *Nature Communications*, 6:10021, 2015.

[184] C. Weedbrook, S. Pirandola, R. Garcia-Patron, N. J. Cerf, T. C. Ralph, J. H. Shapiro, and S. Lloyd. Gaussian quantum information. *Reviews of Modern Physics*, 84:621–669, 2012.

[185] E. C. G. Sudarshan. Equivalence of semiclassical and quantum mechanical descriptions of statistical light beams. *Physical Review Letters*, 10 (7):1963–1965, 1963.

[186] K. Husimi. Some Formal Properties of the Density Matrix. *Proceedings of the Physical Mathematics Society of Japan*, 22:264–314, 1940.

[187] E. Wigner. On the Quantum Correction for Thermodynamic Equilibrium. *Physical Review*, 40:749–759, 1932.

[188] R. L. Hudson. When is the Wigner quasi-probability density non-negative? *Reports on Mathematical Physics*, 6 (2):249–252, 1974.

[189] B. Schumacher. Sending entanglement through noisy quantum channels. *Physical Review A*, 54 (4):2614–2628, 1996.

[190] J. Li, G. Li, J.-M. Wang, S.-Y. Zhu, and T.-C. Zhang. A comparison of two nonclassical measures, entanglement potential and the negativity of the Wigner function. *Journal of Physics B: Atomic, Molecular and Optical Physics*, 43:085504, 2010.

[191] T. Kiesel. *Verification of nonclassicality in phase space*. Ph.D. thesis, Universität Rostock, 2011.

[192] H.-W. Lee. Theory and application of the quantum phase-space distribution functions. *Physics Reports*, 259:147–211, 1995.

[193] M.-A. Lemonde, N. Didier, and A. A. Clerk. Antibunching and unconventional photon blockade with Gaussian squeezed states. *Physical Review A*, 90:063824, 2014.

[194] A. Kenfack and K. Zyczkowski. Negativity of the Wigner function as an indicator of non-classicality. *Journal of Optics B: Quantum Semiclassical Optics*, 6:396–404, 2004.

[195] M. Revzen, P. A. Mello, A. Mann, and L. M. Johansen. Bell's inequality violation with non-negative Wigner functions. *Physical Review A*, 71:022103, 2005.

[196] R. W. Spekkens. Negativity and Contextuality are Equivalent Notions of Nonclassicality. *Physical Review Letters*, 101:020401, 2008.

[197] C. W. Gardiner. Adiabatic elimination in stochastic systems. I. Formulation of methods and application to few-variable systems. *Physical Review A*, 29 (5):2814–2822, 1984.

[198] C. J. Gardner and P. Zoller. *Quantum Noise: A Handbook of Markovian and Non-Markovian Quantum Stochastic Methods with Applications to Quantum Optics*. Springer, Berlin, 2004.

[199] H.-A. Bachor and T. C. Ralph. *A Guide to Experiments in Quantum Optics*. Wiley-VCH, 2nd edition, 2004.

[200] E. D. Black. An introduction to Pound-Drever-Hall laser frequency stabilization. *American Journal of Physics*, 69 (1):79–87, 2001.

[201] S. Mahajan, N. Agarwal, A. B. Bhattacherjee, and ManMohan. Achieving the quantum ground state of a mechanical oscillator using a Bose–Einstein condensate with back-action and cold damping feedback. *Journal of Physics B: Atomic, Molecular and Optical Physics*, 46:085301, 2013.

[202] P. Treutlein, C. Genes, K. Hammerer, M. Poggio, and P. Rabl. Hybrid Mechanical Systems. *arXiv*, [quant-ph] 1210.4151v, 2012.

[203] V. Giovannetti, S. Lloyd, and L. Maccone. Quantum-Enhanced Measurements: Beating the Standard Quantum Limit. *Science*, 306:1330–1336, 2004.

[204] A. Serafini. Feedback Control in Quantum Optics: An Overview of Experimental Breakthroughs and Areas of Application. *International Scholarly Research Network Optics*, 2012:275016, 2012.

[205] A. V. Tsukanov. Optomechanical Systems and Quantum Computing. *Mikroelektronika (Russian Microelectronics)*, 40 (5):359–369, 2011.

[206] C. A. Muschik, H. Krauter, K. Hammerer, and E. S. Polzik. Quantum information at the interface of light with atomic ensembles and micromechanical oscillators. *Quantum Information Processing*, 10:839–863, 2011.

[207] K. Stannigel, P. Komar, S. J. M. Habraken, S. D. Bennett, M. D. Lukin, P. Zoller, and P. Rabl. Optomechanical Quantum Information Processing with Photons and Phonons. *Physical Review Letters*, 109:013603, 2012.

[208] T. Rocheleau, T. Ndukum, C. Macklin, J. B. Hertzberg, A. A. Clerk, and K. C. Schwab. Preparation and detection of a mechanical resonator near the ground state of motion. *Nature*, 463 (7):72–75, 2010.

[209] S. Mancini, D. Vitali, and P. Tombesi. Optomechanical Cooling of a Macroscopic Oscillator by Homodyne Feedback. *Physical Review Letters*, 80 (4):688–691, 1998.

[210] J. Courty, A. Heidmann, and M. Pinard. Quantum limits of cold damping with optomechanical coupling. *The European Physical Journal D*, 17:399–408, 2001.

[211] A. C. Doherty, A. Szorkovszky, G. I. Harris, and W. P. Bowen. The quantum trajectory approach to quantum feedback control of an oscillator revisited. *Philosophical Transactions of the Royal Society A: Mathematical, Physical and Engineering Sciences*, 370:5338–5353, 2012.

[212] K. Jacobs. Twenty open problems in quantum control. *arXiv*, [quant-ph] 1304.0819v3, 2014.

[213] R. Hamerly and H. Mabuchi. Advantages of Coherent Feedback for Cooling Quantum Oscillators. *Physical Review Letters*, 109:173602, 2012.

[214] S. K. Ruddell, K. E. Webb, I. Herrera, A. S. Parkins, and M. D. Hoogerland. Collective strong coupling of cold atoms to an all-fiber ring cavity. *Optica*, 4 (5):576–579, 2017.

[215] R. Grimm, M. Weidemüller, and Y. Ovchinnikov. Optical dipole traps for neutral atoms. *Advances in Atomic, Molecular and Optical Physics*, 95:95–170, 2000.

[216] J. Dalibard and C. Cohen-Tannoudji. Dressed-atom approach to atomic motion in laser light: the dipole force revisited. *Journal of the Optical Society of America B*, 2:1707–1720, 1985.

[217] T. J. Kippenberg and K. J. Vahala. Cavity Opto-Mechanics. *Optics Express*, 15 (25):74–77, 2007.

[218] T. J. Kippenberg and K. J. Vahala. Cavity Optomechanics: Back-Action at the Mesoscale. *Science*, 321:1172–1176, 2008.

[219] V. I. Balykin, V. G. Minogin, and V. S. Letokhov. Electromagnetic trapping of cold atoms. *Reports on Progress in Physics*, 63:1429–1510, 2000.

[220] J. P. Gordon and A. Ashkin. Motion of atoms in a radiation trap. *Physical Review A*, 21 (5):1606–1617, 1980.

[221] K. Murr, P. Maunz, P. W. H. Pinkse, T. Puppe, I. Schuster, D. Vitali, and G. Rempe. Momentum diffusion for coupled atom-cavity oscillators. *Physical Review A*, 74:043412, 2006.

[222] D. A. Steck. Rubidium 87 D Line Data, revision 1.6, 2003.

[223] H. Habibi, E. Zeuthen, M. Ghanaatshoar, and K. Hammerer. Quantum feedback cooling of a mechanical oscillator using variational measurements: tweaking Heisenberg's microscope. *Journal of Optics*, 18:084004, 2016.

[224] J.-M. Courty, F. Grassia, and S. Reynaud. Thermal and Quantum Noise in Active Systems. In M. Planat, editor, *Noise, Oscillators and Algebraic Randomness - From Noise in Communication Systems to Number Theory*, chapter 3, pages 71–83. Springer, Chapelle des Bois, 2000.

[225] S. Schmid, K. D. Jensen, K. H. Nielsen, and A. Boisen. Damping mechanisms in high-Q micro and nanomechanical string resonators. *Physical Review B*, 84:165307, 2011.

[226] G. Brawley, J. Bennett, R. Cole, W. P. Bowen, S. Schmid, and A. Boisen. High cooperativity between nanostring mechanical oscillators and whispering gallery mode resonators. *Proceedings of OSA QO VI*, pages 6–7, 2012.

[227] E. Vetsch, S. T. Dawkins, R. Mitsch, D. Reitz, P. Schneeweiss, and A. Rauschenbeutel. Nanofiber-based optical trapping of cold neutral atoms. *IEEE Journal of Quantum Electronics*, 18:1763, 2012.

[228] A. J. Kerman, V. Vuletic, C. Chin, and S. Chu. Beyond Optical Molasses: 3D Raman Sideband Cooling of Atomic Cesium to High Phase-Space Density. *Physical Review Letters*, 84 (3):439–442, 2000.

[229] K. Hammerer, K. Mølmer, E. S. Polzik, and J. I. Cirac. Light-matter quantum interface. *Physical Review A*, 70:044304, 2004.

[230] E. Peter, P. Senellart, D. Martrou, A. Lemaître, J. Hours, J. M. Gérard, and J. Bloch. Exciton-Photon Strong-Coupling Regime for a Single Quantum Dot Embedded in a Microcavity. *Physical Review Letters*, 95:067401, 2005.

[231] M. Montinaro, G. Wurst, M. Munsch, Y. Fontana, E. Russo-Averchi, M. Heiss, A. Fontcuberta i Morral, R. J. Warburton, and M. Poggio. Quantum Dot Opto-Mechanics in a Fully Self-Assembled Nanowire. *Nano Letters*, 14:4454–4460, 2014.

[232] S. Putz, D. O. Krimer, R. Amsüss, A. Valookaran, T. Nöbauer, J. Schmiedmayer, S. Rotter, and J. Majer. Protecting a spin ensemble against decoherence in the strong-coupling regime of cavity QED. *Nature Physics*, 10:720–724, 2014.

[233] C. Grezes, B. Julsgaard, Y. Kubo, M. Stern, T. Umeda, J. Isoya, H. Sumiya, H. Abe, S. Onoda, T. Ohshima, V. Jacques, J. Esteve, D. Vion, D. Esteve, K. Mø lmer, and P. Bertet. Multimode Storage and Retrieval of Microwave Fields in a Spin Ensemble. *Physical Review X*, 4:021049, 2014.

[234] A. Dantan, M. Albert, J. P. Marler, P. F. Herskind, and M. Drewsen. Large ion Coulomb crystals: A near-ideal medium for coupling optical cavity modes to matter. *Physical Review A*, 80:041802(R), 2009.

[235] A. Stute, B. Casabone, P. Schindler, T. Monz, P. O. Schmidt, B. Brandstätter, T. E. Northup, and R. Blatt. Tunable ionphoton entanglement in an optical cavity. *Nature*, 485:482–486, 2012.

[236] J. Bochmann, A. Vainsencher, D. D. Awschalom, and A. N. Cleland. Nanomechanical coupling between microwave and optical photons. *Nature Physics*, 9:712–716, 2013.

[237] T. Bagci, A. Simonsen, S. Schmid, L. G. Villanueva, E. Zeuthen, J. Appel, J. M. Taylor, A. Sørensen, K. Usami, A. Schliesser, and E. S. Polzik. Optical detection of radio waves through a nanomechanical transducer. *Nature*, 507:81–85, 2014.

[238] K. Xia, M. R. Vanner, and J. Twamley. An opto-magneto-mechanical quantum interface between distant superconducting qubits. *Scientific Reports*, 4:5571, 2014.

[239] Y.-D. Wang and A. A. Clerk. Using Interference for High Fidelity Quantum State Transfer in Optomechanics. *Physical Review Letters*, 108:153603, 2012.

[240] R. W. Andrews, R. W. Peterson, T. P. Purdy, K. Cicak, R. W. Simmonds, C. A. Regal, and K. W. Lehnert. Bidirectional and efficient conversion between microwave and optical light. *Nature Physics*, 10:321–326, 2014.

[241] X. Chen, Y.-C. Liu, P. Peng, Y. Zhi, and Y.-F. Xiao. Cooling of macroscopic mechanical resonators in hybrid atom-optomechanical systems. *Physical Review A*, 92:033841, 2015.

[242] C. Genes, H. Ritsch, and D. Vitali. Micromechanical oscillator ground-state cooling via resonant intracavity optical gain. *Physical Review A*, 80:061803(R), 2009.

[243] W.-J. Gu and G.-X. Li. Quantum interference effects on ground-state optomechanical cooling. *Physical Review A*, 87:025804, 2013.

[244] R. Filip. Excess-noise-free recording and uploading of nonclassical states to continuous-variable quantum memory. *Physical Review A*, 78:012329, 2008.

[245] P. Marek and R. Filip. Noise-resilient quantum interface based on quantum nondemolition interactions. *Physical Review A*, 81:042325, 2010.

[246] F. Khalili, S. Danilishin, H. Miao, H. Müller-Ebhardt, H. Yang, and Y. Chen. Preparing a Mechanical Oscillator in Non-Gaussian Quantum States. *Physical Review Letters*, 105:070403, 2010.

[247] D. Vitali, S. Gigan, A. Ferreira, H. R. Böhm, P. Tombesi, A. Guerreiro, V. Vedral, A. Zeilinger, and M. Aspelmeyer. Optomechanical Entanglement between a Movable Mirror and a Cavity Field. *Physical Review Letters*, 98:030405, 2007.

[248] S. Mancini, D. Vitali, and P. Tombesi. Scheme for Teleportation of Quantum States onto a Mechanical Resonator. *Physical Review Letters*, 90 (13):137901, 2003.

[249] R. Benguria and M. Kac. Quantum Langevin Equation. *Physical Review Letters*, 46 (1):1–4, 1981.

[250] D. J. Wilson. *Cavity Optomechanics with High-Stress Silicon Nitride Films Thesis*. Ph.D. thesis, California Institute of Technology, 2012.

[251] S. Chakram, Y. S. Patil, L. Chang, and M. Vengalattore. Dissipation in Ultrahigh Quality Factor SiN Membrane Resonators. *Physical Review Letters*, 112:127201, 2014.

[252] J. F. Shackelford and W. Alexander, editors. *Materials Science and Engineering Handbook*. CRC Press LLC, 2001.

[253] S. M. Meenehan, J. D. Cohen, S. Gröblacher, J. T. Hill, A. H. Safavi-Naeini, M. Aspelmeyer, and O. Painter. Silicon optomechanical crystal resonator at millikelvin temperatures. *Physical Review A*, 90:011803(R), 2014.

[254] Y.-C. Liu, R.-S. Liu, C.-H. Dong, Y. Li, Q. Gong, and Y.-F. Xiao. Cooling mechanical resonators to the quantum ground state from room temperature. *Physical Review A*, 91:013824, 2015.

[255] R. A. Norte, J. P. Moura, and S. Gröblacher. Mechanical Resonators for Quantum Optomechanics Experiments at Room Temperature. *Physical Review Letters*, 116:147202, 2016.

[256] J. Etesse, M. Bouillard, B. Kanseri, and R. Tualle-Brouri. Experimental Generation of Squeezed Cat States with an Operation Allowing Iterative Growth. *Physical Review Letters*, 114:193602, 2015.

[257] A. Laghaout, J. S. Neergaard-Nielsen, I. Rigas, C. Kragh, A. Tipsmark, and U. L. Andersen. Amplification of realistic Schrödinger-cat-state-like states by homodyne heralding. *Physical Review A*, 87:043826, 2013.

[258] H. Takahashi, K. Wakui, S. Suzuki, M. Takeoka, K. Hayasaka, A. Furusawa, and M. Sasaki. Generation of Large-Amplitude Coherent-State Superposition via Ancilla-Assisted Photon Subtraction. *Physical Review Letters*, 101:233605, 2008.

[259] H. Jeong and M. S. Kim. Efficient quantum computation using coherent states. *Physical Review A*, 65:042305, 2002.

[260] T. C. Ralph, A. Gilchrist, G. J. Milburn, W. J. Munro, and S. Glancy. Quantum computation with optical coherent states. *Physical Review A*, 68:042319, 2003.

[261] A. P. Lund, H. Jeong, T. C. Ralph, and M. S. Kim. Conditional production of superpositions of coherent states with inefficient photon detection. *Physical Review A*, 70:020101, 2004.

[262] J. Anders and M. Esposito. Focus on quantum thermodynamics. *New Journal of Physics*, 19:010201, 2017.

[263] S. Vinjanampathy and J. Anders. Quantum thermodynamics. *Contemporary Physics*, 57 (4):545–579, 2016.

[264] F. Brandão, M. Horodecki, N. Ng, J. Oppenheim, and S. Wehner. The second laws of quantum thermodynamics. *Proceedings of the National Academy of Sciences of the United States of America*, 112 (11):3275–3279, 2015.

[265] L. Masanes and J. Oppenheim. A general derivation and quantification of the third law of thermodynamics. *Nature Communications*, 8:14538, 2017.

[266] J. Goold, M. Huber, A. Riera, L. del Rio, and P. Skrzypczyk. The role of quantum information in thermodynamics a topical review. *Journal of Physics A: Mathematical and Theoretical*, 49:143001, 2016.

[267] S. W. Kim, T. Sagawa, S. D. Liberato, and M. Ueda. Quantum Szilard Engine. *Physical Review Letters*, 106:070401, 2011.

[268] W. Hübner, G. Lefkidis, C. D. Dong, D. Chaudhuri, L. Chotorlishvili, and J. Berakdar. Spin-dependent Otto quantum heat engine based on a molecular substance. *Physical Review B*, 90:024401, 2014.

[269] M. Brunelli, A. Xuereb, A. Ferraro, G. De Chiara, N. Kiesel, and M. Paternostro. Out-of-equilibrium thermodynamics of quantum optomechanical systems. *New Journal of Physics*, 17:035016, 2015.

[270] A. Mari, A. Farace, and V. Giovannetti. Quantum optomechanical piston engines powered by heat. *Journal of Physics B: Atomic, Molecular and Optical Physics*, 48:175501, 2015.

[271] C. Elouard, M. Richard, and A. Auffeves. Reversible work extraction in a hybrid opto-mechanical system. *New Journal of Physics*, 17:055018, 2015.

[272] A. Alecce, F. Galve, N. Lo Gullo, L. Dell'Anna, F. Pastina, and R. Zambrini. Quantum Otto cycle with inner friction: finite-time and disorder effects. *New Journal of Physics*, 17:075007, 2015.

[273] M. Campisi, J. Pekola, and F. Rosario. Nonequilibrium fluctuations in quantum heat engines: theory, example, and possible solid state experiments. *New Journal of Physics*, 17:035012, 2015.

[274] G. W. Ford and R. F. O'Connell. The rotating wave approximation (RWA) of quantum optics: serious defect. *Physica A*, 243:377–381, 1997.

[275] W. Ford, J. T. Lewos, and R. F. O'Connell. Quantum Langevin equation. *Physical Review A*, 37 (11):4419–4428, 1988.

[276] V. Peano, M. Marthaler, and M. I. Dykman. Sharp Tunneling Peaks in a Parametric Oscillator: Quantum Resonances Missing in the Rotating Wave Approximation. *Physical Review Letters*, 109:090401, 2012.

[277] M. Mirzaee and M. Batavani. Atomfield entanglement in the Jaynes Cummings model without rotating wave approximation. *Chinese Physics B*, 24:040306, 2015.

[278] A. Kurcz, A. Capolupo, A. Beige, E. Del Fiudice, and G. Vitiello. Rotating wave approximation and entropy. *Physics Letters A*, 374:3726–3732, 2010.

[279] A. Kurcz, A. Capolupo, A. Beige, E. D. Giudice, and G. Vitiello. Energy concentration in composite quantum systems. *Physical Review A*, 81:063821, 2010.

[280] J. Larson. On the rotating wave approximation in the adiabatic limit. *arXiv*, [quant-ph] 1208.1981v1, 2012.

[281] J. P. Pekola, V. Brosco, M. Mottonen, P. Solinas, and A. Shnirman. Decoherence in Adiabatic Quantum Evolution: Application to Cooper Pair Pumping. *Physical Review Letters*, 105:030401, 2010.

[282] P. Solinas, M. Mottonen, J. Salmilehto, and J. P. Pekola. Decoherence of adiabatically steered quantum systems. *Physical Review B*, 82:134517, 2010.

[283] J. Salmilehto, P. Solinas, and M. Mottonen. Conservation law of operator current in open quantum systems. *Physical Review A*, 85:032110, 2012.

[284] Y. B. Band. Open quantum system stochastic dynamics with and without the RWA. *Journal of Physics B: Atomic, Molecular and Optical Physics*, 48:04501, 2015.

[285] A. Schliesser, R. Rivière, G. Anetsberger, O. Arcizet, and T. J. Kippenberg. Resolved-sideband cooling of a micromechanical oscillator. *Nature Physics*, 4:415–419, 2008.

[286] J. P. Pekola. Towards quantum thermodynamics in electronic circuits. *Nature Physics*, 11:118–123, 2015.

[287] G. Lindblad. On the Generators of Quantum Dynamical Semigroups. *Communications in Mathematical Physics*, 48:119–130, 1976.

[288] V. Gorini, A. Kossakowski, and E. C. G. Sudarshan. Completely positive dynamical semigroups of N-level systems. *Journal of Mathematical Physics*, 17 (5):821–825, 1976.

[289] J. E. Geusic, E. O. Schulz-DuBois, and H. E. D. Scovil. Quantum Equivalent of the Carnot Cycle. *Physical Review*, 156 (2):343–351, 1967.

[290] R. Alicki. The quantum open system as a model of the heat engine. *Journal of Physics A: Mathematical and General*, 12 (5):103–107, 1979.

[291] R. Kosloff. A quantum mechanical open system as a model of a heat engine. *Journal of Chemical Physics*, 80 (4):1625–1631, 1984.

[292] E. Geva and R. Kosloff. The quantum heat engine and heat pump: An irreversible thermodynamic analysis of the three-level amplifier. *The Journal of Chemical Physics*, 104:7681, 1996.

[293] H. T. Quan, Y.-X. Liu, C. P. Sun, and F. Nori. Quantum thermodynamic cycles and quantum heat engines. *Physical Review E*, 76:031105, 2007.

[294] D. Gelbwaser-Klimovsky, R. Alicki, and G. Kurizki. Minimal universal quantum heat machine. *Physical Review E*, 87:012140, 2013.

[295] D. Gelbwaser-Klimovsky and G. Kurizki. Work extraction from heat-powered quantized optomechanical setups. *Scientific Reports*, 5:7809, 2015.

[296] A. Levy, R. Alicki, and R. Kosloff. Quantum refrigerators and the third law of thermodynamics. *Physical Review E*, 85:061126, 2012.

[297] P. P. Hofer, M. Perarnau-Llobet, J. B. Brask, R. Silva, M. Huber, and N. Brunner. Autonomous quantum refrigerator in a circuit QED architecture based on a Josephson junction. *Physical Review B*, 94:235420, 2016.

[298] K. B. Petersen and M. S. Pedersen. The Matrix Cookbook, version Nov. 14, 2008.

[299] A. Szorkovszky, A. C. Doherty, G. I. Harris, and W. P. Bowen. Mechanical Squeezing via Parametric Amplification and Weak Measurement. *Physical Review Letters*, 107:213603, 2011.

[300] R. Filip, P. Marek, and U. L. Andersen. Measurement-induced continuous-variable quantum interactions. *Physical Review A*, 71:042308, 2005.

[301] D. Kohen, C. C. Marston, and D. J. Tannor. Phase space approach to theories of quantum dissipation. *The Journal of Chemical Physics*, 107 (13):5236–5253, 1997.

[302] S. Joshi, S. Hung, and S. Vengallatore. Design strategies for controlling damping in micromechanical and nanomechanical resonators. *EPJ Techniques and Instrumentation*, 1 (5):1–14, 2014.

[303] V. Cimalla, J. Pezoldt, and A. Ambacher. Group III nitride and SiC based MEMS and NEMS: materials properties, technology and applications. *Journal of Physics D: Applied Physics*, 40:6386–6434, 2007.

[304] K. Brueckner, F. Niebelschuetz, K. Tonisch, C. Foerster, V. Cimala, R. Stephan, J. Pezoldt, T. Stauden, O. Ambacher, and M. A. Hein. Micro- and nano-electromechanical resonators based on SiC and group III-nitrides for sensor applications. *Physica Status Solidi A*, 208 (2):357–376, 2011.

[305] C. A. Zorman and R. J. Parro. Micro- and nanomechanical structures for silicon carbide MEMS and NEMS. *Physica Status Solidi B*, 245 (7):1404–1424, 2008.

[306] P. Kurzawski, C. Hagleitner, and A. Hierlemann. Detection and discrimination capabilities of a multitransducer single-chip gas sensor system. *Analytical Chemistry*, 78 (19):6910–6920, 2006.

[307] D. Yi, A. Greve, J. H. Hales, L. R. Senesac, Z. J. Davis, D. M. Nicholson, A. Boisen, and T. Thundat. Detection of adsorbed explosive molecules using thermal response of suspended microfabricated bridges. *Applied Physics Letters*, 93 (15):154102, 2008.

[308] A. Greve, J. Olsen, N. Privorotskaya, L. Senesac, T. Thundat, W. P. King, and A. Boisen. Micro-calorimetric sensor for vapor phase explosive detection with optimized heat profile. *Microelectronic Engineering*, 87 (5):696–698, 2010.

[309] J. Pei, F. Tian, and T. Thundat. Glucose biosensor based on the microcantilever. *Analytical Chemistry*, 76 (2):292–297, 2004.

[310] X. Yan, H. F. Ji, and Y. Lvov. Modification of microcantilevers using layer-by-layer nanoassembly film for glucose measurement. *Chemical Physics Letters*, 396 (1):34–37, 2004.

[311] J. Fritz, M. K. Baller, H. P. Lang, H. Rothuizen, P. Vettiger, E. Meyer, H.-J. Güntherodt, C. Gerber, and J. K. Gimzewski. Translating Biomolecular Recognition into Nanomechanics. *Science*, 288 (5464):316–318, 2000.

[312] B. Ilic, D. Czaplewski, M. Zalalutdinov, H. G. Craighead, P. Neuzil, C. Campagnolo, and C. Batt. Single cell detection with micromechanical oscillators. *Journal of Vacuum Science and Technology B*, 19 (6):2825–2828, 2001.

[313] A. Boisen, S. R. Dohn, S. S. Keller, S. Schmid, and M. Tenje. Cantilever-like micromechanical sensors. *Reports on Progress in Physics*, 74:036101, 2011.

[314] K. E. Spear and J. P. Dismukes. *Synthetic diamond: emerging CVD science and technology*, volume 25. John Wiley & Sons, 1994.

[315] P. A. Alekseev, M. S. Dunaevskii, A. V. Stovpyaga, M. Lepsa, and A. N. Titkov. Measurements of Young's Modulus of GaAs Nanowires Growing Obliquely on a Substrate. *Semicoductors*, 46 (5):659–664, 2012.

[316] M. E. Levinshtein, S. L. Rumyantsev, and M. S. Shur, editors. *Properties of Advanced Semiconductor Materials: GaN, AIN, InN, BN, SiC, SiGe*. John Wiley & Sons, Inc., 2001.

[317] F. Iacopi, G. Walker, L. Wang, L. Malesys, S. Ma, B. V. Cunning, and A. Iacopi. Orientation-dependent stress relaxation in hetero-epitaxial 3C-SiC films. *Applied Physics Letters*, 102:011908, 2013.

[318] N. G. Wright and Kirk-Othmer, editors. *Encyclopedia of Chemical Technology*. John Wiley & Sons, Inc., 2007.

[319] Z. Jiang, D. E. Leaird, J. Caraquitena, A. M. Weiner, C.-B. Huang, D. Leaird, J. Caraquitena, and A. Weiner. Spectral line-by-line shaping for optical and microwave arbitrary waveform generations. *Laser & photonics reviews.*, 2 (4):227–248, 2008.

[320] B. El-Kareh. *Fundamentals of Semiconductor Processing Technology*. Springer Science and Business Media, 1995.

[321] A. R. Kermany, G. Brawley, N. Mishra, E. Sheridan, W. P. Bowen, and F. Iacopi. Microresonators with *Q*-factors over a million from highly stressed epitaxial silicon carbide on silicon. *Applied Physics Letters*, 104:081901, 2014.

[322] A. Severino, C. Locke, R. Anzalone, M. Camarda, N. Piluso, A. La Magna, S. E. Saddow, G. Abbondanza, G. D'Arrigo, and F. La Via. 3C-SiC film growth on Si substrates. *ECS Transactions*, 35 (6):99–116, 2011.

[323] P. M. Sarro. Silicon carbide as a new MEMS technology. *Sensors and Actuators A: Physical*, 82:210–218, 2000.

[324] N. G. Wright and A. B. Horsfall. SiC sensors: a review. *Journal of Physics D: Applied Physics*, 40:6345–6354, 2007.

[325] H.-p. Phan, D. V. Dao, K. Nakamura, S. Dimitrijev, and N.-T. Nguyen. The Piezoresistive Effect of SiC for MEMS Sensors at High Temperatures: A Review. *Journal of Microelectromechanical Systems*, 24 (6):1663–1677, 2015.

[326] R. G. Azevedo, D. G. Jones, A. V. Jog, B. Jamshidi, D. R. Myers, L. Chen, X.-A. Fu, M. Mehregany, M. B. J. Wijesundara, and A. P. Pisano. A SiC MEMS Resonant Strain Sensor for Harsh Environment Applications. *IEEE Sensors Journal*, 7 (4):568–576, 2007.

[327] J. M. Leger, J. Haines, and B. Blanzat. Materials potentially harder than diamond: Quenchable high-pressure phases of transition metal dioxides. *Journal of Materials Science Letters*, 13:1688–1690, 1994.

[328] A. Pradeepkumar, N. Mishra, A. R. Kermany, J. J. Boeckl, J. Hellerstedt, M. S. Fuhrer, and F. Iacopi. Catastrophic degradation of the interface of epitaxial silicon carbide on silicon at high temperatures. *Applied Physics Letters*, 109:011604, 2016.

[329] A. Ellison, J. Zhang, J. Peterson, A. Henry, Q. Wahab, J. P. Bergman, Y. N. Makarov, A. Vorob'ev, A. Vehanen, and E. Janzén. High temperature CVD growth of SiC. *Materials Science and Engineering B*, 61:113–120, 1999.

[330] C. A. Zorman, A. J. Fleischman, A. S. Dewa, M. Mahregany, C. Jacob, S. Nishino, and P. Pirouz. Epitaxial growth of 3C-Sic films on 4 in. diam (100) silicon wafers by atmospheric pressure chemical vapor deposition. *Journal of Applied Physics*, 78 (8):5136, 1995.

[331] M. Syvajarvi, R. Yakimova, H. H. Radamson, N. T. Son, Q. Wahab, I. G. Ivanov, and E. Janze. Liquid phase epitaxial growth of SiC. *Journal of Crystal Growth*, 197:147–154, 1999.

[332] Y. Chen and K. Sun. Unified Matrix Presentation of Maxwell's and Wave Equations Using Generalized Differential Matrix Operators. *IEEE Transactions on Education*, 41 (1):61–69, 1998.

[333] S. Nishino, J. A. Powell, and H. A. Will. Production of large-area single-crystal wafers of cubic SiC for semiconductor devices. *Applied Physics Letters*, 42 (5):460–462, 1983.

[334] L. Wang, S. Dimitrijev, J. Han, A. Iacopi, L. Hold, P. Tanner, and H. B. Harrison. Growth of 3CSiC on 150-mm Si (100) substrates by alternating supply epitaxy at 1000°C. *Thin Solid Films*, 519:6443–6446, 2011.

[335] R. Anzalone, A. Severino, G. D' Arrigo, C. Bongiorno, G. Abbondanza, G. Foti, S. Saddow, and F. La Via. Heteroepitaxy of 3C-SiC on different on-axis oriented silicon substrates. *Journal of Applied Physics*, 105:084910, 2009.

[336] N. Mishra, L. Hold, A. Iacopi, B. Gupta, N. Motta, and F. Iacopi. Controlling the surface roughness of epitaxial SiC on silicon. *Journal of Applied Physics*, 115:203501, 2014.

[337] F. Iacopi, R. E. Brock, A. Iacopi, L. Hold, and R. H. Dauskardt. Evidence of a highly compressed nanolayer at the epitaxial silicon carbide interface with silicon. *Acta Materialia*, 61:6533–6540, 2013.

[338] J. Pezoldt, O. Ambacher, M. P. M., P. Weih, and C. Zgheib. Stress Control in 3C-SiC Films Grown on Si(111). In *Silicon Carbide and Related Materials 2003*, volume 457 of *Materials Science Forum*, pages 301–304. Trans Tech Publications, 2004.

[339] J. Pezoldt, R. Nader, F. Niebelschütz, V. Cimalla, T. Stauden, C. Zgheib, and P. Masri. Stress and stress monitoring in SiC-Si heterostructures. *Physica Status Solidi A*, 205 (4):867–871, 2008.

[340] R. Anzalone, M. Camarda, C. Locke, D. Alquier, A. Severino, M. Italia, D. Rodilosso, C. Tringali, A. La Magna, G. Foti, S. E. Saddow, F. La Via, and G. D' Arrigo. Low Stress Heteroepitaxial 3C-SiC Films Characterized by Microstructure Fabrication and Finite Elements Analysis. *Journal of the Electrochemical Society*, 157 (4):438–442, 2010.

[341] M. Zielinski, J. F. Michaud, S. Jiao, T. Chassagne, A. E. Bazin, A. Michon, M. Portail, and D. Alquier. Experimental observation and analytical model of the stress gradient inversion in 3C-SiC layers on silicon. *Journal of Applied Physics*, 111:053507, 2012.

[342] G. Stemme. Resonant silicon sensors. *Journal of Micromechanics and Microengineering*, 1:113–125, 1991.

[343] R. D. Blevins and R. Plunkett. Formulas for natural frequency and mode shape. *Journal of Applied Mechanics*, 47:461, 1980.

[344] H. Yamaguchi, K. Kato, Y. Nakai, K. Onomitsu, S. Warisawa, and S. Ishihara. Improved resonance characteristics of GaAs beam resonators by epitaxially induced strain. *Applied Physics Letters*, 92 (25):251913, 2008.

[345] Y. J. Yi, Y. D. Kim, J. H. Bak, S. R. Lee, K. Heo, S. Hong, K. Char, and Y. D. Park. Effects of tensile stress on the resonant response of Al thin-film and Al-CNT nanolaminate nanomechanical beam resonators. *Current Applied Physics*, 11 (3):746–749, 2011.

[346] Y. T. Yang, K. L. Ekinci, X. M. H. Huang, L. M. Schiavone, M. L. Roukes, C. A. Zorman, and M. Mehregany. Monocrystalline silicon carbide nanoelectromechanical systems. *Applied Physics Letters*, 78 (2):162–164, 2001.

[347] A. W. McFarland, M. A. Poggi, L. A. Bottomley, and J. S. Colton. Characterization of microcantilevers solely by frequency response acquisition. *Journal of Micromechanics and Microengineering*, 15 (4):785, 2005.

[348] N. V. Lavrik, M. J. Sepaniak, and P. G. Datskos. Cantilever transducers as a platform for chemical and biological sensors. *Review of scientific instruments*, 75 (7):2229–2253, 2004.

[349] S. S. Verbridge, J. M. Parpia, R. B. Reichenbach, L. M. Bellan, and H. G. Craighead. High quality factor resonance at room temperature with nanostrings under high tensile stress. *Journal of Applied Physics*, 99 (12):124304, 2006.

[350] R. Sandberg, K. Mølhave, A. Boisen, and W. Svendsen. Effect of gold coating on the Q-factor of a resonant cantilever. *Journal of Micromechanics and Microengineering*, 15 (12):2249, 2005.

[351] F. R. Blom, S. Bouwstra, M. Elwenspoek, and J. H. J. Fluitman. Dependence of the quality factor of micromachined silicon beam resonators on pressure and geometry. *Journal of Vacuum Science and Technology B*, 10 (1):19–26, 1992.

[352] H. Hosaka, K. Itao, and S. Kuroda. Damping characteristics of beam-shaped micro-oscillators. *Sensors and Actuators A: Physical*, 49 (1):87–95, 1995.

[353] W. E. Newell. Miniaturization of tuning forks. *Science*, 161 (3848):1320–1326, 1968.

[354] K. M. Goeders, J. S. Colton, and L. A. Bottomley. Microcantilevers: Sensing Chemical Interactions via Mechanical Motion. *Chemical Review*, 108:522–542, 2008.

[355] M. Imboden and P. Mohanty. Dissipation in nanoelectromechanical systems. *Physics Reports*, 534(3):89–146, 2014.

[356] S. Schmid, L. G. Villanueva, and M. L. Roukes. *Fundamentals of Nanomechanical Resonators*. Springer, 2016.

[357] M. C. Cross and R. Lifshitz. Elastic wave transmission at an abrupt junction in a thin plate with application to heat transport and vibrations in mesoscopic systems. *Physical Review B: Condensed Matter*, 64 (8):085324, 2001.

[358] D. M. Photiadis and J. A. Judge. Attachment losses of high Q oscillators. *Applied Physics Letters*, 85 (3):482–484, 2004.

[359] S. W. Yoon, S. Lee, N. C. Perkins, and K. Najafi. Analysis and wafer-level design of a high-order silicon vibration isolator for resonating MEMS devices. *Journal of Micromechanics and Microengineering*, 21 (1):015017, 2010.

[360] B. P. Harrington and R. Abdolvand. In-plane acoustic reflectors for reducing effective anchor loss in lateral–extensional MEMS resonators. *Journal of Micromechanics and Microengineering*, 21 (8):085021, 2011.

[361] K. Wang, A. C. Wong, and C. C. Nguyen. VHF free-free beam high-Q micromechanical resonators. *Journal of Microelectromechanical Systems*, 9 (3):347–360, 2000.

[362] S. Mohammadi and A. Adibi. Waveguide-based phononic crystal micro/nanomechanical high-Q resonators. *Journal of Microelectromechanical Systems*, 21 (2):379–384, 2012.

[363] Y. Tsaturyan, A. Barg, E. S. Polzik, and A. Schliesser. Ultracoherent nanomechanical resonators via soft clamping and dissipation dilution. *Nature Nanotechnology*, Advanced online publication, 2017.

[364] S. Prabhakar and S. Vengallatore. Theory of thermoelastic damping in micromechanical resonators with two-dimensional heat conduction. *Journal of Microelectromechanical Systems*, 17 (2):494–502, 2008.

[365] K. Y. Yasumura, T. D. Stowe, E. M. Chow, T. Pfafman, T. W. Kenny, B. C. Stipe, and D. Rugar. Quality factors in micron-and submicron-thick cantilevers. *IEEE Journal of Microelectromechanical Systems*, 9 (1):117–125, 2000.

[366] R. Lifshitz and M. L. Roukes. Thermoelastic damping in micro-and nanomechanical systems. *Physical Review B: Condensed Matter*, 61 (8):5600, 2000.

[367] D. Ramos, J. Tamayo, J. Mertens, M. Calleja, and A. Zaballos. Origin of the response of nanomechanical resonators to bacteria adsorption. *Journal of Applied Physics*, 100 (10):106105, 2006.

[368] A. K. Naik, M. S. Hanay, W. K. Hiebert, X. L. Feng, and M. L. Roukes. Towards single-molecule nanomechanical mass spectrometry. *Nature nanotechnology*, 4 (7):445–450, 2009.

[369] E. Buks and B. Yurke. Mass detection with a nonlinear nanomechanical resonator. *Physical Review E: Statistical Physics, Plasmas, Fluids, and Related Interdisciplinary Topics*, 74 (4):046619, 2006.

[370] M. H. Kim, D. Kim, J. B. Choi, and M. K. Kim. Vibrational characteristics of graphene sheets elucidated using an elastic network model. *Physical Chemistry Chemical Physics*, 16 (29):15263–15271, 2014.

[371] R. T. Howe and R. S. Muller. Resonant-microbridge vapor sensor. *IEEE Transactions on Electron Devices*, 33 (4):499–506, 1986.

[372] P. S. Waggoner and H. G. Craighead. Micro-and nanomechanical sensors for environmental, chemical, and biological detection. *Lab on a Chip*, 7 (10):1238–1255, 2007.

[373] M. A. Taylor, A. Szorkovszky, J. Knittel, K. H. Lee, T. G. McRae, and W. P. Bowen. Cavity optoelectromechanical regenerative amplification. *Optics Express*, 20 (12):12742–12751, 2012.

[374] A. Gupta, D. Akin, and R. Bashir. Single virus particle mass detection using microresonators with nanoscale thickness. *Applied Physics Letters*, 84 (11):1976–1978, 2004.

[375] B. Ilic, Y. Yang, K. Aubin, R. Reichenbach, S. Krylov, and H. G. Craighead. Enumeration of DNA molecules bound to a nanomechanical oscillator. *Nano letters*, 5 (5):925–929, 2005.

[376] K. Ekinci, X. Huang, and M. Roukes. Ultrasensitive nanoelectromechanical mass detection. *Applied Physics Letters*, 84 (22):4469–4471, 2004.

[377] Y. T. Yang, C. Callegari, X. L. Feng, K. L. Ekinci, and M. L. Roukes. Zeptogram-scale nanomechanical mass sensing. *Nano letters*, 6 (4):583–586, 2006.

[378] K. Jensen, K. Kim, and A. Zettl. An atomic-resolution nanomechanical mass sensor. *Nature nanotechnology*, 3 (9):533–537, 2008.

[379] X. L. Feng, C. A. Zorman, M. Mehregany, and M. L. Roukes. Dissipation in single-crystal 3C-SiC ultra-high frequency nanomechanical resonators. *Solid-State Sensor, Actuator and Microsystems Workshop*, page 8689, 2006.

[380] A. Cleland and M. Roukes. External control of dissipation in a nanometer-scale radiofrequency mechanical resonator. *Sensors and Actuators A: Physical*, 72 (3):256–261, 1999.

[381] A. Cleland, M. Pophristic, and I. Ferguson. Single-crystal aluminum nitride nanomechanical resonators. *Applied Physics Letters*, 79 (13):2070–2072, 2001.

[382] K. L. Ekinci and M. L. Roukes. Nanoelectromechanical systems. *Review of scientific instruments*, 76 (6):061101, 2005.

[383] E. R. I. Abraham and E. A. Cornell. Teflon feedthrough for coupling optical fibers into ultrahigh vacuum systems. *Applied optics*, 37 (10):1762–1763, 1998.

[384] A. R. Kermany and F. Iacopi. Controlling the intrinsic bending of hetero-epitaxial silicon carbide micro-cantilevers. *Journal of Applied Physics*, 118 (15):155304, 2015.

[385] C. Reinhardt, T. Müller, A. Bourassa, and J. C. Sankey. Ultralow-Noise SiN Trampoline Resonators for Sensing and Optomechanics. *Physical Review X*, 6:021001, 2016.

[386] M. J. Weaver, B. Pepper, F. Luna, F. M. Buters, H. J. Eerkens, G. Welker, B. Perock, K. Heeck, S. de Man, and D. Bouwmeester. Nested trampoline resonators for optomechanics. *Applied Physics Letters*, 108:263501, 2016.

[387] M. Samoylova, N. Piovella, G. R. M. Robb, R. Bachelard, and P. W. Courteille. Synchronization of Bloch oscillations by a ring cavity. *Optics Letters*, 23 (11):14823–14835, 2015.

[388] S. Chesi, Y.-D. Wang, and J. Twamley. Diabolical points in multi-scatterer optomechanical systems. *Scientific Reports*, 5:7816, 2015.

[389] M. Albiez, R. Gati, J. Fölling, S. Hunsmann, M. Cristiani, and M. K. Oberthaler. Direct Observation of Tunneling and Nonlinear Self-Trapping in a Single Bosonic Josephson Junction. *Physical Review Letters*, 95:010402, 2005.

[390] V. Giovannetti and D. Vitali. Phase-noise measurement in a cavity with a movable mirror undergoing quantum Brownian motion. *Physical Review A*, 63:023812, 2001.

[391] W. G. Unruh and W. H. Zurek. Reduction of a wave packet in quantum Brownian motion. *Physical Review D*, 40 (4):1071–1094, 1989.

Appendix A

Appendices

A.1 Coherent state and displacement operator properties

The displacement operator is defined by

$$\hat{D}(\alpha) = \exp\left\{\alpha a^\dagger - \alpha^* a\right\}$$

where a is the bosonic lowering operator ($\left[a, a^\dagger\right] = 1$).

The following useful properties are often employed.

$$\begin{aligned}
\hat{D}(\alpha)^\dagger \hat{D}(\alpha) &= \hat{D}(\alpha)\hat{D}(\alpha)^\dagger = 1 \\
\hat{D}(\alpha)^\dagger &= \hat{D}(-\alpha) \\
\hat{D}(\alpha)^\dagger a \hat{D}(\alpha) &= a + \alpha \\
\hat{D}(\alpha)^\dagger a^\dagger \hat{D}(\alpha) &= a^\dagger + \alpha^* \\
\hat{D}(\alpha)\hat{D}(\beta) &= \hat{D}(\alpha+\beta)\exp\left\{\frac{1}{2}(\beta^*\alpha - \alpha^*\beta)\right\}.
\end{aligned}$$

The coherent states $|\alpha\rangle$ may be generated by application of the displacement operator on the vacuum, *viz.*

$$|\alpha\rangle = \hat{D}(\alpha)|0\rangle.$$

The coherent states obey the following properties.

$$\begin{aligned}
|\alpha\rangle &= \mathrm{e}^{-\frac{1}{2}|\alpha|^2} \sum_{\mathrm{n}=0}^{\infty} \frac{\alpha^n}{\sqrt{n!}} |n\rangle \\
a|\alpha\rangle &= \alpha|\alpha\rangle \\
\langle\beta|\alpha\rangle &= \exp\left\{-\frac{1}{2}|\alpha|^2 - \frac{1}{2}|\beta|^2 + \beta^*\alpha\right\} \\
\langle\alpha|\alpha+\beta\rangle &= \exp\left\{-\frac{1}{2}|\beta|^2 + \frac{1}{2}(\alpha^*\beta - \beta^*\alpha)\right\} \\
|\langle\beta|\alpha\rangle|^2 &= \exp\left\{-|\alpha-\beta|^2\right\} \\
\mathbb{1} &= \frac{1}{\pi}\int \mathrm{d}^2\alpha\ |\alpha\rangle\langle\alpha|.
\end{aligned}$$

A.2 Thermal noise operator

The noise operator ξ has the properties [198, 249]

$$\begin{aligned}
\left\langle \xi(t)\,\xi\left(t'\right)\right\rangle &= \int_0^\infty \mathrm{d}\omega \left\{ \frac{\omega}{\pi\omega_\mathrm{M}} \coth\left(\frac{\hbar\omega}{2k_\mathrm{B}T_\mathrm{B}}\right)\cos\omega\left(t-t'\right)\right\} \\
&\quad + \frac{\mathrm{i}}{2\omega_\mathrm{M}}\left(\frac{\partial}{\partial t}-\frac{\partial}{\partial t'}\right)\delta\left(t-t'\right), \\
\left[\xi(t), X_\mathrm{M}(t)\right] &= \mathrm{i}\sqrt{2\Gamma}, \\
\left[Y(t), \xi\left(t'\right)\right] &= \frac{1}{\omega_\mathrm{M}}\sqrt{\frac{\Gamma}{2}}\frac{\mathrm{d}}{\mathrm{d}t'}\left\{u\left(t-t'\right)\left[Y(t), X_\mathrm{M}\left(t'\right)\right]\right\},
\end{aligned}$$

where u is the piecewise step function equal to $1/2$ at the origin, 1 for positive arguments and 0 otherwise. $Y(t)$ is an arbitrary system operator. These properties are necessary for preservation of the canonical commutator of X_M and P_M [249]. In the high-temperature limit (where $\hbar\omega \ll 2k_\mathrm{B}T_\mathrm{B}$ for all relevant frequencies ω) we may approximate the former by

$$\left\langle \xi(t)\,\xi\left(t'\right)\right\rangle = (2\bar{n}_\mathrm{H}+1)\,\delta\left(t-t'\right) + \frac{\mathrm{i}}{2\omega_\mathrm{M}}\left(\frac{\partial}{\partial t}-\frac{\partial}{\partial t'}\right)\delta\left(t-t'\right)$$

where $\bar{n}_\mathrm{H}$ is the average occupancy of the mechanical mode when in thermal equilibrium with its bath.

A.3 Independent oscillator model

The independent oscillator model is the most general microscopic model for a linear, passive heat bath [274, 275]. It is also the starting point for deriving the Born–Markov master equation. In the following we will provide a general outline of the derivation of Eqn (3.20) from the independent oscillator model.

A.3.1 Independent oscillator Hamiltonian

The full Hamiltonian of the system and bath is

$$\hat{H}_\mathrm{tot} = \hat{H}_\mathrm{sys} + \sum_{j=1}^{N}\left(\frac{p_j^2}{2m_j} + \frac{m_j\omega_j^2\left(x_j-x\right)^2}{2}\right),$$

where the bath oscillators $j=\{1,2,\ldots,N\}$ have frequencies ω_j and masses m_j. The system Hamiltonian $\hat{H}_\mathrm{sys}$ includes the free system Hamiltonian $\hat{H}_0$ plus any control Hamiltonians $\hat{H}_\mathrm{con}$.

If we introduce the nondimensionalised position and momentum operators then the Hamiltonian reads

$$\hat{H}_\mathrm{tot} = \hat{H}_\mathrm{sys} + \sum_{j=1}^{N}\left\{\hat{H}_j + \frac{\hbar}{4}\left(\omega_j\eta_j\left(\eta_j X^2 - 2X_j X\right)\right)\right\}. \tag{A.1}$$

in which the free Hamiltonian of a bath oscillator is $\hat{H}_j = \hbar\omega_j\left(X_j^2+P_j^2\right)/4$. We have introduced the symbol

$$\eta_j = \sqrt{\frac{m_j\omega_j}{M\omega_\mathrm{M}}}$$

which characterises the mismatch between the system oscillator's mass m and frequency ω_{M} and those of the j^{th} bath oscillator.

A.3.2 Formal solution of bath equations of motion

It is straightforward to calculate the equation of motion for the bath oscillators from (A.1), yielding

$$\frac{\mathrm{d}a_j}{\mathrm{d}t} = -i\omega_j a_j + \frac{\mathrm{i}}{2}\omega_j \eta_j X.$$

This is then integrated using the method of integrating factors, *viz.*

$$a_j(t) = a_j(t_0)\,\mathrm{e}^{-\mathrm{i}\omega_j(t-t_0)} + \mathrm{i}\frac{\omega_j\eta_j}{2}\int_{t_0}^{t}\mathrm{d}t'\,X\left(t'\right)\mathrm{e}^{\mathrm{i}\omega_j(t'-t)}. \tag{A.2}$$

A.3.3 Equation of motion for system

The Heisenberg equations of motion for the system operators are

$$\dot{X} = \frac{\mathrm{i}}{\hbar}\left[\hat{H}_{\mathrm{sys}}, X\right] \tag{A.3}$$

$$\dot{P} = \frac{\mathrm{i}}{\hbar}\left[\hat{H}_{\mathrm{sys}}, P\right] + \sum_j \omega_j\eta_j\left(X_j - \eta_j X\right). \tag{A.4}$$

Substituting (A.2) into (A.4) gives us

$$\begin{aligned}\dot{P} &= \frac{\mathrm{i}}{\hbar}\left[\hat{H}_{\mathrm{sys}}, P\right] + \sum_j \omega_j\eta_j\left\{X_j(t_0)\cos\omega_j(t-t_0) + P_j(t_0)\sin\omega_j(t-t_0)\right\} \\ &\quad + \sum_j \omega_j\eta_j^2\left\{-X + \omega_j\int_{t_0}^{t}\mathrm{d}t'\,X\left(t'\right)\sin\omega_j\left(t-t'\right)\right\}.\end{aligned}$$

Let us gather these terms as follows;

$$\begin{aligned}\dot{P} &= \frac{\mathrm{i}}{\hbar}\left[\hat{H}_{\mathrm{sys}}, P\right] + \mathscr{N}(t) + L(t), \\ \mathscr{N}(t) &= \sum_j \omega_j\eta_j\left\{X_j(t_0)\cos\omega_j(t-t_0) + P_j(t_0)\sin\omega_j(t-t_0)\right\}, \\ L(t) &= \sum_j \omega_j\eta_j^2\left\{-X + \omega_j\int_{t_0}^{t}\mathrm{d}t'\,X\left(t'\right)\sin\omega_j\left(t-t'\right)\right\}.\end{aligned}$$

$\mathscr{N}(t)$ is the precursor to the noise operator, whilst the loss is encapsulated by L.

A.3.4 Loss term

First we may integrate by parts to find that

$$\begin{aligned}\omega_j\int_{t_0}^{t}\mathrm{d}t'\,X\left(t'\right)\sin\omega_j\left(t-t'\right) &= X(t) - X(t_0)\cos\omega_j(t-t_0) \\ &\quad - \int_{t_0}^{t}\mathrm{d}t'\,\frac{\mathrm{i}}{\hbar}\left[\hat{H}'_{\mathrm{sys}}, X'\right]\cos\omega_j\left(t-t'\right),\end{aligned}$$

in which we made use of (A.3). Upon substitution into L we obtain

$$L = -\sum_j \omega_j \eta_j^2 \left\{ X(t_0)\cos\omega_j(t-t_0) + \int_{t_0}^{t} \mathrm{d}t' \, \frac{\mathrm{i}}{\hbar}\left[\hat{H}_{\mathrm{sys}}(t'), X(t')\right]\cos\omega_j(t-t') \right\}.$$

In order to obtain an irreversible Langevin equation we require a smooth coupling between the system and bath across a range of frequencies [70]. Let us begin by assuming the bath spectrum is bounded between 0 and Ω, and that the density of bath oscillators per frequency increment is $\frac{\mathrm{d}n}{\mathrm{d}\omega}$. We then take the continuum limit;

$$L = -\int_0^{\Omega} \mathrm{d}\omega \, \omega\eta^2(\omega)\frac{\mathrm{d}n}{\mathrm{d}\omega}\left(X(t_0)\cos\omega(t-t_0) + \int_{t_0}^{t} \mathrm{d}t' \, \frac{\mathrm{i}}{\hbar}\left[\hat{H}_{\mathrm{sys}}(t'), X(t')\right]\cos\omega(t-t') \right).$$

Assuming that the coupling to the bath is equal across frequencies is tantamount to setting $\omega\eta^2(\omega)\frac{\mathrm{d}n}{\mathrm{d}\omega} = A$, with A being a constant.

Now we follow [390] and introduce

$$\check{\delta}(\tau) = \frac{1}{\pi}\int_0^{\Omega} \mathrm{d}\omega \, \cos\omega\tau$$

such that

$$\lim_{\Omega\to\infty} \check{\delta}(\tau) = \delta(\tau).$$

and hence write

$$L = -A\pi\left(X(t_0)\check{\delta}(t-t_0) + \int_{t_0}^{t} \mathrm{d}t' \, \frac{\mathrm{i}}{\hbar}\left[\hat{H}_{\mathrm{sys}}(t'), X(t')\right]\check{\delta}(t-t') \right).$$

Now we may separate out the contributions of $\hat{H}_0$ and $\hat{H}_{\mathrm{con}}$.

$$\begin{aligned} L = & -A\pi\left(X(t_0)\check{\delta}(t-t_0) + \int_{t_0}^{t} \mathrm{d}t' \, \omega_{\mathrm{M}} P(t')\check{\delta}(t-t') \right) \\ & -A\pi\left(\int_{t_0}^{t} \mathrm{d}t' \, \frac{\mathrm{i}}{\hbar}\left[\hat{H}_{\mathrm{con}}(t'), X(t')\right]\check{\delta}(t-t') \right). \end{aligned}$$

To fix the value of A, note that in the infinite-bath-bandwidth limit the second term becomes

$$\lim_{\Omega\to\infty}\left\{ \int_{t_0}^{t} \mathrm{d}t' \, \omega_{\mathrm{M}} P(t')\check{\delta}(t-t') \right\} = \frac{\omega_{\mathrm{M}}}{2}P(t),$$

where the factor of two arises because only half of the δ enters the integral. Thus by identifying the coefficient of this term as the decay rate Γ we see

$$-A\pi\frac{\omega_{\mathrm{M}}}{2} = -\Gamma \rightarrow A\pi = \frac{2\Gamma}{\omega_{\mathrm{M}}}.$$

It follows that

$$\begin{aligned} L = & -\frac{2\Gamma}{\omega_{\mathrm{M}}}X(t_0)\check{\delta}(t-t_0) - 2\Gamma\int_{t_0}^{t} \mathrm{d}t' \, P(t')\check{\delta}(t-t') \\ & -\frac{2\Gamma}{\omega_{\mathrm{M}}}\int_{t_0}^{t} \mathrm{d}t' \, \frac{\mathrm{i}}{\hbar}\left[\hat{H}_{\mathrm{con}}(t'), X(t')\right]\check{\delta}(t-t'). \end{aligned} \tag{A.5}$$

The first line of (A.5) is precisely that expected, giving a momentum-dependent loss at rate Γ (in the $\Omega\to\infty$ limit) and an 'initial slip' term that is negligibly small in the case that $Q \gg 1$. Note that there is an unexpected third contribution which is not typically included in the Langevin equation, arising from the 'control' Hamiltonian. This could be expected to contribute in the case that $\hat{H}_{\mathrm{con}}$ fails to commute with X, as is the case for a squeezing operation. However, unless the control Hamiltonian is extremely strongly coupled the $1/Q$ dependence of the extra term will render it unimportant.

A.4 Multimode Wigner functions

Consider n modes with quadrature operators $X_j = a_j^\dagger + a_j$ and $P_j = \mathrm{i}\left(a_j^\dagger - a_j\right)$. For any valid density operator $\hat{\rho}$ over these modes one may calculate the characteristic function

$$\chi(\beta) = \mathrm{Tr}\left\{\hat{\rho}\hat{D}(\boldsymbol{\beta})\right\},$$

where the multimode displacement operator is simply the product of single mode displacements, *à la*

$$\hat{D}(\boldsymbol{\beta}) = \hat{D}(\beta_1) \otimes \hat{D}(\beta_2) \otimes \cdots \otimes \hat{D}(\beta_n).$$

In general, $\chi(\boldsymbol{\beta})$ is a complex-valued function of $\boldsymbol{\beta} \in \mathbb{C}$. It will be convenient to consider $\boldsymbol{\beta}$ as having the form of a $2n$-long vector with real elements.

$$\boldsymbol{\beta} = \begin{pmatrix} \Re\{\beta_1\} \\ \Im\{\beta_1\} \\ \Re\{\beta_2\} \\ \Im\{\beta_2\} \\ \vdots \end{pmatrix}.$$

The corresponding Wigner function lives on the phase space composed of $2n$ real variables, which we shall write as a $2n$ vector

$$\boldsymbol{r} = \begin{pmatrix} \boldsymbol{r}_1 \\ \boldsymbol{r}_2 \\ \vdots \end{pmatrix}$$

where each $\boldsymbol{r}_j = \left(x_j,\, p_j\right)^{\mathrm{T}}$ represents a point in the plane formed by the eigenspectra of X_j and P_j.

The Wigner function is given by

$$W(\boldsymbol{r}) \;=\; \frac{1}{(2\pi)^{2n}} \int \mathrm{d}^{2n}\boldsymbol{\beta}\, \mathrm{Tr}\left\{\hat{\rho}\hat{D}(\boldsymbol{\beta})\right\} \exp\left\{-\mathrm{i}\boldsymbol{r}\cdot\Omega\boldsymbol{\beta}\right\}, \tag{A.6}$$

in which the $2n \times 2n$ matrix Ω is the n-fold block diagonal matrix with diagonal blocks

$$\boldsymbol{\varpi} = \begin{pmatrix} 0 & 1 \\ -1 & 0 \end{pmatrix}$$

and all other entries equal to zero (note that $\Omega^{\mathrm{T}} = -\Omega$ and $\Omega\,\Omega^{\mathrm{T}} = \Omega^{\mathrm{T}}\Omega = -\mathbb{1}$). The inverse transformation is

$$\chi(\boldsymbol{\beta}) = \int \mathrm{d}^{2n}\boldsymbol{r}\, W(\boldsymbol{r}) \exp\left\{+\mathrm{i}\boldsymbol{r}\cdot\Omega\boldsymbol{\beta}\right\}.$$

All properties of the multimode Wigner function are essentially identical to those of the single-mode, with appropriate generalisation of the phase space representations of operators. However, it is worth noting that the reduced density operator for mode j is represented by

$$W_j\left(\boldsymbol{r}_j\right) = \left\{\prod_{\mathrm{k}=1,\,\mathrm{k}\neq\mathrm{j}}^{n} \int \mathrm{d}^2\boldsymbol{r}_k\right\} W(\boldsymbol{r}).$$

The corresponding characteristic function is simply $\chi(\boldsymbol{\beta})$ evaluated with all $\beta_{k\neq j} = 0$.

A.5 Dirac Delta properties

The Dirac delta distribution is represented as δ, and has the properties

$$\int_{-\infty}^{\infty} \mathrm{d}t\ \delta(t) = 1 \tag{A.7a}$$

$$\int_{-\infty}^{\infty} \mathrm{d}t\ \delta(t-\tau) f(t) = f(\tau) \tag{A.7b}$$

$$\int_{\tau-\varepsilon}^{\tau+\varepsilon} \mathrm{d}t\ \delta(t-\tau) f(t) = f(\tau)\ \forall\ \varepsilon > 0 \tag{A.7c}$$

$$\int_{-\infty}^{\infty} \mathrm{d}t\ \frac{\mathrm{d}\delta(t)}{\mathrm{d}t} f(t) = -\left.\frac{\mathrm{d}f}{\mathrm{d}t}\right|_{\mathrm{t}=0}. \tag{A.7d}$$

.

We also have the key relationships (for $c \in \mathbb{R}$)

$$\delta(\omega) = \frac{1}{2\pi}\int_{-\infty}^{\infty} \mathrm{d}t\ \mathrm{e}^{\mathrm{i}\omega t}$$

$$\int_{-\infty}^{\infty} \mathrm{d}t\ \mathrm{e}^{\mathrm{i}c\omega t} = \frac{\delta(\omega)}{c},$$

which underpin Eqn (A.9f) and Eqn (A.9g).

A.6 Time–frequency domain relations

A number of useful relationships between the time and frequency domain can be established;

$$f(t) \Leftrightarrow \tilde{f}(\omega) \tag{A.9a}$$

$$\frac{\mathrm{d}f}{\mathrm{d}t} \Leftrightarrow -\mathrm{i}\omega\tilde{f}(\omega) \tag{A.9b}$$

$$\frac{\mathrm{d}^2 f}{\mathrm{d}t^2} \Leftrightarrow -\omega^2\tilde{f}(\omega) \tag{A.9c}$$

$$f(t+\tau) \Leftrightarrow \tilde{f}(\omega)\,\mathrm{e}^{-\mathrm{i}\omega\tau} \tag{A.9d}$$

$$f(t)\,\mathrm{e}^{\mathrm{i}\Omega t} \Leftrightarrow \tilde{f}(\omega+\Omega) \tag{A.9e}$$

$$c \Leftrightarrow 2\pi c\,\delta(\omega) \tag{A.9f}$$

$$c\,\delta(t) \Leftrightarrow c. \tag{A.9g}$$

In these relations τ is an arbitrary time delay, Ω is an arbitrary frequency, and c is a constant. Note that there is an important phase relationship between positive and negative frequencies when the time domain function (operator) is everywhere real (Hermitian), namely

$$f(t) \in \mathbb{R}\ \forall\ t \Leftrightarrow \tilde{f}(\omega) = \tilde{f}^{\dagger}(-\omega).$$

In general, the Fourier transform of the Hermitian conjugate of an operator is *not* equal to the Hermitian conjugate of the Fourier transform of that operator. We will use $\tilde{f}^{\dagger}$ to refer to the conjugate of the transform.

A.7 Alternative lossy mechanical squeezing model

As discussed in Chapter 6, a conceptually clean model of a lossy squeezer is to subdivide each squeezer S'_j into a perfect squeezing step S_j followed by a beamsplitter operation with a cold thermal mode. However, one might suspect that in a physical implementation of the squeezer S'_j the cold bath temperature would potentially be a function of μ due to effects such as pump depletion. We will therefore consider a slightly more complicated model, and show that it reproduces essentially the same predictions for low to moderate μ.

Instead of subdividing S' into one perfect squeezer and one beamsplitter we will consider subdividing it into $2N$ substeps of perfect squeezing followed by loss on a beamsplitter. Each sub-squeezer squeezes by an amount $\mu_k = \mu^{1/N}$, such that the net squeezing parameter (in the absence of loss) is $\mu = \Pi_{k=1}^{N} \mu_k$. Similarly, each attenuation step is characterised by $\varepsilon_k = 1-(1-\varepsilon)^{1/N}$, such that the total attenuation is $1-\varepsilon$.

After one substep (k) of squeezing and loss we have

$$V^{(1)} = (1-\varepsilon_k)\, S_k\, V^{(0)}\; S_k^{\mathrm{T}} + \varepsilon_k\,(2\bar{n}_{\mathrm{C}}+1)\,\mathbb{1},$$

then

$$\begin{aligned}
V^{(2)} &= (1-\varepsilon_k)^2\, S_k^2\, V^{(0)}\; {S_k^{\mathrm{T}}}^2 + (1-\varepsilon_k)\,\varepsilon_k\,(2\bar{n}_{\mathrm{C}}+1)\, S_k\, S_k^{\mathrm{T}} + \varepsilon_k\,(2\bar{n}_{\mathrm{C}}+1)\,\mathbb{1} \\
V^{(3)} &= (1-\varepsilon_k)^3\, S_k^3\, V^{(0)}\; {S_k^{\mathrm{T}}}^3 + (1-\varepsilon_k)^2\,\varepsilon_k\,(2\bar{n}_{\mathrm{C}}+1)\, S_k^2\, {S_k^{\mathrm{T}}}^2 + \\
&\quad (1-\varepsilon_k)\,\varepsilon_k\,(2\bar{n}_{\mathrm{C}}+1)\, S_k\, S_k^{\mathrm{T}} + \varepsilon_k\,(2\bar{n}_{\mathrm{C}}+1)\,\mathbb{1} \\
&\cdots \\
V^{(N)} &= (1-\varepsilon_k)^N\, S_k^N\, V^{(0)}\; {S_k^{\mathrm{T}}}^N + \varepsilon_k\,(2\bar{n}_{\mathrm{C}}+1) \sum_{k=0}^{N-1} (1-\varepsilon_k)^k\, S_k^k\, {S_k^{\mathrm{T}}}^k.
\end{aligned}$$

Taking the $N\to\infty$ limit then yields the full model of the squeezer

$$\begin{aligned}
V &= \lim_{\mathrm{N}\to\infty} V^{(N)} \qquad\qquad (A.10)\\
&= (1-\varepsilon)\, S\, V^{(0)}\; S^{\mathrm{T}} + \ln(1-\varepsilon)\,(2\bar{n}_{\mathrm{C}}+1)\,\mathrm{diag}\left\{ \frac{1-(1-\varepsilon)\,\mu^{-2}}{\ln(1-\varepsilon)-2\ln\mu}, \frac{1-(1-\varepsilon)\,\mu^{+2}}{\ln(1-\varepsilon)+2\ln\mu} \right\}.
\end{aligned}$$

The homogeneous component of the evolution is the same as the simple model, but the added noise is now a function of μ in addition to ε and $\bar{n}_{\mathrm{C}}$.

We have not employed this model in Chapter 6 because it yields results that are qualitatively very similar to the simpler two-step squeezer model in the regime of interest. An example of this is shown in Fig. A.1.

A.8 Sylvester equations

The general Sylvester equation reads

$$AV + VB = C$$

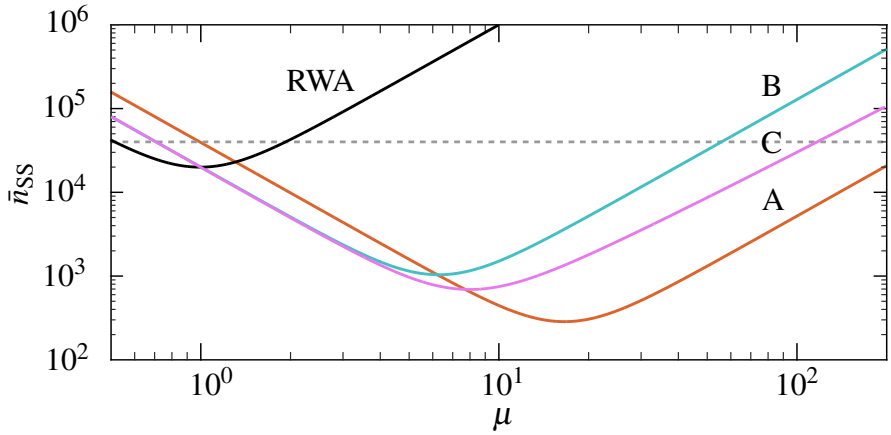

Figure A.1: Comparison of the steady-state occupancy $\bar{n}_{SS}$ as a function of squeezing parameter μ for three noise models. Line A shows the result for perfect squeezing operations; line B incorporates the simple lossy squeezing model employed in the main text; and line C is calculated using the more complicated loss model described above. Note that B and C agree well at low-to-moderate μ. Parameters are given in the main text (lines A and B are identical to Fig. 6.3 panel *iii*)).

where A, V and C are $n \times n$ matrices. The solution is [298]

$$\mathrm{vec}\{V\} = \left(\mathbb{1} \otimes A + B^{\mathrm{T}} \otimes \mathbb{1}\right)^{-1} \mathrm{vec}\{C\},$$

given in terms of the vectorisation operation ($\mathrm{vec}\{\cdots\}$) and the Kronecker product ($\otimes$).

The Kronecker product of two $n \times n$ matrices is defined by

$$A \otimes B = \begin{pmatrix} A_{11}B & A_{12}B & \cdots & A_{1n}B \\ A_{21}B & A_{22}B & \cdots & A_{2n}B \\ \vdots & & & \vdots \\ A_{11}B & A_{12}B & \cdots & A_{nn}B \end{pmatrix}.$$

The vectorisation operation 'stacks' the columns of a matrix on top of one another to produce a larger vector. For a 2×2 matrix V,

$$\mathrm{vec}\{V\} = \begin{pmatrix} V_{11} \\ V_{21} \\ V_{21} \\ V_{22} \end{pmatrix}.$$

This has the useful property that $\mathrm{vec}\{AVB\} = \left(B^{\mathrm{T}} \otimes A\right) \mathrm{vec}\{V\}$.

A.9 Squeezed optical pulses

An input field with fluctuations $\delta a_{\mathrm{d}}(t)$ that are squeezed across a wide frequency band satisfies

$$\begin{aligned} \langle \delta a_{\mathrm{d}}(t) \rangle &= 0, \\ \langle \delta a(t+\tau)\, \delta a(t) \rangle &= M\delta(\tau), \\ \left\langle \delta a^{\dagger}(t+\tau)\, \delta a(t) \right\rangle &= N\delta(\tau), \end{aligned}$$

where $N \in \mathbb{R}$ and $M \in \mathbb{C}$ are constrained by the Heisenberg uncertainty induced by $\left[a(t), a^{\dagger}(t+\tau)\right] = \delta(\tau)$ (as in Chapter 10 of [198]). It is straightforward to confirm that the resulting collective pulse quadratures X_{L} and P_{L} are also squeezed, with a complex squeezing parameter $\xi = r_{\mathrm{s}} \mathrm{e}^{\mathrm{i}2\theta_{\mathrm{s}}}$, *viz.*

$$\begin{aligned} N &= \frac{1}{2}\left(\cosh(2r_{\mathrm{s}}) - 1\right), \\ M &= -\frac{1}{2}\sinh(2r_{\mathrm{s}})\,\mathrm{e}^{+\mathrm{i}2\theta_{\mathrm{s}}}, \end{aligned}$$

A.10 Notes on Markovian master equations

Markovian master/Langevin equations are an incredibly useful tool in quantum optomechanics (amongst many, many other disciplines within quantum mechanics). It therefore came as a great surprise to never encounter the following theorem in the optomechanics literature;

"No Markovian theory can satisfy all three criteria of positivity, translational invariance, and asymptotic approach to the canonical equilibrium state [...] except in special cases." [301].

Consequently, any Markovian theory must violate at least one of these criteria.

1. An equation of motion that preserves positivity guarantees that an arbitrary (physical) initial state evolves into a physical state for any time t. In other words, it preserves the trace of the density operator. If an equation of evolution violates positivity then there exists physical states that are mapped onto non-physical (*e.g.* non-normalised, Heisenberg-uncertainty-violating) states at later times.
2. 'Translational invariance' means that there is no position-dependent loss in the equations of motion. We might reasonably expect this property to hold for many systems, such as mechanical oscillators.
3. Finally, a system that asymptotically approaches the canonical equilibrium state satisfies

$$\lim_{t\to\infty} \hat{\rho} = \frac{\mathrm{e}^{-\beta \hat{H}_{\mathrm{sys}}}}{\mathrm{Tr}\left\{\mathrm{e}^{-\beta \hat{H}_{\mathrm{sys}}}\right\}} \tag{A.11}$$

   where $\beta = 1/k_{\mathrm{B}}T$ is the inverse temperature and $\hat{H}_{\mathrm{sys}}$ is the free Hamiltonian of the system. The right-hand side of Eqn (A.11) is recognisable as the quantum generalisation of the Gibbs ensemble. This can be violated by either approaching a steady-state that is not the Gibbs ensemble of $\hat{H}_{\mathrm{sys}}$, or by never reaching a steady-state at all.

The momentum-damped Langevin equations (Eqn (3.20)) that we have used throughout this work clearly satisfy properties 2 and 3 (consider Eqn (3.25)), hence must violate property 1. This is indeed the case. To see this, set the bath temperature to zero and then propagate a momentum-squeezed state through a short time of evolution; the result violates the Heisenberg uncertainty principle. However, we stress that this equation of motion can be positive for arbitrary initial states provided that the bath temperature is sufficiently high.

It is worth noting that any equation of Lindblad form maintains positivity [287].

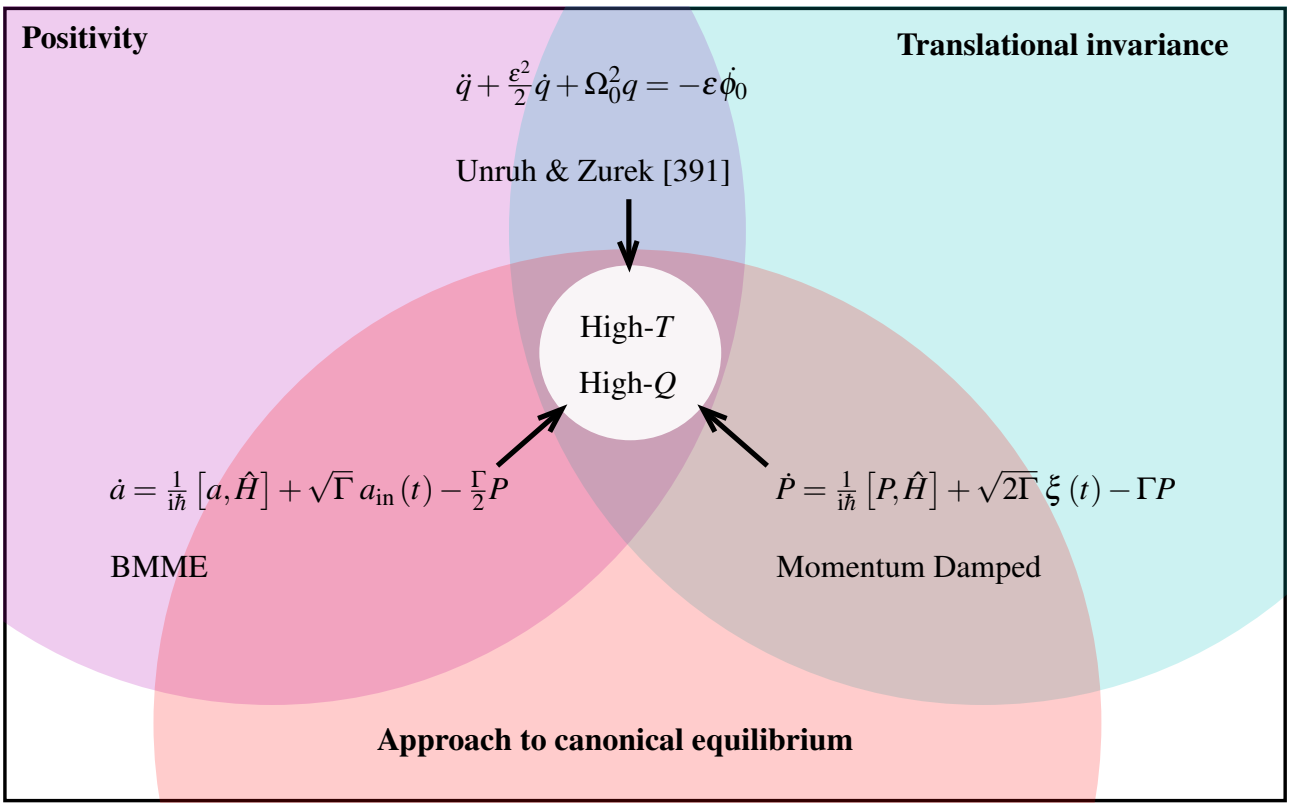

Figure A.2: Graphical summary of properties of Markovian loss theories. A Markovian theory can exactly satisfy at most two of these properties. The descriptions approximately coincide in the high-Q and high-temperature limit.

The standard Born–Markov master equation satisfies properties 1 and 3 by sacrificing property 2. This is plainly seen when the equations of motion are written in terms of quadratures (Eqn (6.2)). Of course, this is not detrimental if the oscillator is of sufficiently high-Q and one is not interested in the short-time ($t \ll \omega_{\mathrm{M}}^{1-}$) behaviour [70].

An example of the third minimal-violation case—violating property 3 in order to satisfy properties 1 and 2—is the theory of wave packet reduction developed by Unruh and Zurek [391]. This does relax towards an equilibrium state, but not the canonical (Gibbs) state.

In short, we need to be careful to select an appropriate Langevin equation based on the situation at hand. It is worth noting, however, that the majority of descriptions coincide in the high-Q, high-T limit.

A graphical representation of these is given in Fig. A.2.

"I hope no one who reads this book has been quite as miserable as Susan and Lucy were that night: but if you have been—if you've been up all night and cried till you have no more tears left in you—you will know that there comes in the end a sort of quietness."

C. S. Lewis,
'The Lion, the Witch and the Wardrobe'